



**High Power Impulse Magnetron Sputtering  
(HiPIMS): The effect of stationary magnetic field  
on the deposition rate and ionized flux fraction**

Hamidreza Hajihoseini



**Faculty of Physical Science  
University of Iceland  
2020**





# **High Power Impulse Magnetron Sputtering (HiPIMS): The effect of stationary magnetic field on the deposition rate and ionized flux fraction**

Hamidreza Hajihoseini

Dissertation submitted in partial fulfillment of a  
*Philosophiae Doctor* degree in Physics

Advisor

Dr. Jón Tómas Guðmundsson

PhD Committee

Dr. Daniel Lundin

Dr. Snorri Þorgeir Ingvarsson

Opponents

Dr. Peter J. Kelly

Dr. Matjaž Panjan

Faculty of Physical Science  
School of Engineering and Natural Sciences  
University of Iceland  
Reykjavik, May 2020

High Power Impulse Magnetron Sputtering (HiPIMS): The effect of stationary magnetic field on the deposition rate and ionized flux fraction  
High Power Impulse Magnetron Sputtering (HiPIMS)  
Dissertation submitted in partial fulfillment of a *Philosophiae Doctor* degree in Physics

Copyright © Hamidreza Hajihoseini 2020  
All rights reserved

Faculty of Physical Science  
School of Engineering and Natural Sciences  
University of Iceland  
Tæknigarði, Dunhaga 5  
107, Reykjavík  
Iceland

Telephone: 525-4000

Bibliographic information:  
Hamidreza Hajihoseini, 2020, *High Power Impulse Magnetron Sputtering (HiPIMS): The effect of stationary magnetic field on the deposition rate and ionized flux fraction*, PhD dissertation, Faculty of Physical Science, University of Iceland, 148 pp.

ISBN 978-9935-9514-2-7

Printing: Háskólaprent  
Reykjavík, Iceland, May 2020

## Abstract

High power impulse magnetron sputtering (HiPIMS) is a rather recent deposition method capable of depositing dense and smooth thin films by providing high amount of ionized sputtered material. However, the high quality thin films come at the cost of low deposition rate which hinders HiPIMS to be widely utilized in industry. Here the results of an experimental study on the effect of stationary magnetic field on the deposition rate, ionized flux fraction and properties of thin films deposited using the HiPIMS process, are presented. This includes vanadium, vanadium nitride and nickel thin films deposition using the HiPIMS technique under various conditions, including varying confining magnetic field, working gas pressure, substrate bias and tilt angle. In each case, the properties of HiPIMS deposited films were compared with corresponding dcMS deposited films under the same conditions. For this aim, various characterization techniques are used to determine the mass density, surface roughness, film composition, micro structure, magnetic and electrical properties of the deposited films. For the second part of the project a variable magnet is utilized in order to systematically study the influence of magnetic field on the HiPIMS process. For each magnetic field configuration, a series of deposition rate and ionized flux fraction measurements are carried out at various positions in front of a cathode target to develop a picture of spatial distribution of neutrals and ionized sputtered material. This part of the study continued by measurement of sideways deposition rate and ionized flux fraction for both HiPIMS and dcMS. This is to examine the link between an increase in sideways material transport in HiPIMS and commonly reported reduction of the deposition rate in HiPIMS compared to dcMS.



# Útdráttur

Háafspúlusöð segulspæta (HiPIMS) er fremur nýleg aðferð til að rækta þunnar húðir og gefur þéttar húðir með mjög slétt firborð. Þetta er gert með því að framkalla hátt jónunarhlutfall spætra agna. Þessi miklu gæði þessara ræktuðu húða eru á kosnað ræktunarhraða, sem hefur í komið í veg fyrir viðtaka notkun (HiPIMS) í iðnaði. Hér eru kynntar niðurstöður tilrauna þar sem áhrif sístæðs segulsviðs á ræktunarhraða, jónunarhlutfall, og eiginleika þunnra húða sem eru ræktaðar með háafspúlusaðri segulspætu. Vanadín, vandín nítríð og nikkell þunnhúðir eru ræktaðar með háafspúlusaðri segulspætu þar sem ýmsum eiginleikum afhleðslunnar var breytt, þar með talið breytingu á styrk hremmisegulsviðs, þrýstingi vinnugassins, spennu sem lögð er á undirlagið og horni milli undirlags og skotmarks. Fyrir hvert þessara tilfella eru eiginleika húðar sem ræktaðar eru með háafspúlusaðri segulspætu bornir saman við tilsvareandi húðir sem ræktaðar eru með dc segulspætu við sömu skilyrði. Til þess að fá þennan samanburð var beitt ýmsum greiningaraðferðum til að ákvarða eðlismassa, hrjúfleika yfirborðs, samsetningu húðar, formgerð, segul- og rafeiginleika ræktaðra húða. Í síðari hluta verkefnisins var notað breytilegt segulsvið til að rannsaka kerfisbundið áhrif segulsviðs á eiginleika háafspúlusaðrar segulspætu. Fyrir sérhverja formgerð segulsviðsins, voru ræktunarhraði og jónunarhlutfall mæld fyrir nokkrar staðsetningar framan við skotmarkið til að fá mynd af dreifingu hlutlausra agna og jónuðum ögnum í rúminu. Hér voru einnig mældur ræktunarhraði og jónunarhlutfall út til hliðanna, samsíða skotmarki fyrir bæði háafspúlusaða og dc segulspætu. Þetta var gert til að skoða tengsl milli aukins flutnings agna til hliðanna í háafspúlusaðri segulspætu sem oft er nefnd sem ein ástæða lægri ræktunarhraða í háafspúlusaðri samanborið við dc segulspætu.



*Dedication*

*To Sahar, my beloved wife*





# Table of Contents

<b>Abstract</b>	<b>iii</b>
<b>Útdráttur</b>	<b>v</b>
<b>Dedication</b>	<b>vii</b>
<b>Table of Contents</b>	<b>ix</b>
<b>List of Figures</b>	<b>xi</b>
<b>List of Tables</b>	<b>xiii</b>
<b>List of Original Papers</b>	<b>xv</b>
<b>Abbreviations</b>	<b>xvii</b>
<b>Acknowledgments</b>	<b>xix</b>
<b>1 Introduction</b>	<b>1</b>
<b>2 Magnetron sputtering discharge</b>	<b>3</b>
2.1 Sputtering . . . . .	3
2.2 DC diode sputtering . . . . .	4
2.3 Magnetron sputtering . . . . .	4
2.4 Direct Current Magnetron Sputtering (dcMS) . . . . .	6
<b>3 High Power Impulse Magnetron Sputtering (HiPIMS)</b>	<b>9</b>
3.1 Principle of HiPIMS . . . . .	9
3.2 Voltage-current waveform . . . . .	10
3.3 Deposition rate . . . . .	14
3.3.1 Physics behind deposition rate loss . . . . .	15
3.3.2 Increasing the deposition rate . . . . .	16
3.4 Ionized fraction of depositing particles . . . . .	18
3.5 Ionized flux fraction in HiPIMS . . . . .	19
<b>4 Sputtering instruments and plasma characterization</b>	<b>21</b>
4.1 Sputtering apparatus . . . . .	21
4.1.1 Thin film deposition . . . . .	21
4.1.2 Ionized flux measurement . . . . .	22
4.2 Magnet assembly . . . . .	23
4.2.1 Thin film deposition . . . . .	23
4.2.2 Ionized flux measurement . . . . .	23
4.3 Ionized flux fraction measurement . . . . .	24
<b>5 Material characterization techniques</b>	<b>29</b>
5.1 X-ray diffraction . . . . .	29
5.1.1 Principle of X-ray diffraction . . . . .	29

---

5.1.2	X-ray Reflectometry (XRR) . . . . .	30
5.1.3	Grazing incidence X-ray diffraction (GIXRD) . . . . .	32
5.1.4	X-ray pole figure . . . . .	33
5.2	Atomic force microscopy (AFM) . . . . .	35
5.3	Scanning Electron Microscope (SEM) . . . . .	36
5.4	Electron Micro-Probe (EMP) . . . . .	39
5.5	Four-point probe resistivity measurement . . . . .	40
<b>6</b>	<b>Summary of papers</b>	<b>43</b>
<b>7</b>	<b>Conclusions</b>	<b>51</b>
	<b>Paper I</b>	<b>53</b>
	<b>Paper II</b>	<b>67</b>
	<b>Paper III</b>	<b>75</b>
	<b>Paper IV</b>	<b>99</b>
	<b>Paper V</b>	<b>109</b>
	<b>Paper VI</b>	<b>123</b>
	<b>References</b>	<b>139</b>

## List of Figures

2.1	Schematic of the sputtering process . . . . .	3
2.2	A schematic of the balanced and unbalanced magnets . . . . .	6
3.3	Pulse duty cycle vs peak power density . . . . .	9
3.4	Current voltage characteristic of the dcMS and HiPIMS discharge . . . . .	10
3.5	Time resolved tunable diode-laser absorption spectroscopy in a HiPIMS discharge . . . . .	12
3.6	Deposition rates for dcMS and HiPIMS for different target materials . . . . .	14
3.7	Plasma potential versus axial distance . . . . .	17
3.8	Ionized flux fraction measurements in HiPIMS . . . . .	20
4.9	A schematic of the magnetron sputtering chamber. . . . .	22
4.10	Cross-section scheme of planar magnet. . . . .	24
4.11	The measured magnetic field for the 4 inch. VTec Magnetron. . . . .	25
4.12	Discharge current and magnetic null point. . . . .	26
4.13	Gridless QCM analyzer. . . . .	27
5.14	constructive and destructive interference. . . . .	30
5.15	Measured and simulated XRR data . . . . .	31
5.16	The geometry in grazing incidence diffraction. . . . .	32
5.17	$\alpha$ and $\beta$ of pole figure measurement. . . . .	34
5.18	Pole figures of (111) and (200) planes for VN films. . . . .	34
5.19	Schematics of atomic force microscopy operation. . . . .	35
5.20	Basic construction of SEM. . . . .	37
5.21	Energy distribution of electrons. . . . .	38
5.22	Four-point probe configuration . . . . .	40
6.23	GiXRD of V and VN thin films. . . . .	43
6.24	VN properties deposited at various substrate bias. . . . .	45
6.25	$F_{\text{flux}}$ in a HiPIMS discharge using various magnet configurations. . . . .	46
6.26	Cross sectional SEM image of the Ni films. . . . .	47
6.27	Ratio of sideways to axial integrated flux. . . . .	48
6.28	Relation between process and flux parameters. . . . .	49



## List of Tables

4.1	Specifications of magnets used for film deposition . . . . .	23
4.2	Specifications of 4 inch. VTec Magnetron . . . . .	26



## List of Original Papers

- Paper I:** H. Hajihoseini and J. T. Gudmundsson. 2017. Vanadium and vanadium nitride thin films grown by high power impulse magnetron sputtering. *Journal of Physics D: Applied Physics* **50**(50) (2017) 505302.
- Paper II:** H. Hajihoseini, M. Kateb, S. Ingvarsson and J. T. Gudmundsson. 2018. Effect of substrate bias on properties of HiPIMS deposited vanadium nitride films. *Thin Solid Films* **663** (2018) 126 - 130.
- Paper III:** H. Hajihoseini, M. Čada, Z. Hubička, S. Unaldi, N. Brenning, M. A. Raadu, J. T. Gudmundsson and D. Lundin. 2019. The Effect of Magnetic Field Strength and Geometry on the Deposition Rate and Ionized Flux Fraction in the HiPIMS Discharge. *plasma* **2**(2) (2019) 201 - 221.
- Paper IV:** H. Hajihoseini, M. Kateb, S. Ingvarsson and J. T. Gudmundsson. 2019. Oblique angle deposition of nickel thin films by high power impulse magnetron sputtering. *Beilstein Journal of Nanotechnology* **10** (2019) 1914 - 1921.
- Paper V:** H. Hajihoseini, M. Čada, Z. Hubička, S. Unaldi, N. Brenning, M. A. Raadu, J. T. Gudmundsson and D. Lundin. 2020. Sideways deposition rate and ionized flux fraction in dc and high power impulse magnetron sputtering. *Journal of Vacuum Science and Technology A* **38** (2020) 033009.
- Paper VI:** N. Brenning, A. Butler, H. Hajihoseini, M. Rudolph, M. A. Raadu, J. T. Gudmundsson, T. Minea and D. Lundin. 2020. Optimization of HiPIMS discharges: the selection of pulse power, pulse length, gas pressure, and magnetic field strength. *Journal of Vacuum Science and Technology A* **38** (2020) 033008.

### Publication that are not included in this thesis

- Paper VII:** M. Kateb, H. Hajihoseini, J. T. Gudmundsson and S. Ingvarsson. 2018. Comparison of magnetic and structural properties of permalloy Ni<sub>80</sub>Fe<sub>20</sub> grown by dc and high power impulse magnetron sputtering. *Journal of Physics D: Applied Physics* **51**(28) (2018) 285005.

- Paper VIII:** M. Kateb, H. Hajihoseini, J. T. Gudmundsson and S. Ingvarsson. 2019. Role of ionization fraction on the surface roughness, density, and interface mixing of the films deposited by thermal evaporation, dc magnetron sputtering, and HiPIMS: An atomistic simulation. *Journal of Vacuum Science and Technology A* **37** 031306.
- Paper IX:** M. Rudloph, N. Brenning, M. A. Raadu, H. Hajihoseini, A. Andres, J. T. Gudmundsson, and D. Lundin. 2020. Optimizing the deposition rate and ionized flux fraction by tuning the pulse length in high-power impulse magnetron sputtering. *Plasma Sources Science and Technology* **Accepted**.



## Abbreviations

PVD	Physical vapor deposition
IPVD	Ionized physical vapour deposition
CVD	Chemical vapor deposition
ALD	Atomic layer deposition
MS	Magnetron sputtering
dcMS	Direct current magnetron sputtering
HiPIMS	High power impulse magnetron sputtering
MPPMS	Modulated pulse power magnetron sputtering
GiXRD	Grazing angle x-ray reflection
XRR	X-ray reflectometry
SEM	Scanning electron microscope
EBSD	Electron Back Scatter Diffraction
SE	Secondary electron
BSE	Back scattered electron
AFM	Atomic force microscope
SPM	Scanning probe microscopy
STM	Scanning tunneling microscopy
ECR	Electron cyclotron resonance
FIB	Focus ion beam
EMP	Electron micro-probe
CRT	Cathode ray tub
LED	Light emitting diodes
QCM	Quartz crystal micro-balance
g-QCM	Gridded quartz crystal micro-balance
m-QCM	Modified quartz crystal micro-balance



## Acknowledgments

I would like to express my gratitude to my director of studies, Prof. Jón Tómas Guðmundsson, for giving me invaluable supervision and support during the Ph.D. project. His expertise, understanding and patience helped me grow as a scientist and as a person. I appreciate his knowledgeable comments and his assistance in writing journal papers. Deepest gratitude is also due to the doctoral committee, Dr. Daniel Lundin and Prof. Snorri Þorgeir Ingvarsson for their assistance at all levels of the research project and for a highly knowledgeable input in this thesis. This study would not have been successful without their knowledge and assistance.

I want to thank all members of Nanotechnology Centre for sharing the experience and invaluable assistance. Thanks also go to Dr. Unnar Arnalds and Mr. Einar Baldur for unrelenting enthusiasm in technical support. I also like to thank Prof. Tiberia Minea and Dr. Mykola Nickolay Ivchenko for hosting me at Université Paris-Sud and KTH Royal Institute of Technology, respectively. I would also like to thank to all colleagues that shared the office with me that added to international experience.

I would also like to convey thanks to the University of Iceland for providing laboratory facilities and SENS staff for administration help. In conclusion, I recognize that this research would not have been possible without the financial assistance of the Icelandic Research Fund and the University of Iceland Research Fund for Doctoral students and express my gratitude to these organisations. I would like to express my gratitude to my parents and my sisters for their unlimited support. Last but not least, I would like to give my special thanks to my wife and best friend without whose love and encouragement I would not have finished this thesis.



# 1 Introduction

Thin films and coatings with thicknesses ranging from parts of a nanometer to several micrometers play an essential part in many modern day technologies. They are used to enhance the surface properties of materials or to add new functionalities to the underlying substrate. Some examples include insulating barriers in electronic devices, anti-reflective coatings in optics, and protective coatings for cutting tools. Due to the technological importance of thin films, the synthesis methods are being vigorously developed. Some of the most popular thin film synthesis methods include electroplating used in automobile industry, and various types of chemical vapor deposition (CVD) and physical vapor deposition (PVD) methods used extensively in the semiconductor industry.

Physical vapor deposition (PVD) methods, such as magnetron sputtering, are widely used both in research and in industry to deposit a wide range of thin films for various applications. In PVD, the film forming material is ejected from a solid or liquid target and subsequently is transported to the substrate as a vapor. Some advantages of PVD over CVD and atomic layer deposition (ALD) methods are off-thermal equilibrium film growth, allowing the use of heat-sensitive substrate materials, and higher deposition rates (Sarakinis and Martinu, 2020). DC magnetron sputtering (dcMS) is an example of a highly successful PVD deposition technique that is widely used in industrial applications (Kelly and Arnell, 2000). However, it suffers from low ionization of the sputtered species. Ionized PVD (IPVD) methods, such as high power impulse magnetron sputtering (HiPIMS), can be used to overcome shortcomings associated with common PVD methods, and open up possibilities to further tailor the film properties while still maintaining the favorable aspects of the PVD methods (Ohring, 2002; Lundin and Sarakinis, 2012).

HiPIMS is a novel method of depositing thin films where the power is supplied in short highly energetic pulses followed by a long off time gap. The greatest advantage of the HiPIMS process compared to the other existing PVD methods is the production of the highly ionized flux of the film forming species towards the substrate (Bohlmark et al., 2006a; Hajihoseini et al., 2019b) which can be controlled via the substrate biasing (Alami et al., 2007). This enables tailoring thin films with exceptional properties such as low surface roughness (Ehiasarian et al., 2003; Hajihoseini and Gudmundsson, 2017), improved adhesion to the substrate (Ehiasarian et al., 2007), and higher hardness (Paulitsch et al., 2010). In addition, functional properties of thin films such as electrical (Magnus et al., 2012; Hajihoseini et al., 2018), mechanical (Paulitsch et al., 2010), optical (Sultan et al., 2019, 2020) and magnetic (Hajihoseini et al., 2019a) properties, can be engineered when highly ionized flux of sputtered material is available.

However, a high ionized flux fraction commonly comes at a cost of lower deposition

---

rate, which has thus far limited the use of HiPIMS in industry (Helmersson et al., 2006; Lundin and Sarakinos, 2012). There have been a number of attempts to increase the deposition rate in HiPIMS operation. This includes varying the pulse length (Konstantinidis et al., 2006b; Velicu et al., 2014; Ferrec et al., 2016), chopping the pulse into a train of shorter pulses (Antonin et al., 2015; Barker et al., 2013), increase the target temperature (Tesař et al., 2011), varying the magnetic (B) field strength (Čapek et al., 2013; Bradley et al., 2015; Mishra et al., 2010) modifying the B-field geometry (Yu et al., 2013; Raman et al., 2015, 2016) adding external B-field in target vicinity (Bohlmark et al., 2006b; Ganesan et al., 2018). Among these approaches, modifying the B-field configuration is known as the most effective way of controlling the deposition rate and ionized flux fraction. However, due to the complexity of controlling the B-field, there is a lack of systematic study in this area.

The specific aim of the work discussed in this thesis is to systematically explore the effect of B-field configuration on the HiPIMS process and compare it with the dcMS process. This includes studying the impact of the B-field strength  $|\mathbf{B}|$  and geometry (degree of unbalancing) on the properties of the HiPIMS discharge as well as on properties of the deposited thin films. The deposition rate and ionized flux fraction were measured for HiPIMS and dcMS discharges at various B-field configurations. Those parameters are recorded at various radial and axial positions in front of cathode target. It enables us to map out a spatial profile of neutrals and ionized sputtered materials and their connection with the B-field configuration. Lundin et al. (2008) showed that a significant fraction of the sputtered metal species is deposited sideways in HiPIMS discharge and suggest it could be one of the reasons for the lower deposition rate observed. To examine that phenomena and to investigate its relationship with B-field configuration, the sideways deposition rate and  $F_{\text{flux}}$  were measured for both HiPIMS and dcMS operations. Besides, thin films of vanadium and vanadium nitride are deposited using two magnets with different magnetic strength and geometry using both HiPIMS and dcMS methods. The surface roughness, mass density, grain size and the micro structure of the deposited films are characterized and related to the variation in magnetic field strength. Combining the results of film deposition and ionized flux fraction measurement gives a broad picture of the effect of B-field configuration on the HiPIMS and dcMS process.

## 2 Magnetron sputtering discharge

### 2.1 Sputtering

Sputtering in gas discharges was discovered in the mid 19th century by Grove (1852). However, the physical principle of sputtering was described much later by Sigmund (1969, 1987). The basic sputtering process can be described as an ejection of material from a cathode (target) due to impinging of the positive working gas ions from the discharge. Positive gas ions passing through the sheath region, that develops next to the target surface, gain energy and strike the cathode surface and transfer momentum to the target atoms. Momentum transfer does not affect only the impinging ion and one target atom, but inside the target collision cascades are formed affecting multiple atomic layers. If the energy supplied to the target atoms is high enough to break atomic bonds and the momentum direction is oriented outwards, sputtering occurs. This is shown schematically in Fig. 2.1. The average number of atoms ejected from the target per incident ion is called the sputter yield. Besides sputtering the incoming ions can stick to the target surface, scatter, get implanted in the first few atomic layers, change the topography of the target surface, or simply transfer heat (Ohring (2002)).

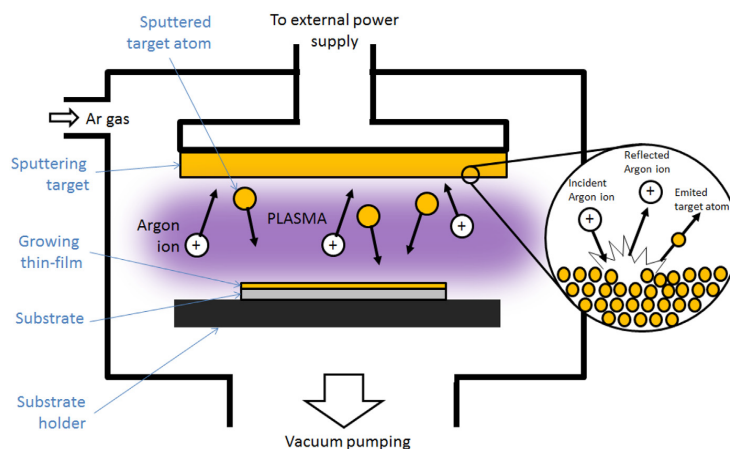


Figure 2.1. Schematic of the sputtering process in a dc diode device. From Pessoa et al. (2015).

One of the most striking characteristics of sputtering is its universality. Since the film forming material is converted into vapour phase by a mechanical rather than a

---

chemical or thermal process, virtually any material can be deposited. The resulting coating is held firmly to the surface by mechanical forces, although, in some cases, chemical bonds may result. Sputtering has proven to be a successful method to coat a variety of substrates with thin films of electrically conductive or non-conductive materials. Direct current (dc) can be used to sputter conductive materials, while pulsed dc or rf is used for non-conductive materials to alleviate arcing from the target (Schiller et al., 1993).

## 2.2 DC diode sputtering

In a conventional dc diode sputtering which consists of two conducting electrode, the sputtering species are inert working gas ions. A gas is introduced at specified pressure between 2 and 4 Pa (Mattox, 1998). Then a high potential of several thousand volts is applied between the two electrodes. This applied potential difference results in an electric field between the electrodes that exerts a force on the free electrons, caused by cosmic rays and already available in the gas, and accelerates them. These accelerated electrons collide with gas atoms and ionise them. The ions, thus produced, are accelerated by the field towards the cathode target and sputter the target material. The impact of the working gas ions on the cathode target may also release some electrons from the target. These released electrons, known as secondary electrons, play an important role in sustaining the discharge. This dc sputtering technique suffers from the serious drawback of low ionization efficiency that can be improved by the various ways such applying higher voltage between the electrodes and increasing the average working gas pressure (Chapman (1980)). Application of high voltage between the electrodes results in significant target heating and arcing that cause damage to the coatings being deposited. Increasing the working gas pressure enhances the ionization efficiency, though the number of sputtered particles that reach the substrate and the energy of the bombarding particles onto the substrate are significantly reduced, due to the higher collisions among the particles in the space between the target and the substrate. This, in turn, results in poor quality coatings and low deposition rate. Due to these issues the dc diode sputter tool is not in much use today.

## 2.3 Magnetron sputtering

A possible method to increase the ionization efficiency is to confine the electrons in the vicinity of the cathode target by using magnetic field. This technique is known as magnetron sputtering (Gill and Kay, 1965; Kay, 1963). The magnetron sputtering discharge incorporates a specially shaped magnetic field to a diode sputtering system. The principle is that the cathode surface is immersed in a magnetic field such that electron traps are created so that  $\mathbf{E} \times \mathbf{B}$  drift currents close in on themselves. The principle was discovered as far back as the 1930s by Penning (1936) and has been used in the magnetron sputter deposition context for many decades. In essence, the operation of a magnetron sputter source relies on the fact that primary and secondary



electrons are trapped in a localized region close to the cathode in an endless 'racetrack'. In this manner their chance of experiencing an ionizing collision with a working gas atom is vastly increased and so the ionization efficiency is increased. This causes the impedance of the plasma to drop and the magnetron sputter source operates at much lower voltages (several hundreds volts) than convectional dc diode systems (several kV). This greater ionization efficiency leads directly to an increase in ion current density onto the cathode target which is proportional to the erosion rate of the target. Compared to the formerly used planar dc diode tool, the planar magnetron sputtering discharge revolutionized the sputter process, by enabling to sputter at much lower working gas pressures with much higher deposition rate and thin film quality (Chapin (1974); Schiller et al. (1993)). In addition, substrate heating is reduced and sputtering from the substrate and chamber walls is avoided (Rohde (1994)). Magnetron sputtering however has one major drawback, due to the nature of magnetic confinement the plasma is distributed non-uniformly over the target, which causes uneven ion bombardment, resulting in inhomogeneous target sputtering. There are two negative effects of the inhomogeneous target sputtering; first, the thin film is deposited unevenly (Swann, 1987; Kelly and Arnell, 2000) and second, the area of the target where the highest sputtering erodes and forms a racetrack. For a circular target, this type of erosion leads to a large amount of waste, as high as 75 % of the target material is not used. The former issue can be solved by suitable configuration of the sputter system, such as substrate rotation, change of substrate position, substrate biasing or optimization of the confining magnetic field. The latter, the area of highest target erosion (racetrack) where the magnetic field lines are perpendicular to the target surface, can not be avoided, but can be improved. Target utilization in a typical planar configuration is 25 – 35 % (Chapin (1974); Braüer et al. (2010)). By using rotating and tilted magnets it is possible to increase the target utilization up to 80 % (Iseki (2009)).

A conventional or balanced magnetron sputtering system consists of planar cathode with permanent magnets placed directly behind the cathode in such a way that magnetic field lines make a closed loop starting from and ending on the cathode surface. The magnetron assembly consists of the cathode target and the magnets that create the confining magnetic field and are often water cooled. The anode, which is usually a ring placed around the cathode, is often grounded and serves as the plasma boundary.

The magnetron assembly can be configured in two modes of operations i.e. balanced or conventional and unbalanced, depending on the magnetic configuration. In the balanced magnetron, the magnetic flux through the outer and inner magnets is identical (Fig. 2.2.(a)). Thus, the plasma is strongly confined in the target vicinity. Generally it is difficult to deposit fully dense films on a large, or a complex component using conventional balanced magnetrons (Musil and Kadlec (1990)) because positioning the substrate outside of the plasma within the confined region prohibits the growing film from receiving sufficient ion bombardment. By strengthening and weakening one of the poles, an unbalanced magnetron can be achieved. Unbalanced magnetron can further be divided into two modes namely type I and type II depending on the location of the null field zone. In type I unbalanced magnetron, the null field zone is far from the target as compared to type II. The strength of the inner magnet is higher than the outer one which directs some of magnetic field lines toward the side walls (Fig. 2.2.(b)). In type II the strength of outer magnets is higher and as a result not all magnetic field lines are

directed to the inner magnet, some are opened towards the substrate (Fig. 2.2.(c)). The highly ionized plasma is thus not confined as strongly as in the balanced case enabling the high plasma density area to be prolonged to the substrate. Subsequently, inducing high ion bombardment of the substrate without a need of biasing the substrate.

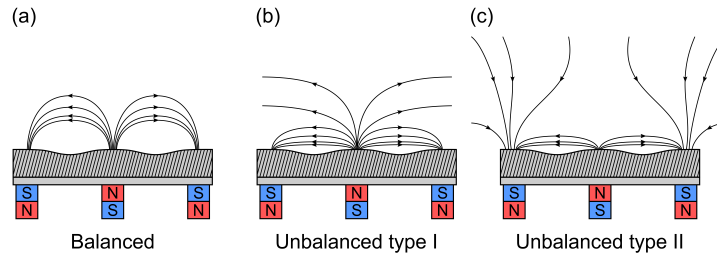


Figure 2.2. A schematic of the magnetic design commonly used in magnetron sputtering discharges. The three cases, (a) balanced, (b) unbalanced type I, and (c) unbalanced type II. Reprinted from Gudmundsson and Lundin (2020) with permission from Elsevier.

Window and Savvides (1986) studied seven planar magnetrons with differing magnetic field configurations. They find the type II magnetron assemblies yielded a five- to nearly 100-fold increase in the ion current collected by a -100 V probe compared to the type I magnetron assemblies. The ion to deposited atom ratio measured up to 2 for type II configurations, while for type I it was 0.00025. Thus, type I configuration provided very little substrate ion bombardment, while type II configuration provided considerable ion bombardment at low ion energies.

## 2.4 Direct Current Magnetron Sputtering (dcMS)

There are three general ways of applying power into a magnetron sputtering discharge; continuous (i.e., dcMS), pulsed (i.e., MPPMS, HiPIMS and other pulsed techniques) and oscillatory (i.e., RFMS). The most popular and simplest method is using a continuous power supply known as direct current magnetron sputtering or dcMS. The typical voltage needed for dcMS process ranges around several hundreds of volts depending on the target material and the experimental arrangement. The power density is up to 10s of  $W/cm^2$ . Up to 80 % of the supplied power is transformed to heat, so efficient cooling is needed in order to avoid target melting (Vossen and Cuomo, 1978). In dcMS the main ionized species are those of the working gas, however due to Penning ionisation the target material ions can also be detected (Christou and Barber, 2000). As a result, dcMS is known as a line-of-sight process, since it generates mostly neutral sputtered atoms whose trajectory and energy cannot be easily controlled, therefore rather low pressures are used to minimize scattering of the sputtered atoms (Lieberman and Gottscho, 1994). Majority of the sputtered particles have energies of a few eVs, however the tail of the distribution function ranges up to tens of eVs (Kadlec et al., 1997).

The limitation of the dcMS process however is a low ion flux towards the substrate.

Ion flux is mandatory for tailoring specific thin films properties (Window and Savvides, 1986). However, ion bombardment can be enhanced by utilizing unbalanced magnetic field (Kelly and Arnell, 2000; Svadkovski et al., 2002), biasing the substrate (Low et al., 2014), increasing the ionization by introducing either secondary radio frequency (rf) discharge (Rossnagel and Hopwood, 1993; Rossnagel, 2000) in the path between the cathode target and substrate, adding external magnetic field (Yang et al. (2009)), or using sideways dual magnetron sputtering (Aijaz et al. (2010)). When the sputtered flux consists of more ions than neutrals, i.e.  $\Gamma_i > \Gamma_n$ , it can be referred to as ionized physical vapour deposition (IPVD) (Gudmundsson (2008); Hopwood (2000)). Magnetron sputtering methods affiliated to IPVD processes are inductively coupled plasma assisted magnetron sputtering (ICP-MS) (Rossnagel and Hopwood (1994)), electron cyclotron resonance assisted magnetron sputtering (ECR-MS) (Musil et al. (1991)), hollow cathode magnetron (HCM) (Klawuhn et al. (2000)) and high power impulse magnetron sputtering (HiPIMS) (Gudmundsson et al., 2012).



# 3 High Power Impulse Magnetron Sputtering (HiPIMS)

## 3.1 Principle of HiPIMS

The idea behind the HiPIMS technique is to focus the power into highly energetic pulse in order to create a high density plasma. This ensures a very high ion flux towards the substrate, enabling to customize thin films properties such as low surface roughness (Ehiasarian et al. (2003)), improve adhesion to the substrate (Ehiasarian et al. (2007)), or increase hardness (Paulitsch et al., 2010). The average power supplied to the magnetron sputtering discharge is however limited by the target cooling. To put the thermal load of the target under control, HiPIMS has to be operated at low frequency (10 – 5000 Hz) and low duty cycle (less than 2 %).

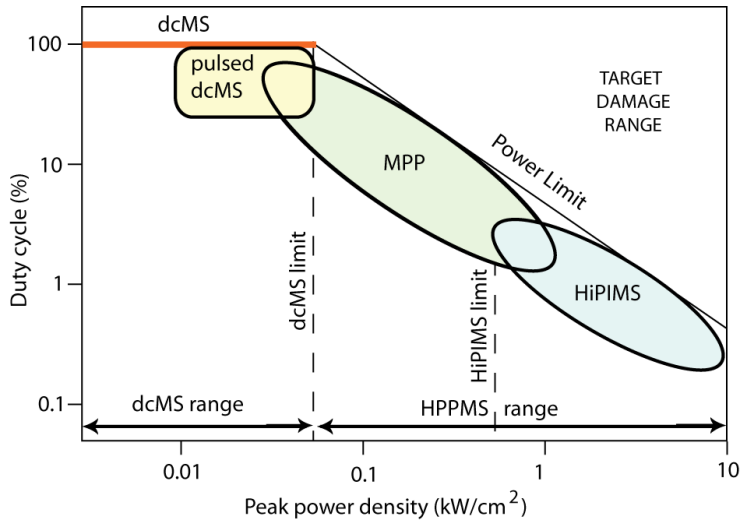


Figure 3.3. Trade off between pulse duty cycle and peak power density in magnetron sputter operation. From Gudmundsson et al. (2012).

The first report on the high power pulse magnetron sputtering technique was published by Fetisov et al. (1991) and continued exploration was reported by Mozgrin (1994), Mozgrin et al. (1995), and Fetisov et al. (1999). However, HiPIMS was finally noticed when it was introduced by Kouznetsov et al. (1999), where a magnetron sput-

tering discharge was reported that reached power density of  $2600 \text{ W/cm}^2$  which led to ion current density up to  $3.4 \text{ A/cm}^2$ . Such high power density is a distinctive character of HiPIMS compared to the other pulsed magnetron sputtering methods. Commonly it is known that there is a trade off between pulse duty cycle and peak power density as demonstrated in Fig 3.3. Hence, HiPIMS peak power density is two and one orders of magnitude higher than the conventional dcMS and modulated pulse power magnetron sputtering (MPPMS), respectively.

The application of the short and intense power pulse to the magnetron target can lead to electron densities of up to  $10^{19} \text{ m}^{-3}$  in the vicinity of the target. This in turn enhances the probability of ionization of both the background gas and importantly the sputtered neutral flux, leading to ionized density fraction at the substrate over 90 %, depending on the target material and process parameters (Bohlmarm et al., 2005).

### 3.2 Voltage-current waveform

During the HiPIMS pulse the discharge current is time dependent parameter evolving according to the dominant processes present in the discharge (i.e. ionization, gas rarefaction, self-sputtering). Any slight variation of deposition parameter can change the dominant process which is immediately reflected in the discharge current waveforms.

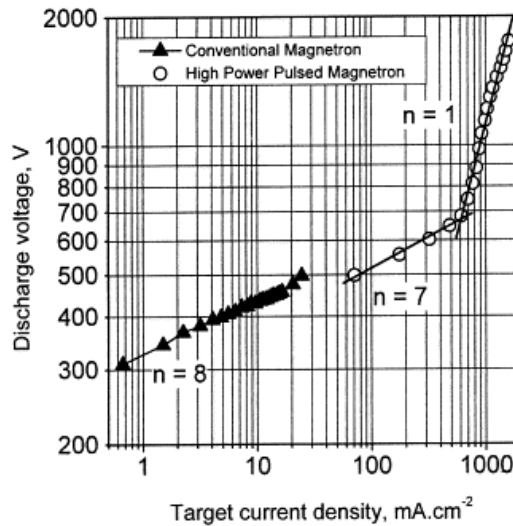


Figure 3.4. The peak discharge current voltage characteristic of the conventional magnetron and HiPIMS discharge.  $n$  is the exponent in the relationship  $I_D = kV_D^n$ . Reprinted from Ehasarian et al. (2002), with permission from Elsevier.

In dcMS discharge,  $I_D - V_D$  characteristic follows the relationship  $I_D = kV_D^n$ , where the exponent  $n$  ranges from 5 to 15 as reported by Rossnagel and Kaufman (1988).

Ehiasarian et al. (2002) and Alami et al. (2006) found the  $I_D - V_D$  characteristic of the HiPIMS discharge consisting of two phases, and is shown in Fig. 3.4. At low discharge currents  $n$  is similar to the coefficient found in dcMS discharge while at the higher discharge currents the exponent changes and additional increasing of target voltage does not result in increase in the discharge current.

A typical HiPIMS discharge current waveform can be divided into five phases (Lundin et al., 2020a). Different kind of physical mechanisms are involved in each phases.

- **Phase 1 - Ignition**

In this phase although a negative voltage is applied to the target there is a negligible plasma in the bulk volume of the chamber. However, the discharge ignites as a localized glow close to the anode where the electric field is very strong. This delay which takes about 10  $\mu\text{s}$  depends on the working gas pressure (Hajihoseini and Gudmundsson (2017)) and composition (Hala et al. (2010)), cathode voltage (Yushkov and Anders (2010)), target material (Hecimovic and Ehiasarian (2011)) and magnetic field (Hajihoseini et al. (2019b)). In order to shorten the delay, a dc pre-ionizer can be used which can speed up the current rise time by two orders of magnitude (Poolcharuansin and Bradley, 2010; Revel et al., 2018). A measurement by Vitelaru et al. (2012) using time-resolved tunable diode-laser absorption spectroscopy showed a very strong increase of the density of the metastable working gas atoms ( $\text{Ar}^m$ ), in the ignition phase as can be seen in Fig. 3.5. A short burst of hot electrons in the range of 70 to 100 eV was detected by Poolcharuansin and Bradley (2010) within the first 10  $\mu\text{s}$  of the HiPIMS pulse. It can explain the increase in the number of metastable  $\text{Ar}^m$  atoms due to the electron impact excitation. In addition, the metastable density being built up practically without any losses which results in sudden rise in the  $\text{Ar}^m$  density (Stancu et al. (2015)).

- **Phase 2 - Current rise**

In this phase the bulk plasma breakdown occurs which leads to a strong initial current increase. A strong axial ion current (perpendicular to the target surface) created toward the edge and the center of the target, where the magnetic field lines intersect the cathode target (Lundin et al. (2011)). This ion current is produced by ionization of the neutral working gas by secondary electrons (hot electrons) and electrons created in the ionization region close to the target (cold electrons). In phase 2 a dense plasma torus appears above the target race track. In addition, the metal atom and argon metastable densities build up, while working gas depletion sets in, mainly due to ionization losses (Huo et al. (2012)). However,  $\text{Ar}^m$  density subsequently decreases due to Penning ionization of the sputtered atoms as well as electron impact ionization of neutral metastable gas atoms, has come into play (Vitelaru et al. (2012); Gudmundsson et al. (2015)). As the peak in the discharge current approaches towards the end of phase 2 there is a strong decrease in the density of the metastable argon atoms while the neutral argon temperature begins to increase (Fig. 3.5).

- **Phase 3 - current decay (transition)**

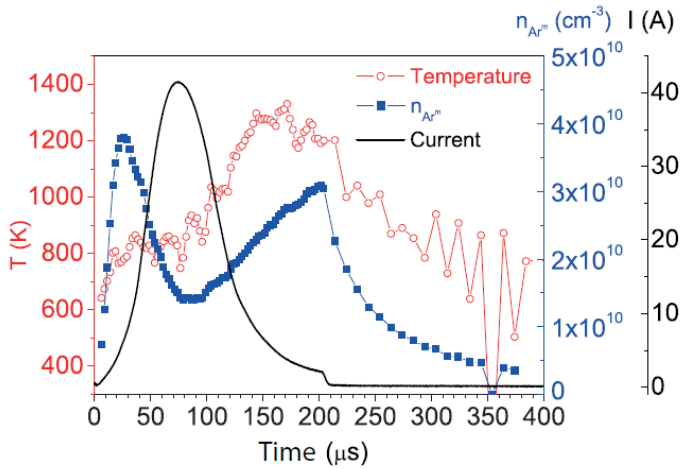


Figure 3.5. The black curve displays the HiPIMS discharge current waveform  $I_D(t)$  of a 200  $\mu\text{s}$  pulse at an Ar working gas pressure of 1.3 Pa, the red curve with circles shows the temperature of the metastable working gas atoms  $\text{Ar}^m$  and the blue curve with squares is the  $\text{Ar}^m$  density. From Vitelaru et al. (2012). © IOP publishing. Reproduced with permission. All right reserved.

Phase 3 starts with a discharge current decay which can sometimes be significant. Decrease in the discharge current leads to a greater refill of argon gas from the surrounding gas reservoir, and therefore the Ar density increases again. As a result, the metastable density increases as the current decreases which can be seen in Fig. 3.5. This Phase does not exhibit a steady state and the discharge either goes into the decay phase characterized by a decrease in the discharge current or an ion recycling regime (Brenning et al. (2017)) characterized by yet another discharge current increase or at least a sustained high current mode.

During phase 3, a more extended axial current in the the bulk plasma can be detected. This is because the bulk plasma density rises remarkably to admit current closure across the magnetic field lines. It starts at the larger distances from cathode at first, finally the plasma density grows high enough at the racetrack and encourage electrons to cross the magnetic field lines.

When the discharge current peaks, a strong reduction of the working gas density occurs, which is known as gas rarefaction. In fact, the gas rarefaction was known to exists in dc discharge. Kadlec (2007) introduced gas expansion as a reason of rarefaction in dcMS where the plasma density is low. He claimed the expansion is a result of heating due to collisions between the working gas atoms and the increasing amount of sputtered species as well as reflected working gas atoms. However, for highly ionized plasma such as HiPIMS, the impact of ionization of the working gas becomes significant (Huo et al., 2012). Raadu et al. (2011) showed that the role of electron impact ionization is dominant due to the



significantly higher plasma densities in the HiPIMS discharge as compared to for example dcMS.

- **Phase 4 - plateau (runaway)**

During this phase a dense, plasma torus is now maintained above the target race track, which leads to considerable ionization in this region (Lundin et al. (2011)). Axial cross-B current transport is now the dominant fraction of the measured total current, a significant change compared to phases 1 and 2, where most of the discharge current crosses the B-field radially and close to the target surface.

Depending on the amplitude of the discharge current two scenarios could happen.

**Low discharge current:** If the plateau current is lower than the peak current the plasma density during phase 4 decreases due to working gas rarefaction. As a result the ionization of the working gas and of sputtered particles reduces which leads to a reduced sputtering (Lundin et al., 2009). Similar to the dcMS discharge, the low current discharge mainly consists of neutrals (working gas and sputtered material). Thus, a modest gas heating and gas depletion is expected similar to dcMS operation.

**High discharge current:** This regime typically involves a combination of working gas recycling and self-sputter recycling, which increases the discharge current to become higher than the critical current and thereby leads to significantly higher current compared to the dcMS case. Note that the discharge at such current amplitudes is neither defined as being pure working gas sputtering nor self-sustained self-sputtering, but instead known as working gas-sustained self-sputtering, where the working gas ion current acts as a seed for a stronger metal ion current (Huo et al. (2014)). Hala et al. (2010) reported an intense emission from both neutrals and ions of the sputtered material in this phase. However, there is another possibility referred to as self-sputter runaway. Anders (2008) showed that this regime requires that self-sputter parameter fulfills  $\pi_{SS} = \alpha_t \beta_t Y_{SS} > 1$ . Since  $\alpha_t$  and  $\beta_t$  are always  $\leq 1$ , for self-sputter runaway  $Y_{SS} > 1$  is necessary.

- **Phase 5 - afterglow**

Afterglow begins when cathode voltage is turned off and thereby discharge current drops sharply. The HiPIMS discharge plasma can survive for a long time during the off-time, where a weak electron density (Poolcharuansin and Bradley (2010)) as well as ions from the working gas and the sputtered metal (Hecimovic and Ehasarian (2011)) were detected for up to 10 ms after the pulse was switched off.

In the afterglow the electron density decreases steeply in the first 30  $\mu s$  and then keeps decreasing slowly up to 3500  $\mu s$  (Poolcharuansin and Bradley (2010)). As one can see in Fig. 3.5, the same pattern has been observed for the density of  $Ar^m$  in afterglow discharge (Vitelaru et al. (2012)). This is due to the rapid disappearance of the energetic electrons which reduces the rate of electron-impact population of  $Ar^m$  from the Ar ground state.

### 3.3 Deposition rate

For dcMS, the deposition rates are found to be linearly proportional to the power delivered to the target (Waits (1978)). However, in HiPIMS discharge, by increasing the discharge current the rate of increasing deposition rate decreases. Generally, the deposition rate during HiPIMS operation is known to be lower than the dcMS one at the same average power. As can be seen in Fig 3.6, Samuelsson et al. (2010) observed that the HiPIMS rates are in the range of 30 — 85 % of the dcMS rates depending on target material after exploring Ti, Cr, Zr, Al, Cu, Ta, Pt and Ag discharges.

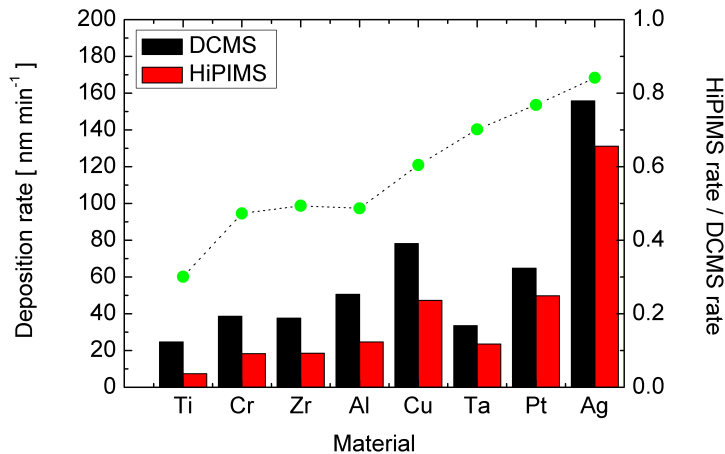


Figure 3.6. Bar graph of deposition rates for dcMS and HiPIMS discharges for the different target materials (left axis). The ratio of the deposition rate of HiPIMS over dcMS deposition rate is shown as a scatter plot (right axis). Reprinted from Samuelsson et al. (2010) with permission from Elsevier.

In the HiPIMS regime, due to the pulsed nature of the discharge the situation is more complex than in dcMS. The applied power can be increased either by increasing the amplitude of the applied voltage and the current amplitude of the pulses or maintaining the pulse amplitudes and instead increase the pulse frequency and pulse length. However, the resulting deposition rates will not be the same (Hajihoseini et al. (2019b)).

A long off time duration between the HiPIMS pulses has a negative effect on plasma formation, the pulses are so far apart in time that there is a small pre-ionisation effect left from preceding pulse (Sarakinos et al. (2010)). This should have the major negative effect on the deposition rate of the thin film as a high amount of energy is consumed to restart the ionization in each cycle. It turns out that this is not the case, average deposition rate for the low current HiPIMS is very similar to the dcMS for the same average supplied power, but as the peak discharge current increases the deposition rate decreases (Alami et al. (2006)). In addition, Konstantinidis et al. (2006a) found that the HiPIMS deposition rate increases from 20 % to 70 % of the dcMS values as the pulse

length is shortened from 20 to 5  $\mu\text{s}$  for the same average power.

### 3.3.1 Physics behind deposition rate loss

The processes responsible for deposition rate loss in HiPIMS are not fully understood. However, there have been several suggestions for the cause of the low deposition rate. These suggestions include:

- **Back-attraction of the ionized sputtered material:** The neutrals that are sputtered off from the target are likely to undergo an ionizing collision in the high density plasma in the cathode target vicinity. The probability of ionization of the target atoms is denoted by  $\alpha_i$  and varies with the plasma conditions. Part of those ions that are created close enough to the cathode target and also have a low enough kinetic energy will be back-attracted to the target (Christie, 2005). The probability of back-attraction is denoted by  $\beta_i$  and depends on how far the electric field extends outside the cathode sheath and into the dense plasma, where most of the ionization occurs. It is believed that the attraction of the sputtered ions back towards the target in HiPIMS plays the major role in lowering the deposition rate (Helmersson et al. (2005)).
- **Self-sputtering:** Back attracting ionized sputtered material comes with a two-fold impact. As the self-sputter yield is generally 10 – 15% lower than the yield of  $\text{Ar}^+$  ions, the efficiency of sputtering process in HiPIMS is decreased (Anders (2010)). Also a back attracted ion is lost from forming a film on the substrate.
- **Gas rarefaction:** Gas rarefaction leads to lower density of the working gas in front of the target and thus a reduction in the number of ions available for sputtering. This subsequently leads to a reduction in the deposition rate, in particular for long pulses.
- **Sideways transport of charged particles:** Lundin et al. (2008) show that a significant fraction of the sputtered metal species is deposited sideways. This enhanced radial transport (across the magnetic field lines) increases the deposition rates perpendicular to the target surface, but decreases the amount of sputtered material that reaches a substrate in front of the target. Leroy et al. (2011) carried out similar investigations using a rotating cylindrical magnetron. However, they did not observe an increase in sideways deposition and suggest that anomalous transport might work differently in these devices. However, this we have shown is not an explanation for lower deposition rate in HiPIMS as the sideways transport of film forming material is often higher in dcMS operation Hajihoseini et al. (2020).
- **Film effects:** HiPIMS is known to produce dense thin films. It is clear that film with higher density implies a lower thickness at equal number of deposited atoms. However, this effect can generally expected to be small. In addition, substrate bombardment by energetic species can result in re-sputtering from growing film. This effect can be very significant when the substrate is negatively biased (Anders (2004, 2010); Hajihoseini et al. (2018)).

- 
- **Non-linear scaling of sputter yield:** Deposition rate comparisons between dcMS and HiPIMS usually carry out at the same average power in the literature. However, Emmerlich et al. (2008) argue that the nonlinear scaling of the sputter yield with the cathode voltage is not taken into account (often  $Y \propto \sqrt{V_D}$ ) when comparing dcMS and HiPIMS discharges operated at the same average power. This would reduce the sputter rate since in HiPIMS operation the target voltage is significantly higher than for a dcMS discharge. It is therefore not reasonable to compare the two methods at the same average power. Also, Alami et al. (2006) address the difference in discharge voltage and discharge current between dcMS and HiPIMS and suggest that the lower deposition rate in HiPIMS is at least partially due to a lower average discharge current at the same average power. They conclude that comparison should be made for the same average discharge current.

### 3.3.2 Increasing the deposition rate

There have been extensive attempts to increase the deposition rate in the HiPIMS process. This includes using short pulses (Antonin et al., 2015), adding positive kick pulse (Wu et al., 2018), adding secondary discharge (Konstantinidis et al., 2006c), increasing the target temperature (Anders, 2010), and manipulating the magnetic field (Čapek et al., 2013).

There are a few reports on utilizing train of micro-pulses to increase the deposition rate in HiPIMS. The methods such as chopped HiPIMS by Barker et al. (2013) and Antonin et al. (2015), modulated pulse power magnetron sputtering (MPPMS) by Liebig et al. (2011) and deep oscillation magnetron sputtering (DOMS) by Ferreira et al. (2014) are built on this approach. Since the back-attracting electric field disappears at the pulse end, the available ions in the ionization region at this time will experience an abruptly lowered  $\beta_t$ . As a result, those ions have a considerably higher chance to leave the ionization region and reach the substrate position. Therefore, by shortening the pulse length (and increasing the pulse frequency) the number of ions from after glow which contribute to film forming can be increased significantly.

In another attempt, Konstantinidis et al. (2006c) added an inductive coil, halfway between the target and the substrate, to make a secondary inductively coupled discharge. They claim this secondary discharge could be used to minimize the decrease in the deposition rate as it would increase the conductivity of the inter-electrode volume plasma and make it easier for the metal ions to leave the magnetic trap (reduced  $\beta_t$ ).

Wu et al. (2018) report a deposition rate increase of up to 19 % when sputtering Cu by bipolar HiPIMS. They applied 100  $\mu$ s long HiPIMS pulses to the target followed by a 100  $\mu$ s positive pulse with amplitude of maximum 150 V. The authors believe that the positive pulse creates a positive sheath at the target which accelerates more positive ions toward the substrate and thereby increases the deposition rate. However, implementation of the same method when sputtering Cu by Nakano et al. (2013), Ti by Britun et al. (2018) and Keraudy et al. (2019) did not lead to a higher deposition rate.

Also, an increase in deposition rate by increasing the target source temperature has been reported. Vlcek et al. (2009) demonstrated an increase between 1.9 to 2.9 times in the HiPIMS deposition rate of Ti by increasing the target surface temperature up to

1700°C. However, it is likely that part of rate increase is due to sublimation (in particular the race track zone) and evaporation at these temperatures (Anders (2010); Behrisch and Eckstein (1993)).

Decrease of the magnetic field strength is a promising way to increase the deposition rate. Several groups have investigated the effect of magnetic ( $B$ ) field strength on the HiPIMS deposition rate using either permanent magnets or electromagnets. Čapek et al. (2013) reported on the increase of Nb deposition rate by a factor of 5 when they lowered the  $B$ -field placing spacers of different widths behind the cathode. Similarly, Mishra et al. (2010), found a six fold increase in the deposition rate of Ti by weakening the  $B$ -field by 33 % which led to a weaker electric field in vicinity of the target as shown in Fig 3.7. They proposed a reduced  $\beta_t$ , due to the weaker electric field, increases the ion flux to the substrate. However, Bradley et al. (2015) later analysed the same experimental data and argued that there was also a lower ionization probability  $\alpha_t$  at the weaker magnetic fields. This gives an alternative explanation for the increased deposition rate. Because at lower  $\alpha_t$ , ions are replaced by neutrals which are not back-attracted.

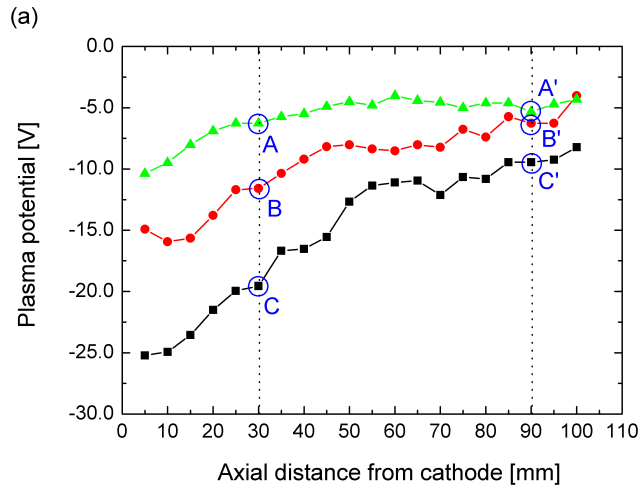


Figure 3.7. The plasma potential versus axial distance from the cathode measured at discharge current maximum. Results for three different  $B$ -field configurations are shown: profiles A (weakest  $|\mathbf{B}|$ ), B, and C (strongest  $|\mathbf{B}|$ ), and with parts marked A-A', B-B', and C-C'. Adapted from Mishra et al. (2010).

There are also reports of a deposition rate increase achieved by guiding the ionized flux using external magnetic fields. Bohlmark et al. (2006a) placed a coil in front of magnetron target which carries a current in a way that generated a magnetic field opposing the field from the center pole of the magnetron assembly. They observed an increase of 80 % in deposition rate for the sample placed in the front of target while the deposition rate was strongly decreased on samples placed to the side of the target. Ganesan et al. (2018) reported on increase in deposition rate by factor of 3 using an externally applied  $B$ -field produced by a solenoid in front of target as well as application

---

of substrate bias. They claimed this is a result of enhancement of the ionization of neutral atoms by broadening in region of intense plasma over the racetrack as well as improvement in transport efficiency of ions toward the substrate position.

There have also been a few attempts to modify the B-field geometry in order to improve the deposition rate. This includes the work of Yu et al. (2013) that used a 36 cm diameter copper target with spiral magnet pack assembly, in order to produce uniform plasma in the substrate vicinity and to improve target utilization. However, their design suffers from low electron trapping efficiency because of the open B-field lines in this B-field configuration. As a result, their discharge did not work in the high discharge current mode and was limited to be ignited at pressures higher than 5 Pa and target diameter bigger than 10 cm. More recently, Raman and coworkers proposed new types of the B-field configurations, called ‘epsilon ( $\epsilon$ )’ magnet pack (Raman et al., 2015) and ‘TriPack’ magnet pack (Raman et al., 2016). The new magnet packs lead to doubling of the deposition rates compared to the conventional magnet assemblies and also improved deposition uniformity. The increase in deposition rate is achieved by confinement of the electrons further away from cathode, where metal ions have a better chance to tackle the potential barrier and thus arrive at the substrate position. Using fast imaging measurements they demonstrate a more expanded ionization zone (25 % wider racetrack) in discharges with the ‘ $\epsilon$ ’ and ‘TriPack’ than running by conventional dipole B-field configuration. However, those designs encounter some difficulties when scaled down to a smaller cathode size.

### 3.4 Ionized fraction of depositing particles

Significant fraction of ionized metal particles is the key feature of the HiPIMS discharge. To describe this requires knowledge of the absolute fraction of ionized sputtered particles. Different descriptions have been used in the literature which causes some confusion concerning the ionized fraction. Three approaches are typically used to describe the degree (or fraction) of ionization: the ionized flux fraction  $F_{\text{flux}}$ , the ionized density fraction  $F_{\text{density}}$  and the fraction  $\alpha_t$  of the sputtered metal atoms that become ionized in the plasma (probability of ionization). First, following Hopwood (1998), we define the ionized flux fraction as

$$F_{\text{flux}} = \frac{\Gamma_i}{\Gamma_i + \Gamma_n} \quad (1)$$

where  $\Gamma_i$  and  $\Gamma_n$  are the ion and neutral fluxes of the sputtered species arriving at the substrate, respectively. Second, the ionized density fraction is defined as

$$F_{\text{density}} = \frac{n_i}{n_i + n_n} \quad (2)$$

where  $n_i$  and  $n_n$  are the ion and neutral densities of the sputtered species in the volume, respectively. Third, the probability of ionization  $\alpha_t$  was originally introduced by Christie (2005) when describing a target material pathways model for HiPIMS. It is defined as the fraction of the total amount of sputtered atoms that are ionized by the magnetron

plasma.  $F_{\text{flux}}$  is the most convenient to measure, as discussed in Section 4.13, and consequently the most commonly reported fraction of ionization.

### 3.5 Ionized flux fraction in HiPIMS

Kouznetsov et al. (1999) made the first attempts to estimate the ionized flux fraction  $F_{\text{flux}}$  in a HiPIMS discharge, where they deposited Cu on a substrate at a distance of 6 cm from the target. The experiment was carried out with a pulse discharge power density of 2.8 kW/cm<sup>2</sup> at an Ar working gas pressure of 0.065 Pa. By comparing the thickness of two thin copper films deposited on a conductive Si substrate using either an applied bias of +140 V to repel positive ions or -50 V (depositing both neutrals and ions) they could estimate the  $F_{\text{flux}} \approx 70\%$ . However, there is at least 10 % error in the reported ionized flux fraction due to the difference in film mass density when depositing from a combination of ions and neutrals or only from neutrals. In addition, the resulting error from thickness measurements could be significant due to film roughness.

Macák et al. (2000) continued these measurements using the same HiPIMS system with a Ti<sub>0.5</sub>Al<sub>0.5</sub> target, pulse power density of 0.6 kW/cm<sup>2</sup> at an Ar working gas pressure of 0.13 Pa. A planar probe with an area of 1.77 cm<sup>2</sup> biased to -70 V and was placed at a distance of 10 cm from the target. The temporal evolution of the measured ion current on the probe revealed a two-peak structure, which could be deconvoluted to separate argon and metal ions. By integrating the area below the metal and argon component of the measured ion current, the authors could calculate the number of ionized particles depositing on the probe. By measuring the total deposition rate the ionization flux fraction of deposited particles could be estimated to 40 % with error margin of 20 % originated from the fitting of the experimentally measured ion current waveform.

Two decades later, more accurate measurements of the ionized flux fraction have been carried out by a number of groups using the gridded and grid-less QCM. The details of instruments are described in Section 4.13. These measurements were performed by several authors using various targets and discharge conditions. A summary of these measurements can be seen in Fig. 3.8. A few general features can be tracked in these measurement:

For peak current densities around 1 A/cm<sup>2</sup> and working gas pressures in the range of 0.5 – 2.0 Pa the  $F_{\text{flux}}$  is higher than 50 %. By increasing the working gas pressure up to 4 Pa, the  $F_{\text{flux}}$  exhibits a strong decrease. Typically, increasing peak discharge current density leads to an increase in the ionized flux fraction. There is no strong dependency on target material, however, Ti and Al targets exhibit a slightly higher  $F_{\text{flux}}$  than a Cu target. This is probably because the ionization potential of Cu is higher than Ti and Al as well as a considerably lower electron impact ionization collision cross section (Samuelsson et al., 2010).

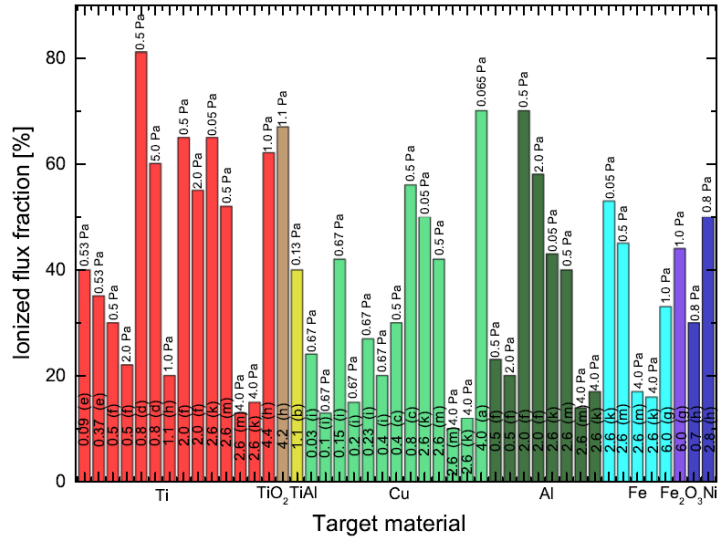


Figure 3.8. Compiled data on ionized flux fraction measurements in HiPIMS for eight different material systems. The discharges were operated in either pure Ar or in an Ar/O<sub>2</sub> mixture with the pressure given above each bar (0.05 – 4.0 Pa). The values inside the bars denote the discharge current density averaged over the entire target (0.03 – 6 A/cm<sup>2</sup>). The letters beside the discharge current densities refer to results from different authors i.e. (a) Kouznetsov et al. (1999), (b) Macák et al. (2000), (c) Vlček et al. (2007), (d) Kudláček et al. (2008), (e) Poolcharuansin and Bradley (2010), (f) Lundin et al. (2015), (g) Hubička et al. (2013), (h) Kubart et al. (2014), (i) Meng et al. (2014), (k) Stranak et al. (2014)(HiPIMS+ECWR), and (m) Stranak et al. (2014) (HiPIMS). Reprinted from Lundin et al. (2020b), with permission from Elsevier.



## 4 Sputtering instruments and plasma characterization

The experimental work was performed using two sputter chambers along with a number of power supplies and magnet assemblies. The thin film deposition was performed at the University of Iceland, Reykjavik, Iceland, while the plasma characterization was performed at Université Paris Sud, Orsay, France.

### 4.1 Sputtering apparatus

#### 4.1.1 Thin film deposition

Vanadium, vanadium nitride and nickel thin films were deposited in a custom built magnetron sputtering chamber (Arnalds et al., 2007) located at the University of Iceland Nanotechnology and Materials Science Centre. The chamber base pressure was  $4 \times 10^{-6}$  Pa and working gas was argon of 99.999 % purity mixed with nitrogen gas of 99.999 % purity for reactive deposition of vanadium nitride. The flow of injection gases into the chamber was controlled using mass flow controllers. A throttle valve was used to adjust the working gas pressure. The vanadium and nickel targets were 75 mm in diameter and of 99.995 % and 99.95 % purity, respectively.

The substrates used were thermally oxidized Si(001) with an oxide thickness of 100 nm or 1  $\mu$ m. The substrate temperature was adjusted during growth with a 1.5 inch (3.8 cm) diameter circular plate heater, separated from the substrate holder by a 2 mm gap. The substrate holder design is described in more detail by Arnalds et al. (2007). All depositions were made while keeping the substrate holder grounded. However, in paper II where the effect of substrate bias voltage was studied, a negative dc bias applied to the substrate.

For film deposition by HiPIMS discharge, the power was supplied by a SPIK1000A pulse unit (Melec GmbH) operating in the unipolar negative mode at constant pulse voltage, which in turn was charged by a dc power supply (ADL GS30). The discharge current and voltage was monitored using a combined current transformer and a voltage divider unit (Melec GmbH) and the data were recorded with a the data were recorded with a custom-made LabVIEW program. The pulse length was 200  $\mu$ s and the pulse repetition frequency was 100 Hz. For dcMS operation, a dc power supply (MDX 1 K, Advanced Energy) was connected to the magnetron.

The results presented in papers I, II and IV are extracted from thin films which were deposited using above mentioned apparatuses.

### 4.1.2 Ionized flux measurement

To measure ionized flux fraction  $F_{\text{flux}}$  and deposition rate at various magnetic field configurations, a custom-built cylindrical vacuum chamber (height 50 cm and diameter 45 cm) made of stainless steel, located at the Laboratoire de Physique des Gaz et Plasmas—LPGP, Université Paris-Sud, Orsay, France, was used. A base pressure of  $4 \times 10^{-6}$  Pa was achieved using a turbo molecular pump backed by a roughing pump. The working gas pressure was adjusted to 1 Pa by injecting 50 sccm Ar gas into the chamber and adjusting a butterfly valve located between chamber and turbo pump. The deposition system was equipped with a circular 4 inch (10.16 cm) Ti target. The magnetron assembly, as well as a probe holder used during measurements, was mounted on movable bellows controlled with millimeter precision, as seen in Figure 4.9. A dc power supply (SR1.5-N-1500, Technix, Créteil, France) and a HiPIMS power supply (HiPSTER 1, Ionautics, Linköping, Sweden) were used to ignite the discharge in dc and HiPIMS operation, respectively. For both cases, an average discharge power was maintained at 300 W. The HiPIMS pulse was always kept at a constant length of 100  $\mu\text{s}$  and the discharge was regulated in two different ways. The first mode of operation is referred to as fixed voltage mode, and was realized by keeping the cathode voltage fixed during the pulse at -625 V and varying the pulse frequency to achieve the desired average power. The second operating mode is referred to as fixed peak current mode and was realized by changing the cathode voltage to maintain the peak discharge current at  $I_{D,\text{peak}} = 40$  A, corresponding to current density  $J_{D,\text{peak}} = 0.5$  A/cm<sup>2</sup>.

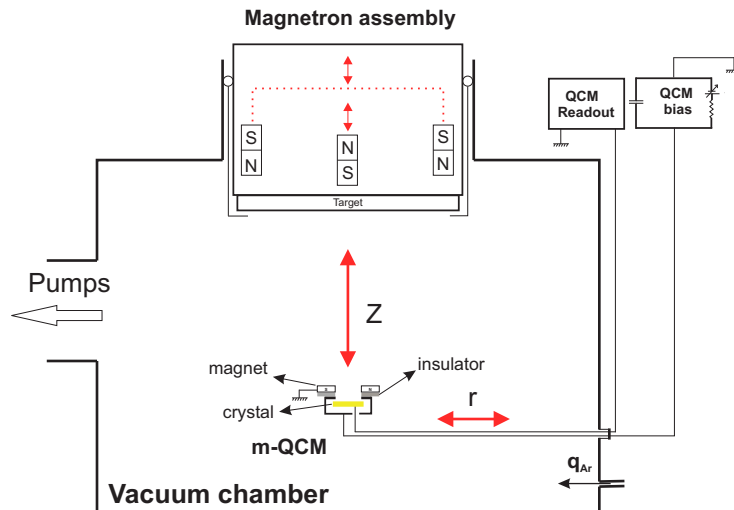


Figure 4.9. Schematic of the magnetron sputtering chamber. The magnetron assembly and the probe holder with the m-QCM are mounted on movable bellows that can be controlled with millimeter precision. The red arrows indicate linear motion. From Hajihoseini et al. (2019b).

## 4.2 Magnet assembly

### 4.2.1 Thin film deposition

To investigate the effect of magnetic field on the film properties, two magnets with different strength were used. Both magnets are 3 inches in diameter and were purchased from Angstrom Science. We determine the total magnetic flux of center and ring magnets (North and South poles). The method allows us to illustrate the balance and unbalance property of the magnets in a quantitative way. To this end, magnetic flux density (MDF) was measured at different points of the magnets (close to the surface) to achieve an average MDF over each magnet. Then the magnetic flux density is multiplied by the cross-section area of the magnets to achieve the total magnetic flux. By comparing the magnetic field strength of the two poles, it is easy to determine how unbalanced the magnetron is. Table 4.1 summarizes measured and calculated specifications of the two magnets. The magnetic fields were measured in a bench measurement by a Hall probe over the center of the race track. For the strong magnet, the average out of plane and in plane magnetic field are 18 and 93 mT, respectively, and for the weak magnet those are 4 mT and 36 mT, respectively. Moreover, the imbalance coefficient  $K$  is calculated as the ratio of the magnetic fluxes of the center magnet and the outer magnetic ring. Thus a magnetron is balanced if  $K = 1$ . The geometrical imbalance coefficient  $K_G$  is the ratio of the distance between the magnetic zero of the magnetron (the point along the middle axis where  $B_{\perp}$  changes its orientation, i.e.  $B_{\perp} = 0$ ) and the target surface, and the diameter of the erosion groove on the target (Alami et al., 2015). The cross-section scheme of the magnet assembly is shown in Fig. 4.10. Details on calculations and definitions of the two coefficients can be found in the work of Svadkovski et al. (2002).

*Table 4.1. Measured and calculated specifications of the two magnets which were used for the thin film deposition of vanadium and vanadium nitride. Both magnets are 3 inches in diameter. Ring thickness refers to the difference between the inner and outer diameters of the ring magnet. From Hajihoseini and Gudmundsson (2017).*

Magnet	Center diameter [mm]	Ring thickness [mm]	MFD of center (average)	MFD of Ring (average)	magnetic flux of center (total)	magnetic flux of Ring (total)	$K$	$K_G$
Weak	14	10	0.322 T	0.314 T	49 $\mu$ Wb	690 $\mu$ Wb	0.07	1
Strong	30	8	0.396 T	0.367 T	279 $\mu$ Wb	664 $\mu$ Wb	0.42	2.9

### 4.2.2 Ionized flux measurement

For the sake of ionized flux fraction measurement, the deposition system was equipped with a circular 4 inch. VTec Magnetron (Gencoa, UK). The magnetron assembly, as well as a probe holder used during measurements, were mounted on movable bellows controlled with millimeter precision. This made it possible to perform radial as well as axial scans with high precision. It is possible to vary the absolute magnetic field strength  $|\mathbf{B}|$  as well as the geometry of the magnetic field (degree of balancing) above the magnetron target by displacing the center magnet (C) and the outer ring magnet at the target edge (E) using two micrometer screws located on the outer side of the

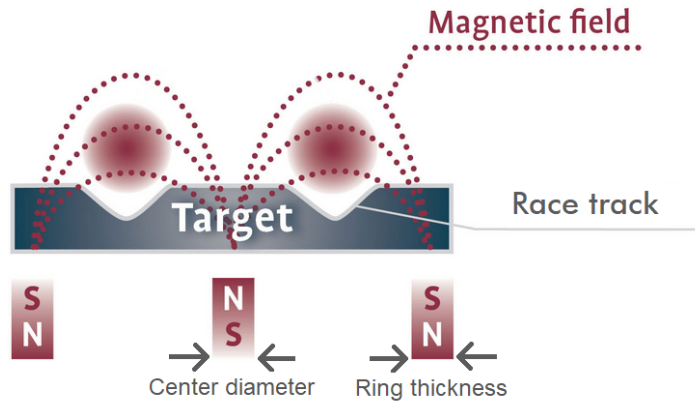


Figure 4.10. The cross-section scheme of the planar magnetron which was used for the film deposition .

magnetron. We refer to each configuration using the displaced distance (in mm) of each magnet from the target backing plate with the notation  $C_xE_y$ . Thus, the notation  $C0E0$  refers to a magnetron configuration where the center and outer magnets touch the backing plate (zero displacement, i.e., the strongest magnetic field above the target).

In paper III and paper V, we investigated seven different magnetron configurations:  $C0E0$ ,  $C5E5$  and  $C10E10$ ,  $C0E5$ ,  $C0E10$ ,  $C5E0$ , and  $C10E0$ . For all of these configurations the magnetic field above the target was mapped out using a Lake Shore 425 Gauss meter (Lake Shore Cryotronics, USA) equipped with a Hall probe. The magnetic field distribution above the target for each configuration is shown in Figure 4.11. Axial symmetry was assumed. The magnetic null point for the different cases is located at 43 – 74 mm and shown in Fig. 4.12 (b), which determines the ability of the electrons to escape from the magnetic trap and is a measure of the degree of balancing. For the configurations investigated, it is seen that a null point is always present and located fairly close to the target surface, which means that all the configurations are categorized as unbalanced type II (Window and Savvides, 1986). Note however, that the case  $C0E10$  is only weakly unbalanced, i.e. close to being balanced ( $z_{\text{null}} = 74$  mm), whereas  $C10E0$  is strongly unbalanced ( $z_{\text{null}} = 43$  mm). Table 4.2 summarizes the magnetic field strength at the race track and null point position for the seven investigated magnet configurations.

### 4.3 Ionized flux fraction measurement

The IPVD technique has been proven to be able to improve the quality of thin films deposited and to facilitate uniform coating of objects with complex shapes. The presence of ionized sputtered material is the main reason for this improvement. Thus, there have been intensive attempts to increase the fraction of ionized material which raised the need for a reliable technique to measure the ionization fraction of the flux to the substrate.

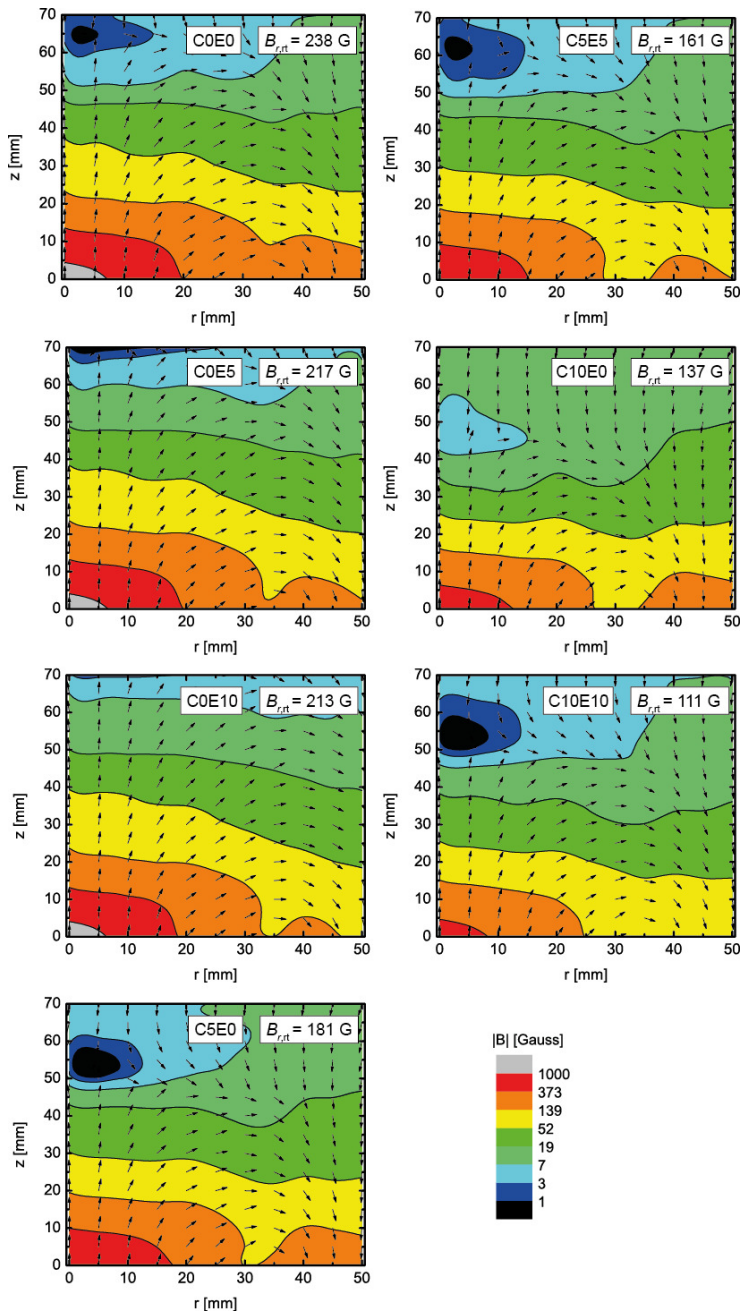


Figure 4.11. The measured magnetic field (flux density  $\mathbf{B}$ ) and field line directions for the seven magnetic field configurations using 4 inch. VTec Magnetron. Normalized arrows indicate the magnetic field direction, the color scale indicates the magnitude of magnetic field  $|\mathbf{B}| = \sqrt{B_r^2 + B_z^2}$ . From Hajihoseini et al. (2019b).

Table 4.2. The measured magnetic field strength at race track  $B_{r,rt}$  and magnetic null point position  $z_{null}$  for the seven investigated magnetic field configurations using 4 inch. VTec Magnetron. From Hajihoseini et al. (2019b).

Magnet configuration	$B_{r,rt}$ [Gauss]	$z_{null}$ [mm]
C0E0	238	66
C5E5	161	59
C10E10	111	52
C5E0	181	53
C10E0	137	43
C0E5	217	70
C0E10	213	74

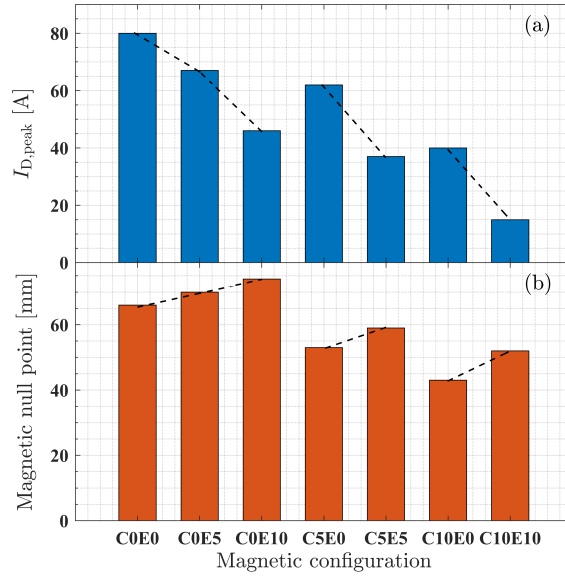


Figure 4.12. (a)  $I_{D,peak}$  for HiPIMS discharge operated in fixed voltage mode, and (b) degree of magnetic unbalance quantified by  $z_{null}$ . The dashed lines are drawn to highlight a saw-tooth pattern which is discussed in the text. The magnet configurations are sorted based one magnetic field strength from left to right i. e. the C0E0 produced the strongest and C10E10 produced the weakest magnetic field at the race track. From Hajihoseini et al. (2020).

An experiment by Yamashita (1989) used a control mesh grid which was biased to repel ionized metal. He placed the control mesh grid directly above the sample holder. By comparing the deposition between a sample with metal ions admitted and a sample with metal ions repelled, the ionization fraction in the discharge was determined. Rosnagel and Hopwood (1993) used a gridded quartz crystal micro-balance (g-QCM) to determine the ionized metal fraction in a dc magnetron sputtering system assisted by a rf inductively coupled plasma. The g-QCM can measure the deposition rate from both ions and neutrals separately by changing the bias voltages applied to the grids. The setup was capable of fast and spatially resolved determination of the ionized fraction to the substrate. Since then, a few researchers have improved the g-QCM setup and employed it to various systems. Green et al. (1997) enhanced the reliability of the instrument at low plasma densities and incorporated it in measurement of ionized Al flux fraction. Wu et al. (2010) employed the same setup to analyze a hollow cathode magnetron deposition of Cu. Later on, Poolcharuansin et al. (2012) reported ionized flux fraction in the range of 30 to 50 % in HiPIMS deposition of Ti by using a g-QCM instrument.

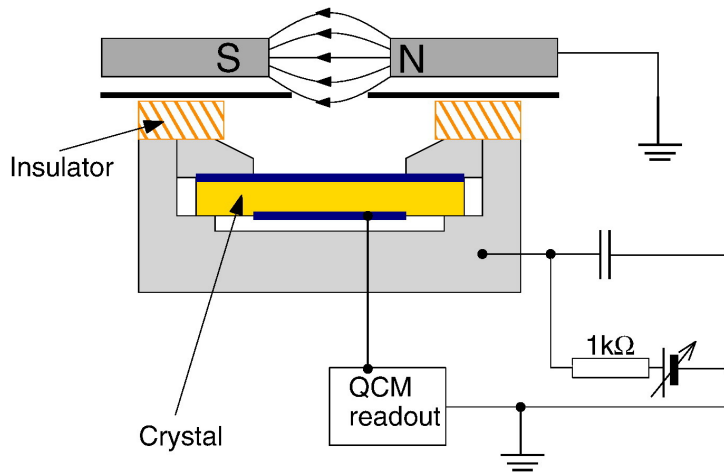


Figure 4.13. Gridless QCM analyzer. Magnetic field repels the electrons, which prevents the electrons from reaching the biased top QCM electrode. Reprinted from Kubart et al. (2014), with permission from Elsevier.

In papers III and VI of this study a gridless m-QCM is employed as an ion meter to measure the axial and sideways ionized flux fraction in HiPIMS discharge with Ti target. The design inspired by a modified Katsumata probe (Čada et al., 2013). Kubart et al. (2014) used this design for investigation of ionized metal flux fraction in HiPIMS discharges with Ni and Ti (pure and reactive) targets. More recently, Lundin et al. (2015) used gridless ion meter to study ionized flux fraction of HiPIMS discharges with Al, Ti and C targets. As can be seen in Fig. 4.13, in this design cylindrical SmCo magnets with a diameter of 8 mm and length of 5 mm are placed in front of the QCM in order to prevent electrons from bombarding the crystal. This configuration produces

---

localized homogeneous magnetic field of about 0.4 T, which did not influence the magnetron magnetic field inside the magnetic trap. The QCM control unit with the oscillator was connected directly to the crystal electrode. The electrode was grounded for measurements of both ions and neutrals, or biased to +40 V to collect only the neutrals and repel positive ions. The dc bias voltage was connected to the QCM collecting electrode through a 1 k $\Omega$  resistor, to protect the crystal in case of arcing, and the ground of the oscillator and the readout unit were connected to the crystal collecting electrode through a 150 nF capacitor such that dc current was blocked while rf current could flow from the crystal through this capacitor back to the ground of the oscillator and give a readout. In this configuration, the top crystal electrode could be readily biased without any influence on the QCM operation. The ionized fraction of the metal flux can be calculated from

$$F_{\text{flux}} = \frac{R_t - R_n}{R_t}, \quad (3)$$

where  $R_t$  is the total mass deposition rate and  $R_n$  is the mass deposition rate of neutrals. To minimize errors that originate from QCM crystal heating during the process, the recording time was kept short, typically less than 120 s. The total error of  $F_{\text{flux}}$  was estimated to be less than 15% for a single result mainly based on the accuracy of the mass deposition rate determination. No significant collimation of the ions is expected at this stage since the QCM electrode is grounded during the measurement of the total deposition rate and plasma potential is typically around 2 – 4 V (Green et al., 1997). The ion meter was mounted on the probe holder shown in Fig. 4.9 and could thereby map out the same region of interest as the standard QCM. However, due to interference with the plasma discharge, it was not possible to move it closer than  $z \leq 30$  mm.

The described gridless ion meter was used to measure ionized flux fraction in papers III and V. The results are reused in paper VI to determine optimized magnetic field.



## 5 Material characterization techniques

Here a brief overview of characterization techniques employed for structural investigation, surface analysis, and electrical measurements of the sputtered thin films is given.

### 5.1 X-ray diffraction

In the current study, X-ray reflectometry was applied to determine the layer thickness, film mass density and surface roughness. Structural properties of the deposited thin films were studied by grazing incidence X-ray diffractometry (GIXRD). Complimentary structural investigation was performed by X-ray pole scan to determine the preferred crystal orientation of the VN films deposited under various substrate bias voltage.

#### 5.1.1 Principle of X-ray diffraction

For the first time, Laue (1912) found that crystalline materials behave as three-dimensional diffraction gratings for a X-ray beam. X-ray diffraction (XRD) is based on constructive interference of monochromatic X-rays in a crystalline sample (Birkholz (2006); Widjonarko (2016)). The X-rays signal originates in elastic scattering of monochromatic X-ray by core electrons of atoms in a sample. The regularly spaced atoms in a crystal lattice diffract the X-rays which leads to production of the well-known XRD patterns, similar to diffraction of visible light by gratings. The principle is based on that an electron in an alternating electromagnetic field will oscillate at the same frequency as that of the field. Thus, when an X-ray beam hits an atom, the electrons around the atom start to oscillate with the same frequency as the incoming beam. Almost in all directions, we will have destructive interference which is due to combining out of phase waves. As a result, there will be no energy leaving the solid sample (Widjonarko (2016)). Fig. 5.14 schematically illustrates constructive and destructive interferences. The atoms in a crystalline form are arranged in a regular pattern, and as a result we will have constructive interference (Fig. 5.14 (a)). This implies that the waves will be in phase and there will be well defined X-ray beams leaving the sample in various directions (Birkholz (2006)). Thus, a diffracted beam can be described as a beam composed of a large number of scattered rays mutually reinforcing each other. However, the intensities of obtained peaks are determined by the distribution of the electrons in the unit cell because the electron density is the highest around an atom. The intensities depend on the type of atom and their location in the unit cell. Plane waves going through high electron density areas will reflect strongly, whereas, plane waves passing through low

electron density will give weak intensities.

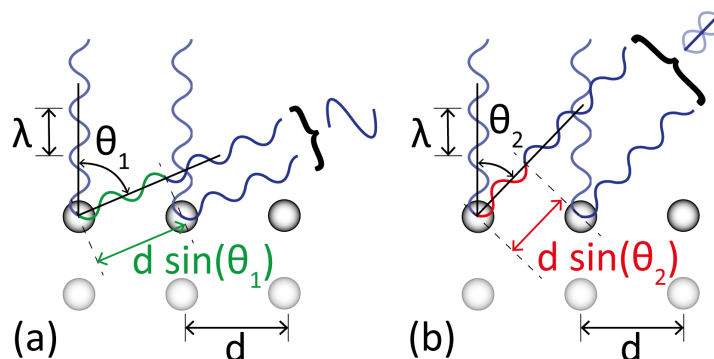


Figure 5.14. Different angles of the diffracted waves exhibit (a) constructive and (b) destructive interference, depending on the path difference. From Murphy (2014).

By scanning the sample through a range of  $2\theta$  angles, all possible diffraction directions of the lattice should be attained. For constructive interference, XRD signal is known to mathematically follow Bragg's Law

$$2d \sin(\theta) = n\lambda \quad (4)$$

Where,  $d$  is the separation between the Bragg planes,  $\theta$  is the Bragg angle,  $n$  is the diffraction order, and  $\lambda$  is the X-ray wavelength. Since each material has a set of unique  $d$ -spacing, conversion of the diffraction peaks to  $d$ -spacing allows to chemical identity of the sample. Typically, this is achieved by comparing the experimentally obtained results with  $d$ -spacing from standard reference patterns.

### 5.1.2 X-ray Reflectometry (XRR)

X-ray reflectivity is a technique based on specular reflection of X-rays from surfaces and interfaces. The reflection is based on the different electron densities of the layers. The method can be used to determine thin film thickness, density, surface roughness, and multilayer structures in a glancing angle  $\omega/2\theta$  configuration, where the incident and reflected angle are equal ( $\omega = \theta$ ). Below the critical angle  $\theta_c$ , the incident beam undergoes total external reflection. For  $\theta > \theta_c$  the reflected intensity starts to fall due to absorption in the material. A double critical angle can be observed if the film is less dense than the substrate (Ferrari et al., 2000). In this case the X-rays first penetrate the film when the incident angle exceeds the film critical angle and are reflected at the film–substrate interface. Above  $\theta_c$  the reflections from different interfaces interfere and give rise to interference fringes. The period of the fringes along with the fall in intensity can be used to determine the thickness and roughness of the layers (Gibson, 2011). For

a mono-layer film, the film thickness can be obtained from

$$n\lambda = 2t \sin \theta \sqrt{1 + \frac{\eta^2 - 1}{\sin^2 \theta}}, \quad (5)$$

where  $n$  is an integer,  $\lambda$  is the wavelength of incident X-rays,  $t$  is the film thickness, and  $\eta$  is the film's complex refractive index. To assess properties such as density and surface roughness, the recorded data can be iteratively fitted with a suitable theoretical model of the sample, if the film composition is known (Gibson, 2011).

In this study thickness, surface roughness and mass density of deposited films were determined by low-angle XRR measurements with an angular resolution of  $0.005^\circ$ . The experimental data were fitted using the PANalytical X'Pert Reflectivity software incorporating the Parrat formalism (Parratt, 1954). A low density surface layer on top of the film had to be included in the model in order to achieve a good fit. This is due to a formation of oxide or oxynitride surface layer after the films were removed from the vacuum chamber (Ingason et al., 2009). Figure 5.15 shows measured XRR curves and corresponding simulated data for Ni thin films deposited by dcMS and HiPIMS under  $0^\circ$  and  $70^\circ$  tilt angles.

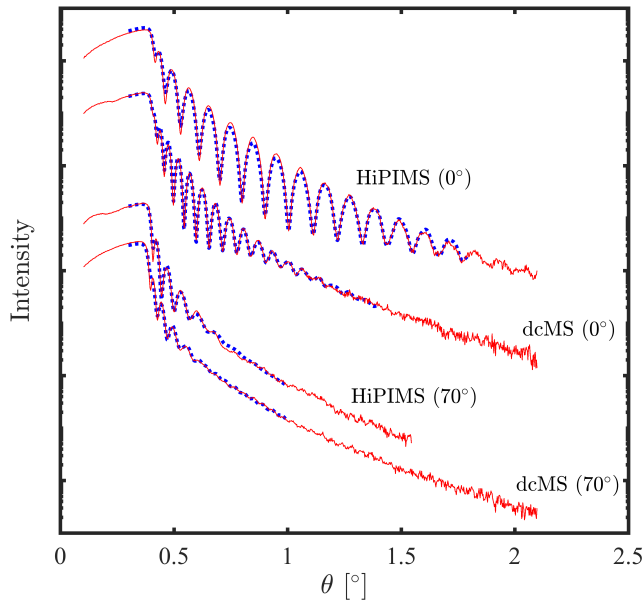


Figure 5.15. The measured (red solid) and simulated (blue dot) XRR data of HiPIMS and dcMS deposited Ni films under  $0^\circ$  and  $70^\circ$  tilt angles. The patterns are shifted to avoid overlapping. From Hajihoseini et al. (2019a).

### 5.1.3 Grazing incidence X-ray diffraction (GIXRD)

The penetration depth of X-rays are found to be in the range of 10 – 100  $\mu\text{m}$ . This is corresponding to the  $1/\mu$  value, where  $\mu$ , is the absorption coefficient. However, in most thin-film studies the film thickness is remarkably smaller which causes a significant fraction of the diffraction pattern to originate from the substrate rather than the deposited thin film structure (Birkholz, 2006). In other word, when film thickness is in the few nanometer range, negligible information from structural properties can be gained using symmetric  $\theta : 2\theta$  configuration. This is due to the short path traveled by the X-ray in the sample, which is not long enough for typical Bragg angles to deliver sufficient X-ray reflections and leads to unacceptable signal-to-noise ratio. In such cases, a complementary X-ray diffraction technique have been introduced as discussed by Widjonarko (2016), for which the primary beam enters the sample at very small angles of incidence and hence named as grazing incidence X-ray diffraction (GIXRD). This small angle of incidence leads to a significant increase in the path traveled by the X-rays and the structural information contained in the diffractogram to come primarily from the thin film.

As can be seen in Fig. 5.16, the GIXRD configuration is asymmetric and the angle between the incoming beam and the sample surface is very small. This angle is often denoted by  $\alpha$ . The GIXRD measurement is performed when  $\alpha$  is kept constant, while the detector is moved along the  $2\theta$  circle. This is the main difference compared to the symmetric configuration where the entrance angle  $\theta$  is also changed during the measurement (Birkholz, 2006; Widjonarko, 2016).

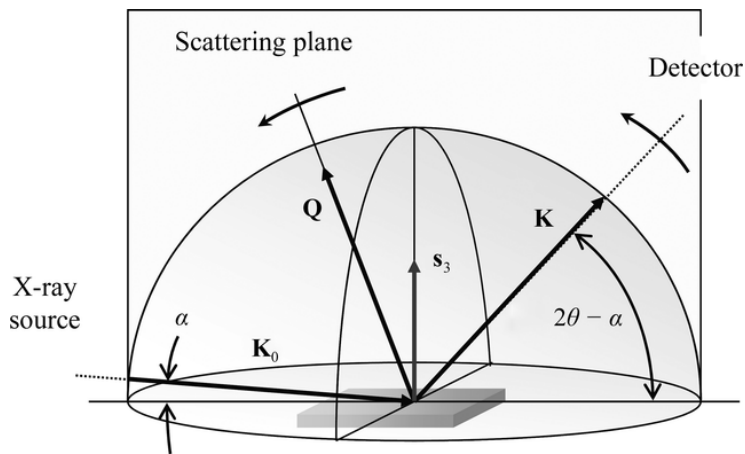


Figure 5.16. The geometry in grazing incidence diffraction is characterized by a small angle  $\alpha$  that is kept constant during the measurement. From Birkholz (2019).

In papers I, II and IV GIXRD analysis were carried out to determine the structural properties of vanadium, VN, and Ni thin films. The analysis was performed using a Philips X'pert diffractometer (Cu  $K\alpha$ , wavelength 0.15406 nm) mounted with a hybrid monochromator/mirror on the incident side and a  $0.27^\circ$  collimator on the diffracted side.

A line focus was used with a beam width of approximately 1 mm. The GIXRD scans were carried out with the incident beam at  $\alpha = 1^\circ$ .

#### 5.1.4 X-ray pole figure

Control over crystal orientation and the degree of preferred orientation is crucial in thin film deposition due to its effect on the functional properties of the thin films.

Historically, a combination of the Electron Back Scatter Diffraction (EBSD) and the Scanning Electron Microscope (SEM) has been used for determining crystal orientation and distribution in the field of material science. However, nowadays many X-ray diffraction machines are capable of doing more complex measurements such as determining the pole figure. Pole figure by X-ray diffraction has two advantages over EBSD and SEM. Firstly, it allows the texture analysis of samples with larger area, and secondly, the measurement can be performed at ambient condition or even at controlled temperature environment.

Pole figure measurement is based on the XRD technique. In this method diffracted intensity is collected when the diffraction angle ( $2\theta$ ) is fixed while two other geometrical parameters,  $\alpha$  and  $\beta$ , are being varied.  $\alpha$  ( $\psi$ ) is deviation from sample surface normal direction and  $\beta$  ( $\phi$ ) is rotation angle around sample surface normal direction (Mahieu et al., 2006). Generally, the center and the outer end of the pole figure are defined as  $\alpha = 0^\circ$  and  $\alpha = 90^\circ$ , respectively. At  $\alpha = 0^\circ$  the lattice plane normal is parallel to the sample surface and thus  $\alpha = 0^\circ$  means the lattice plane normal is perpendicular to the sample.  $\beta$  indicates the rotation angle around the sample surface normal and starts at the top of the figure and is circularly coordinated with a counter clockwise rotation. Hereby, 9 o'clock and 3 o'clock are defined as  $\beta = 90^\circ$  and  $\beta = 270^\circ$ , respectively. (Fig. 5.17).

The variation in intensity at fixed  $\beta$  along a varying  $\alpha$  is due to the tilting motion. On the other hand, twisting motion corresponds to the intensity variation along varying  $\beta$  at a fixed  $\alpha$  (Nagao and Kagami, 2011). The latter configuration is often used for the in-homogeneity analysis. For an accurate quantitative analysis such as for determining the degree of preferred orientation, the intensity needs to be normalized using the data obtained from a reference sample with randomly oriented crystallites.

In this study the pole figure measurement was carried out to explore the texture of vanadium nitride thin films deposited under various substrate bias, as discussed in paper II. Briefly, a pole scan was performed for a specific  $d$ -spacing, i.e. a fixed  $\theta - 2\theta$  peak while the specimen is rotated in-plane ( $\phi$ ) at different out-of-plane ( $\psi$ ) angles. Normally, a single pole scan is not enough to fully determine the orientation distribution within a specimen. Thus, pole figures were obtained for the (111), (200) and (220) planes at corresponding peaks. However, since our films are polycrystalline the main focus of the present study is on the pole figure for the (111) and (200) planes. The pole scans were performed at  $2\theta$  peaks of  $37.611^\circ$ ,  $43.697^\circ$  and  $63.533^\circ$  for each sample using  $0.25^\circ$  slit and  $90^\circ$  and  $360^\circ$  rotation respectively for  $\psi$  and  $\phi$  with a step size  $3^\circ$  and 4 s counting time at each step. The pole figures of a bare substrate were subtracted from original pole figures of the films for clarity. Fig. 5.18 illustrates pole figures of the (111) and (200) planes of VN films deposited at -50 V substrate bias voltage.

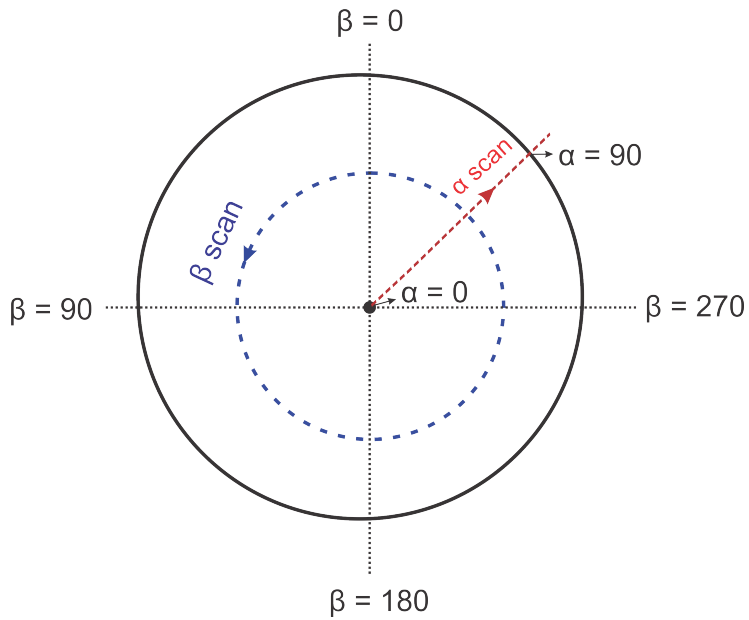


Figure 5.17.  $\alpha$  and  $\beta$  of pole figure measurement. Reprinted from (Nagao and Kagami, 2011).

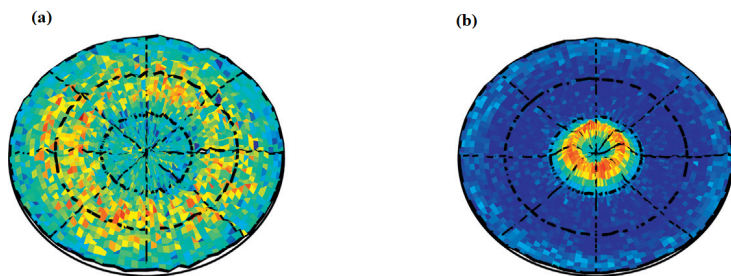


Figure 5.18. Pole figures of (a) (111) and (b) (200) planes for VN films which were deposited by HiPIMS at -50 V substrate bias voltage. Reprinted from Hajihoseini et al. (2018) with permission from Elsevier.

## 5.2 Atomic force microscopy (AFM)

AFM is part of a microscopy method group called scanning probe microscopy (SPM), which is used to map the topography and to study the properties of material on a nano-scale. AFM was first invented at IBM Zurich by Binnig et al. (1986), based on the principle of scanning tunneling microscope (STM) which was invented in 1981. But unlike STM, which is limited to conducting samples, an AFM can also be used for characterization insulating samples. In AFM the probing tip is a spring like cantilever with one end fixed and the other end having tip that interacts with the sample surface (Binnig et al., 1987). The tip that is attached to the free end of the cantilever comes in contact or close proximity of the sample surface. Thus attractive or repulsive forces as a result of interactions between the tip and the surface, cause either a negative or positive bending of the cantilever (Jagtap and Ambre, 2006) which can be translated to topographic information of the sample.

The force between tip and sample can be measured using the deflection of the cantilever. The cantilever behaves as a spring and its deflection is proportional to the force between tip and sample surface. The force can be determined by measuring the bending of the cantilever if the spring constant of the cantilever  $k$  is known. Hooke's law gives

$$F = -kz, \quad (6)$$

where  $F$  is the force and  $z$  is the distance the cantilever spring is bent relative to its equilibrium position without the sample present. The deflection of the lever is measured using a laser beam reflected from the back of the cantilever into a split photo diode as shown in Fig. 5.19.

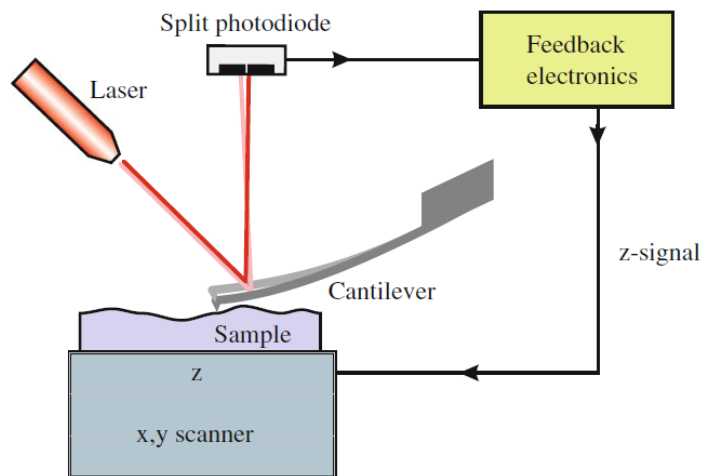


Figure 5.19. A schematic of the atomic force microscopy operation. From Voigtländer (2015).

---

An AFM system can be operated in two modes based on the tip-sample situation.

**Static mode (contact mode)**

In the static mode, the surface contour is mapped while the tip-sample distance is kept constant. For this aim, the corresponding changes in the  $z$ -position, which is required to maintain a constant tip-sample distance (i.e. constant force), correspond to the topography of the sample. The operating mode is called contact mode if the measurement is performed in the repulsive regime of the force-distance curve since the last atoms of the tip are in direct contact with the surface atoms (Voigtländer, 2015, Chapter 1).

**Dynamic mode (non-contact mode)**

In the dynamic mode, the cantilever vibrates close to its free resonance frequency during scanning the surface. When the AFM tip approaches the surface, the interaction between the tip and sample changes the resonance frequency of the cantilever. The tip-sample force can be expressed by a second spring behaving in addition to the cantilever spring. This additional spring changes the resonance frequency of the cantilever and thereby changes the cantilever amplitude. The change of amplitude can be used as a scheme of force detection and can be used as the feedback signal for regulating the tip-sample distance (Voigtländer, 2015, Chapter 1).

In this study, an AFM is utilized to explore the surface topography of VN films in Paper I (contact mode) as well as for thickness measurement of Ni thin film in Paper IV (non-contact mode). The employed AFM machine is a Park System, PSIA XE-100, mounted over Table Stable, TS-155 and utilizes a Light Bank LS-F100HS for live imaging. The software used to examine the topographic images is a XEP 1.8.0 Data Acquisition Program and Gwyddion (32-bit) software.

## 5.3 Scanning Electron Microscope (SEM)

The scanning electron microscope (SEM) is an instrument that creates magnified images which reveal microscopic-scale information on the size, shape, composition, crystallography, and other physical and chemical properties of a specimen. The principle of the SEM was developed theoretically by Knoll (1935) and Knoll and Theile (1939) with the first true SEM being developed by Von Ardenne (1938). The basic operating principle of the SEM involves the creation of a finely focused beam of energetic electrons by means of emission from an electron source. The energy of the electrons in this beam, is typically selected in the range from 0.1 to 30 keV. After acceleration to high energy, the electron beam is modified by series of apertures, magnetic and electrostatic lenses, and electromagnetic coils in order to reduce the beam diameter. The basic construction of the SEM is shown in Fig. 5.20. The beam has to be scanned in a raster ( $x$ - $y$ ) pattern at a series of closely spaced but discrete locations on the sample. At each location in the scan pattern, the interaction of the electron beam with the specimen produces two outgoing electron products, backscattered electrons (BSEs), and secondary electrons (SEs). These outgoing electron signals are measured at each beam location using one or more electron detectors, a SE detector which is sensitive to both SEs and BSEs and a BSE detector that is insensitive to SEs. The measured signal at each individual



raster scan location on the sample is digitized and recorded into computer memory, and is subsequently used to determine the gray level at the corresponding location of a computer display screen, forming a single pixel.

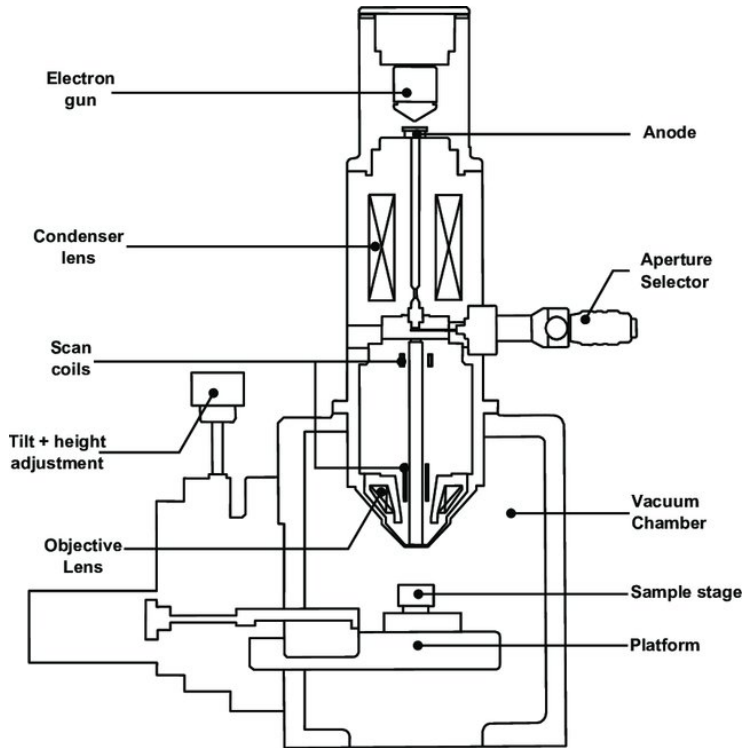


Figure 5.20. Basic construction of SEM. From Marturi (2013).

### Secondary-Electron Images

Any energy lost by a primary electron beam must appear as a gain in energy of the atomic electrons that are responsible for the inelastic scattering. If these electrons are valence or conduction electrons weakly bound to atomic nuclei, only a small part of this acquired energy will be used to release them from the confinement of a particular atom. The rest will be retained as kinetic energy, allowing the ejected electrons to travel through the solid as SEs. Those SEs which are created close enough to the surface may escape into the vacuum. On average, the escaping secondaries are generated only within 2 nm below the surface, which is called the escape depth. As a result, the SE image is mainly a property of the surface topography of the specimen rather than any underlying structure.

### Backscattered-Electron Images

A backscattered electron (BSE) is a primary electron that has been ejected from a solid by scattering angle greater than  $90^\circ$ . Because elastic scattering involves only a small energy exchange, most BSEs escape from the sample with energies close to

the primary-beam energy. The secondary and backscattered electrons can therefore be distinguished on the basis of their kinetic energy. Fig 5.21 shows the energy distribution of the electrons emitted from a specimen. Since the cross-section for high-angle elastic scattering is proportional to  $Z^2$ , we can expect strong atomic-number contrast in a SEM images that used BSEs as signal for imaging. In practice the fraction of primary electrons that escape as BSE increases with atomic number. In general, BSE images show contrast due to variations in chemical composition of a specimen, whereas SE images reflect mainly its surface topography. In the case of a BSE image, the depth from which the information originates is significantly larger than from a SE image. For electron beam energies above 3 kV, this depth is on the order of hundreds of nm which is considerably larger than the SE escape depth which is shorter than 2 nm (Egerton, 2016, Chapter 5).

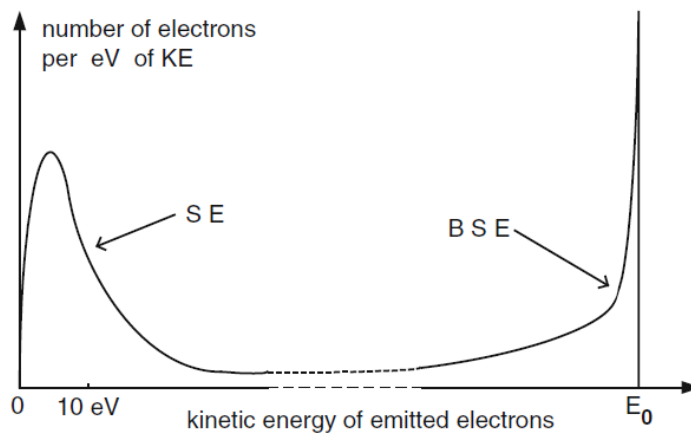


Figure 5.21. Energy distribution of electrons emitted from the SEM specimen. From Egerton (2016, Chapter 5).

### Electron beam size

The electron current can affect the quality of an image drastically and needs to be optimized depending on the specimen properties. A small beam diameter can be selected for high spatial resolution imaging, with extremely fine scale detail. However, a negative consequence of choosing a small beam size is that the beam current is reduced as the inverse square of the beam diameter. Low beam current means that visibility is compromised for features that produce weak contrast. On the other hand, a high beam current improves visibility of low contrast objects. For any combination of beam current, pixel dwell time, and detector efficiency there is always a threshold contrast below which features of the specimen will not be visible. This threshold contrast depends on the relative size and shape of the feature of interest. The visibility of large objects and extended linear objects persists when small objects have dropped below the visibility threshold. This threshold can only be lowered by increasing the beam current, pixel dwell time, and detector efficiency. Selecting higher beam current means

a larger beam size, causing resolution to deteriorate. Thus, there is a dynamic contest between resolution and visibility leading to inevitable limitations on feature size and feature visibility that can be achieved (Goldstein et al., 2018, Chapter 8).

Two SEM machines were employed to explore the thin film properties. In Paper I, the surface and cross section features of the vanadium nitride films were studied using a FEI Nova 200 dual beam machine, focused ion beam-scanning electron microscope systems (FIB-SEM). The acceleration voltage of the electron and ion beam were set to 10 and 30 kV, respectively. The FIB was applied to prepare the samples in order to take cross sectional SEM images. The working distance was kept at 5 mm for all the images presented. In Paper IV, the cross section of the Ni films were studied using a Leo Supra 25 scanning electron microscope. For this purpose the acceleration voltage of the electron beam was set to 20 kV and the working distance was kept at 3.5 mm.

## 5.4 Electron Micro-Probe (EMP)

The first electron micro-probe analyzer (EMP) was developed in the early 1950s by Castaing (1952) at the University of Paris, France. The instrument excites X-rays from a small region in the range of a few micrometers on a sample using a focused electron beam. The wavelength distribution of the excited X-rays is analyzed by crystal-diffraction spectrometers. Elemental composition can then be identified using Moseley's law which uniquely relates the wavelength of each observed spectral line to a specific element through the relationship

$$1/\lambda = k(Z - \sigma)^{1/2} \quad (7)$$

where  $\lambda$  is the X-ray wavelength,  $k$  is a constant for each spectral-line series,  $Z$  is the atomic number of the element which emitted X-rays, and  $\sigma$  is a constant correlated with the atomic screening effects. In order to perform quantitative analysis, a standard sample is needed. This is done by converting measured X-ray line intensities, normalized by pure elemental-standard intensities, to compositions using a variety of reasonably well-developed fundamental parameter quantitation schemes. Samples for EMP analysis are normally solid with smooth surface. The desired regions to be analyzed are selected by using a light microscope placed co-axially with the electron optical system. In addition, majority of EMPs come with secondary-electron detectors, electron-deflection systems, and cathode ray tube (CRT) displays which allow them to be operated as a SEM. This feature makes it possible to obtain elemental distribution information in one dimension (line scans) or in two dimensions (distribution maps) (Lifshin, 2001).

In Paper II of this study, EMP was performed using the JEOL JXA-8230 Superprobe. For all analyses an electron beam with the accelerating voltage of 15 keV and and the beam current of 10 nA and the spot size of 10  $\mu\text{m}$  were utilized. A VN film was used as a standard for nitrogen. For nitrogen, the counting time was 480 s on the peak and 120 s for each of the lower and higher backgrounds. To minimize the noise effect, an average of 5 measurement points on each sample is reported.

---

## 5.5 Four-point probe resistivity measurement

The specific electrical resistance or resistivity  $\rho$  of a solid is used to classify metals, semiconductors and insulators. This quantity is extremely important and is widely used for the characterization of materials as well as sophisticated device structures, since it influences the series resistance, capacitance, threshold voltage and other essential parameters of many devices, e.g. diodes, light emitting diodes (LEDs) and transistors (Sze and Ng, 2006).

Precise measurement of the resistance is closely related to other metrological units. In general, when an electric field  $E$  is applied to a material it causes an electric current. In the diffusive transport regime, the resistivity  $\rho$  of the isotropic material is defined by the ratio of the electric field and the current density  $J$ :

$$\rho = E/J, \quad (8)$$

Thereby, the resistivity of the material is measured in  $\Omega\text{cm}$ , the electric field in  $\text{V/cm}$  and the current density in  $\text{A cm}^{-2}$ . Experimentally, a resistance  $R$  is deduced from the ratio of an applied voltage  $V$  and the current  $I$ . Only when the geometry of the set-up is well-known can the resistivity be accurately calculated.

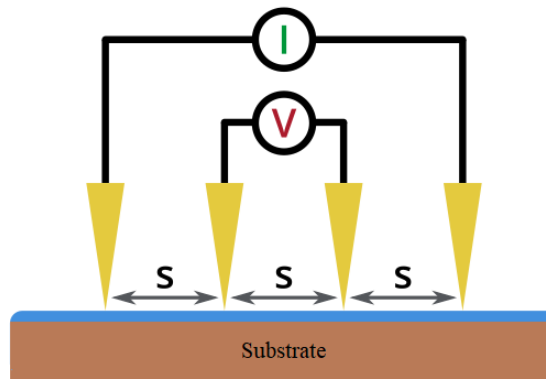


Figure 5.22. Schematic of the four-point probe configuration for measuring sheet resistivity.

The most common technique used to measure resistivity in semiconductors or thin films is the four-point probe method. The set-up consists of four-point collinear probes, where a constant current is applied in the two outer probes and the voltage drop is measured in the inner probes as demonstrated in Fig. 5.22. Then, the sheet resistivity is given by

$$\sigma = CF \times \frac{V}{I}, \quad (9)$$

where  $CF$  is the correction factor based on the ratio of the probe to wafer diameter and on the ratio of wafer thickness to probe separation. If the spacing between the probe

points is constant, and the conducting film thickness is less than 40 % of the spacing, and distance from any probe to the nearest boundary is more than 4 times the spacing distance from the measurement point, the sheet resistance is given by

$$\sigma = \frac{\pi}{\ln 2} \times \frac{V}{I}, \quad (10)$$

The thickness of the film  $t$  and its resistivity are related to  $\sigma$  by

$$\rho = \sigma \times t \quad (11)$$

Therefore, if the thickness of a film is known the resistivity can be calculated (Miccoli et al., 2015).

In Paper II, the electrical resistivity of the VN films was measured using a linear four-point probe station with a tip diameter of 200  $\mu\text{m}$  and a probe distance of 1 mm. Voltage-current waveforms were recorded through a Kiethley 2400 source meter and custom made Labview software. The current was swept from -100 mA to 100 mA and the corresponding voltage was recorded. To minimize the error arising from placement of the probes the resistivity was averaged over four separate measurements on each sample.



## 6 Summary of papers

### Paper I: Vanadium and vanadium nitride thin films grown by high power impulse magnetron sputtering

We demonstrate the growth of vanadium and vanadium nitride thin films by non-reactive and reactive HiPIMS, respectively, while varying the magnetic field strength. We see that mixture of 5 sccm  $N_2$  and 40 sccm Ar is sufficient to grow  $\delta$ -VN polycrystalline films as can be seen in diffractogram of Fig 6.23. We explored the influence of the stationary magnetic confinement field strength on the film properties and the process parameters. The deposition rate is found to be much lower for non-reactive sputtering by HiPIMS than for dcMS. Furthermore, for both dcMS and HiPIMS the deposition rate is lower for strong magnetic confinement.

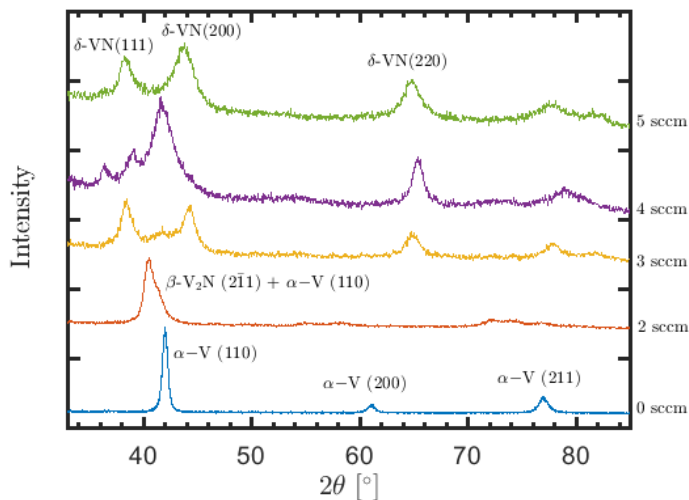


Figure 6.23. GiXRD pattern from vanadium nitride films which were grown by HiPIMS at different nitrogen flow rates with weak confinement magnet, at 0.9 Pa, 150 W average power, pulse length 200  $\mu$ s and repetition frequency of 100 Hz. The GiXRD patterns are shifted to aid peak identification. From Hajihoseini and Gudmundsson (2017).

Structural characterization was carried out using X-ray diffraction and reflection methods as well as AFM and SEM. Both dcMS and HiPIMS deposited vanadium films are polycrystalline with similar grain size regardless of magnetic field strength. For

---

dcMS deposited vanadium films the surface roughness is higher when we use a strong magnetic field. For both non-reactive growth of vanadium and reactive growth of vanadium nitride the HiPIMS process produces denser films with lower surface roughness than dcMS does. Lowering the magnetic field strength increases the deposition rate significantly for reactive HiPIMS while it increases only slightly in the reactive dcMS case. The films deposited by HiPIMS with strong magnetic confinement exhibit higher density and lower surface roughness. We find that the operating pressure, growth temperature, cathode voltage and film thickness has influence on the properties of HiPIMS deposited vanadium nitride films. The films are denser when grown at high substrate temperature and high cathode voltage and low pressure such as  $< 1$  Pa. The mass density of those films are inversely proportional to its thickness and thicker films consist of larger grain size. In all conditions, higher density coincides with lower surface roughness. Thus, the deposition method, the magnetic field strength, growth temperature, cathode voltage, film thickness and growth pressure have a significant influence on the film quality and structural properties, including the grain size for the various orientations.



## Paper II: Effect of substrate bias on properties of HiPIMS deposited vanadium nitride films

We explored the effect of substrate bias on the structure, texture, composition and electrical resistivity of HiPIMS deposited VN films. The optimum substrate bias is found to be -50 V, which gives the highest film density, the lowest electrical resistivity, and the lowest surface roughness at the highest deposition rate as demonstrated in Fig 6.24. We demonstrate how increasing the substrate bias voltage leads to a highly textured film. The preferred orientation of the film changes from (111) to (200) as the substrate bias voltage is increased. An X-ray pole scan shows that the (111) plane grows parallel to the SiO<sub>2</sub> substrate when the substrate is grounded while it is gradually replaced by the (200) plane as the substrate bias voltage is increased up to -200 V. The lowest electrical resistivity is measured as 48.4  $\mu\Omega\text{cm}$  for the VN film deposited under substrate bias of -50 V. This is among the lowest room temperature resistivity values that have been reported for a VN film. We found that the nitrogen concentration presents a decline by 6.5 percentage points as the substrate bias is changed from ground to -200 V.

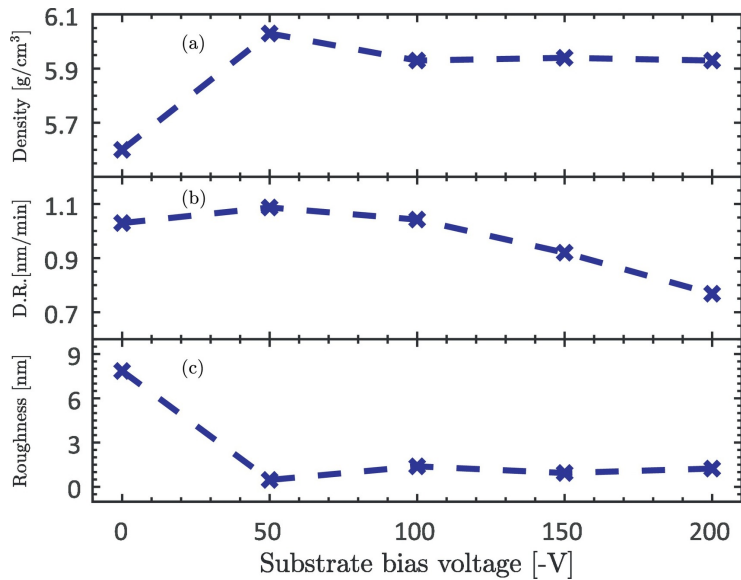


Figure 6.24. (a) Film mass density, (b) deposition rate, and (c) surface roughness of vanadium nitride films deposited as a function of substrate bias voltage. Data extracted from XRR measurement and all films are deposited at 0.9 Pa, 250 W average power, pulse length of 200  $\mu\text{s}$  and repetition frequency of 100 Hz. Reprinted from Hajihoseini et al. (2018), with permission from Elsevier.

### Paper III: The effect of magnetic field strength and geometry on the deposition rate and ionized flux fraction in the HiPIMS discharge

The effect of the magnetic confinement on the deposition rate and the ionized flux fraction was explored for both dcMS and HiPIMS deposition from a Ti target. The HiPIMS discharge was run in two operating modes. The first one we refer to as 'fixed pulse voltage mode' where the cathode voltage is kept fixed during the pulse at -625 V. The second mode we refer to as 'fixed peak current mode' is carried out by adjusting the cathode voltage maintain the peak discharge current at 40 A. In both modes, the pulse repetition frequency is varied to achieve the desired time average power (300 W). Our results show that the dcMS deposition rate is barely sensitive to  $|\mathbf{B}|$  variations while the deposition rate during HiPIMS operated in fixed voltage mode changes from 30 % to 90 % of the dcMS deposition rate. However, when operating the HiPIMS discharge in fixed peak current mode the deposition rate is almost independent of  $|\mathbf{B}|$  while it is sensitive to the degree of balancing. In fixed voltage mode, the higher the deposition rate, the lower the  $F_{\text{flux}}$ . In the fixed current mode, although the same deposition rate, the weaker  $|\mathbf{B}|$  strength results in a higher  $F_{\text{flux}}$  which can be seen in Fig 6.25.

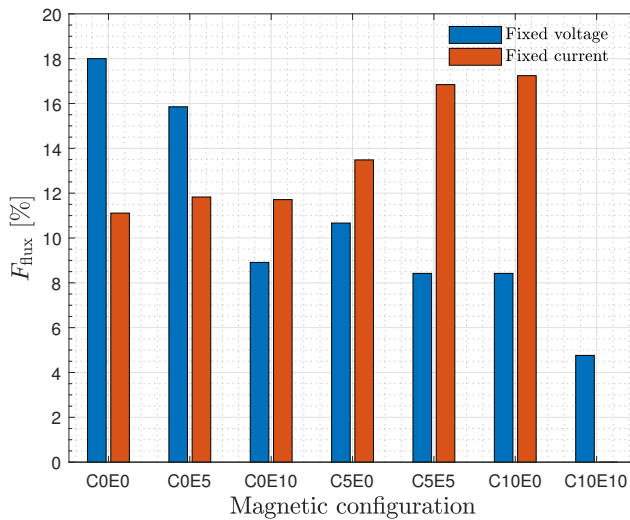


Figure 6.25. The Ti ionized flux fraction in a HiPIMS discharge using various magnet configurations. The values measured at 7 cm axial distance over center of the cathode. From Hajihoseini et al. (2019b).

Thickness uniformity measurements illustrate that the dcMS deposition rate is hardly sensitive to  $|\mathbf{B}|$  while both HiPIMS modes are highly sensitive to  $|\mathbf{B}|$ . The HiPIMS deposition rate uniformity can be 10 % lower up to 10 % higher than the dcMS rate depending on  $|\mathbf{B}|$ . We show that when operating a HiPIMS discharge in fixed voltage mode, the ionization probability is varied with  $|\mathbf{B}|$  and  $\beta_t$  remained roughly constant, while, in the fixed current mode,  $\beta_t$  varied with  $|\mathbf{B}|$  and at remained roughly constant.

**Paper IV: Oblique angle deposition of nickel thin films by high power impulse magnetron sputtering**

Oblique angle deposition is known for encouraging columnar grain growth which is tilted in the direction of the deposition flux. Deposition using this technique combined with HiPIMS can induce unique properties in ferromagnetic thin films. We report on the deposition of 50 nm polycrystalline nickel thin films by dcMS and HiPIMS as the tilt angle with respect to the substrate normal is varied from  $0^\circ$  to  $70^\circ$ . The HiPIMS deposited films are always denser, with a smoother surface and are magnetically softer than dcMS deposited films for otherwise same deposition conditions. The obliquely deposited HiPIMS films are significantly more uniform in terms of thickness. The cross sectional SEM images which are shown in Fig 6.26 reveal that the dcMS deposited film under  $70^\circ$  tilt angle consists of well defined inclined nano-columnar grains while grains of HiPIMS deposited films are smaller and less tilted. Both deposition methods result in in-plane isotropic magnetic behavior at small tilt angles while larger tilt angles result in uniaxial magnetic anisotropy. The transition tilt angle varies with deposition method and is measured around  $35^\circ$  for dcMS and  $60^\circ$  for HiPIMS.

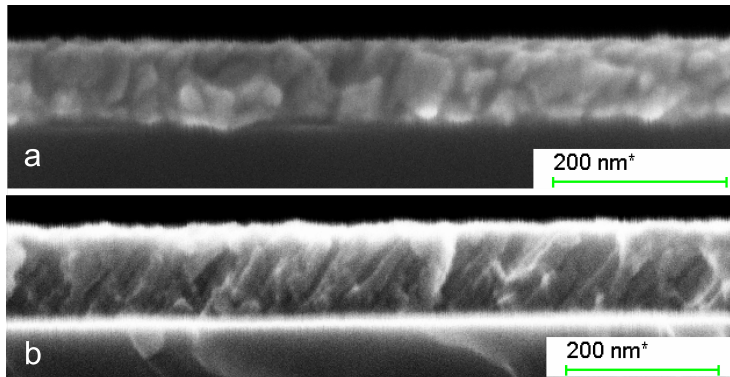


Figure 6.26. Cross sectional SEM image of the nickel films which are deposited by (a) HiPIMS, and (b) dcMS methods at  $70^\circ$  substrate tilt angle, at 0.6 Pa, and 150 W average power. From Hajihoseini et al. (2019a).

---

## Paper V: Sideways deposition rate and ionized flux fraction in dc and high power impulse magnetron sputtering

The effect of magnetic field strength  $|\mathbf{B}|$  and geometry (degree of balancing) on the deposition rate and ionized flux fraction radially, sideways, perpendicular to the target surface, is explored experimentally in HiPIMS when depositing titanium. We observe a significant deposition of the film forming material parallel to the target surface. This sideways deposition decreases with increasing axial distance from the target surface. The sideways deposition rate is always the highest in dc operation while it is lower for HiPIMS operation. The magnetic field strength has a strong influence on the sideways deposition rate in HiPIMS but not in dcMS. Furthermore, in HiPIMS operation the radial ion deposition rate is always at least as large as the axial ion deposition rate, and often around two times higher. Thus there are significantly higher number of ions traveling radially in the HiPIMS discharge. A comparison of the total radial as well as axial fluxes across the entire investigated plasma volume between the target and the substrate position allows for revised estimates of radial over axial flux fractions for different magnetic field configurations. As can be seen in Fig 6.27 the relative radial flux of film forming material is greater in dcMS compared to HiPIMS for almost all cases investigated. We therefore conclude that the commonly reported reduction of the (axial) deposition rate in HiPIMS compared to dcMS does not seem to be linked with an increase in sideways material transport in HiPIMS.

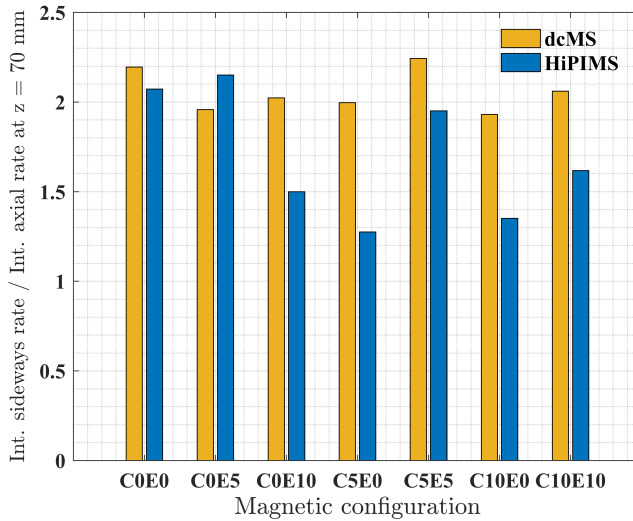


Figure 6.27. The integrated sideways deposition rate across the cylindrical surface extending from  $z = 30$  to  $70$  mm divided by the integrated sideways deposition rate across the bottom surface at  $z = 70$  mm for dcMS and HiPIMS discharges. All data was recorded using a standard QCM. From Hajihoseini et al. (2020).

### Paper VI: Optimization of HiPIMS discharges: the selection of pulse power, pulse length, gas pressure, and magnetic field strength

The main goals in a HiPIMS operation are to achieve high ionized flux fraction of the sputtered target material and high deposition rate. We demonstrate that the former always comes at the cost of the latter. This makes a choice necessary, which we call the HiPIMS compromise. We here propose that this compromise is most easily made by varying the discharge current amplitude, which opens up for optimization of additionally four external process parameters: the pulse length, the working gas pressure, the magnetic field strength, and the degree of magnetic unbalance to achieve the optimum combination of the ionized flux fraction and the deposition rate.

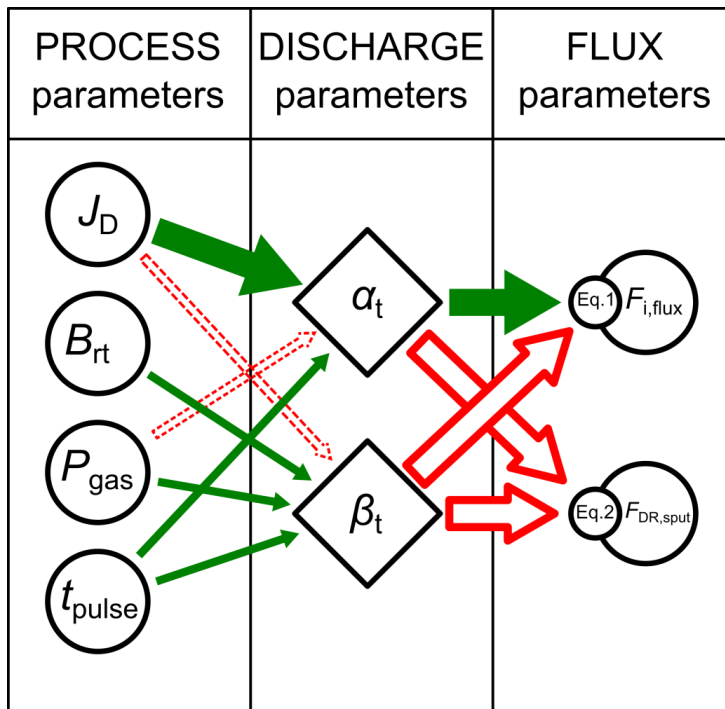


Figure 6.28. A flow chart which shows the main influences from the external process parameters (to the left), through internal processes represented by the parameters  $\alpha_t$  and  $\beta_t$  (in the middle column), and finally to the two flux parameters  $F_{i,\text{flux}}$  and  $F_{\text{DR},\text{sput}}$  that are to be optimized (to the right). Green (filled) arrows indicate a co-correlation, and red (unfilled) arrows mark a counter-correlation. The widths of the arrows indicate the strength of their influence. From Brenning et al. (2020)

As a figure of merit, useful for comparing different discharges, we identify  $(1 - \beta_t)$  which is the fraction of ionized sputtered material that escapes back-attraction toward the cathode target. We show that a discharge with a higher value of  $(1 - \beta_t)$  always can be arranged to give better combinations of ionization and deposition rate than a

---

discharge with a lower  $(1 - \beta_t)$ . Maximization of  $(1 - \beta_t)$  is carried out empirically, based on measured data from two discharges with Ti targets in Ar working gas. These discharges were first modeled in order to convert measured plasma parameters to values of  $(1 - \beta_t)$ . The combined effects of varying the different process parameters were then analyzed using a process flow chart model. The effect of varying the degree of unbalance in the studied range was small. For the remaining three parameters, we find that optimum is achieved by minimizing the magnetic field strength, minimizing the working gas pressure, and minimizing the pulse length as far as compatible with the requirement to ignite and maintain a stable discharge. Fig 6.28 illustrates how the process parameters affect flux parameters (ionized flux fraction and deposition rate) through discharge parameters ( $\alpha_t$  and  $\beta_t$ ).

## 7 Conclusions

In conclusion, this thesis discusses the influence of the confining magnetic field on film properties, on one hand, and on the discharge properties, the deposition rate and ionized flux fraction in HiPIMS discharge, on the other hand. To systematically study the role of magnetic field experimentally, a variable magnet assembly capable of manipulating magnetic configuration and strength is used with a Ti target. For HiPIMS operated in the fixed pulse voltage mode, we found that there is a trade-off between the deposition rate (decreased by more than a factor of two) and the ionized flux fraction (increased by a factor of 4 – 5). The back attraction probability of the ions of the sputtered material in a HiPIMS discharge was found to be high and roughly constant independent of magnetic field strength and the ionization probability of the sputtered species increased with increasing magnetic field strength due to a increased discharge current when operating in the fixed pulse voltage mode. For HiPIMS operated in the fixed peak current mode, we found concurring, but smaller trends in the two parameters: decreasing magnetic field strength improved both the deposition rate (by 38 %) and the ionized flux fraction (by 53 %). When operating in the fixed peak current mode, the ionization probability of the sputtered species was roughly constant while the parameter  $(1 - \beta_r)$  increased roughly 30 % with decreasing magnetic field strength. In short, when operating a HiPIMS discharge in fixed voltage mode, the ionization probability  $\alpha_i$  at varied with magnetic field strength and  $\beta_r$  remained roughly constant, while, in the fixed peak current mode,  $\beta_r$  varied with magnetic field strength and at remained roughly constant.

These results are in line with properties of vanadium and vanadium nitride films deposited using two magnets with different characteristics. The films deposited by HiPIMS with strong magnetic confinement were generally denser and exhibited lower surface roughness. Higher film density and lower surface roughness can be explained by higher amount of available ionized sputtered species that we expect using stronger magnet. In addition, lowering the magnetic field strength increases the deposition rate significantly for non-reactive and reactive HiPIMS while it increases only slightly in the dcMS case. In this case, the films are less dense with rougher surface which is expected when ionized flux fraction is low.

A lower deposition rate compared to dcMS is the main drawback of the HiPIMS process. Besides back attraction of ionized material, sideways transport of sputtered material has been suggested to play an important role in the loss of axial HiPIMS deposition rate. To study this hypothesis, we placed an ion meter at the edge of the target cathode and perpendicular to the target surface. We observed that a significant portion of the sputtered material is deposited radially. For the same operating conditions, the sideways deposition rate is always the highest in dc operation while it is lower for HiPIMS operation, which is in line with our axial deposition rate measurements at the

---

substrate position. This radial deposition rate decreases with increasing axial distance from the target surface. Furthermore, depending on the magnetic field configuration, the radial ion deposition rate is 1 – 2 times higher than the axial ion deposition rate. Thus, there are significantly higher number of ions traveling radially than axially in the HiPIMS discharge. A comparison of the total radial as well as axial fluxes across the entire investigated plasma volume between the target and the substrate position allows for revised estimates of radial over axial flux fractions for different magnetic field configurations. It is here found that the total radial flux of film forming material is greater in dcMS compared to HiPIMS for almost all cases investigated. We therefore conclude that the commonly reported reduction of the axial deposition rate in HiPIMS compared to dcMS does not seem to be linked with an increase in sideways material transport in HiPIMS.



# Paper I

## **Vanadium and vanadium nitride thin films grown by high power impulse magnetron sputtering.**

H. Hajihoseini and J. T. Gudmundsson. 2017.

*Journal of Physics D: Applied Physics* **50**: 505302.

Copyright © by the Journal of Physics D: Applied Physics. All rights reserved. Permission for reproduction in this thesis granted by the copyright owner.



# Vanadium and vanadium nitride thin films grown by high power impulse magnetron sputtering

H Hajjoseini<sup>1,2</sup>  and J T Gudmundsson<sup>1,2,3</sup> 

<sup>1</sup> Science Institute, University of Iceland, Dunhaga 3, IS-107 Reykjavik, Iceland

<sup>2</sup> Department of Space and Plasma Physics, School of Electrical Engineering, KTH–Royal Institute of Technology, SE-100 44, Stockholm, Sweden

E-mail: [tumi@hi.is](mailto:tumi@hi.is)

Received 31 July 2017, revised 20 October 2017

Accepted for publication 30 October 2017

Published 23 November 2017



CrossMark

## Abstract

Thin vanadium and vanadium nitride films were grown on SiO<sub>2</sub> by non-reactive and reactive high power impulse magnetron sputtering (HiPIMS), respectively. The film properties were compared to films grown by conventional dc magnetron sputtering (dcMS) at similar conditions. We explored the influence of the stationary magnetic confinement field strength on the film properties and the process parameters. The deposition rate is much lower for non-reactive sputtering by HiPIMS than for dcMS. Furthermore, for both dcMS and HiPIMS the deposition rate is lower for strong magnetic confinement. Structural characterization was carried out using x-ray diffraction and reflection methods as well as atomic force microscopy and scanning electron microscope. Both dcMS and HiPIMS grown vanadium films are polycrystalline with similar grain size regardless of magnetic field strength. For dcMS grown vanadium films the surface roughness is higher when a strong magnetic field is used. For both non-reactive growth of vanadium and reactive growth of vanadium nitride the HiPIMS process produces denser films with lower surface roughness than dcMS does. Lowering the magnetic field strength increases the deposition rate significantly for reactive HiPIMS while it increases only slightly in the reactive dcMS case. The films grown by HiPIMS with strong magnetic confinement exhibit higher density and lower roughness. We find that the operating pressure, growth temperature, discharge voltage and film thickness has influence on the properties of HiPIMS grown vanadium nitride films. The films are denser when grown at high temperature, high discharge voltage and low pressure. The density of those films is lower for thicker films and thicker films consist of larger grain size. For all the films explored, higher density coincides with lower surface roughness. Thus, the deposition method, magnetic field strength, growth temperature, discharge voltage, film thickness and growth pressure have a significant influence on the film quality and structural properties, including the grain size for the various orientations.

Keywords: vanadium, vanadium nitride, magnetron sputtering, high power impulse magnetron sputtering, thin film, HiPIMS

(Some figures may appear in colour only in the online journal)

## 1. Introduction

Transition-metal (TM) nitrides such as VN, TaN and NbN are known to exhibit the B1 NaCl structure at room temperature

<sup>3</sup> Author to whom any correspondence should be addressed.

[1, 2]. The TM nitrides have many preferred properties like high melting point, high hardness, chemical stability and metallic conductivity. Among the TM nitrides, vanadium nitride has received attention as a hard material. Polycrystalline vanadium nitride thin films are used in a number of applications

including diffusion barriers in micro electronic devices [3, 4], as hard wear and scratch-resistant coatings [5], as a friction material in dry slicing against stainless steel [6], as a potential electrode material for energy storing systems (super capacitors) [7], and as anodes in rechargeable lithium ion batteries [8]. Furthermore vanadium nitride is known to exhibit superconductivity at low temperature [9]. Due to its material properties vanadium nitride has been suggested as a candidate for high-performance barrier material for Cu interconnects [3, 4, 10–12]. Takeyama *et al* [4, 11] have demonstrated that nanocrystalline textured vanadium nitride films grown between Cu and SiO<sub>2</sub> are chemically inert, and do not react with the adjoining layers, and are structurally stable. In the past, vanadium nitride films have been grown by atomic layer deposition [10, 13], direct nitridation of vanadium films at elevated temperature [7], reactive electron beam evaporation [6], reactive dc sputtering [4, 14, 15], pulsed laser deposition [16, 17], reactive magnetron sputtering [5, 18–22] and reactive ion beam sputtering [12]. It is known that the chemical composition, microstructure and hence, the material properties (such as optical, electrical and magnetic properties) of vanadium nitride films depend heavily on deposition parameters. Qiu *et al* [19] explored the influence of the nitrogen partial pressure and substrate bias on the film hardness and residual stress when depositing vanadium nitride by reactive magnetron sputtering on a Si(100) substrate. With increased nitrogen partial pressure the coatings became more compact and exhibited higher hardness. Chun [20] explored the growth of vanadium nitride thin films by inductively coupled plasma assisted magnetron sputtering (ICP-MS) and finds that the power applied to the ICP discharge and thus the metal ion flux has a significant influence on the film properties. The coating microstructure evolved from a porous columnar structure to a highly dense structure as the ICP power, and thus the ionization fraction of the sputtered material was increased. The vanadium-nitrogen phase diagram indicates that two stable phases exist: the hexagonal  $\beta$ -V<sub>2</sub>N and the cubic  $\delta$ -VN phases [2].

The high power impulse magnetron sputtering (HiPIMS) discharge is an ionized physical vapor deposition technique that has attracted much interest lately [23, 24]. By pulsing the target to a high power density with unipolar voltage pulses, a low duty cycle, and low frequency, high electron density is achieved, and thus a high ionization fraction of the sputtered material [23, 24]. Earlier we have shown that HiPIMS-deposited TiN films produce denser films at lower deposition temperatures, have significantly lower surface roughness [25], and have significantly lower electrical resistivity than dc magnetron sputtered (dcMS) films on SiO<sub>2</sub> at all growth temperatures, due to reduced grain boundary scattering [26]. We also demonstrated that ultrathin continuous TiN films have superior electrical characteristics and are more resistant to oxidation than the dcMS grown films. The largest change in resistivity was seen for films grown at room temperature. One major drawback with HiPIMS is the low deposition rate compared to conventional dc and mid-frequency magnetron sputtering. Recent studies have shown that a small decrease in the magnetic field strength can lead to a significant increase

in the deposition rate [27, 28]. Furthermore, Bradley *et al* [29] explored the influence of the magnetron magnetic field strength on the deposition rate and showed that the deposition rate increases with increased magnetic field for dcMS and mid-frequency magnetron sputtering, while it increases with decreasing magnetic field for HiPIMS. Čapek *et al* [30] have shown that target erosion leads to increased discharge current, which they relate to increased magnetic field strength due to the thinner target. They point out that this can lead to poor process reproducibility of the HiPIMS process.

Here, we study and compare the growth and film properties of vanadium and vanadium nitride films by HiPIMS and dcMS. We demonstrate that the HiPIMS technique provides thin vanadium and vanadium nitride films of superior quality compared to dcMS grown films (higher density, smoother surface). However, the deposition rate is significantly lower. We explore the influence of the magnetic field strength, growth temperature, reactive gas flow rate, and working gas pressure on the deposition rate, the film structure and morphology in order to optimize the film quality. Also we explore the trade-off between the film quality and the deposition rate as the magnetic field is varied. In section 2 we discuss the deposition tools and the characterization methods applied. In section 3 we explore how the properties of vanadium and vanadium nitride films vary for different operating conditions. Section 4 summarizes our findings.

## 2. Experimental apparatus and method

The vanadium and the vanadium nitride thin films were grown in a custom built magnetron sputtering chamber [31] with a base pressure of  $4 \times 10^{-6}$  Pa. The working gas was argon of 99.999% purity mixed with nitrogen gas of 99.999% purity. The argon flow rate was  $q_{Ar} = 40$  sccm and the nitrogen flow rate varied from  $q_{N_2} = 0$  to  $q_{N_2} = 5$  sccm. A throttle valve was used to maintain a total working pressure at 0.9 Pa. The vanadium target was 75 mm in diameter and of 99.995% purity.

The substrates used were thermally oxidized Si(001) with an oxide thickness of 1  $\mu$ m. The substrate temperature was maintained at 400 °C during growth (unless stated otherwise) with a 1.5 inch (3.8 cm) diameter circular plate heater, separated from the substrate holder by a 2 mm gap. The substrate holder design is described in more detail by Arnalds *et al* [31]. All depositions have been made while keeping the substrate holder grounded.

For HiPIMS operation, the power was supplied by a SPIK1000A pulse unit (Melec GmbH) operating in the unipolar negative mode at constant voltage, which in turn was charged by a dc power supply (ADL GS30). The discharge current and voltage was monitored using a combined current transformer and a voltage divider unit (Melec GmbH) and the data were recorded with a digital storage oscilloscope (Agilent 54624A). The pulse length was 200  $\mu$ s and the pulse repetition frequency was 100 Hz. For dcMS, a dc power supply (MDX 1K, Advanced Energy) was connected to the magnetron. In both methods, depositions were made at 150 W average power. To investigate the effect of magnetic field strength on the film properties, two magnets with different

**Table 1.** Measured and calculated specifications of two magnets.

Magnet	Center diameter (mm)	Ring diameter (mm)	MFD of center (average)	MFD of ring (average)	Magnetic flux of center (total)	Magnetic flux of ring (total)	$K$	$K_G$
Weak	14	10	0.322 T	0.314 T	49 $\mu$ Wb	690 $\mu$ Wb	0.07	1
Strong	30	8	0.396 T	0.367 T	279 $\mu$ Wb	664 $\mu$ Wb	0.42	2.9

strength have been used. Both magnets are 3 inches in diameter and were purchased from Angstrom Science. We determine the total magnetic flux of center and ring magnets (north and south poles). The method allows us to illustrate the balance and unbalance property of the magnets in a quantitative way. To this end, magnetic flux density (MFD) has been measured at different points of the magnets (close to the surface) to achieve an average MDF over each magnet. Then it is multiplied by the cross-section area of the magnets to achieve the total magnetic flux. By comparing the magnetic field strength of the two poles, it is easy to determine how unbalanced the magnetron is. Table 1 summarizes measured and calculated specifications of the two magnets. The magnetic fields were measured in a bench set up by a Hall probe over the center of the race track. For the strong magnet, the average out of plane and in plane magnetic field are 18 and 93  $\mu$ T, respectively, and for the weak magnet those are 4  $\mu$ T and 36  $\mu$ T, respectively. Moreover, the imbalance coefficient  $K$  is calculated as the ratio of the magnetic fluxes of the center magnet and the outer magnetic ring. Thus a magnetron is balanced if  $K = 1$ . The geometrical imbalance coefficient  $K_G$  is the ratio of the distance between the magnetic zero of the magnetron (the point along the middle axis where  $B_{\perp}$  changes its orientation, i.e.  $B_{\perp} = 0$ ) and the target surface, and the diameter of the erosion rill on the target surface [32, 33]. Details on calculations and definitions of the two coefficients can be found in the work of Svadkovski *et al* [32].

X-ray diffractometry (XRD) was carried out using a Philips X'pert diffractometer (Cu  $K_{\alpha}$ , wavelength 0.15406 nm) mounted with a hybrid monochromator/mirror on the incident side and a 0.27° collimator on the diffracted side. A line focus was used with a beam width of approximately 1 mm. The grazing incidence XRD (GIXRD) scans were carried out with the incident beam at  $\theta = 1^{\circ}$ . We performed low-angle x-ray reflectivity (XRR) measurements with an angular resolution of 0.005° to determine the film thickness, density and roughness and its data was fitted using Parrat formalism [34] for reflectivity. Adding a low density surface layer on top of the film was required to achieve a good fit. This may be interpreted as being due to a formation of oxide or oxynitride surface layer after the films were removed from the vacuum chamber, as previously observed [35]. The film surface morphology was characterized by contact-mode atomic force microscope (AFM) analysis in an XE-100 multi-mode AFM system (PSIA Inc.) in air (*ex situ*).

The surface and cross section features of the vanadium nitride films were studied using a FEI Nova 200 dual beam, focused ion beam-scanning electron microscope systems (FIB-SEM). The acceleration voltage of the electron and ion beam were set to 10 and 30kV, respectively. The FIB was

applied to prepare the samples in order to take cross sectional SEM images. The working distance was kept at 5 mm for all the images presented.

### 3. Results and discussion

Vanadium and vanadium nitride films were grown by HiPIMS and dcMS while varying the various process parameters. Section 3.1 discusses the growth of vanadium films in the bcc  $\alpha$ -V phase by HiPIMS and dcMS and two magnetic field strengths. In section 3.2 we explore how adding nitrogen gas leads to the formation of vanadium nitride. For low nitrogen flowrate we observe the hexagonal  $\beta$ -V<sub>2</sub>N phase and at higher flowrate we get the fcc  $\delta$ -VN phase. Once we have established the nitrogen flowrate that gives the  $\delta$ -VN phase we explore how the magnetic field strength influences the deposition rate and the film quality in section 3.3. We explore how film thickness influences the film density, surface roughness and grain size in section 3.4. Then we study the effect of the growth temperature in section 3.5, the discharge voltage in section 3.6 and pressure in section 3.7.

#### 3.1. Vanadium deposition with varying magnetic field strength

Roughly 120 nm thick Vanadium (V) films were deposited by both dsMS and HiPIMS and with both weak and strong magnets. The GIXRD pattern for pure vanadium film (0 sccm N<sub>2</sub>) grown by HiPIMS is shown in figure 1. The peak at  $2\theta = 42.3^{\circ}$  corresponds to the (1 1 0) orientation of the bcc vanadium film, the  $\alpha$ -V phase [36, p 58]. GIXRD measurements show that both HiPIMS and dcMS grown V films have polycrystalline structure with similar grain size and using different magnetic field strength does not affect the structural properties significantly. Table 2 shows the data which are extracted from AFM and XRR measurements for the four cases explored here. With both strong and weak magnets, HiPIMS growth results in significantly denser films than grown by dcMS. In the case of HiPIMS, the vanadium film (excluding a top low density layer), which was grown by the strong magnet has higher density than that grown by the weak magnet. It is vice versa for the dcMS grown film. The higher density achieved by HiPIMS has been observed before for various metallic films including Ti, Cr, Zr, Al, Ta, Pt and has been explained in terms of high metal ionization degree [37]. There it is found that the HiPIMS grown metallic films were generally 5–15% denser than dcMS grown films. Furthermore, it has been demonstrated that using strong magnet results in elevating the metal ion charge states [38]. Similar findings are reported by Huo *et al* [39] for a Ti target where a stronger magnet enhances the Ti<sup>2+</sup> fraction in the discharge current and lowers the Ti<sup>+</sup>

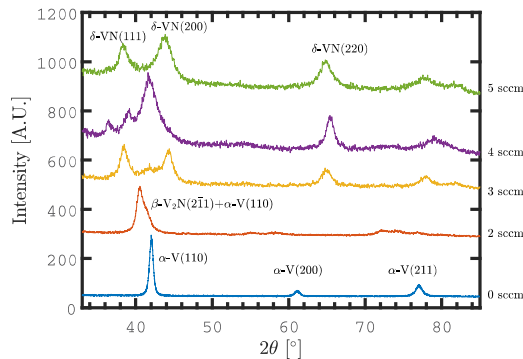


**Figure 1.** GIXRD pattern from vanadium nitride films which were grown by HiPIMS at different nitrogen flow rates with weak magnet, at 0.9 Pa, 150 W average power, pulse length 200  $\mu$ s and repetition frequency of 100 Hz.

fraction. As with higher ionization degree, increased density of doubly ionized metal atoms can further improve the density of HiPIMS grown films.

The data listed in table 2 shows that for dcMS grown vanadium films the surface roughness is similar for both magnet strengths, while HiPIMS grown films exhibit lower roughness, and the lowest roughness is achieved when the film is grown utilizing a strong magnet. Figure 2 shows the surface topology of the aforementioned vanadium films. We see that the two HiPIMS grown films (figures 2(a) and (b)) are significantly smoother than the dcMS grown films (figures 2(c) and (d)), and for HiPIMS grown films that using a strong magnet (figure 2(a)) leads to significantly smoother surface than a weak magnet (figure 2(b)), which agrees with the numbers given in table 2.

We also observe that the deposition rate for HiPIMS grown films is much lower than for dcMS grown films. This is consistent with what has been reported by Samuelsson *et al* [37] and Helmersson *et al* [23] on the ratio of the deposition rates (DR),  $DR_{\text{HiPIMS}}/DR_{\text{dcMS}}$  for pure metals. Although in both of these reports, the ratios are less than one, they are not the same. One reason for this variation could be the use of different magnetic field strength during deposition. Our results show for both dcMS and HiPIMS deposition, that film growth by the strong magnet exhibits lower deposition rate than growth with the weak magnet. The ratio  $DR_{\text{HiPIMS}}/DR_{\text{dcMS}}$  for vanadium films is 0.37 and 0.77 for the strong and weak magnets, respectively. The variation of the magnetic field strength in a sputtering system could strongly affect the ionization and transport of the ionized species from the plasma to the growing film by changing the confinement strength for the electrons. Previously, Mishra *et al* [27] have identified a large potential barrier in HiPIMS deposition for the transport of the sputtered post-ionized species from target to the substrate. They demonstrated that a small reduction in the magnetic field strength can effectively reduce this barrier effect, thereby increasing the HiPIMS deposition rate significantly.

### 3.2. Vanadium nitride deposition with varying nitrogen flow rate

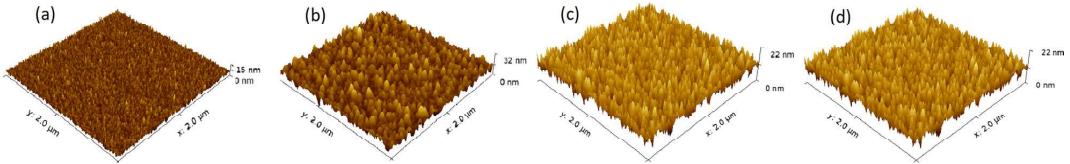
To grow vanadium nitride films, an Ar/N<sub>2</sub> mixture was injected into the chamber. Figure 1 shows GIXRD pattern for films which were grown by HiPIMS at 0 (121 nm), 2 (102 nm), 3 (71 nm), 4 (66 nm) and 5 (63 nm) sccm nitrogen flow rates. Comparing the obtained GIXRD peaks with reference peaks indicates that 5 sccm nitrogen flow rate is sufficient to grow polycrystalline  $\delta$ -VN films. At 5 sccm flow rate the peak at  $2\theta = 43.6^\circ$  is dominant in the GIXRD pattern. This peak has been assigned to the cubic fcc  $\delta$ -VN(200) [21, 22]. So at nitrogen flow rate of 5 sccm the films are polycrystalline and the preferred orientation is (200). The peak at  $2\theta = 39^\circ$  is assigned to the cubic fcc  $\delta$ -VN(1 1 1) and the peak at  $2\theta = 65^\circ$  to the cubic  $\delta$ -VN(220). The film grown at 2 sccm exhibits a peak at  $41^\circ$  which we believe is due to coexistence of (2̄1 1) facet of the hexagonal  $\beta$ -V<sub>2</sub>N phase and the (1 1 0) facet of the  $\alpha$ -V phase. Similar observation was reported by Farges *et al* [21]. The two phases  $\delta$ -VN and  $\beta$ -V<sub>2</sub>N seem to coexist for films grown at nitrogen flow rates of 3 and 4 sccm, and the cubic  $\delta$ -VN phase dominants for flow rate of 3 sccm. Similarly, Geuddaoui *et al* [22] explored the growth of vanadium nitride thin films while varying the nitrogen flow rate. The films crystallize dominantly into the hexagonal  $\beta$ -V<sub>2</sub>N<sub>1-x</sub> phase at low nitrogen gas flows and into the cubic  $\delta$ -VN<sub>1-x</sub> phase at high nitrogen gas flows. They found the as-deposited vanadium nitride films to be highly textured and that the texture depends on the nitrogen gas flow. In all the vanadium nitride films grown, the peaks of cubic (fcc) (1 1 1), (200), (220), and (3 1 1) were observed (JCPDS 25–1252). Chun [20] found that from x-ray diffraction analysis that the films grown by ICP-MS are single-phase  $\delta$ -VN coatings. They also reported that the intensities of the peaks vary with increased ICP power, and that the preferred orientation was changed from (1 1 1) texture, to (200) texture, and then to (220) texture with an increase in ICP power, or increased ion flux towards the substrate. Similarly, Ge *et al* [18] saw that the films exhibit different preferred orientations, which ranged from a strong (1 1 1) texture when growing with dcMS only to a dominating (200) texture when co-sputtering from two targets, one pulsed at 350 kHz or 100 kHz and the other with applied rf power.

Figure 3(a) shows 200  $\mu$ s long voltage pulses applied to discharges at different nitrogen flow rates to achieve 150 W average power and its related current waveforms. It is noticeable that higher nitrogen flow rates contribute to more delay on plasma ignition as well as higher discharge current. We have earlier seen an increased delay with increased oxygen flow rate when operating with Ti target [40], and also seen increased delay with decreasing repetition frequency when operating Ar/O<sub>2</sub> discharge [41] and Ar/N<sub>2</sub> discharge [42] with Ti target. It can be considered being due to a change in the ionization processes, increased collisional energy loss per electron-ion pair created, due to rotational, vibrational and dissociation processes of the molecules, as well as the target surface condition



**Table 2.** Extracted data from XRR and AFM measurements of vanadium films.

Method	Magnet	Density (g cm <sup>-3</sup> )	DR (nm min <sup>-1</sup> )	Roughness (nm)	Orientation grain size (nm)		
					(110)	(200)	(211)
HiPIMS	Strong	5.79	0.98	2.41	16	12.5	11.1
HiPIMS	Weak	5.59	2.54	5.76	15.8	12.3	10.4
dcMS	Strong	5.11	2.66	8.41	16.2	13	10.5
dcMS	Weak	5.23	3.36	8.30	16	12.5	11.4



**Figure 2.** The surface morphology of vanadium films grown with (a) HiPIMS and strong magnet, (b) HiPIMS and weak magnet, (c) dcMS and strong magnet, and (d) dcMS and weak magnet.

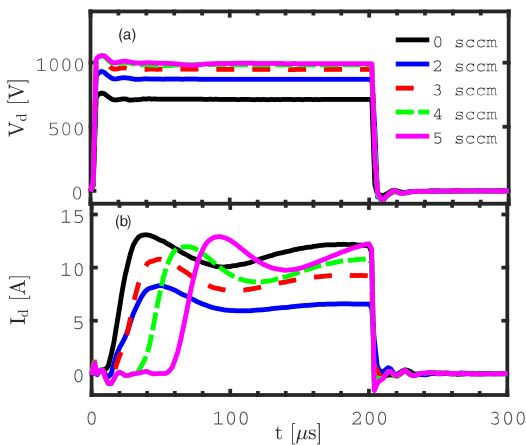


**Figure 3.** The (a) discharge voltage, and (b) discharge current waveforms captured during HiPIMS deposition with different nitrogen flow rates and vanadium target. The neutral gas pressure is 0.9 Pa, voltage pulse is 200 µs long and the pulse frequency is 100 Hz. The relatively higher current in the non-reactive mode is due to using eroded vanadium target.

[43]. The current waveforms can be described by three distinct regions, as previously described by Lundin *et al* [44] (I) plasma initiation and a current maximum, followed by (II) a decay to a minimum and then (III) a steady state regime that remains as long as the discharge voltage level is maintained. The initial peak in the discharge current is a result of strong gas compression due to the sudden large flux of atoms from the target. Collisions of the sputtered atoms with the working gas atoms results in heating and expansion of the working gas, known as rarefaction. The rarefaction causes the discharge current to fall. As a result, the sputtered atoms replace the working gas atoms in the vicinity of the cathode target to some extent as the pulse evolves. We also note that the discharge current increases with increased nitrogen partial pressure. An increase in the discharge current upon the addition of reactive molecular

**Table 3.** Extracted data from XRR measurements of vanadium nitride films grown at 400 °C, at average power of 150W, and 0.9 Pa. The HiPIMS pulse was 200 µs long and the repetition frequency 100 Hz.

Method	Magnet	Density (g cm <sup>-3</sup> )	DR (nm min <sup>-1</sup> )	Roughness (nm)
HiPIMS	Strong	6.14	0.83 (nm min <sup>-1</sup> )	0.63
HiPIMS	Weak	5.79	1.35 (nm min <sup>-1</sup> )	2.53
dcMS	Strong	5.25	1.55 (nm min <sup>-1</sup> )	5.44
dcMS	Weak	5.17	1.59 (nm min <sup>-1</sup> )	4.17

gas has been reported for various gas and target combinations [41, 42, 45, 46]. Recently this discharge current increase has been explained as being due to working gas recycling as the target becomes increasingly poisoned in an Ar/O<sub>2</sub> discharge with Ti target [47]. This discharge current increase can also be due to self sputter recycling [48]. In addition, we observed a decrement in the deposition rate by increasing the nitrogen partial pressure which is in agreement with what was reported previously for reactive dcMS [19, 22].

### 3.3. Vanadium nitride deposition with varying magnetic field strength

Here, the vanadium nitride film properties and its discharge characteristics captured during growth while varying the magnetic field strength are presented. Depositions have been made by both HiPIMS and dcMS methods and using both weak and strong magnets for each method and all films are roughly 48 nm thick. All the films are grown at  $q_{Ar} = 40$  sccm and  $q_{N_2} = 5$  sccm. The film density, deposition rate and surface roughness are compared in table 3. The film grown by HiPIMS and the strong magnet exhibits the highest density (6.14 g cm<sup>-3</sup>) which is similar to the bulk VN density (6.13 g cm<sup>-3</sup> [49]). Similar to the pure V films, using the weak magnet in the HiPIMS process, the film density decreased slightly (5.79 g cm<sup>-3</sup>). For the dcMS grown films the density is smaller and remained roughly constant at 5.25 and 5.17 g

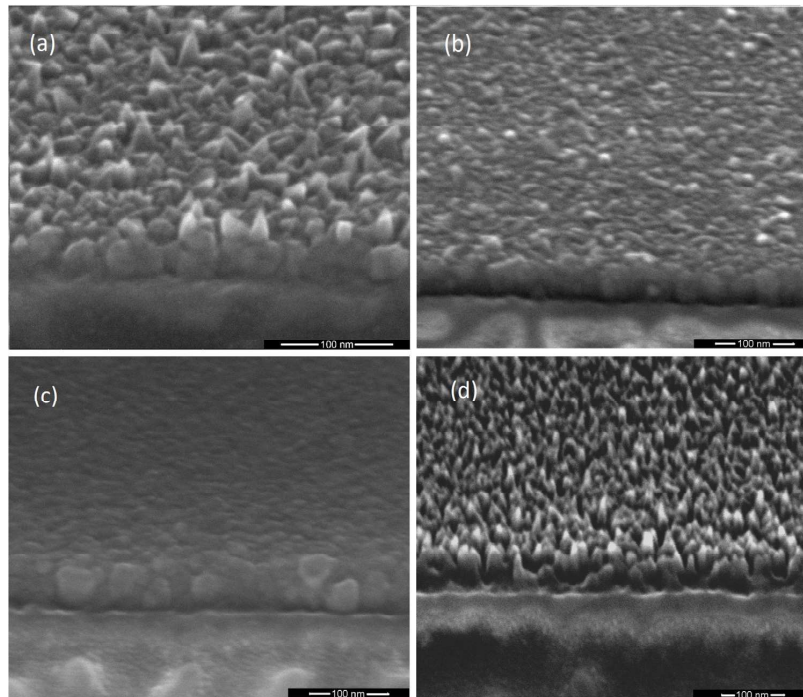


**Figure 4.** SEM images of VN films grown at 0.9 Pa by (a) dcMS with weak magnet at 400 °C, (b) HiPIMS with weak magnet at 400 °C, (c) HiPIMS with strong magnet at 400 °C, and (d) HiPIMS with strong magnet at 30 °C. Images were taken at an angle of 52°.

$\text{cm}^{-3}$  while we change from the strong to the weak magnet. Although these dcMS grown VN films show similar densities, this behavior is different from pure V film growth where using the strong magnet resulted in slightly lower density (section 3.1). By looking at the deposition rates in table 3, we see that the film grown with dcMS and the weak magnet has the highest deposition rate while that grown with HiPIMS and the strong magnet exhibits the lowest deposition rate. The ratio  $DR_{\text{HiPIMS}}/DR_{\text{dcMS}}$  is 0.53 and 0.85 for strong and weak magnets, respectively, which are higher than the ratios calculated for pure V films in the section 3.1. Table 3 also lists the surface roughness for the four films. Figure 4 shows the SEM images of VN films grown at 400 °C and 30 °C with weak and strong magnets, with dcMS and HiPIMS, respectively. HiPIMS grown films exhibit significantly smoother surfaces than dcMS grown ones as seen by comparing figure 4(a) for dcMS and (b) for HiPIMS with the weak magnet. The HiPIMS grown film by strong magnet exhibits the smoothest film with 0.63 nm surface roughness also seen as very smooth surface in figure 4(c). For HiPIMS, using the stronger magnet results in smoother film as seen comparing figures 4(a) and (c), while dcMS leads to slightly rougher surfaces as seen in figure 4(a). These SEM images are consistent with the numerical values listed in table 3. This behavior also agrees with what was observed for pure V films which discussed in section 3.1.

The vanadium nitride films are polycrystalline, that means the films are made up of a large number of small crystallites. The microstructure is to a large extent determined by

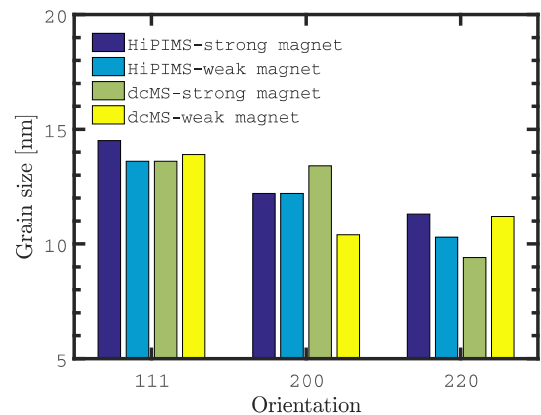


**Figure 5.** Calculated  $\delta$ -VN films grain size from GIXRD spectrum of (1 1 1), (2 0 0) and (2 2 0) orientations. The films were grown at pressure of 0.9 Pa and growth temperature of 400 °C.

the grain size and the grain boundary morphology. The grain size can be calculated from the full width at half maximum of the peaks using the Scherrer formula. Figure 5 shows grain size calculated for the (1 1 1), (2 0 0) and (2 2 0) crystallites of the cubic  $\delta$ -VN films. In contradiction to what was observed for pure V films, using HiPIMS and dcMS methods and different magnets has some effects on the grain size of the  $\delta$ -VN films. In all the films, 111 grains are the largest ones which is predictable due to the fcc structure of  $\delta$ -VN [50]. HiPIMS



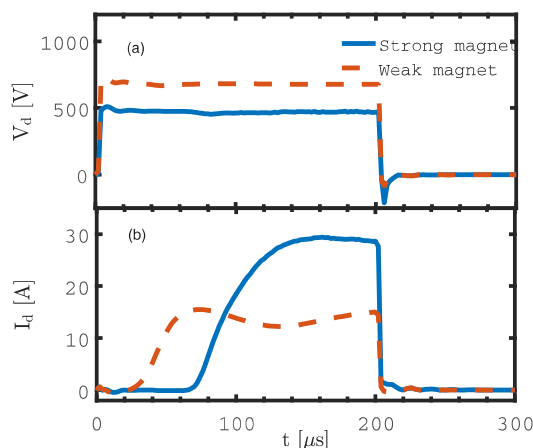


**Figure 6.** The (a) discharge voltage, and (b) discharge current waveforms captured during vanadium nitride HiPIMS deposition with strong and weak magnets. The voltage pulse is 200  $\mu\text{s}$  long and the pulse frequency is 100 Hz.

film grown by the strong magnet shows 14.5 nm grains which is the largest 111 grain size. Other films exhibit roughly the same grain size with 13.5 nm size. The (111) texture is relatively independent of the growth method and magnetic field strength. The film grown by dcMS and strong magnet has the biggest (200) grain with 13.4 nm size. On the other hand, dcMS grown film by weak magnet exhibits the smallest 200 grains with 10.4 nm size. The strength of the magnet does not affect the (200) grain size for HiPIMS grown films and they show 12.2 nm grain size. In addition using dcMS and the weak magnet, similar to using HiPIMS and the strong magnet results in roughly 11.3 nm 220 grain size which is larger than other films. HiPIMS with the weak magnet and dcMS with the strong magnet are in second and third ranks with 10.3 nm and 9.4 nm grains, respectively. It is not clear from the literature if HiPIMS or dcMS grown films are expected to exhibit smaller grain size. Smaller grain size has been reported for polycrystalline TiN [25] and TaN [51] films grown by HiPIMS compared to dcMS grown films, while for AlN [52], TiO<sub>2</sub> [53], and CrN [54] films grown by HiPIMS the grain size is larger than for dcMS grown films. Rudolph [51] found that the grain size decreases with increased discharge cathode potential and argued that due to the high mass of Ta in the cathode, these can reach considerable energies at the highest cathode potential and thus these backscattered neutrals lead to the smaller grains observed in HiPIMS grown films compared to dcMS grown films. In this regard, V is of similar mass as Ti, so we could expect VN and TiN growth to exhibit similar behavior. Chun [20] reported a decreased grain size in VN films with increased ICP power, or increased metal ion flux, when grown by ICP-MS, from 10.1 to 4 nm. This indicates that increased ionization of the sputtered material leads to smaller grain size. However, we observe somewhat larger grain size for HiPIMS grown films reported here as seen in figure 5.

Figure 6 shows voltage and current waveforms which were captured during HiPIMS deposition by strong and weak magnets. The magnetron discharge voltage was 700V and 500V for weak and strong magnets, respectively, to achieve 150W average power as seen in figure 6(a). It results in 30 A and 16 A maximum discharge current for strong and weak magnets, respectively. This decrease in the discharge current with decreased magnetic field strength has been demonstrated by Čapek *et al* [30] which placed spacers between the magnets and the target in order to lower the magnetic field strength at the target surface. In figure 6(b) it can be seen that the discharge with weak magnet exhibits current peak at 60  $\mu\text{s}$  after pulse initiation and approaches a plateau 200  $\mu\text{s}$  after the pulse onset while by strong magnet the current increases monotonically and the peak appears 160  $\mu\text{s}$  after starting the pulse. Likewise the current starts to rise 70  $\mu\text{s}$  after applying voltage pulse to the cathode target with strong magnet which is roughly 30  $\mu\text{s}$  later than for the weak magnet. The presence of a magnetic field drives the electrons into helical path close to the target. By increasing the strength of magnetic field, electrons are forced to travel longer convoluted paths before an ionizing occurs. This can contribute to increased delay on the breakdown and discharge onset [43]. Besides, applying lower voltage to the strong magnet is another reason for the longer delay [43]. However, the effect of the magnetic field strength on the current delay onset remains to be explained.

#### 3.4. Vanadium nitride deposition up to different thickness

To investigate the effect of vanadium nitride film thickness on other properties of the film, 13, 41.2 and 94 nm thick  $\delta$ -VN films were grown by HiPIMS with the weak magnet at  $q_{\text{Ar}} = 40 \text{ sccm}$  and  $q_{\text{N}_2} = 5 \text{ sccm}$  and 0.9 Pa operating pressure, and growth temperature of 400 °C. Figure 7 shows that the film density is slightly reduced by growing thicker films. The surface roughness shows a significant dependence on the film thickness, and increases from roughly 1 nm for 13 nm thick film to 5 nm for 94 nm thick film. Moreover, thicker films consist of bigger grain sizes for all orientations (figure 8). These results clearly demonstrate the importance of noting the film thickness to achieve reliable comparison of the film properties.

#### 3.5. Vanadium nitride deposition at different growth temperatures

GIXRD measurements of the HiPIMS deposited  $\delta$ -VN films at  $q_{\text{Ar}} = 40 \text{ sccm}$  and  $q_{\text{N}_2} = 5 \text{ sccm}$  and operating pressure of 0.9 Pa, using weak magnet, are shown in figure 9. The results demonstrate that the films are polycrystalline and that the (111), (200) and (220) crystal orientations are present in all samples. Grains oriented in the (111) direction are dominant for growth temperatures of 200 °C and below whereas the (200) orientation becomes more prominent with increasing growth temperature. These observations are consistent with our previous studies of TiN [25] and can be attributed to the competition between the temperature dependent fast lateral

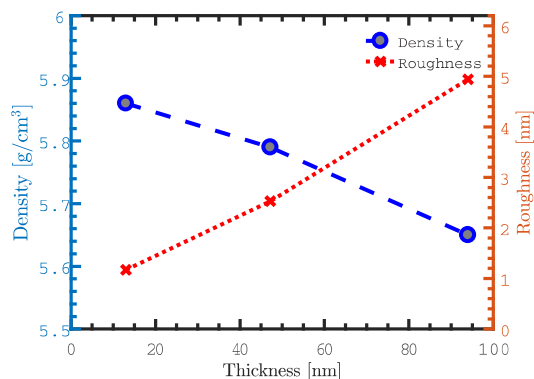


**Figure 7.** The density and surface roughness of  $\delta$ -VN HiPIMS deposited films versus the film thickness. The films were grown at 0.9 Pa with 200  $\mu$ s long pulses at 100 Hz repetition frequency, and growth temperature of 400  $^{\circ}$ C.

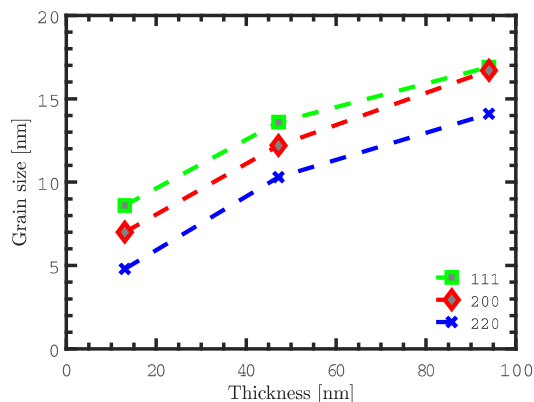


**Figure 8.** Average grain size of the (111), (200) and (220) crystallites of 10, 42.7 and 94 nm thick  $\delta$ -VN films. Grain sizes are calculated from the full width at half-maximum of the corresponding GIXRD scans using the Scherrer formula. HiPIMS grown films at 0.9 Pa, with pulse length 200  $\mu$ s, repetition frequency of 100 Hz, and growth temperature of 400  $^{\circ}$ C.

growth rate of the (200) oriented grains and the large geometric growth rate of the (111) oriented grains [55]. In other words, Ti adatoms form one N back bond on (100) surfaces and three N back bonds on (111) surfaces. Thus, cation diffusivities and potential energies are higher on (001)-oriented grains than on (111)-oriented grains and thus Ti adatoms have a larger chance of becoming trapped at (111) sites. This has the consequence that (111)-oriented grains slowly and relentlessly expand at the expense of the (200) grains under low temperature growth conditions [50]. We would expect the same behavior with V and N while forming  $\delta$ -VN films. The grain size of the (111), (200) and (220) crystallites are shown versus growth temperature in figure 10. The (200) grain size increases steadily with increasing temperature from 5 to 13 nm when the growth temperature is increased from 30 to 600  $^{\circ}$ C, whereas the size of the (111) oriented grains decreases from 13.4 nm for growth at 30  $^{\circ}$ C to a minimum of 12.1 nm for growth at 400  $^{\circ}$ C after which it starts to increase

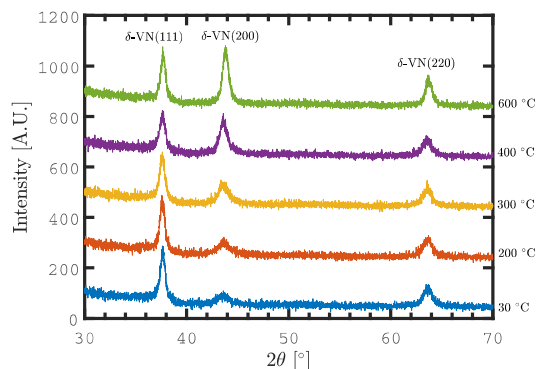


**Figure 9.** GIXRD scans of the  $\delta$ -VN films, grown by HiPIMS at different temperatures shown on the right and  $q_{Ar} = 40$  sccm and  $q_{N_2} = 5$  sccm. The curves are shifted for clarity. The films are polycrystalline with the (111), (200) and (220) orientations present at all growth temperatures.

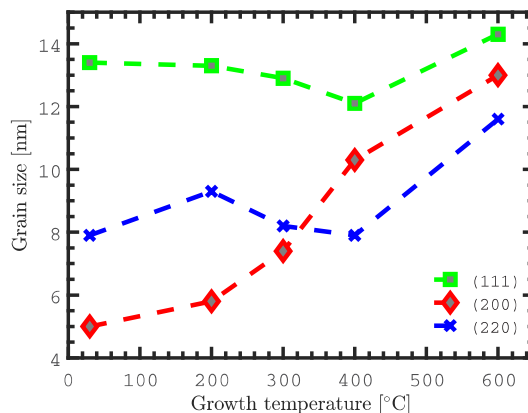


**Figure 10.** Average grain size of the (111), (200) and (220) crystallites in the  $\delta$ -VN films calculated from the full width at half-maximum of the corresponding GIXRD scans using the Scherrer formula. The (111) grains are the largest at low temperature whereas the (200) grain size increases with temperature. HiPIMS grown films at 0.9 Pa, with pulse length 200  $\mu$ s and repetition frequency of 100 Hz.

with temperature to 14.3 nm at 600  $^{\circ}$ C. The (200) crystallites are smaller than the (111) crystallites for all growth temperatures. XRR measurements were performed to determine the film thickness, density and roughness. The XRR scans are shown in figure 11 where the trend of increasing density and decreasing roughness with increasing growth temperature is apparent. The results of fitting the data are shown in figure 12. Interestingly, different layer models are required to obtain a good fit to films grown at different temperatures. Films grown at 400 and 600  $^{\circ}$ C are well represented by a single  $\delta$ -VN layer model whereas for the films grown at 30, 200 and 300  $^{\circ}$ C a low density interface layer, a few nanometer thick, must be introduced between the  $\delta$ -VN film and the  $\text{SiO}_2$  substrate. This can be interpreted as being due to the damage done to the  $\text{SiO}_2$  surface by the ion bombardment present during HiPIMS deposition [56]. This damage is repaired by annealing at the

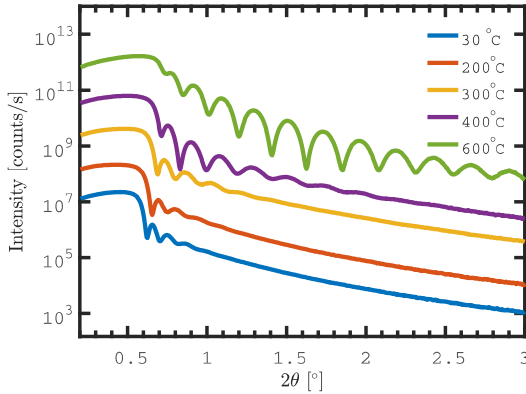


**Figure 11.** XRR measurements of the vanadium nitride films grown at the temperatures. The data for the films grown at 200–600 °C are shifted by a factor of  $10$ ,  $10^2$ ,  $10^3$  and  $10^4$ , respectively. The critical angle can be seen to increase with increasing growth temperature due to the increase in density.

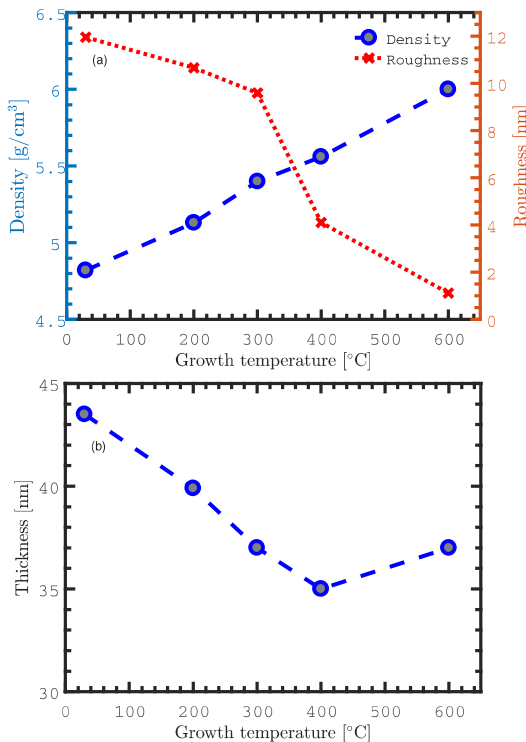


**Figure 12.** Results from fitting XRR measurements. The (a) density and roughness, and (b) thickness of  $\delta$ -VN films grown by HiPIMS at different temperatures for  $q_{Ar} = 40$  sccm and  $q_{N_2} = 5$  sccm and pressure 0.9 Pa. The dashed lines are guides to the eye.

higher growth temperatures. For these films a low density surface layer on top of the  $\delta$ -VN film is also required to achieve a good fit. This we interpret as being due to a combination of the high surface roughness of these films (figure 4(d)) and the formation of an oxynitride surface layer after the films

are removed from the vacuum, as previously seen for the TiN films [25, 35].

The density of the  $\delta$ -VN layer (excluding the thin interface/surface layers) is approximately  $6 \text{ g cm}^{-3}$  for films grown at 600 °C (the bulk value is  $6.13 \text{ g cm}^{-3}$  [49]). Note that the high density of the 400 °C grown HiPIMS film coincides with the minimum in the (1 1 1) grain size as seen in figure 10. Barna *et al* [57], proposed a structure zone model (SZM) for characterizing microstructure evolution in pure elemental films, which was later applied to the compound mode (reactive) by Petrov *et al* [50]. The SZM consists of three regions: Zone I corresponds to very low deposition temperatures at which adatom diffusion is negligible; surface diffusion becomes significant in the transition Zone T; and Zone II represents film growth at deposition temperatures for which both surface and bulk diffusion are operative. The boundaries between the zones are diffuse and transitions occur gradually over wide ranges in  $T_s/T_m$  where  $T_s$  and  $T_m$  are deposition temperature and melting point, respectively. During film growth in the low- $T_s$  Zone I regime, an underdense structure with a fine fiber texture develops. Initial in-plane grain sizes are set by the saturation nucleation density. Adatom mobilities are low and columns preserve the random orientation of the nuclei as predicted by ballistic models [58]. The columns are generally not single grains, but are composed of smaller more equiaxed grains, or can be completely amorphous. Surface roughness develops in a fractal geometry [59] which, due to wide angular distribution of the deposition flux, atomic shadowing, and limited surface diffusion, leads to extensive porosity [50]. The film thickness is tied closely to the density as can be seen in figure 12. All the films are grown for 35 min. Despite the constant growth time the film thickness is seen to decrease with increasing growth temperature, as the films become denser. However, the thickness increases for growth temperature between 400 and 600 °C remains unexplained. This increment was also observed before in TiN deMS grown films [25].

### 3.6. Vanadium nitride deposition at different discharge voltages

Three films were grown at 620V, 730V and 1000V discharge voltages and their properties are depicted in figure 13. All three films are roughly 36 nm thick and were deposited at  $q_{Ar} = 40$  sccm and  $q_{N_2} = 5$  sccm. Deposition at higher discharge voltage increases the film density while surface roughness decreases with increased discharge voltage (figure 13). Besides, the deposition rate increases significantly with increased discharge voltage from  $1 \text{ nm min}^{-1}$  at 620V to  $2.1 \text{ nm min}^{-1}$  at 730V and then to  $3.7 \text{ nm min}^{-1}$  at 1000V discharge voltage. Petrov *et al* [50] reported on an increase in the layer density and decrease in surface roughness from underdense  $\delta$ -TaN layers with intercolumnar voids and self-organized growth mounds separated by deep surface trenches to fully dense layers with smoother surfaces with increasing ion flux. They believe that the densification is attributed to less pronounced kinetic roughing due to ion-irradiation enhanced surface mobilities resulting in smoother surfaces with less atomic shadowing. Figure 14 illustrates that there is no

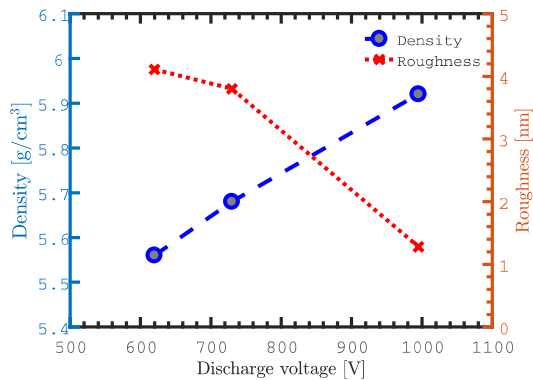


**Figure 13.** The density and surface roughness of HiPIMS grown  $\delta$ -VN films with weak magnet versus discharge voltage. The pulse length was 200  $\mu$ s, the pulse repetition frequency was 100 Hz, and growth temperature of 400  $^{\circ}$ C.

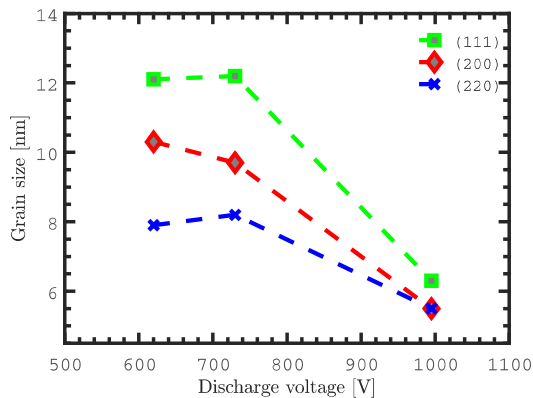


**Figure 14.** The grain size of HiPIMS grown  $\delta$ -VN films with weak magnet versus discharge voltage. The neutral gas pressure was 0.9 Pa, the pulse length was 200  $\mu$ s, the pulse repetition frequency was 100 Hz, and growth temperature of 400  $^{\circ}$ C.

significant change in grain size when increasing the discharge voltage from 620 V to 730 V, while rising the voltage up to 1000 V leads to remarkable decrement of the grains size in all the three orientations. This is consistent with other reports of the grain size in HiPIMS deposited films. Alami *et al* [54] have demonstrated a transition from polycrystalline to nanocrystalline films when the discharge current is increased (increased ion flux) in HiPIMS deposition of CrN. Ion irradiation induces surface defects that promote renucleation (or a secondary nucleation) of new islands that cause apparent periodical disruption of the individual grain growth [50]. In HiPIMS deposition this can result in column free films with nanosized grains that are not observed in the dcMS process [54, 60]. This also agrees with the findings of Rudolph [51] which claims that increased energy of backscattered neutrals in HiPIMS leads to smaller grain size. This behavior were also seen by Chun *et al* [20] that investigated effect of ICP power on  $\delta$ -VN grain size, and found that increasing the metal ion flux leads to smaller grain size.

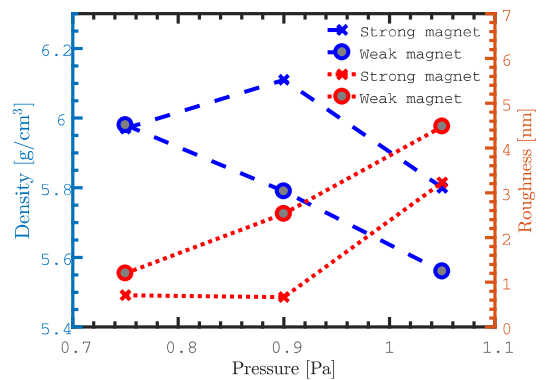


**Figure 15.** The density and surface roughness of HiPIMS grown  $\delta$ -VN films with weak and strong magnets versus pressures. The average power was 150 W, the pulse length 200  $\mu$ s, the pulse repetition frequency was 100 Hz, and growth temperature of 400  $^{\circ}$ C.

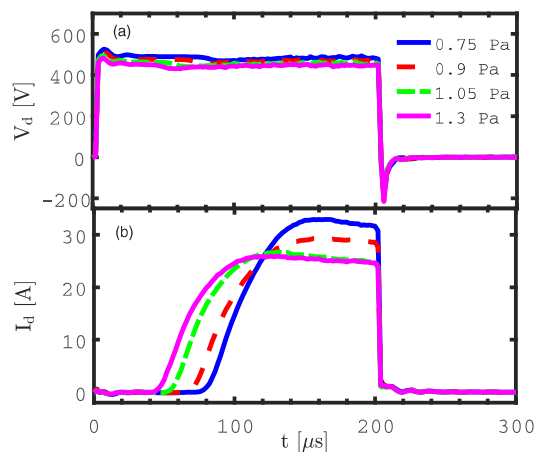


**Figure 16.** The (a) discharge voltage, and (b) discharge current captured during vanadium nitride HiPIMS deposition with strong magnet at different pressures. The average power was 150 W, the pulse length 200  $\mu$ s, and the pulse repetition frequency 100 Hz.

### 3.7. Vanadium nitride deposition at different pressures

To investigate the effect of the total gas pressure on the quality of HiPIMS grown  $\delta$ -VN films, the chamber pressure was changed by a throttle valve which is placed between chamber and the turbo molecular pump. In all cases a mixture of 40 sccm Ar and 5 sccm N<sub>2</sub> was injected to the chamber and all films are approximately 47 nm thick while the growth temperature was maintained at 400  $^{\circ}$ C. Figure 15 shows the film density and surface roughness versus the discharge operating pressure for HiPIMS grown films with both strong and weak magnets. We see that the film density decreases with increased discharge pressure while surface roughness increases. As before, we see that using weaker magnet leads to lower density and higher surface roughness.

By increasing the pressure, slight lowering of the discharge voltage is needed to reach the same average power while the



maximum current increases as seen in figure 16(a). There is also a shorter delay between the initiation of the voltage pulse and discharge ignition with increased discharge pressure as seen in figure 16(b). This can be understood because electrons can cause ionizing collisions earlier and the ionization may be occur closer to the target at higher pressure [43].

Liao *et al* [61] explored the influence of pressure on the crystallographic structure of  $\delta$ -VN films. At a low pressure of 0.5 Pa, the peak at  $43.6^\circ$  dominated in the XRD spectrum, which is the reflection of the cubic  $\delta$ -VN(200) texture while at 1.0 Pa, only a weak sign of the (200) texture is observed, and the (1 1 1) texture dominates at 2 Pa. Similarly we find that the (200) texture is dominating at 0.75 Pa (not shown) and it changes to the (1 1 1) texture being dominating at 1.3 Pa when  $\delta$ -VN films are grown by HiPIMS.

#### 4. Conclusion

We demonstrate the growth of vanadium and vanadium nitride thin films using both dcMS and HiPIMS while varying the magnetic field strength. We found that HiPIMS growth leads to denser films and smoother surfaces than films grown by dcMS. The films grown by HiPIMS with strong magnetic confinement are generally denser and exhibit lower surface roughness. Lowering the magnetic field strength increases the deposition rate significantly for reactive HiPIMS while it increases only slightly in the reactive dcMS case. We explored the vanadium nitride HiPIMS deposition at various nitrogen flow rates, different thicknesses, growth temperatures, discharge voltages and operating pressure. We see that mixture of 5 sccm  $N_2$  and 40 sccm Ar is sufficient to grow  $\delta$ -VN polycrystalline films. Increasing the growth temperature and discharge voltage as well as lowering the deposition pressure leads to the denser films. The density of the  $\delta$ -VN film decreases with increasing film thickness and thicker films exhibit larger grain size. For all the films explored, higher density coincides with lower surface roughness. For all of the cases we also show the influence of the process parameters on the discharge voltage and discharge current waveforms.

#### Acknowledgments

This work was partially supported by the University of Iceland Research Fund for Doctoral students, the Icelandic Research Fund Grant No. 130029, and the Swedish Government Agency for Innovation Systems (VINNOVA) contract no. 2014-04876.

#### ORCID iDs

H Hajihoseini  <http://orcid.org/0000-0002-2494-6584>

J T Gudmundsson  <https://orcid.org/0000-0002-8153-3209>

#### References

- [1] Mei A B, Hellman O, Wireklint N, Schlepütz C M, Sangiovanni D G, Alling B, Rockett A, Hultman L, Petrov I and Greene J E 2015 *Phys. Rev. B* **91** 054101

- [2] Carlson O N, Smith J F and Nafziger R H 1986 *Metall. Mater. Trans. A* **17** 1647
- [3] Takeyama M B, Itoi T, Satoh K, Sakagami M and Noya A 2004 *J. Vac. Sci. Technol. B* **22** 2542
- [4] Takeyama M B, Itoi T and Noya A 2010 *Japan. J. Appl. Phys.* **49** 05FA05
- [5] Chu X, Barnett S A, Wong M S and Sproul W D 1996 *J. Vac. Sci. Technol. A* **14** 3124
- [6] Wiklund U, Casas B and Stavlid N 2006 *Wear* **261** 2
- [7] Bondarchuk O, Morel A, Bélanger D, Goikolea E, Brousse T and Mysyk R 2016 *J. Power Sources* **324** 439
- [8] Sun Q and Fu Z-W 2008 *Electrochim. Acta* **54** 403
- [9] Toth L E, Wang C P and Yen G M 1966 *Acta Metall.* **14** 1403
- [10] Takeyama M B, Sato M, Sudoh H, Machida H, Ito S, Aoyagi E and Noya A 2011 *Japan. J. Appl. Phys.* **50** 05EA06
- [11] Takeyama M B, Sato M, Itoi T, Aoyagi E and Noya A 2016 *Japan. J. Appl. Phys.* **55** 02BC10
- [12] Qu X-P, Zhou M, Chen T, Xie Q, Ru G-P and Li B-Z 2006 *Microelectron. Eng.* **83** 236
- [13] Rampelberg G, Devloo-Casier K, Deduytsche D, Schaekers M, Blasco N and Detavernier C 2013 *Appl. Phys. Lett.* **102** 111910
- [14] Gray K E, Kampwirth R T, Capone D W, Vaglio R and Zasadzinski J 1988 *Phys. Rev. B* **38** 2333
- [15] Zasadzinski J, Vaglio R, Rubino G, Gray K E and Russo M 1985 *Phys. Rev. B* **32** 2929
- [16] D'Anna E, Cristoforo A D, Fernández M, Leggieri G, Luches A, Majni G, Mengucci P and Nanai L 2002 *Appl. Surf. Sci.* **186** 496
- [17] Dai Z N, Miyashita A, Yamamoto S, Narumi K and Naramoto H 1999 *Thin Solid Films* **347** 117
- [18] Ge F, Zhu P, Meng F, Xue Q and Huang F 2014 *Surf. Coat. Technol.* **248** 81
- [19] Qiu Y, Zhang S, Li B, Lee J-W and Zhao D 2012 *Procedia Eng.* **36** 217
- [20] Chun S-Y 2017 *J. Korean Ceram. Soc.* **54** 38
- [21] Farges G, Beauprez E and Degout D 1992 *Surf. Coat. Technol.* **54–55** 115
- [22] Gueddaoui H, Schmerber G, Abes M, Guemmas M and Parlebas J 2006 *Catal. Today* **113** 270
- [23] Helmersson U, Lattemann M, Bohlmark J, Ehiassarian A P and Gudmundsson J T 2006 *Thin Solid Films* **513** 1
- [24] Gudmundsson J T, Brenning N, Lundin D and Helmersson U 2012 *J. Vac. Sci. Technol. A* **30** 030801
- [25] Magnus F, Ingason A S, Sveinsson O B, Olafsson S and Gudmundsson J T 2011 *Thin Solid Films* **520** 1621
- [26] Magnus F, Ingason A S, Olafsson S and Gudmundsson J T 2012 *IEEE Electron Device Lett.* **33** 1045
- [27] Mishra A, Kelly P J and Bradley J W 2010 *Plasma Sources Sci. Technol.* **19** 045014
- [28] Čapek J, Hála M, Zabeida O, Klemberg-Sapieha J E and Martinu L 2013 *J. Phys. D: Appl. Phys.* **46** 205205
- [29] Bradley J W, Mishra A and Kelly P J 2015 *J. Phys. D: Appl. Phys.* **48** 215202
- [30] Čapek J, Hála M, Zabeida O, Klemberg-Sapieha J E and Martinu L 2012 *J. Appl. Phys.* **111** 023301
- [31] Arnalds U B, Agustsson J S, Ingason A S, Eriksson A K, Gylfason K B, Gudmundsson J T and Olafsson S 2007 *Rev. Sci. Instrum.* **78** 103901
- [32] Svadkovski I V, Golosov D A and Zavatskiy S M 2002 *Vacuum* **68** 283
- [33] Alami J, Stranak V, Herrendorf A-P, Hubicka Z and Hippler R 2015 *Plasma Sources Sci. Technol.* **24** 045016
- [34] Parratt L G 1954 *Phys. Rev.* **95** 359
- [35] Ingason A S, Magnus F, Agustsson J S, Olafsson S and Gudmundsson J T 2009 *Thin Solid Films* **517** 6731
- [36] Swanson H E, McMurdie H F, Morris M C, Evans E H, Paretzkin B, DeGroot J H and Carmel S J 1971 Standard x-ray diffraction powder patterns: National Bureau of

- Standards Monograph 25 *Technical Report* section 9 (Washington, DC: National Bureau of Standards)
- [37] Samuelsson M, Lundin D, Jensen J, Raadu M A, Gudmundsson J T and Helmersson U 2010 *Surf. Coat. Technol.* **202** 591
- [38] Yushkov G, Anders A, Frolova V, Nikolaev A, Oks E M and Vodopyanov A V 2015 *IEEE Trans. Plasma Sci.* **43** 2310
- [39] Huo C, Lundin D, Gudmundsson J T, Raadu M A, Bradley J W and Brenning N 2017 *J. Phys. D: Appl. Phys.* **50** 354003
- [40] Gudmundsson J T, Magnus F, Tryggvason T K, Shayestehaminzadeh S, Sveinsson O B and Olafsson S 2013 *Proc. of the XII Int. Symp. on Sputtering and Plasma Processes* pp 192–4
- [41] Magnus F, Tryggvason T K, Olafsson S and Gudmundsson J T 2012 *J. Vac. Sci. Technol. A* **30** 050601
- [42] Magnus F, Sveinsson O B, Olafsson S and Gudmundsson J T 2011 *J. Appl. Phys.* **110** 083306
- [43] Yushkov G Y and Anders A 2010 *IEEE Trans. Plasma Sci.* **38** 3028
- [44] Lundin D, Brenning N, Jadernas D, Larsson P, Wallin E, Lattemann M, Raadu M A and Helmersson U 2009 *Plasma Sources Sci. Technol.* **18** 045008
- [45] Moreira M A, Törndahl T, Katardjiev I and Kubart T 2015 *J. Vac. Sci. Technol. A* **33** 021518
- [46] Gudmundsson J T 2016 *Plasma Phys. Control. Fusion* **58** 014002
- [47] Gudmundsson J T, Lundin D, Brenning N, Raadu M A, Huo C and Minea T M 2016 *Plasma Sources Sci. Technol.* **25** 065004
- [48] Brenning N, Gudmundsson J T, Raadu M A, Petty T J, Minea T and Lundin D 2017 *Plasma Sources Sci. Technol.* **26** 125003
- [49] Perry D L 2011 *Handbook of Inorganic Compounds* 2nd edn (Boca Raton, FL: CRC Press)
- [50] Petrov I, Barna P B, Hultman L and Greene J E 2003 *J. Vac. Sci. Technol. A* **21** S117
- [51] Rudolph M 2017 *PhD Thesis* Université Paris-Sud
- [52] Jouan P-Y, Le Brizoual L, Cardinaud C, Tricot S and Djouadi M A 2010 *IEEE Trans. Plasma Sci.* **38** 3089
- [53] Agnarsson B, Magnus F, Tryggvason T K, Ingason A S, Leosson K, Olafsson S and Gudmundsson J T 2013 *Thin Solid Films* **545** 445
- [54] Alami J, Sarakinos K, Uslu F and Wuttig M 2009 *J. Phys. D: Appl. Phys.* **42** 015304
- [55] Mahieu S and Depla D 2009 *J. Phys. D: Appl. Phys.* **42** 053002
- [56] Lattemann M, Helmersson U and Greene J E 2010 *Thin Solid Films* **518** 5978
- [57] Barna P B and Adamik M 1998 *Thin Solid Films* **317** 27
- [58] Leamy H J and Dirks A G 1977 *J. Phys. D: Appl. Phys.* **10** L95
- [59] Messier R 1986 *J. Vac. Sci. Technol. A* **4** 490
- [60] Greczynski G and Hultman L 2010 *Vacuum* **84** 1159
- [61] Liao M Y, Gotoh Y, Tsuji H and Ishikawa J 2004 *J. Vac. Sci. Technol. A* **22** 146–50

# Paper II

## **Effect of substrate bias on properties of HiPIMS deposited vanadium nitride films.**

H. Hajihoseini, M. Kateb, S. Ingvarsson and J. T. Gudmundsson. 2018.

*Thin Solid Films* **663**: 126 – 130.

Copyright © by Elsevier. All rights reserved. Permission for reproduction in this thesis granted by the copyright owner.







## Effect of substrate bias on properties of HiPIMS deposited vanadium nitride films



H. Hajihoseini<sup>a,b</sup>, M. Kateb<sup>a</sup>, S. Ingvarsson<sup>a</sup>, J.T. Gudmundsson<sup>a,b,\*</sup>

<sup>a</sup> Science Institute, University of Iceland, Dunhaga 3, IS-107, Reykjavik, Iceland

<sup>b</sup> Department of Space and Plasma Physics, School of Electrical Engineering and Computer Science, KTH–Royal Institute of Technology, SE-100 44 Stockholm, Sweden

### ARTICLE INFO

#### Keywords:

Vanadium nitride  
Magnetron sputtering  
Substrate bias  
High power impulse magnetron sputtering  
HiPIMS

### ABSTRACT

We report on the effect of varying the substrate bias on the morphology, composition, structural, and electrical properties of vanadium nitride films deposited by high power impulse magnetron sputtering (HiPIMS). The optimum substrate bias is found to be  $-50$  V, which gives the highest film density, the lowest electrical resistivity, and the lowest surface roughness at the highest deposition rate. We demonstrate how increasing the substrate bias voltage leads to a highly textured film. The preferred orientation of the film changes from (111) to (200) as the substrate bias voltage is increased. An X-ray pole scan shows that the (111) plane grows parallel to the  $\text{SiO}_2$  substrate when the substrate is grounded while it is gradually replaced by the (200) plane as the substrate bias voltage is increased up to  $-200$  V. The lowest electrical resistivity is measured as  $48.4 \mu\Omega \text{ cm}$  for the VN film deposited under substrate bias of  $-50$  V. This is among the lowest room temperature values that have been reported for a VN film. We found that the nitrogen concentration presents a decline by 6.5 percentage points as the substrate bias is changed from ground to  $-200$  V.

### 1. Introduction

Nitride based coatings have been widely studied and have a range of applications due to their unique physical and mechanical properties. Some of the transition-metal (TM) nitrides such as VN, TiN, TaN and NbN exhibit the cubic B1 NaCl structure at room temperature [1, 2]. Those transition metal nitrides that belong to group IVb–Vb–Vib (including TiN, ZrN, HfN, VN, NbN, TaN, MoN, and WN) belong to the category of conductive ceramics and exhibit rather good electrical conductivity [3]. Furthermore, the vanadium nitride thin film is known for its hardness [4], in particular when arranged in TiN/VN multilayers [5], good chemical stability, high melting point of 2593 K ([6], p.451) as well as superconductivity below 8.6 K [7].

High power impulse magnetron sputtering (HiPIMS) utilizes unipolar high voltage pulses, that are applied at low duty cycle, and low repetition frequency, which gives high electron density and a high ionization fraction of the sputtered material [8, 9]. This high ionization fraction of the sputtered material leads to dense [10], almost void-free films [11], with smooth surfaces [12, 13], and low electrical resistivity [14, 15]. However, the deposition rate tends to be lower than for conventional dc magnetron sputtering (dcMS) [10, 16]. Earlier, we have shown that HiPIMS deposition of TiN films produces denser films at lower deposition temperatures that have significantly lower

electrical resistivity, and lower surface roughness [13] than dcMS deposited TiN films on  $\text{SiO}_2$  at all deposition temperatures [15]. There we also demonstrated that these films are more resistant to oxidation than the dcMS deposited films. The largest change in resistivity was observed for films deposited at room temperature. More recently, Jablonka et al. [14] compared the resistivity of HiPIMS and dcMS deposited Co thin films. They reported resistivity as low as 14 and  $35 \mu\Omega \text{ cm}$  for film thicknesses of 40 and 6 nm, respectively, using a HiPIMS process with a substrate bias of  $-300$  V, significantly lower resistivity than for dcMS deposited Co films.

The ion bombardment during the deposition process is known to play an important role in dictating the mechanical and electrical properties of thin films as it is known to influence the film morphology, structure, and composition [17, 18]. The ion bombardment energy can be controlled by applying a negative bias voltage to the substrate. This can significantly modify the film properties due to enhancement of adatom mobility along with direct effects of the ion bombardment. It is known that the HiPIMS deposition process offers much higher metallic ion fraction than conventional sputtering like dcMS [8, 16]. In order to make use of this high ionization fraction a substrate bias voltage needs to be applied properly to attract the ions toward the substrate as well as to control the kinetic energy of the ions. However, there have been rather limited investigations on the effect of substrate bias voltage on

\* Corresponding author at: Science Institute, University of Iceland, Dunhaga 3, IS-107, Reykjavik, Iceland.  
E-mail address: [tumi@hi.is](mailto:tumi@hi.is) (J.T. Gudmundsson).

<https://doi.org/10.1016/j.tsf.2018.06.060>

Received 23 March 2018; Received in revised form 13 June 2018; Accepted 13 June 2018  
Available online 11 August 2018

0040-6090/© 2018 Elsevier B.V. All rights reserved.

the microstructure and properties of HiPIMS deposited films, and in particular, on thin transition metal nitride films. Ding et al. [19] were able to change the preferred orientation of a reactively HiPIMS deposited NbN film from (200) to (111), along with rapid decline in the films surface roughness, with increasing substrate bias voltage, while they did not observe any remarkable stoichiometry dependency. Guimaraes et al. [20] investigated the effect of substrate bias voltage on dcMS and HiPIMS deposited CrN films at various repetition frequencies. They optimized a preferential orientation of (311) when a substrate bias of  $-60$  V was applied and related this preferred orientation to higher observed hardness for HiPIMS deposited films. Furthermore, HiPIMS deposited films showed higher hardness and lower surface roughness than dcMS deposited films throughout the investigated range of substrate bias. Also Kong et al. [21] deposited CrN thin films using medium frequency magnetron sputtering while applying various negative substrate bias voltages. As the negative substrate bias voltage was raised from  $-100$  V to  $-300$  V, a strong CrN (111) texture appears while the surface roughness decreased dramatically. However, tensile stresses were generated in the films. Further increasing the substrate bias voltage up to  $-500$  V leads to a change in the preferred texture from (111) to (200), along with increased surface roughness, and development of compressive stresses. Furthermore, the films grain size decreased along with decreased deposition rate, with increased substrate bias voltage. Also it has been demonstrated that the substrate bias voltage can contribute to a change in the preferred orientation in TiN-MoS<sub>x</sub> composite films deposited by pulsed dc sputtering [22].

Earlier we studied and compared the growth and film properties of vanadium and vanadium nitride films deposited by HiPIMS and dcMS [23]. There we explored the influence of the magnetic field strength, cathode voltage and working gas pressure on the deposition rate, the film structure and morphology. Here, we study and compare the growth and film properties of vanadium nitride films deposited by HiPIMS as we vary the substrate bias. We explore the influence of the substrate bias on the deposition rate, the film structure, texture, composition and electrical resistivity. In Section 2 we discuss the deposition arrangement and growth method and the characterization methods applied. In Section 3 we discuss how the film properties of vanadium nitride films vary for different substrate bias. Section 4 summarizes our findings.

## 2. Experimental apparatus and method

The vanadium nitride thin films were deposited by magnetron sputtering in a custom built chamber [24]. The chamber base pressure was  $4 \times 10^{-6}$  Pa. The working gas was argon of 99.999% purity mixed with nitrogen gas of 99.999% purity. An Ar/N<sub>2</sub> mixture consisting of  $q_{Ar} = 40$  sccm and  $q_{N_2} = 5$  sccm was injected into the chamber. We have shown previously that this mixture is appropriate to deposit cubic polycrystalline  $\delta$ -VN films [23]. The total working pressure was maintained at 0.9 Pa by a throttle valve. The vanadium target was 75 mm in diameter and of 99.95% purity and 6.35 mm thick and was almost 50% eroded at the racetrack center.

The substrates used were thermally oxidized Si(001) up to an oxide thickness of 1  $\mu$ m. During deposition the substrate temperature was maintained at 400 °C with a 1.5 in. (3.8 cm) diameter circular plate heater, separated from the substrate holder by a 2 mm gap. The substrate holder design is described in more detail by Arnalds et al. [24]. The depositions were performed for various dc substrate bias conditions.

For HiPIMS deposition, the power was supplied by a SPIK1000A pulse unit (Melec GmbH) which was operated in the unipolar negative mode at constant voltage, which in turn was charged by a dc power supply (ADL GS30). The discharge current and voltage was monitored using a combined current transformer and a voltage divider unit (Melec GmbH). The pulse length was set at 200  $\mu$ s and the pulse repetition frequency was kept at 100 Hz throughout this study. The waveform data were recorded with a digital storage oscilloscope (Agilent

**Table 1**

Measured and calculated specifications of the magnet.

Center diameter [mm]	Ring diameter [mm]	MFD of center (average)	MFD of ring (average)	Magnetic flux of center (total)	Magnetic flux of ring (total)	$K$	$K_G$
14	10	0.322 T	0.314 T	49 $\mu$ Wb	690 $\mu$ Wb	0.07	1

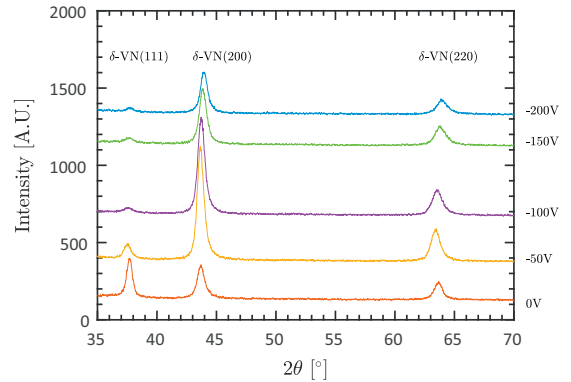


**Fig. 1.** GiXRD pattern from vanadium nitride films which were grown by HiPIMS at different substrate bias voltage at 0.9 Pa, 250 W average power, pulse length of 200  $\mu$ s and repetition frequency of 100 Hz.

54624A). For dcMS deposition, a dc power supply (MDX 1 K, Advanced Energy) was connected to the magnetron target. For all films, depositions were made at 250 W average power. The magnetron magnet is 3 in. in diameter and was purchased from Angstrom Sciences. Table 1 summarizes measured and calculated specifications of the magnet. For the magnet, the average out of plane and in plane magnetic fields are 4 and 36 mT over the race track, respectively. Moreover, the imbalance coefficient  $K$  is calculated as the ratio of the magnetic fluxes of the center magnet and the outer magnetic ring. A value of  $K = 1$  indicates a balanced magnetron. The geometrical imbalance coefficient  $K_G$  is the ratio of the distance between the magnetic zero of the magnetron (the point along the middle axis where  $B_{\perp}$  changes its orientation, i.e.  $B_{\perp} = 0$ ) and the target surface, and the diameter of the erosion rill on the target [25, 26]. Further details on calculations and definitions of the two coefficients can be found in the work of Svadkovski et al. [25].

X-ray diffractometry (XRD) was carried out using a Philips X'pert diffractometer (Cu  $K_{\alpha}$ , wavelength 0.15406 nm) mounted with a hybrid monochromator/mirror on the incident side and a 0.27° collimator on the diffracted side. A line focus was used with a beam width of approximately 1 mm. Grazing incidence (GI)XRD scans were carried out with the incident beam at  $\theta = 1^{\circ}$ . The film thickness and density were determined by low-angle X-ray reflectivity (XRR) measurements where the angular resolution was 0.005°. The XRR data was fitted using Parrat formalism [27] for reflectivity. A low density surface layer had to be added on top of the film in order to achieve a good fit. This is due to a formation of oxide or oxynitride surface layer after the films were removed from the vacuum chamber, as previously observed [28].

X-ray pole scans were performed which enable detecting the texture evolution in sputtered films [29]. Briefly, a pole scan is done for a specific  $d$ -spacing, i.e. a fixed  $\theta - 2\theta$  peak while the specimen is rotated in-plane ( $\phi$ ) at different out-of-plane ( $\psi$ ) angles. Normally, a single pole scan is not enough to fully determine the orientation distribution within a specimen. To this end, pole figures were obtained for the (111), (200) and (220) planes at corresponding peak location. However, since our films are polycrystalline the main focus of the present study is on the

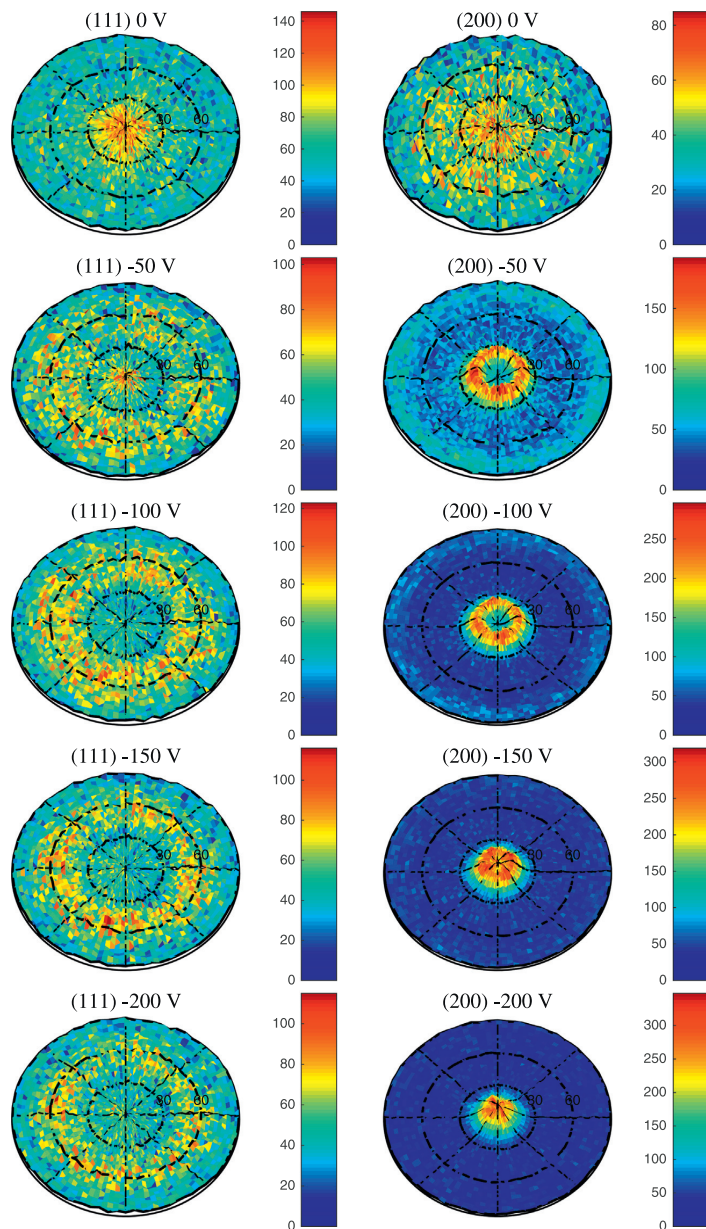


**Fig. 2.** Pole figures of (111) and (200) planes for vanadium nitride films which were grown by HiPIMS for various substrate bias voltages, at 0.9 Pa, 250 W average power, pulse length of 200  $\mu$ s and repetition frequency of 100 Hz.

**Table 2**  
Nitrogen amount in VN films deposited by varying substrate bias voltage.

Substrate bias voltage [V]	Nitrogen content [%]
0	54.52
-50	51.60
-100	50.61
-150	49.22
-200	48.02

pole figure for the (111) and the (200) planes. The pole scans were performed at  $2\theta$  peaks of 37.611, 43.697 and 63.533° for each sample using 0.25° slit and 90 and 360° rotation respectively for  $\psi$  and  $\phi$  with a step size 3° and 4 s counting time at each step. The pole figures of a bare substrate were subtracted from the original pole figures of the films for clarity.

Electron microprobe analysis (EMPA) was acquired with the JEOL JXA-8230 Superprobe at the Institute of Earth Sciences, University of Iceland. For all analyses the operating potential and the beam current

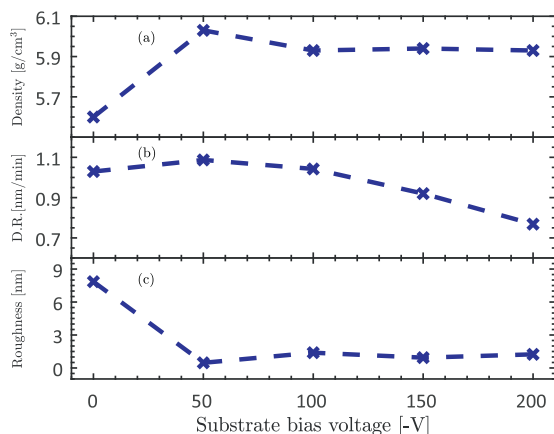


**Fig. 3.** (a) Film density, (b) deposition rate, and (c) surface roughness of vanadium nitride films deposited as a function of substrate bias voltage. Data extracted from XRR measurement and all films are deposited at 0.9 Pa, 250 W average power, pulse length of 200  $\mu$ s and repetition frequency of 100 Hz.

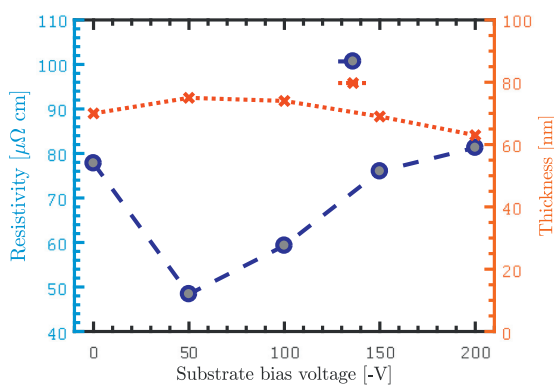


**Fig. 4.** The resistivity and thickness of vanadium nitride films deposited as a function of substrate bias voltage. All films are deposited at 0.9 Pa, 250 W average power, pulse length of 200  $\mu$ s and repetition frequency of 100 Hz.

were 15 keV and 10 nA respectively. A spot size of 10  $\mu$ m was used for all analyses. A VN film was used as a standard for nitrogen. For nitrogen, the counting time was 480 s on the peak and 120 s for each of the lower and higher backgrounds. To minimize the effect of noise, an average of 5 measurement points on each sample is reported.

The electrical resistivity of the VN films was measured using a linear four-point probe station with a tip diameter of 200  $\mu$ m and a probe distance of 1 mm. Voltage-current waveforms were recorded through a Keithley 2400 source meter and custom made Labview software. The current was swept from  $-100$  mA to 100 mA and the corresponding voltage was recorded. To minimize the error arising from placement of the probes the resistivity was averaged over four separate measurements on each sample.

### 3. Results and discussion

Fig. 1 shows the GiXRD pattern for films which were deposited by HiPIMS with substrate bias voltages at 0,  $-50$ ,  $-100$ ,  $-150$  and  $-200$  V. At grounded substrate the peak at  $2\theta = 37.695^\circ$  is dominant in the GiXRD pattern. This peak has been assigned to the cubic fcc  $\delta$ -VN

(111) [30, 31]. The peak at  $2\theta = 43.805^\circ$  is assigned to the cubic fcc  $\delta$ -VN(200) and the peak at  $2\theta = 63.678^\circ$  to the cubic  $\delta$ -VN(220). One can see that, by increasing bias voltage to  $-50$  V, the (200) peak is significantly intensified and becomes the dominant one. Increasing the bias voltage further up to  $-200$  V leads to a gradual decrease in the (200) intensity while that still remains the dominant peak. Since the substrate bias voltage affects the GiXRD pattern remarkably, it is likely to change the texture of the VN film. To explore the film texture, the pole figures of the (111) and the (200) planes for VN films deposited at different substrate biases are displayed in Fig. 2. It can be seen that the film deposited at grounded substrate has uniformly distributed orientation of (200) planes while the (111) planes show an intense spot around  $\psi = 0$  indicating considerable  $\langle 111 \rangle$  texture normal to the substrate. However, when the substrate is biased at  $-50$  V the (200) planes exhibit a ring at  $\psi = 20^\circ$  along with an intense spot at  $\psi = 0$  for (111) planes. Thus, there is a competition between these planes to grow normal to the substrate and in this regard the  $\langle 111 \rangle$  texture is dominant. Increase of the substrate bias to  $-100$  V causes the  $\langle 111 \rangle$  texture to disappear but the (200) plane shows up at  $\psi = 15^\circ$  with respect to the substrate normal. Further increase in the substrate bias results in dominant  $\langle 200 \rangle$  texture normal to the substrate. The results of the GiXRD scans and the symmetric pole figures are in complete agreement. For instance, the samples biased at  $-50$  and  $-100$  V show higher intensity of the (200) peaks than higher biased samples. This can be explained by the GiXRD configuration i.e. the (200) peak is detected under an angle with respect to the substrate normal and thus, the (200) peak shows higher intensity in off-normal texture.

Another parameter which describes the VN films stoichiometry is the percentage of nitrogen in the film. To measure the contribution of nitrogen in the VN films, electron micro-probe analysis (EMPA) were carried out. As presented in Table 2, the VN film deposited with grounded substrate shows the highest nitrogen content of 54.52%. As the negative substrate bias is increased, the films become more vanadium rich. At substrate bias voltage of  $-200$  V, only 48.02% of the film is made of nitrogen which is 6.5 percentage points lower than for VN film deposited with grounded substrate. It may be described by the atomic mass of N (14 u) which is lighter than V (50.9 u). Thus, N atoms are prone to being sputtered by impinging ions with higher ion bombarding energy. Kong et al. [21] reported a decrease of the nitrogen concentration in CrN film when the substrate bias voltage is raised from  $-300$  V up to  $-50$  V. However, for substrate bias between  $-100$  and  $-300$  V the nitrogen amount presents only a slight increase. Based on the fact that CrN has the fcc structure, they argued that pure nitrogen layers and pure chromium layers alternately sit in the (111) planes, whereas the (200) planes include both nitrogen and chromium atoms. This suggests that the (200) plane is not a favorable accommodation for nitrogen atoms. It is argued that the N concentration would decrease as the (200)-oriented structure is dominating in the film. The same explanation can be used for the VN films due to the same structure and (200) being the dominant orientation (Fig. 1).

Fig. 3 gives information about the development of the film density, deposition rate, and surface roughness as the substrate bias is varied. Overall, the data extracted from the XRR measurements exhibit that VN film deposited at  $-50$  V substrate bias is the most dense, with the highest deposition rate and the lowest surface roughness among all the films. In terms of density, the film deposited with  $-50$  V substrate bias has mass density of 6.03  $\text{g}/\text{cm}^3$  which is significantly denser than the one deposited with grounded substrate with 5.60  $\text{g}/\text{cm}^3$  which is the lowest density among the films. Increasing the substrate bias voltage to  $-100$  V leads to a slight density decrements to 5.93  $\text{g}/\text{cm}^3$ . At higher substrate bias voltages, up to  $-200$  V the film densities remain almost unchanged (Fig. 3(a)). The deposition rate was calculated from the measured film thickness and the corresponding deposition time. As can be seen in Fig. 3(b) deposition rate at  $-50$  V is 1.09 nm/min which is slightly higher than for the film deposited at 0 V (grounded substrate) (1.03 nm/min) while at higher bias voltages the deposition rates are



1.04, 0.92, and 0.77 nm/min at  $-100$ ,  $-150$  and  $-200$  V substrate bias, respectively. There are numerous data in the literature that report that the higher the absolute value of the substrate bias voltage, the lower the deposition rate [21, 32, 33]. A decline in the deposition rate under substrate bias voltage higher than  $-100$  V can be explained by an increase in re-sputtering effect on the growing films as a consequence of high energy ion bombardment. Fig. 3(c) depicts how applying the bias voltage to the substrate can result in remarkably smoother VN film surface. Similar to the film density,  $-50$  V is the optimal substrate bias to achieve a smooth surface apposed to the grounded substrate which leads to the roughest surface (0.47 nm and 8.2 nm average surface roughness, respectively). By increasing the bias voltage beyond  $-50$  V, the VN films become slightly rougher. This behavior was seen previously in CrN growth where the turning point is observed at substrate bias voltage of  $-200$  V [21]. Low roughness at  $-50$  V is related to increased atomic movement and densification of the film material as a result of the increased ion flux and ion bombarding energy as the substrate bias is increased while the substrate voltage is low. Bombardment by higher energy ions increases the production of surface defects and thus roughens the film surface.

The electrical resistivity and thickness of the VN films are presented in Fig. 4. The resistivity ranges from 48.4 to 81.1  $\mu\Omega$  cm. The film resistivity increases linearly, from this lowest value, with increased substrate bias. Thus the films deposited at substrate bias of  $-50$  and  $-200$  V exhibit the lowest and highest resistivity, respectively. The low resistivity of the film deposited at  $-50$  V substrate voltage can be attributed to the high density and low surface roughness of the film. From Fig. 4 it is evident that increasing the substrate bias voltage leads to higher electrical resistivity. The film deposited with grounded substrate shows a resistivity of 77.8  $\mu\Omega$  cm which is close to the resistivity of a VN film deposited at  $-150$  V substrate bias. The films thickness ranges from 63 to 75 nm. Thus the films have similar thickness and surface roughness but the resistivity increases with increased sample bias. We also note that there is broadening of the (200) peak with increased substrate bias, as seen in Fig. 1, which indicates smaller grain size with increased substrate bias, that may explain the increasing film electrical resistivity. It is worth noting that electrical resistivity of 48.4  $\mu\Omega$  cm, observed for films deposited with substrate bias of  $-50$  V, is among the lowest resistivities which are reported in literature for the VN thin film. The lowest room temperature resistivity of VN thin films that has been reported is 50  $\mu\Omega$  cm [34] and 40–100  $\mu\Omega$  cm [35] for reactively dc sputtered single crystal films, 105  $\mu\Omega$  cm rf magnetron sputtered films from a compound target [36], and 120  $\mu\Omega$  cm for atomic layer deposited (ALD) films [37].

#### 4. Conclusion

We explored the effect of substrate bias on the structure, texture, composition and electrical resistivity of HiPIMS deposited VN films. It was shown that the substrate bias voltage changes the dominant peak from (111) to (200) in the GiXRD pattern. Besides, unlike the VN film deposited with grounded substrate, biased substrate leads to a highly textured film. It is shown that a grounded substrate results in a considerable  $\langle 111 \rangle$  texture normal to the substrate. Low substrate bias encourages off-normal  $\langle 200 \rangle$  texture while high substrate bias leads to only  $\langle 200 \rangle$  texture normal to the substrate. From the XRR measurements it is found that  $-50$  V is the substrate voltage which results in higher density and deposition rate and lower surface roughness than other substrate bias voltage. EMPA analysis indicates that a lower amount of nitrogen is included in the VN films deposited at higher bias voltage. Finally, 4-point probe resistivity measurement proves that although low substrate bias voltage like  $-50$  V can increase the room

temperature electrical conductivity of VN films, high substrate bias like  $-200$  V can result in even higher film resistivity than deposition with a grounded substrate.

#### Acknowledgements

The authors are thankful to Dr. Arni S. Ingason for assistance with the interpretation of the polar figure data. This work was partially supported by the University of Iceland Research Fund for Doctoral Students, the Icelandic Research Fund Grant No. 130029, and the Swedish Government Agency for Innovation Systems (VINNOVA) contract no. 2014-04876.

#### References

- [1] A.B. Mei, O. Hellman, N. Wireklint, C.M. Schlepütz, D.G. Sangiovanni, B. Alling, A. Rockett, L. Hultman, I. Petrov, J.E. Greene, *Phys. Rev. B* 91 (2015) 054101.
- [2] O.N. Carlson, J.F. Smith, R.H. Nafziger, *Metall. Mater. Trans. A* 17 (1986) 1647.
- [3] P. Patsalas, N. Kalfagiannis, S. Kassaravetis, G. Abadias, D.V. Bellas, C. Lekka, E. Lidorikis, *Mater. Sci. Eng. R* 123 (2018) 1.
- [4] X. Chu, S.A. Barnett, M.S. Wong, W.D. Sproul, *J. Vac. Sci. Technol. A* 14 (1996) 3124.
- [5] U. Helmersson, S. Todorova, S.A. Barnett, J.-E. Sundgren, L.C. Markert, J.E. Greene, *J. Appl. Phys.* 62 (1987) 481.
- [6] D.L. Perry, *Handbook of Inorganic Compounds*, 2nd ed., CRC Press, Boca Raton, Florida, 2011.
- [7] B.R. Zhao, L. Chen, H.L. Luo, M.D. Jack, D.P. Mullin, *Phys. Rev. B* 29 (1984) 6198.
- [8] U. Helmersson, M. Lattemann, J. Bohlmark, A.P. Ehiassarian, J.T. Gudmundsson, *Thin Solid Films* 513 (2006) 1.
- [9] J.T. Gudmundsson, N. Brenning, D. Lundin, U. Helmersson, *J. Vac. Sci. Technol. A* 30 (2012) 030801.
- [10] M. Samuelsson, D. Lundin, J. Jensen, M.A. Raadu, J.T. Gudmundsson, U. Helmersson, *Surf. Coat. Technol.* 202 (2010) 591.
- [11] J. Alami, P.O.A. Petersson, D. Music, J.T. Gudmundsson, J. Bohlmark, U. Helmersson, *J. Vac. Sci. Technol. A* 23 (2005) 278.
- [12] K. Sarakinos, J. Alami, M. Wuttig, *J. Phys. D: Appl. Phys.* 40 (2007) 2108.
- [13] F. Magnus, A.S. Ingason, O.B. Sveinsson, S. Olafsson, J.T. Gudmundsson, *Thin Solid Films* 520 (2011) 1621.
- [14] L. Jablonka, L. Riekehr, Z. Zhang, S.-L. Zhang, T. Kubart, *Appl. Phys. Lett.* 112 (2018) 043103.
- [15] F. Magnus, A.S. Ingason, S. Olafsson, J.T. Gudmundsson, *IEEE Electron Device Letters* 33 (2012) 1045.
- [16] D. Lundin, K. Sarakinos, *J. Mater. Res.* 27 (2012) 780.
- [17] L. Hultman, J.E. Sundgren, R.F. Bunshah (Ed.), *Handbook of Hard Coatings: Deposition Technologies, Properties and Applications*, (Noyes Publications, Park Ridge, New Jersey, 2001, pp. 108–180).
- [18] M. Sakaki, T. Sakakibara, *IEEE Transactions on Plasma Science*, 22 (1994), p. 1049.
- [19] J. Ding, T. Zhang, H. Mei, J.M. Yun, S.H. Jeong, Q. Wang, K.H. Kim, *Coatings*, 8 (2018), p. 10.
- [20] M.C.R. Guimaraes, B.C.N.M. de Castilho, T. de Souza Nossa, P.R.T. Avila, S. Cucatti, F. Alvarez, J.L. Garcia, H.C. Pinto, *Surf. Coat. Technol.* 340 (2018) 112.
- [21] Q. Kong, H. Li, X. Liu, Y. Wang, J. Chen, H. Zhou, *Mater. Sci. Eng. B* 176 (2011) 850.
- [22] S. Gangopadhyay, R. Acharya, A. Chattopadhyay, S. Paul, *Vacuum* 84 (2010) 843.
- [23] H. Hajihoseini, J.T. Gudmundsson, *J. Phys. D: Appl. Phys.* 50 (2017) 505302.
- [24] U.B. Arnalds, J.S. Agustsson, A.S. Ingason, A.K. Eriksson, K.B. Gylfason, J.T. Gudmundsson, S. Olafsson, *Rev. Sci. Instrum.* 78 (2007) 103901.
- [25] I.V. Svadkovski, D.A. Golosov, S.M. Zavatskiy, *Vacuum* 68 (2002) 283.
- [26] J. Alami, V. Stranak, A.-P. Herrendorf, Z. Hubicka, R. Hippler, *Plasma Sources Sci. Technol.* 24 (2015) 045016.
- [27] L.G. Parratt, *Phys. Rev.* 95 (1954) 359.
- [28] A.S. Ingason, F. Magnus, J.S. Agustsson, S. Olafsson, J.T. Gudmundsson, *Thin Solid Films* 517 (2009) 6731.
- [29] S. Mahieu, P. Ghekiere, D. Depla, R. De Gryse, *Thin Solid Films* 515 (2006) 1229.
- [30] H. Gueddougi, G. Schmerber, M. Abes, M. Guemmaz, J. Parlebas, *Catal. Today* 113 (2006) 270.
- [31] G. Farges, E. Beauprez, D. Degout, *Surf. Coat. Technol.* 54-55 (1992) 115.
- [32] S. Heo, S. Kima, I. Yeo, S. Park, Y. Oh, *Ceram. Int.* 42 (2016) 5231.
- [33] D. Devia, E. Restrepo-Parra, P. Arango, A. Tschiptschin, J. Velez, *Appl. Surf. Sci.* 256 (2011) 6181.
- [34] M.B. Takeyama, T. Itoi, A. Noya, *Jpn. J. Appl. Phys.* 49 (2010) 05FA05.
- [35] J. Zasadzinski, R. Vaglio, G. Rubino, K.E. Gray, M. Russo, *Phys. Rev. B* 32 (1985) 2929.
- [36] M.Y. Liao, Y. Gotoh, H. Tsuji, J. Ishikawa, *J. Vac. Sci. Technol. A* 22 (2004) 146.
- [37] M.B. Takeyama, M. Sato, H. Sudoh, H. Machida, S. Ito, E. Aoyagi, A. Noya, *Jpn. J. Appl. Phys.* 50 (2011) 05EA06.



## Paper III

### **The Effect of Magnetic Field Strength and Geometry on the Deposition Rate and Ionized Flux Fraction in the HiPIMS Discharge.**

H. Hajihoseini, M. Čada, Z. Hubička, S. Ünaldi, N. Brenning, M. A. Raadu, J. T. Gudmundsson and D. Lundin. 2019.







*plasma 2*: 15.





Article

# The Effect of Magnetic Field Strength and Geometry on the Deposition Rate and Ionized Flux Fraction in the HiPIMS Discharge

Hamidreza Hajihoseini <sup>1,2</sup> , Martin Čada <sup>3</sup> , Zdenek Hubička <sup>3</sup> , Selen Ünalđı <sup>2</sup>,  
Michael A. Raadu <sup>4</sup>, Nils Brenning <sup>2,4,5</sup> , Jon Tomas Gudmundsson <sup>1,4</sup>  and  
Daniel Lundin <sup>2,5,\*</sup> 

- <sup>1</sup> Science Institute, University of Iceland, Dunhaga 3, IS-107 Reykjavik, Iceland; hah107@hi.is (H.H.); tumi@hi.is (J.T.G.)
  - <sup>2</sup> Laboratoire de Physique des Gaz et Plasmas—LPGP, UMR 8578 CNRS, Université Paris-Sud, Université Paris Saclay, 91405 Orsay CEDEX, France; selen.unaldi@u-psud.fr (S.Ü.); brenning@kth.se (N.B.)
  - <sup>3</sup> Institute of Physics v. v. i., Academy of Sciences of the Czech Republic, Na Slovance 2, 182 21 Prague 8, Czech Republic; cada@fzu.cz (M.Č.); hubicka@fzu.cz (Z.H.)
  - <sup>4</sup> Department of Space and Plasma Physics, School of Electrical Engineering and Computer Science, KTH Royal Institute of Technology, SE-100 44 Stockholm, Sweden; raadu@kth.se
  - <sup>5</sup> Plasma and Coatings Physics Division, IFM-Materials Physics, Linköping University, SE-581 83 Linköping, Sweden
- \* Correspondence: daniel.lundin@u-psud.fr

Received: 2 April 2019; Accepted: 6 May 2019; Published: 13 May 2019



**Abstract:** We explored the effect of magnetic field strength  $|\mathbf{B}|$  and geometry (degree of balancing) on the deposition rate and ionized flux fraction  $F_{\text{flux}}$  in dc magnetron sputtering (dcMS) and high power impulse magnetron sputtering (HiPIMS) when depositing titanium. The HiPIMS discharge was run in two different operating modes. The first one we refer to as “fixed voltage mode” where the cathode voltage was kept fixed at 625 V while the pulse repetition frequency was varied to achieve the desired time average power (300 W). The second mode we refer to as “fixed peak current mode” and was carried out by adjusting the cathode voltage to maintain a fixed peak discharge current and by varying the frequency to achieve the same average power. Our results show that the dcMS deposition rate was weakly sensitive to variations in the magnetic field while the deposition rate during HiPIMS operated in fixed voltage mode changed from 30% to 90% of the dcMS deposition rate as  $|\mathbf{B}|$  decreased. In contrast, when operating the HiPIMS discharge in fixed peak current mode, the deposition rate increased only slightly with decreasing  $|\mathbf{B}|$ . In fixed voltage mode, for weaker  $|\mathbf{B}|$ , the higher was the deposition rate, the lower was the  $F_{\text{flux}}$ . In the fixed peak current mode, both deposition rate and  $F_{\text{flux}}$  increased with decreasing  $|\mathbf{B}|$ . Deposition rate uniformity measurements illustrated that the dcMS deposition uniformity was rather insensitive to changes in  $|\mathbf{B}|$  while both HiPIMS operating modes were highly sensitive. The HiPIMS deposition rate uniformity could be 10% lower or up to 10% higher than the dcMS deposition rate uniformity depending on  $|\mathbf{B}|$  and in particular the magnetic field topology. We related the measured quantities, the deposition rate and ionized flux fraction, to the ionization probability  $\alpha_t$  and the back attraction probability of the sputtered species  $\beta_t$ . We showed that the fraction of the ions of the sputtered material that escape back attraction increased by 30% when  $|\mathbf{B}|$  was reduced during operation in fixed peak current mode while the ionization probability of the sputtered species increased with increasing  $|\mathbf{B}|$ , due to increased discharge current, when operating in fixed voltage mode.

**Keywords:** ionized physical vapor deposition; magnetron sputtering; high power impulse magnetron sputtering (HiPIMS); ionized flux fraction; deposition rate

## 1. Introduction

Conventional dc magnetron sputtering (dcMS) suffers from a low degree of ionization of the sputtered material. High power impulse magnetron sputtering (HiPIMS) has emerged as a promising alternative, providing a highly ionized material flux, while being compatible with conventional magnetron sputtering deposition systems [1]. HiPIMS operation is characterized by a pulsed high peak power in the range of several kW/cm<sup>2</sup> and consequently a high plasma density of up to 10<sup>19</sup> m<sup>-3</sup> in the cathode target vicinity, which is up to three orders of magnitude higher than in dcMS [2]. Such discharge conditions result in a significant increase of ionization of the sputtered neutrals, where ionized flux fractions  $F_{\text{flux}}$  well above 50% have been reported [3–5]. However, a high ionized flux fraction commonly comes at a cost of lower deposition rate, which has thus far limited the use of HiPIMS in industry [1,6].

Several reports demonstrate the lower deposition rate in (mainly non-reactive) HiPIMS when compared to dcMS operated at the same average power [1,7]. The seminal work of Kouznetsov et al. [3] reports up to 80% lower deposition rate for HiPIMS than for dcMS. Samuelsson et al. [8] compared the deposition rates from eight metal targets (Ti, Cr, Zr, Al, Cu, Ta, Pt, and Ag) in pure Ar for both dcMS and HiPIMS discharges applying the same average power. They observed HiPIMS deposition rates in the range of 30–85% of the dcMS rates depending on target material.

There are several suggestions on the cause of the lower deposition rate observed in HiPIMS deposition [2,7]. It is generally agreed on by the scientific community that back attraction of ionized sputtered material to the target, quantified as back attraction probability  $\beta_t$ , plays a major role in the reduction of the amount of sputtered particles reaching the substrate [9]. The reason is that atoms ionized in the cathode region are likely to be back-attracted to the target due to strong electric fields in the presheath and extended presheath [10,11]. Spatial measurements of the plasma potential in HiPIMS discharges [11–14] have shown that there commonly is a potential uphill, from the cathode sheath edge and reaching far outside the ionization region (several cm), that can vary in the range 7–100 V.

Several attempts have been made to increase the deposition rate in HiPIMS. This includes varying the pulse length [15–17], varying the magnetic field strength  $|\mathbf{B}|$  [13,18,19], modifying the magnetic field geometry [20–22], adding an external magnetic field in the target vicinity [23], chopping the pulse into a train of shorter pulses [24,25], and increasing the target temperature [26]. Several of these reports propose that modifying the magnetic field, using either permanent magnets or electromagnets [13,18,19,27], is one of the most promising approaches. For example, Čapek et al. [18] showed that lowering  $|\mathbf{B}|$  in HiPIMS can have a profound effect on increasing the deposition rate. Using spacers of different thicknesses behind the cathode to reduce  $|\mathbf{B}|$  at the target (and also increasing the average discharge voltages to achieve nominally similar power levels), the deposition rate of Nb was increased by roughly a factor of 5. Similarly, Mishra et al. [13] found a six-fold increase in the deposition rate of Ti by weakening  $|\mathbf{B}|$  by 33%. Bradley et al. [19] reported on a deposition rate increase by a factor of 2 for a Ti target when the magnetic field strength at the target was reduced by 45%. In addition, while weakening  $|\mathbf{B}|$  by 82% a factor of 2.6 higher deposition rate was observed while depositing vanadium films by HiPIMS, although for the weaker magnetic field the films exhibited significantly higher surface roughness and were not as dense [28].

There have also been a few attempts to modify the magnetic field geometry in order to improve the deposition rate. This includes the work of Yu et al. [20], who used a 36 cm diameter magnetron with a spiral-shaped magnet pack assembly to increase the plasma uniformity in the substrate vicinity and to improve target utilization. More recently, Raman et al. [22] modified the magnetic field topology of a HiPIMS discharge, which increased the deposition rate by up to a factor of 2 [22,29]. In the cited studies, the modified magnet pack had a strong magnetic field region over three concentric race track regions (referred to as a TriPack magnetron assembly), but the magnetic field strength fell off more steeply than for a conventional magnet pack when moving away from the target surface. However, those designs encounter some difficulties when scaled down to a smaller cathode size.

The combined effect of weakening  $|\mathbf{B}|$ , the correlation between the deposition rate increase and the lower ionized flux fraction to the substrate, is still poorly understood. One reason is that most HiPIMS studies on ionization indeed quantify  $F_{\text{flux}}$ , but have so far not focused on changing the magnetic field strength/topology. For example, Lundin et al. [5] explored the ionized flux fraction for Al, C and Ti targets using a gridless ion meter. For a Ti target, they found an increase in the ionized flux fraction from roughly 20% to 68% with increased peak discharge current density in the range of 0.7–2.5 A/cm<sup>2</sup>. These values are in line with the work of Poolcharuansin et al. [30] (30–50%) and Kubart et al. [4] (20–60%) for current densities in the range 1–2.5 A/cm<sup>2</sup>. Another reason is that the studies on  $F_{\text{flux}}$  did not in parallel systematically investigate the deposition rate (or the change thereof). The exception is the study of Raman et al. [31], who, in addition to the previously discussed deposition rate study, also estimated the ionized flux fraction during HiPIMS operation using conventional and TriPack magnetrons. They recorded an ionized flux fraction of Cu of approximately 5% for the conventional magnetron and 16% utilizing the TriPack magnetron assembly, which indicates that optimization of the magnetic field can in fact result in increased deposition rate as well as increased ionized flux fraction.

In the present study, we therefore systematically investigated the relationships among  $|\mathbf{B}|$ , the magnetic field geometry (level of balancing), the deposition rate, and the ionized flux fraction during HiPIMS and dcMS operation. Such an approach enabled us to study the combined effects of HiPIMS pulse parameters and magnetic configurations. In the analysis, we used the well known materials pathway model [9,32] to assess both the ionization probability  $\alpha_t$  and the back attraction probability  $\beta_t$  from the experimental data. Finally, we attempted to explain our observations based on the physics behind the transport of charged particles in these devices.

## 2. Materials and Methods

All experiments were carried out in a custom-built cylindrical vacuum chamber (height 50 cm and diameter 45 cm) made of stainless steel. A base pressure of  $4 \times 10^{-6}$  Pa was achieved using a turbo molecular pump backed by a roughing pump. The working gas pressure was adjusted to 1 Pa by injecting 50 sccm Ar into the chamber and adjusting a butterfly valve located between chamber and the turbo pump. The deposition system was equipped with a circular 4 inch diameter VTec Magnetron assembly (Gencoa, Liverpool, UK). The magnetron assembly, as well as a probe holder used during measurements, was mounted on movable bellows controlled with millimeter precision, as shown in Figure 1. This made it possible to perform radial as well as axial scans with high precision. The absolute magnetic field strength  $|\mathbf{B}|$  as well as the geometry of the magnetic field (degree of balancing) above the magnetron target was varied by displacing the center magnet (C) and the outer ring magnet at the target edge (E) using two micrometer screws located on the outer side of the magnetron assembly. We refer to each configuration using the displaced distance (in mm) of each magnet from the target backing plate. Thus, the notation C0E0 refers to a magnetron configuration where the center and outer magnets touch the backing plate (zero displacement, i.e., the strongest magnetic field above the target).

In this work, we investigated seven different magnet configurations: C0E0, C5E5 and C10E10, C0E5, C0E10, C5E0, and C10E0. For all of these configurations, the magnetic field above the target was mapped using a Lake Shore 425 Gauss meter (Lake Shore Cryotronics, Westerville, OH, USA) equipped with a Hall probe. The magnetic field distribution above the target for each configuration is shown in Figure 2. Axial symmetry was assumed. For the configurations investigated, it was found that a magnetic null point was always present, which means that all configurations were categorized as unbalanced type II [33]. The magnetic null was used as a measure of the degree of balancing. The magnetic null point for the different cases was located at 43–74 mm from the target surface above the target center and is given in Table 1 for each configuration. Note, however, that the case C0E10 was only weakly unbalanced, i.e., close to being balanced ( $z_{\text{null}} = 74$  mm), whereas C10E0 was the most strongly unbalanced ( $z_{\text{null}} = 43$  mm). Table 1 also lists the radial component of the magnetic field strength next to the target surface over the race track  $|B_{r,rt}|$ . These values were recorded at  $z = 11$  mm, which was the closest distance that could be probed for the  $B_r$  component.

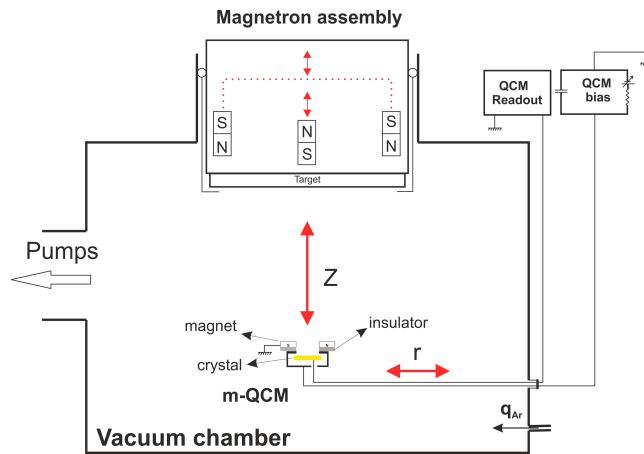


**Figure 1.** A schematic of the magnetron sputtering chamber. The magnetron assembly and the probe holder with the m-QCM are mounted on movable bellows that can be controlled with millimeter precision. The red arrows indicate linear motion.

A dc power supply (SR1.5-N-1500, Technix, Créteil, France) and a HiPIMS power supply (HiPSTER 1, Ionautics, Linköping, Sweden) were used to ignite the discharge in dc and HiPIMS modes, respectively. For both cases, an average discharge power was maintained at 300 W. The HiPIMS pulse was always kept at constant length of 100  $\mu$ s and the discharge was regulated in two different ways. The first mode is referred to as fixed voltage mode, and was realized by keeping the cathode voltage fixed at 625 V and varying the pulse frequency to achieve the desired average power. The second mode is referred to as fixed peak current mode and was realized by changing the cathode voltage to maintain the peak discharge current at  $I_{D,peak} = 40$  A, corresponding to current density  $J_{D,peak} = 0.5$  A/cm<sup>2</sup> for the ionized flux fraction measurements, and  $I_{D,peak} = 80$  A and  $J_{D,peak} = 1.0$  A/cm<sup>2</sup> for the measurements of deposition rate. Again, the pulse frequency was varied to achieve the desired average power. The discharge parameters are summarized in Table 1 for dcMS operation and both operating modes of HiPIMS for all the seven magnet configurations investigated.

**Table 1.** Discharge operating parameters for the investigated dcMS and HiPIMS discharges in fixed voltage and in fixed peak current modes. The average discharge power was kept at 300 W for all the discharges. For HiPIMS discharges, the pulse length was 100  $\mu$ s while the pulse frequency was varied to maintain a constant averaged power. The absolute magnetic field strength and the degree of balancing was varied by displacing the center magnet (C) and the outer ring magnet at the target edge (E). Each configuration is referred to using the displaced distance (in mm) of each magnet from the target backing plate. In this notation, C0E0 refers to a magnetron configuration where the center and outer magnets touch the backing plate.

Magnet	dcMS		HiPIMS Fixed Voltage			HiPIMS Fixed Peak Current			HiPIMS Fixed Peak Current				
	$B_{r,rt}$ [Gauss]	$z_{null}$ [mm]	$V_D$ [V]	$I_D$ [A]	$V_D$ [V]	$I_{D,peak}$ [A]	$f_{pulse}$ [Hz]	$V_D$ [V]	$I_{D,peak}$ [A]	$f_{pulse}$ [Hz]	$V_D$ [V]	$I_{D,peak}$ [A]	$f_{pulse}$ [Hz]
C0E0	238	66	339	0.885	625	80	54	510	40	143	555	80	60
C0E5	217	70	308	0.974	625	54	76	565	40	123	580	80	56
C0E10	213	74	311	0.964	625	35	115	650	40	111			
C5E0	181	53	317	0.946	625	53	80	557	40	129	582	80	58
C5E5	161	59	334	0.926	625	36	97	655	40	97	649	80	295
C10E0	137	43	312	0.961	625	31	134	660	40	99	636	80	295
C10E10	111	52	330	0.909	625	12	450						

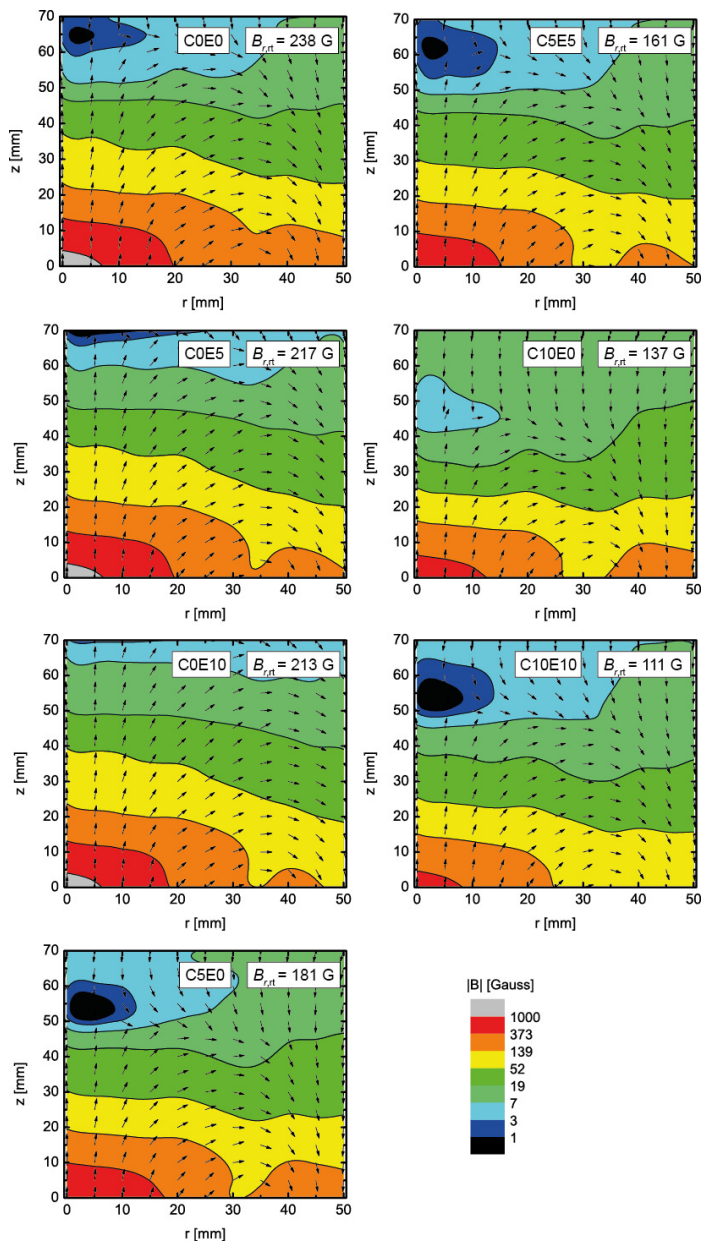


**Figure 2.** The measured magnetic field (flux density  $\mathbf{B}$ ) and field line directions for the various magnetic field configurations. Normalized arrows indicate the magnetic field direction, the color scale indicates the magnitude of the magnetic field  $|\mathbf{B}| = \sqrt{B_r^2 + B_z^2}$ . The value of  $B_r$  above the race track at  $z = 11$  mm is given in the inset for each case.

We captured the discharge current–voltage ( $I_D$ – $V_D$ ) waveforms when operating the HiPIMS discharges at different magnet configurations. Figure 3a depicts the cathode voltage and Figure 3b the discharge current for all seven magnetic field configurations explored when operating in fixed

voltage mode. When moving both the central and outer magnets together,  $I_{D,peak}$  changed from 80 A to 36 A to finally 12 A for the C0E0, C5E5 and C10E10 magnet configurations, respectively. Figure 3b shows that  $I_{D,peak}$  occurred before the pulse end using the C0E0 configuration while for two other magnet configurations the discharge current waveforms had an ascending trend over the entire pulse length. The value of  $I_{D,peak}$  was more sensitive to the absolute strength of the magnetic field than to the degree of balancing. The C5E0 and C0E5 configurations gave  $I_{D,peak} = 53\text{--}54$  A and the C10E0 and C0E10 configurations 31–35 A. Figure 3c depicts the discharge current waveforms captured at fixed peak current mode with various magnet configurations. Although  $I_{D,peak}$  was very similar in all cases, the current rise rate was different and as a result the discharge current peaked at different times. Note that different cathode voltages were applied to achieve the same  $I_{D,peak}$  (see Table 1), but the voltage was not correlated to the time of peak current. For example, the C5E5 magnet configuration exhibited sharper current rise than C0E0 while the corresponding cathode voltage was 150 V higher than for the C0E0 magnet. In contrast, looking at discharge current waveforms for the C5E0 and C10E0 magnets showed that using the C5E0 magnet resulted in sharper current rise than the C10E0 magnet, although the corresponding cathode voltage was approximately 100 V lower.

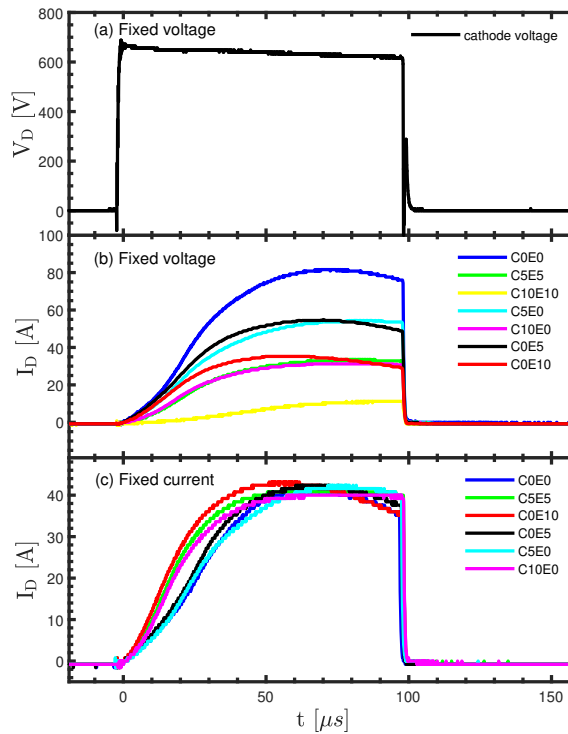


**Figure 3.** The HiPIMS discharge current and voltage waveforms recorded for various magnetic field configurations: (a) the discharge voltage in fixed voltage mode; (b) the discharge current in fixed voltage mode; and (c) discharge current in fixed peak current mode. The Ar pressure was set to 1 Pa. The pulse width was 100  $\mu$ s at an average power of 300 W.

A quartz crystal micro-balance (QCM) with native frequency of 5 MHz and gold coated surface was used to measure the deposition rate. It was mounted on the probe holder shown in Figure 1. By moving the probe holder and/or the magnetron assembly, it was possible to investigate a region defined by  $0 \leq r \leq 50$  and  $20 \leq z \leq 70$  mm, where  $r$  is the radial coordinate parallel to the target



surface and  $z$  is the axial coordinate perpendicular to the target surface, and  $(r, z) = (0, 0)$  marks the center of the target surface. The center of the target race track was located at approximately  $(r, z) = (30, 0)$  mm. In this work, only axial material fluxes were investigated, i.e., mimicking a conventional sputtering setup with a substrate facing the target surface.

The QCM sensor was also used as a main component in the ion meter (or gridless QCM/m-QCM) used for measuring the ionized flux fraction  $F_{\text{flux}}$ . The device is described in detail in a previous work [4] and is here only summarized. The ion meter can measure either the deposition rate from ions and neutrals or from neutrals only by varying a voltage applied to the biased top QCM electrode, allowing for fast (roughly 1 min) determination of the ionized fraction of material flux to the sensor head. The gridless sensor uses a magnetic field configuration consisting of a ferromagnetic yoke and magnetic pole pieces (cylindrical SmCo magnets with a diameter of 8 mm and a length of 5 mm) placed in front of the sensor. This configuration produces a localized homogeneous magnetic field of about 4000 Gauss, which does not significantly affect the magnetic field of the magnetron assembly [4]. The QCM control unit with the oscillator was connected directly to the crystal electrode. The electrode was either grounded for measurements of both ions and neutrals, or biased to +40 V to collect only the neutrals without positive ions. The dc bias voltage was connected to the QCM collecting electrode through a 1 k $\Omega$  resistor, to protect the crystal in case of arcing, and the ground of the oscillator and the readout unit were connected to the crystal collecting electrode through a 150 nF capacitor such that dc current was blocked while rf current could flow from the crystal through this capacitor back to the ground of the oscillator and give a readout (see Figure 1). In this configuration, the top crystal electrode could be readily biased without any influence on the QCM operation. The ionized fraction of the metal flux

$$F_{\text{flux}} = \frac{R_t - R_n}{R_t}, \quad (1)$$

was determined from the total mass deposition rate  $R_t$  and the mass deposition rate of neutral metal atoms  $R_n$ , as discussed by Wu et al. [34]. The deposition rates were recorded by manually recording the film thickness at a chosen time on a readout unit connected to the QCM. In addition, we tried to minimize errors due to the QCM crystal heating up during the process by making short measurements (typically less than 120 s). The total error of  $F_{\text{flux}}$  was estimated to be up to 15% for a single result mainly based on the accuracy of the mass deposition rate determination. Since the QCM electrode was grounded during the measurement of the total deposition rate, no significant collimation of the ions [35] was expected at this stage due to the low plasma potential, which potentially could introduce additional errors in the measurements. The ion meter was mounted on the probe holder shown in Figure 1 and could thereby map out the same region of interest as the standard QCM. However, due to interference with the plasma discharge, it was not possible to move it closer than  $z \geq 30$  mm. In addition, high peak currents in the HiPIMS mode sometimes resulted in strong fluctuations of  $(R_t - R_n)$ , which meant that the HiPIMS series with fixed peak current had to be limited to  $I_{D,\text{peak}} = 40$  A ( $J_{D,\text{peak}} = 0.5$  A/cm<sup>2</sup>) when measuring  $F_{\text{flux}}$ .

### 3. Results

The deposition rates as well as the ionized flux fractions for each of the magnetron configurations shown in Figure 2 and listed in Table 1 are presented here. For the deposition rate results, we chose to focus on the data recorded at a typical target-to-substrate distance of  $z = 70$  mm, which also includes three radial points ( $r = 0, 25, 50$  mm) to determine the expected film thickness profile at that axial distance. However, the deposition rate was also recorded closer to the target and comparisons were made where appropriate. Concerning the ionized flux fraction at  $z = 70$  mm, we only show data recorded above the target center, i.e.,  $(r, z) = (0, 70)$  mm, although all radial positions were used in the analysis. We also show the flux fractions at  $(r, z) = (25, 30)$  mm due to the interest in comparing with other reports of  $F_{\text{flux}}$ , which are typically recorded at the outer edge of the ionization region (the

dense plasma region) above the target race track. We refer to the region where the substrate is typically located as the diffusion region.

### 3.1. Deposition Rate

The deposition rates measured above the center of the target ( $r = 0$  mm) at an axial distance of 70 mm (substrate position) are plotted as a bar chart in Figure 4 for the different discharge types as well as all magnetic configurations investigated. The magnet configurations on the  $x$ -axis are ordered from highest  $|\mathbf{B}|$  at the left to the lowest  $|\mathbf{B}|$  on the right. We have here used the recorded  $|B_{r,rt}|$  value above the race track as a measure of  $|\mathbf{B}|$ . Overall, the dcMS discharges exhibited the highest deposition rates independent of magnetron configuration, with deposition rates in a rather narrow range (92–116 Å/min). Much larger differences were observed for the HiPIMS discharge operated in the fixed voltage mode, where the deposition rate varied between 45 Å/min and 96 Å/min. However, for the fixed peak discharge current mode, the deposition rate varied between 34 Å/min and 47 Å/min with an increasing trend of 38% larger deposition rate at the weakest  $|\mathbf{B}|$  compared to the strongest  $|\mathbf{B}|$ .

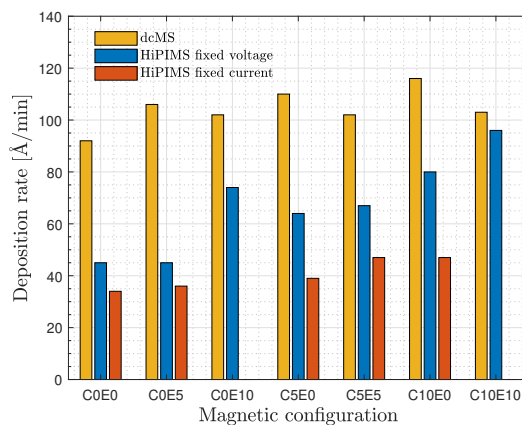


**Figure 4.** The Ti deposition rate from both dcMS and HiPIMS discharges operated in fixed voltage mode and fixed peak current mode using various magnetic field configurations, measured at 70 mm axial distance over center of cathode. The magnet configurations on the  $x$ -axis are ordered from high  $|\mathbf{B}|$  at the left to low  $|\mathbf{B}|$  on the right. The recorded  $|B_{r,rt}|$  value above the race track was used as a measure of  $|\mathbf{B}|$ .

Let us start by comparing the three cases C0E0, C5E5, and C10E10, exhibiting the same magnetic topology but approximately a reduction of 63% of the absolute magnetic field strength at the center of the target surface and a reduction of  $|B_{r,rt}|$  by 53% (configurations C0E0 and C10E10). For the dcMS discharges, only small differences were found. The strongest magnetic field (C0E0) showed the lowest deposition rate (92 Å/min) and the weakest magnetic field (C10E10) showed the highest deposition rate (103 Å/min), i.e., a deposition rate increase of 11%. The HiPIMS discharges operated in fixed voltage mode showed a much more pronounced deposition rate dependence on changes in  $|\mathbf{B}|$ , where a weaker  $|\mathbf{B}|$  resulted in a considerably higher deposition rate. For example, C0E0 exhibited the lowest deposition rate (45 Å/min) and C10E10 the highest deposition rate (96 Å/min), i.e., a rate increase of 113%. It was also observed that this latter HiPIMS case resulted in a deposition rate, which was around 90% of the dcMS rate, i.e., a significantly higher value than what is commonly reported for HiPIMS, as discussed in the Introduction. In contrast, the HiPIMS discharges operated in fixed peak current mode exhibited smaller changes in the measured deposition rate when  $|\mathbf{B}|$  was varied, as observed



when comparing cases C0E0 and C5E5 (no data from C10E10), about 38% increase of the deposition rate when weakening  $|\mathbf{B}|$ . In this discharge mode, the HiPIMS deposition rate was around 40% of the dcMS rate for the equivalent magnetron configurations, which was closer to the value of 30% reported by Samuelsson et al. [8].

For completeness, it is also noted that a significant deposition rate increase could be achieved at closer target-to-substrate distances, as expected. The highest deposition rate values, independent of discharge type and magnet configuration, were recorded at the closest axial distance investigated,  $z = 20$  mm, with on the average, 2.3, 2 and 1.9 times higher values for dcMS, fixed voltage and fixed peak current HiPIMS discharges, respectively, compared to the values measured at  $z = 70$  mm (results not shown here). In general, similar trends in the deposition rate for the different configurations investigated were observed at all distances from the target. However, the closer was the distance to the target, the larger was the radial variation in the recorded deposition rates, which is generally not desired in thin film deposition.

To address the issue of the expected radial film thickness profile at the substrate position, the relative standard deviation (RSD) of the deposition rate was calculated from recorded deposition rates at three radial points,  $r = 0, 25, 50$  mm at  $z = 70$  mm from the target surface. RSD is a standardized measure of dispersion of a probability distribution or frequency distribution. It is often expressed as a percentage, and is defined as

$$RSD = 100 \frac{\sigma}{\mu} \tag{2}$$

where  $\sigma$  is the standard deviation and  $\mu$  is the mean of the dataset. The standard deviation of the deposition rates was calculated as the square root of its variance. Overall, we found a weak trend of decreasing RSD with increasing degree of magnetic balancing. This is illustrated in Figure 5, where the magnet configurations on the  $x$ -axis are ordered with increasing  $z_{\text{null}}$  (increasing degree of magnetic balancing) from left to right (see Table 1).

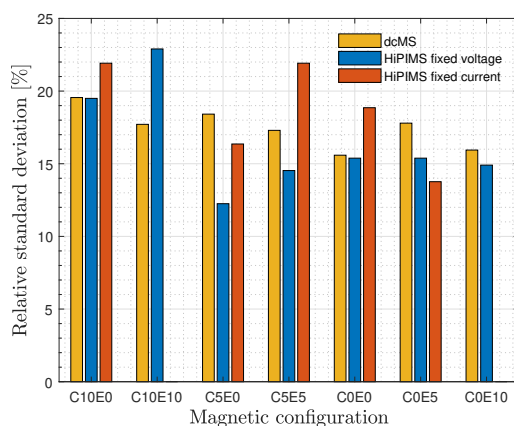


**Figure 5.** The RSD of Ti deposition rates from both dcMS and HiPIMS discharges operated in fixed voltage mode and fixed peak current mode using various magnetic field configurations. The rates measured at 70 mm axial distance over center, race track and edge of cathode. The magnet configurations on the  $x$ -axis are ordered with increasing  $z_{\text{null}}$  from left to right.

In addition, the dcMS discharges exhibited the lowest sensitivity to  $|\mathbf{B}|$ , as can be seen when comparing the three cases C0E0, C5E5, and C10E10. Note that this does not imply that the coating uniformity was the best since RSD was still rather high. Changing the magnet configuration from

weakly to strongly unbalanced configurations (C0E5 to C5E0 and C0E10 to C10E0) barely affected the dcMS deposition rate uniformity, which remained in the range of 16% to 19%.

The deposition rate of a HiPIMS discharge operated in fixed voltage mode exhibited the most uniform deposition rate profile of all cases investigated when using the C5E0 magnetic field geometry with RSD of 12%. The C0E5 and C0E10 configurations led to similar RSDs (15%). The lowest uniformity (highest RSD) achieved was observed for C10E0, just below 20%, i.e., similar to the corresponding dcMS value. In the fixed peak current mode, the maximum RSD recorded was 22% for C10E0 and C5E5, while using C0E5 and C5E0 resulted in RSD values of 14% and 16%, respectively. A similar analysis of the fixed voltage HiPIMS mode showed that the highest RSD was 23% when using the C10E10 configuration and the lowest RSD was 12% with the C5E0 configuration. For the strongest  $|\mathbf{B}|$  case C0E0, the deposition rate profile was similar to the dcMS case. However, the RSD values found for the fixed peak current HiPIMS mode were generally higher with RSD of 19% for C0E0 and RSD of 22% for C5E5. Overall, the deposition uniformity was more dependent on the magnetic configuration than the discharge type. Moving closer to the target ( $z = 20$  mm), the deposition rate became significantly less uniform (about two times higher RSD values) compared to a typical substrate position ( $z = 70$  mm).

### 3.2. Ionized Flux Fraction

The ionized flux fractions  $F_{\text{flux}}$  measured above the center of the target ( $r = 0$  mm) at an axial distance of  $z = 70$  mm are plotted as a bar chart in Figure 6 for the two HiPIMS operating modes (fixed voltage and fixed peak current modes) as well as for all magnet configurations investigated. Note that the magnet configurations on the  $x$ -axis are now ordered from highest  $|\mathbf{B}|$  at the left to the lowest  $|\mathbf{B}|$  on the right where, again,  $|B_{r,rt}|$  from Table 1 was used as a suitable indicator of  $|\mathbf{B}|$ . No dcMS values are presented here, since  $F_{\text{flux}}$  was always very close to 0%, i.e., within the margin of error, and thus in line with the results reported by Kubart et al. [4] using the same technique.

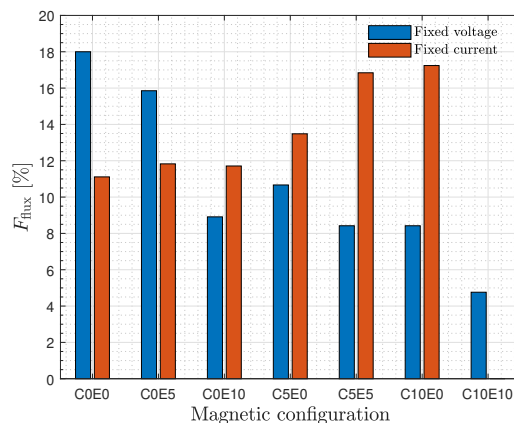


**Figure 6.** The Ti ionized flux fraction in a HiPIMS discharge using various magnet configurations measured at 70 mm axial distance over the center of the cathode. The discharge is operated in the HiPIMS fixed voltage and fixed peak current modes. The magnet configurations on the  $x$ -axis are ordered from high  $|\mathbf{B}|$  at the left to low  $|\mathbf{B}|$  on the right. The recorded  $|B_{r,rt}|$  value above the race track was used as a measure of  $|\mathbf{B}|$ .

Figure 6 shows that the ionized flux fraction decreased with decreasing  $|\mathbf{B}|$  when the HiPIMS discharge was operated in fixed voltage mode. For the HiPIMS discharges operated in fixed

voltage mode, significant differences were found when comparing the three cases C0E0, C5E5, and C10E10 (reduced absolute magnetic field strength  $|\mathbf{B}|$ , while maintaining the same magnet topology). The strongest magnetic field (C0E0) showed the highest  $F_{\text{flux}}$  (18%) and the weakest magnetic field (C10E10) showed the lowest  $F_{\text{flux}}$  (4.7%). In the fixed voltage mode,  $F_{\text{flux}}$  seemed to decrease with the decreased absolute magnetic field strength  $|\mathbf{B}|$  which is correlated with the peak discharge current presented above in Figure 3. This is analyzed in more detail in the next section. However, the corresponding HiPIMS discharges operated in fixed peak current mode clearly did not exhibit such a behavior. Instead, the ionized flux fraction  $F_{\text{flux}}$  increased slightly with decreasing  $|\mathbf{B}|$ . The ionized flux fraction increased from 11% to 16.8% when comparing cases C0E0 and C5E5 (no data from C10E10), i.e., by a factor 1.5 when decreasing  $|\mathbf{B}|$ .

When focusing on changes in the degree of balancing, i.e., comparing the configuration pairs C0E5/C5E0 and C0E10/C10E0, the following observations could be made. For the HiPIMS discharges operated in fixed voltage mode, it was somewhat surprising that the highest  $F_{\text{flux}}$  was recorded for the weakly unbalanced C0E5 configuration (16%), whereas the most strongly unbalanced configuration C10E0 exhibited a much lower value (8.5%), although there was only a small difference compared to C5E0 and C0E10. Any influence on  $F_{\text{flux}}$  from the unbalance was masked by the strong influence of the peak discharge current values on  $F_{\text{flux}}$ . For the HiPIMS discharges operated in fixed peak current mode, the trend observed for  $F_{\text{flux}}$  (Figure 6) was somewhat more expected. The more strongly unbalanced cases exhibited higher  $F_{\text{flux}}$  with a maximum of 17.2% for C10E0.

In addition, by making radial scans of  $F_{\text{flux}}$ , we attained radial profiles at  $z = 70$  mm in the fixed voltage mode (not shown here). In general, only minor differences compared to the results at  $r = 0$  mm were observed. The maximum  $F_{\text{flux}}$  was commonly reached above the target race track position, and it was approximately 2–5 percentage points higher compared to the values reported in Figure 6. However, a few exceptions are worth noting. For the strong  $|\mathbf{B}|$  configuration C0E0, there was a sudden jump in  $F_{\text{flux}}$  towards the region above the target edge ( $r = 50$  mm). Here,  $F_{\text{flux}}$  increased to 27% compared to just below 20% above the target center and race track. In addition, the configuration C5E5 exhibits a striking increase in  $F_{\text{flux}}$  compared to the result presented in Figure 6, and  $F_{\text{flux}}$  peaks at 11.5% above the target race track compared to 8.5% above the target center.

We now turn to investigate  $F_{\text{flux}}$  in the ionization region, since this would provide a better basis for comparison with other reports of the ionized flux fraction, as discussed in the Introduction. Furthermore, these values were indispensable for our ongoing modeling efforts of the internal parameters in HiPIMS using the ionization region model [36,37]. Measurements were therefore taken above the target race track at  $(r, z) = (25, 30)$  mm and a summary is shown in Figure 7.

For HiPIMS discharges operated in fixed voltage mode, we observed the same general trend as shown in Figure 6 but with approximately a 72% increase in  $F_{\text{flux}}$  for C0E10 and C5E0, 66% increase for C0E0, 55% increase for C5E5 and C10E0, 12% increase for C0E5, and almost no change for C10E10 compared to  $F_{\text{flux}}$  measured at  $(r, z) = (0, 70)$  mm. However, HiPIMS discharges operated in fixed peak current mode clearly did not exhibit such a behavior. Instead  $F_{\text{flux}}$  using C0E0 showed 55% increase and reached 17% while  $F_{\text{flux}}$  of C5E5 remained at 17% with no change compared to our measurements at 70 mm (Figure 6). By focusing on changes in the degree of balancing, 17%, 34% and 54% increases in  $F_{\text{flux}}$  were observed using C0E5, C0E10, C5E0, respectively, while C10E0 showed negligible change compared to what is shown in Figure 6. As a consequence, the C5E0 configuration led to the highest  $F_{\text{flux}}$  (20.5%) over the race track and  $z = 30$  mm. In the fixed peak discharge current mode with peak current density of  $J_{D,\text{peak}} = 0.5$  A/cm<sup>2</sup>, the measured values were in the range 14.2–20.5%. For comparison, Lundin et al. [5] reported ionized flux fraction in the range 22–31%, over the race track 40 mm from the target surface, increasing with increased working gas pressure in the range 0.5–2 Pa for a Ti target when operating at peak current density of  $J_{D,\text{peak}} = 0.5$  A/cm<sup>2</sup>, pulse length 100  $\mu$ s, and time averaged power of 200 W. Similarly, Kubart et al. [4] reported ionized flux fraction of 24% 43 mm above the target race track for a Ti target with argon as the working gas at 1 Pa and operating at peak current density of  $J_{D,\text{peak}} = 0.5$  A/cm<sup>2</sup> for 100  $\mu$ s long pulses and time averaged

power of 200 W. The values reported here were thus somewhat lower than the values reported in these earlier studies.

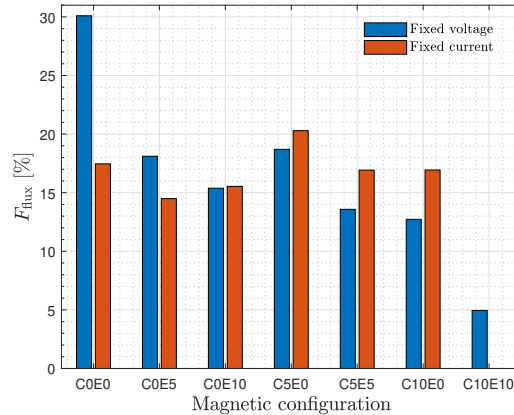


**Figure 7.** The Ti ionized flux fraction in a HiPIMS discharge using various magnet configurations measured at 30 mm axial distance over the center of the cathode. The discharge was operated in the HiPIMS fixed voltage and fixed peak current modes. The magnet configurations on the x-axis are ordered from high  $|\mathbf{B}|$  at the left to low  $|\mathbf{B}|$  on the right. The recorded  $|B_{r,rt}|$  value above the race track was used as a measure of  $|\mathbf{B}|$ .

## 4. Discussion

### 4.1. Discharge Physics

As a background to how the magnetic field influences the ionized flux fraction and the deposition rate, let us discuss how it influences the discharge physics. The magnetic field in sputtering magnetrons makes the discharge more efficient through two mechanisms, Ohmic heating and electron confinement. Ohmic heating [38,39] allows for energizing the large majority of the electrons, those that are created by ionization within the plasma discharge, in addition to the energization through acceleration across the cathode sheath of the small minority of electrons that are created by secondary emission at the target [40]. Electron confinement adds further to the efficiency by reducing the loss of the energetic electrons out of the discharge volume (the ionization region). The magnetic field therefore enables more ionization for a given input energy. Since most of the discharge current at the target surface is carried by ions [36], this results in a higher discharge current for a given voltage. This effect was clearly observed in our experiments. Figure 8 shows two sets of data, both plotted as functions of the magnetic field strength at the race track center, i.e.  $|B_{r,rt}|$  in Table 1: the peak discharge current when operating at fixed voltage, and the discharge voltage when operating at fixed peak current. Let us first look at the fixed voltage case. The peak discharge current varied with  $|\mathbf{B}|$  as expected, from 12 A for the weakest magnetic field, configuration C10E10, to 80 A for the strongest  $|\mathbf{B}|$  configuration, C0E0 (Figure 3b). Extrapolation to weaker  $|\mathbf{B}|$  indicated that, below about 50 Gauss, it would not be possible to ignite a discharge at the set pressure. The fixed peak discharge current case confirmed this picture. A higher voltage was needed to drive the discharge for weaker  $|\mathbf{B}|$ , and, for the weakest  $|\mathbf{B}|$ , a 40 A discharge could not be reached due to the voltage limitation of the power supply.

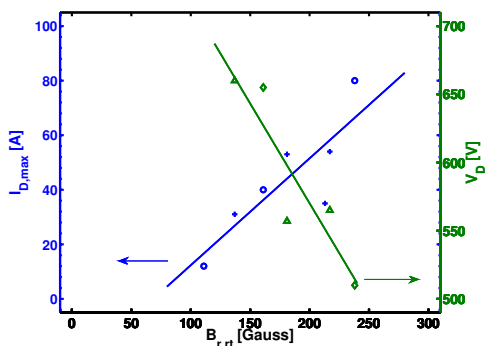


**Figure 8.** The peak discharge current (left  $y$ -axis) when operating in fixed voltage mode ( $V_D = 625$  V) and the discharge voltage (right  $y$ -axis) when operating in fixed peak discharge current mode ( $I_{D,max} = 40$  A) as a function of the magnetic field strength over the race track ( $B_{r,rt}$  in Table 1).  $\circ$  all magnets moved together (C0E0, C5E5, and C10E10) and fixed voltage operation,  $+$  magnets mixed (C0E5, C5E0, C10E0 and C0E10) and fixed voltage operation,  $\diamond$  all magnets moved together (C0E0, C5E5, and C10E10) and fixed peak current operation, and  $\triangle$  magnets mixed (C0E5, C5E0, C10E0 and C0E10) and fixed peak current operation.

A consequence of these effects was that the peak power in the individual HiPIMS pulses varied between the different magnetic field configurations. This variation was around 50% in the fixed peak current studies, and almost an order of magnitude in the fixed voltage studies. For a normalization of the deposition rates to dcMS, it was most practical to operate at constant average power. This was achieved by varying the pulse repetition frequency  $f_{pulse}$ , as given in Table 1. This variation of the discharge impedance between the magnetic field configurations and our compensation by adjusting  $f_{pulse}$  to have constant power are important to keep in mind in the analysis presented below. The most important consequence is that, even if both the cathode voltage and the average power were kept constant, the peak discharge current could vary by almost an order of magnitude between the different magnetic field configurations. This implies a variation of the plasma density of the same order, which in turn implies a large variation in the probability of ionization of the sputtered material as it passes through the plasma [5].

#### 4.2. Deposition Rate and Ionized Flux Fraction

Figure 4 shows that, for HiPIMS operated in the fixed voltage mode, the deposition rate increased with decreasing  $|\mathbf{B}|$ . For dcMS operation, there was only a small change in the deposition rate when  $|\mathbf{B}|$  was varied. However, when operating the HiPIMS discharge in fixed peak current mode, there was a slight increase in the deposition rate as the  $|\mathbf{B}|$  was decreased, as shown in Figure 4. Bradley et al. [19] recently explored the difference in the discharge behavior between dcMS and HiPIMS operation with changing  $|\mathbf{B}|$ . For dcMS and pulsed-dc operation they found that the deposition rate decreases by 25–40% when decreasing  $|\mathbf{B}|$ . They found the opposite for HiPIMS operation and the deposition rate increases significantly with decreasing  $|\mathbf{B}|$ . They used a simple phenomenological model (pathway model) to relate the sputtered particle fluxes and the measured deposition rates to find the combined probabilities of ionization  $\alpha_t$  and subsequent back attraction  $\beta_t$  of the ions of the sputtered species  $\alpha_t\beta_t$  as  $|\mathbf{B}|$  is varied. They found a drop in  $\alpha_t\beta_t$  with decreasing  $|\mathbf{B}|$  and proposed it being due to the weakening of the electrostatic ion back attraction, due to a potential hill seen by the ions of the sputtered material. A fall in  $\alpha_t\beta_t$  gives higher deposition rates.

Here, we expanded on the approach of Bradley et al. [19] and explore how the measured parameters, the deposition rate and the ionized flux fraction  $F_{flux}$ , depend separately on the probability

of ionization  $\alpha_t$  and back attraction of the sputtered species  $\beta_t$ . We derived a few general equations that relate the measured quantities to the parameters  $\alpha_t$  and  $\beta_t$ . Let us call the total flux (atoms/s) of atoms sputtered from the target  $\Gamma_0$  and the flux of sputtered species (ions and neutrals) that leave the ionization region (IR) towards the diffusion region (DR)  $\Gamma_{DR}$ . The useful fraction of the sputtered species becomes

$$F_{DR} = \frac{\Gamma_{DR}}{\Gamma_0} = (1 - \alpha_t\beta_t). \quad (3)$$

Note that this equation does not need to take into account ion focusing (or spreading) en route towards the substrate [37]. This equation indicates a reduced fraction of the sputtered species reaching the substrate when the ionization of the sputtered material increases. Recall that the main drawback using HiPIMS is the low deposition rate. As can be seen in Equation (3), the fraction of the sputtered species leaving the ionization region  $F_{DR}$  and thus the deposition rate can be increased by decreasing the product  $\alpha_t\beta_t$ . Two different mechanisms can achieve this: decrease the probability of ionization of the sputtered atoms  $\alpha_t$ , and/or decrease the ion back attraction probability  $\beta_t$ . There is experimental support for both approaches. Mishra et al. [13] showed that the back attracting electric field  $E_z$  in front of the target decreases with a decreasing  $|\mathbf{B}|$  and thus reduces  $\beta_t$ . In addition, a lower  $|\mathbf{B}|$  with a fixed discharge voltage generally leads to lower peak discharge currents and thus lower  $\alpha_t$ . We also show in Figure 3b that, when operating in the fixed voltage mode, the peak discharge current  $I_{D,peak}$  decreased as  $|\mathbf{B}|$  decreased. This was a consequence of lower magnetic confinement, which led to lower plasma density. For our three magnetic field configurations, where the magnetic pack was moved as a whole, the peak discharge currents were 80 A for the strongest  $|\mathbf{B}|$  (C0E0 configuration), 36 A for the intermediate (C5E5 configuration), and 12 A for the weakest  $|\mathbf{B}|$  (C10E10 configuration). The lower discharge currents at weaker  $|\mathbf{B}|$  corresponded to lower plasma densities in front of the target, which should reduce the probability of ionizing sputtered atoms that pass through the ionization region, i.e., reduce  $\alpha_t$ . As pointed out by Bradley et al. [19], poorer magnetic confinement, lower plasma densities, and lower discharge currents give rise to increased deposition rates. However, this increased deposition rate is at the cost of decreased ionized flux fraction, as discussed in Section 3.2. Thus, decreased discharge current and lower plasma density lead to decreased ionization probability of the sputtered material  $\alpha_t$ . The fraction of the sputtered species reaching the substrate, which is proportional to  $(1 - \alpha_t\beta_t)$ , then increases if  $\beta_t$  remains roughly fixed, which is explored in more detail below in the fixed voltage mode. In the fixed peak current mode, we could assume that the plasma density remained fixed, thus  $\alpha_t$  and decreasing  $\beta_t$  with decreasing  $|\mathbf{B}|$  gave increased deposition rate, which was also examined.

A relationship between the ionization flux fraction  $F_{flux}$  and the parameters  $\alpha_t$  and  $\beta_t$  has been derived from the pathway model [32,37]

$$F_{flux} = \frac{\Gamma_{DR,ions}}{\Gamma_{DR}} = \frac{\Gamma_0\alpha_t(1 - \beta_t)}{\Gamma_0(1 - \alpha_t\beta_t)} = \frac{\alpha_t(1 - \beta_t)}{(1 - \alpha_t\beta_t)} \quad (4)$$

where no additional ionization of the sputtered material in the diffusion region is assumed. Note that that there is a slight difference from the equation derived by Butler et al. [37] as here we neglected ion focusing. Our goal was to assess how much  $|\mathbf{B}|$  and the magnetic field structure influence  $\alpha_t$  and  $\beta_t$ , respectively. To this purpose, we plot a graph that shows  $F_{DR}$  on the horizontal axis, and  $F_{flux}$  on the vertical axis in Figure 9. In this graph, we have used Equations (3) and (4) to plot two sets of lines: (i) lines of constant  $\beta_t$  with  $\alpha_t$  varied from 0 to 1 (green dashed lines in Figure 9); and (ii) lines of constant  $\alpha_t$ , with  $\beta_t$  varied from 0 to 1 (blue solid lines in Figure 9). This gives us a coordinate system  $(\alpha_t, \beta_t)$  transformed into the  $(F_{DR}, F_{flux})$  plane. Plotting the experimentally determined combinations of  $F_{DR}$  and  $F_{flux}$  in this plane gives us estimates of the corresponding values of  $\alpha_t$  and  $\beta_t$ . The ionized flux fraction  $F_{flux}$  generally increases with increasing ionization probability  $\alpha_t$ , as shown in Figure 9 (blue solid lines). Thus, for a fixed  $\beta_t$ , we found that, for decreased ionization probability  $\alpha_t$ , the ionized flux fraction decreased. This is indeed what we observed for the fixed voltage mode operation. In the

HiPIMS discharge,  $F_{\text{flux}}$  was lower than  $\alpha_t$  because only a small fraction of the ions left in the direction of the substrate as  $\beta_t$  was high [37]. At high  $\alpha_t$ , the flux of neutrals was reduced due to high ionization and this flux was only partially replaced by ions since most of the ions were drawn back to the target.

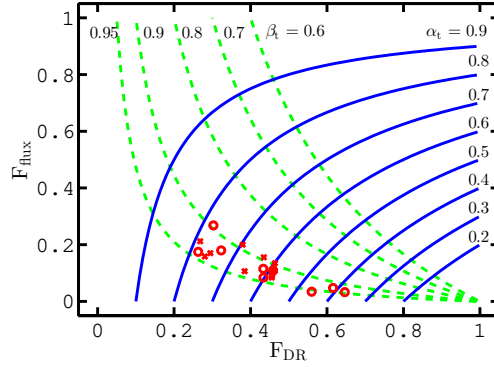


**Figure 9.** Experimentally determined combinations of  $F_{\text{DR}}$  and  $F_{\text{flux}}$  at  $z = 70$  mm, for all three radial positions, and for all magnetic field configurations. The configurations C0E0, C5E5, and C10E10 are denoted by  $\circ$  corresponding to variable  $|\mathbf{B}|$  when all the magnets were moved together. The configurations C0E5, C5E0, C10E0 and C0E10 where the two magnets were moved relative to each other are denoted by  $\times$ . The discharges were operated at constant voltage and constant average power. Lines of constant  $\alpha_t$  (solid blue lines) and constant  $\beta_t$  (dashed green lines), calculated using Equations (3) and (4), respectively, give approximate estimate of these parameters for the studied discharges.

For an exact calculation of  $F_{\text{DR}}$  from Equation (3), we needed the total flux of sputtered atoms that (before ionization) were headed towards the position  $(r, z)$  where the deposition flux  $\Gamma_{\text{DR}}$  is measured. This is not a measured quantity, but it can be estimated from the measured deposition rates in a dcMS discharge operated at the same average power  $\Gamma_{\text{dcMS}}$  as follows. First, we note that all discharges studied here were run at the same average power. This means that the average discharge current obeyed the relation  $I_{\text{D,dcMS}}V_{\text{D,dcMS}} = \langle I_{\text{D,HiPIMS}} \rangle V_{\text{D,HiPIMS}}$  which gives

$$\frac{\langle I_{\text{D,HiPIMS}} \rangle}{I_{\text{D,dcMS}}} = \frac{V_{\text{D,dcMS}}}{V_{\text{D,HiPIMS}}} \tag{5}$$

where  $\langle I_{\text{D,HiPIMS}} \rangle$  is the time averaged discharge current of the HiPIMS discharge. We neglect the small contribution of secondary electron emission to the current at the target surface, and also assume only singly charged ions. In the dcMS discharge, all the sputtering was due to ions of the working gas, the primary ions. The flux of the sputtered material in the dcMS case was then

$$\Gamma_{\text{sput,dcMS}} = \frac{I_{\text{D,dcMS}}}{e} Y_{\text{tg}}(V_{\text{D,dcMS}}) \tag{6}$$

where  $Y_{\text{tg}}(V_{\text{D,dcMS}})$  is the sputter yield for  $\text{Ar}^+$  ions at the ion energy  $\mathcal{E}_{\text{Ar}^+} = eV_{\text{D,dcMS}}$ . The situation in the HiPIMS discharge was more complex and both ions of the working gas and ions of the target material participated in the sputter process [41]. In the HiPIMS case, a fraction  $\zeta = I_{\text{D,Ar}^+} / I_{\text{D,i}}$  of the total ion current to the target was due to ions of the working gas and sputtered the target with sputter yield  $Y_{\text{tg}}(V_{\text{D,HiPIMS}})$ , and the remaining discharge current fraction  $(1 - \zeta)$  was due to ions



of the target material (self sputtering) with sputter yield  $Y_{SS}(V_{D,HiPIMS})$ . This gives the total flux of sputtered species from the target

$$\Gamma_0 = \frac{\langle I_{D,HiPIMS} \rangle}{e} (\zeta Y_{tg}(V_{D,HiPIMS}) + (1 - \zeta) Y_{SS}(V_{D,HiPIMS})). \quad (7)$$

Using Equation (5) to replace currents with voltages in Equations (6) and (7) then gives

$$\Gamma_0 = \Gamma_{\text{sput,dcMS}} \frac{V_{D,\text{dcMS}}}{V_{D,HiPIMS}} \frac{\zeta Y_{tg}(V_{D,HiPIMS}) + (1 - \zeta) Y_{SS}(V_{D,HiPIMS})}{Y_{tg}(V_{D,\text{dcMS}})} \equiv \Gamma_{\text{sput,dcMS}} \Psi \quad (8)$$

All the parameters in this expression were known and easily accessible except the fraction  $\zeta$  of the ion current to the target that was carried by  $\text{Ar}^+$  ions. We used the concept of a critical discharge current introduced by Huo et al. [42] along with the generalized recycling model [41] to estimate this fraction. With argon as the working gas, a gas temperature of 300 K, and the approximation that the race track area  $S_{RT}$  was half the full target area  $S_T$ , the critical discharge current could be approximated as [42]

$$I_{\text{crit}} \approx 0.2 p_g S_T \quad (9)$$

where  $p_g$  is the working gas pressure in Pa and  $S_T$  is the target area in  $\text{cm}^2$ . In our case,  $p_g = 1$  Pa and  $S_T \approx 80 \text{ cm}^2$ , giving a critical current of 16 A. At the critical current, about half the ion current was carried by the working gas ions, and the other half by self-sputter recycling [42]. The discharge current waveforms and peak discharge currents, for the different cases studied here, are given in Figure 3. With only one exception, they were above 30 A, far above  $I_{\text{crit}}$ . In this current range, the ion current was carried mainly by recycled ions, of both the working gas and of the sputtered material. The relative fraction of these depends mainly on the self-sputter yield of the target material [41]. For a Ti target, with argon as working gas, the fraction was typically  $\zeta \approx 50\%$  when  $I_D \geq I_{\text{crit}}$  [36,41]. We assumed here that the titanium was only singly charged, neglecting the fact that, for HiPIMS discharges with Ti target, significant amounts of multiply charged titanium ions are known to exist [36,43,44].

For  $\text{Ar}^+$  ions sputtering titanium, the sputter yield is  $Y_{tg} = 0.0425 \times \mathcal{E}_{\text{Ar}^+}^{0.443}$  and for  $\text{Ti}^+$  ions sputtering titanium (self-sputtering) the sputter yield is  $Y_{SS} = 0.0285 \times \mathcal{E}_{\text{Ti}^+}^{0.484}$  [7]. The ratio  $\Psi = \Gamma_0 / \Gamma_{\text{sput,dcMS}}$  for the fixed voltage case can be calculated using Equation (8) and the discharge voltages during dcMS and HiPIMS operation given in Table 1. For the case of 50/50  $\text{Ar}^+ / \text{Ti}^+$  ions sputtering the target, this ratio is  $\Psi = 0.66$ . For solely  $\text{Ar}^+$  ions, the ratio is 0.61 and, for solely  $\text{Ti}^+$  ions, it is 0.71. The experimental data  $F_{\text{flux}}$  versus  $F_{\text{DR}} = \Gamma_{\text{DR}} / \Gamma_0 = \Gamma_{\text{DR}} / (\Gamma_{\text{sput,dcMS}} \Psi)$  from the fixed voltage operation and taken 70 mm from the target are plotted in Figure 9 for all three locations, center ( $r = 0$ ) mm, over the race track ( $r = 25$  mm), and edge ( $r = 50$  mm). We assumed here that 50% of the ions were  $\text{Ar}^+$  and the other 50% were  $\text{Ti}^+$  and  $\Psi = 0.66$ . We note that all the experimental data fall in a narrow range for the back attraction probability  $\beta_t = 0.90 - 0.95$  while they span a wide range in ionization probability  $\alpha_t$  or 0.38–0.8. Thus, in the fixed voltage mode,  $\beta_t$  was almost constant while  $\alpha_t$  was varied by varying the magnetic field strength. For the fixed current case, the ratio  $\Psi$  was in the range 0.64–0.74 assuming 50/50  $\text{Ar}^+ / \text{Ti}^+$  ions sputtering the target and the variation was due to variation in the discharge voltage.

Finally, we can derive an equation that gives the back attraction probability  $\beta_t$  as a function of the measured quantities  $F_{\text{flux}}$  and  $F_{\text{DR}}$ . An expression in which  $\alpha_t$  is eliminated from Equations (3) and (4) allows estimating  $\beta_t$  directly from the measured quantities:

$$\beta_t = \frac{1 - F_{\text{DR}}}{1 - F_{\text{DR}}(1 - F_{\text{flux}})} \quad (10)$$

and similarly we can derive an equation that gives  $\alpha_t$  as a function of the measured quantities

$$\alpha_t = 1 - F_{\text{DR}}(1 - F_{\text{flux}}). \quad (11)$$



The ionization probability and back attraction probability for the ions of the sputtered species calculated using the measured quantities  $F_{flux}$  and  $F_{DR}$  are shown in Figure 10a,b, respectively, versus the magnetic field strength above the race track for various combination of operating modes, magnetic field configurations and locations over the target surface.

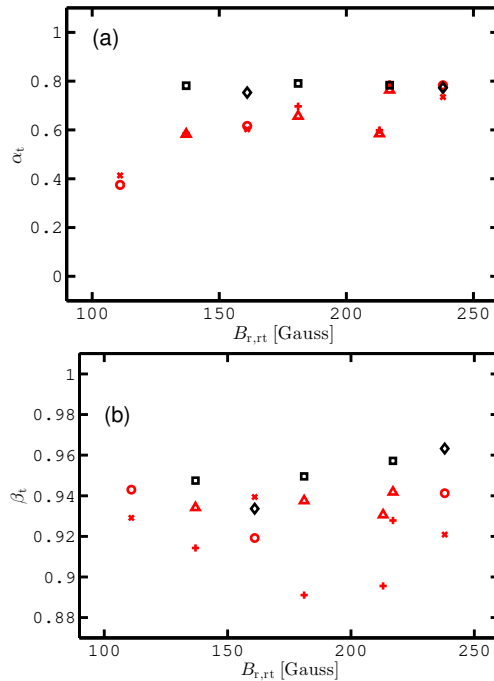


**Figure 10.** (a) The ionization probability  $\alpha_t$  and (b) the back attraction probability  $\beta_t$  for the ions of the sputtered species versus the magnetic field strength above the race track ( $r = 25$  mm).  $\circ$  both magnets moved together (C0E0, C5E5, and C10E10) over race track in fixed voltage operation,  $\times$  both magnets moved together (C0E0, C5E5, and C10E10) over center in fixed voltage operation,  $+$  magnets mixed (C0E5, C5E0, C10E0 and C0E10) over race track in fixed voltage operation,  $\Delta$  magnets mixed (C0E5, C5E0, C10E0 and C0E10) over center in fixed voltage operation,  $\diamond$  both magnets moved together (C0E0, C5E5, and C10E10) over center in fixed peak current operation, and  $\square$  magnets mixed (C0E5, C5E0, C10E0 and C0E10) over center in fixed peak current operation.

Figure 10a shows the ionization probability  $\alpha_t$  above the race track ( $r = 25$  mm) and in the target center ( $r = 0$  mm) versus the magnetic field strength over the race track. When operating in the fixed voltage mode, the ionization probability increased with increased magnetic field strength. The back attraction probability was always high, in the range 0.89–0.96, over the entire range of  $B_{r,rt}$  shown in Figure 10b. In the fixed current mode,  $\beta_t$  increased slightly with increased  $|\mathbf{B}|$  in the range 0.93–0.96 while  $\alpha_t$  was almost constant in a narrow range 0.75–0.79. If we make linear fit of the increase in  $\beta_t$  with  $|\mathbf{B}|$ , the fraction  $(1 - \beta_t)$  was roughly 30% higher at the highest  $|\mathbf{B}|$  than at the lowest  $|\mathbf{B}|$ . This was important since the total flux of ions of the sputtered material away from the target toward the substrate was  $\Gamma_{DR,ions} = \alpha_t(1 - \beta_t)\Gamma_0$ , as a fraction  $\beta_t$  of the ions of the sputtered material went back to the target. Recall that, as shown in Figure 4, there was a 38% increase in the deposition rate when  $|\mathbf{B}|$  decreased from 238 to 111 Gauss when operating at fixed peak discharge current. For the fixed peak current mode the ionization probability  $\alpha_t$  was roughly constant independent of the location of the magnetic null (not shown). In the fixed voltage mode, there was some spread in the ionization

probability values independent of the location of the magnetic null and no clear trend observed (not shown). Figure 11a shows the ionization probability  $\alpha_t$  above the race track and in the target center versus the peak discharge current. We observed that the ionization probability increased roughly linearly with the peak discharge current. Similarly, we observed an increase in the ionized flux fraction with increased peak discharge current in Figure 11b.

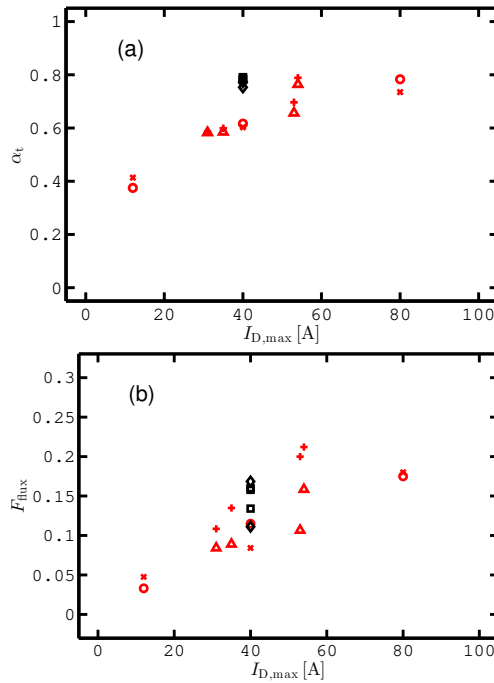


**Figure 11.** (a) The ionization probability of the sputtered species; and (b) the ionized flux fraction above the race track versus the peak discharge current.  $\circ$  both magnets moved together (C0E0, C5E5, and C10E10) over the race track in fixed voltage operation,  $\times$  both magnets moved together (C0E0, C5E5, and C10E10) over center in fixed voltage operation,  $+$  magnets mixed (C0E5, C5E0, C10E0 and C0E10) over race track in fixed voltage operation,  $\triangle$  magnets mixed (C0E5, C5E0, C10E0 and C0E10) over center in fixed voltage operation,  $\diamond$  both magnets moved together (C0E0, C5E5, and C10E10) over center in fixed peak current operation, and  $\square$  magnets mixed (C0E5, C5E0, C10E0 and C0E10) over center in fixed peak current operation

Furthermore, Figure 6 shows that, for operation in the fixed voltage mode, the stronger was the magnetic field, the higher was the  $F_{flux}$ . We can explain why: Figure 3b shows that higher magnetic field strength led to higher peak discharge current, and Figure 11b that higher discharge current gave higher  $F_{flux}$ .

## 5. Conclusions

The effect of the magnetic confinement on the deposition rate and the ionized flux fraction was explored for both dcMS and HiPIMS deposition from a Ti target. The experimental findings at  $z = 70$  mm indicate that, for the dcMS case, there was a small, about 10%, decrease in deposition rate as  $|\mathbf{B}|$  was increased from its weakest value to its strongest value. In the dcMS case, the ionized flux fraction was too small to be of interest. For HiPIMS operated in the fixed voltage mode, we found opposing trends with increasing  $|\mathbf{B}|$  in the studied range: a trade-off between the deposition rate

(decreased by more than a factor of two) and the ionized flux fraction (increased by a factor of 4–5). The back attraction probability of the ions of the sputtered material in a HiPIMS discharge was found to be high and roughly constant independent of  $|\mathbf{B}|$  and the ionization probability of the sputtered species increased with increasing  $|\mathbf{B}|$  due to an increased discharge current when operating in the fixed voltage mode. For HiPIMS operated in the fixed peak current mode, we found concurring, but smaller trends in the two parameters: Decreasing  $|\mathbf{B}|$  improved both the deposition rate (by 38%) and the ionized flux fraction (by 53%). When operating in the fixed peak current mode, the ionization probability of the sputtered species was roughly constant while the parameter  $(1 - \beta_t)$  increased roughly 30% with decreasing  $|\mathbf{B}|$ . In short, when operating a HiPIMS discharge in fixed voltage mode, the ionization probability  $\alpha_t$  varied with  $|\mathbf{B}|$  and  $\beta_t$  remained roughly constant, while, in the fixed peak current mode,  $\beta_t$  varied with  $|\mathbf{B}|$  and  $\alpha_t$  remained roughly constant.

**Author Contributions:** Conceptualization, H.H., J.T.G., M.Č., Z.H., M.A.R., N.B. and D.L.; experiment, H.H., S.Ü., M.Č., Z.H. and D.L.; writing—original draft preparation, H.H., J.T.G. and D.L.; writing—review and editing, H.H., J.T.G., N.B., M.A.R., S.Ü., M.Č., Z.H., and D.L.; and funding acquisition, M.Č., Z.H., D.L. and J.T.G.

**Funding:** This work was partially supported by the University of Iceland Research Fund for Doctoral students, the Icelandic Research Fund Grant Nos. 130029 and 196141, the Czech Science Foundation through project 19-00579S and by Operational Programme Research, Development and Education financed by European Structural and Investment Funds and the Czech Ministry of Education, Youth and Sports (Project No. SOLID21 CZ.02.1.01/0.0/0.0/16\_019/0000760).

**Acknowledgments:** The authors acknowledge the support of Benjamin Sez nec at Université Paris-Sud, Orsay, for his work on interpolating the recorded magnetic field data to draw Figure 2. The authors also acknowledge stimulating discussion with Tiberiu M. Minea at Université Paris-Sud, Orsay

**Conflicts of Interest:** The authors declare no conflict of interest.

## References

- Helmersson, U.; Lattemann, M.; Bohlmark, J.; Ehiassarian, A.P.; Gudmundsson, J.T. Ionized physical vapor deposition (IPVD): A review of technology and applications. *Thin Solid Film.* **2006**, *513*, 1–24. [[CrossRef](#)]
- Gudmundsson, J.T.; Brenning, N.; Lundin, D.; Helmersson, U. The high power impulse magnetron sputtering discharge. *J. Vac. Sci. Technol. A* **2012**, *30*, 030801. [[CrossRef](#)]
- Kouznetsov, V.; Macák, K.; Schneider, J.M.; Helmersson, U.; Petrov, I. A novel pulsed magnetron sputter technique utilizing very high target power densities. *Surf. Coat. Technol.* **1999**, *122*, 290–293. [[CrossRef](#)]
- Kubart, T.; Čada, M.; Lundin, D.; Hubička, Z. Investigation of ionized metal flux fraction in HiPIMS discharges with Ti and Ni targets. *Surf. Coat. Technol.* **2014**, *238*, 152–157. [[CrossRef](#)]
- Lundin, D.; Čada, M.; Hubička, Z. Ionization of sputtered Ti, Al, and C coupled with plasma characterization in HiPIMS. *Plasma Sources Sci. Technol.* **2015**, *24*, 035018. [[CrossRef](#)]
- Lundin, D.; Sarakinos, K. An introduction to thin film processing using high power impulse magnetron sputtering. *J. Mater. Res.* **2012**, *27*, 780–792. [[CrossRef](#)]
- Anders, A. Deposition rates of high power impulse magnetron sputtering: Physics and economics. *J. Vac. Sci. Technol. A* **2010**, *28*, 783–790. [[CrossRef](#)]
- Samuelsson, M.; Lundin, D.; Jensen, J.; Raadu, M.A.; Gudmundsson, J.T.; Helmersson, U. On the film density using high power impulse magnetron sputtering. *Surf. Coat. Technol.* **2010**, *202*, 591–596. [[CrossRef](#)]
- Christie, D.J. Target material pathways model for high power pulsed magnetron sputtering. *J. Vac. Sci. Technol. A* **2005**, *23*, 330–335. [[CrossRef](#)]
- Bradley, J.W.; Thompson, S.; Gonzalvo, Y.A. Measurement of the plasma potential in a magnetron discharge and the prediction of the electron drift speeds. *Plasma Sources Sci. Technol.* **2001**, *10*, 490–501. [[CrossRef](#)]
- Rauch, A.; Mendelsberg, R.J.; Sanders, J.M.; Anders, A. Plasma potential mapping of high power impulse magnetron sputtering discharges. *J. Appl. Phys.* **2012**, *111*, 083302. [[CrossRef](#)]
- Sigurjónsson, P. Spatial and Temporal Variation of the Plasma Parameters in a High Power Impulse Magnetron Sputtering (HiPIMS) Discharge. Master's Thesis, University of Iceland, Reykjavik, Iceland, 2008.
- Mishra, A.; Kelly, P.J.; Bradley, J.W. The evolution of the plasma potential in a HiPIMS discharge and its relationship to deposition rate. *Plasma Sources Sci. Technol.* **2010**, *19*, 045014.

14. Liebig, B.; Bradley, J.W. Space charge, plasma potential and electric field distributions in HiPIMS discharges of varying configuration. *Plasma Sources Sci. Technol.* **2013**, *22*, 045020. [[CrossRef](#)]
15. Konstantinidis, S.; Dauchot, J.P.; Ganciu, M.; Hecq, M. Influence of pulse duration on the plasma characteristics in high-power pulsed magnetron discharges. *J. Appl. Phys.* **2006**, *99*, 013307. [[CrossRef](#)]
16. Velicu, I.L.; Tiron, V.; Popa, G. Dynamics of the fast-HiPIMS discharge during FINEMET-type film deposition. *Surf. Coat. Technol.* **2014**, *250*, 57–64. [[CrossRef](#)]
17. Ferrec, A.; Kéraudy, J.; Jouan, P.Y. Mass spectrometry analyzes to highlight differences between short and long HiPIMS discharges. *Appl. Surf. Sci.* **2016**, *390*, 497–505. [[CrossRef](#)]
18. Čapek, J.; Hála, M.; Zabeida, O.; Klemberg-Sapieha, J.E.; Martinu, L. Deposition rate enhancement in HiPIMS without compromising the ionized fraction of the deposition flux. *J. Phys. D Appl. Phys.* **2013**, *46*, 205205.
19. Bradley, J.W.; Mishra, A.; Kelly, P.J. The effect of changing the magnetic field strength on HiPIMS deposition rates. *J. Phys. D Appl. Phys.* **2015**, *48*, 215202. [[CrossRef](#)]
20. Yu, H.; Meng, L.; Szott, M.M.; Meister, J.T.; Cho, T.S.; Ruzic, D.N. Investigation and optimization of the magnetic field configuration in high-power impulse magnetron sputtering. *Plasma Sources Sci. Technol.* **2013**, *22*, 045012. [[CrossRef](#)]
21. Raman, P.; Shchelkanov, I.A.; McLain, J.; Ruzic, D.N. High power pulsed magnetron sputtering: A method to increase deposition rate. *J. Vac. Sci. Technol. A* **2015**, *33*, 031304. [[CrossRef](#)]
22. Raman, P.; Shchelkanov, I.; McLain, J.; Cheng, M.; Ruzic, D.; Haehlein, I.; Jurczyk, B.; Stubbers, R.; Armstrong, S. High Deposition Rate Symmetric Magnet Pack for High Power Pulsed Magnetron Sputtering. *Surf. Coat. Technol.* **2016**, *293*, 10–15. [[CrossRef](#)]
23. Ganesan, R.; Akhavan, B.; Dong, X.; McKenzie, D.R.; Bilek, M.M.M. External magnetic field increases both plasma generation and deposition rate in HiPIMS. *Surf. Coat. Technol.* **2018**, *352*, 671–679. [[CrossRef](#)]
24. Antonin, O.; Tiron, V.; Costin, C.; Popa, G.; Minea, T.M. On the HiPIMS benefits of multi-pulse operating mode. *J. Phys. D Appl. Phys.* **2015**, *48*, 015202. [[CrossRef](#)]
25. Barker, P.M.; Lewin, E.; Patscheider, J. Modified high power impulse magnetron sputtering process for increased deposition rate of titanium. *J. Vac. Sci. Technol. A* **2013**, *31*, 060604. [[CrossRef](#)]
26. Tesař, J.; Martan, J.; Rezek, J. On surface temperatures during high power pulsed magnetron sputtering using a hot target. *Surf. Coat. Technol.* **2011**, *206*, 1155–1159. [[CrossRef](#)]
27. Alami, J.; Maric, Z.; Busch, H.; Klein, F.; Grabowy, U.; Kopnarsk, M. Enhanced ionization sputtering: A concept for superior industrial coatings. *Surf. Coat. Technol.* **2014**, *255*, 43–51. [[CrossRef](#)]
28. Hajihoseini, H.; Gudmundsson, J.T. Vanadium and vanadium nitride thin films grown by high power impulse magnetron sputtering. *J. Phys. D Appl. Phys.* **2017**, *50*, 505302.
29. McLain, J.; Raman, P.; Patel, D.; Spreadbury, R.; Uhlig, J.; Shchelkanov, I.; Ruzic, D.N. Linear magnetron HiPIMS high deposition rate magnet pack. *Vacuum* **2018**, *155*, 559–565. [[CrossRef](#)]
30. Poolcharuansin, P.; Bowes, M.; Petty, T.J.; Bradley, J.W. Ionized metal flux fraction measurements in HiPIMS discharges. *J. Phys. D Appl. Phys.* **2012**, *45*, 322001. [[CrossRef](#)]
31. Raman, P.; Weberski, J.; Cheng, M.; Shchelkanov, I.; Ruzic, D.N. A high power impulse magnetron sputtering model to explain high deposition rate magnetic field configurations. *J. Appl. Phys.* **2016**, *120*, 163301. [[CrossRef](#)]
32. Vlček, J.; Burcalová, K. A phenomenological equilibrium model applicable to high-power pulsed magnetron sputtering. *Plasma Sources Sci. Technol.* **2010**, *19*, 065010.
33. Window, B.; Savvides, N. Charged particle fluxes from planar magnetron sputtering sources. *J. Vac. Sci. Technol. A* **1986**, *4*, 196–202. [[CrossRef](#)]
34. Wu, L.; Ko, E.; Dulkan, A.; Park, K.J.; Fields, S.; Leeser, K.; Meng, L.; Ruzic, D.N. Flux and energy analysis of species in hollow cathode magnetron ionized physical vapor deposition of copper. *Rev. Sci. Instrum.* **2010**, *81*, 123502. [[CrossRef](#)] [[PubMed](#)]
35. Green, K.M.; Hayden, D.B.; Juliano, D.R.; Ruzic, D.N. Determination of flux ionization fraction using a quartz crystal microbalance and a gridded energy analyzer in an ionized magnetron sputtering system. *Rev. Sci. Instrum.* **1997**, *68*, 4555–4560. [[CrossRef](#)]
36. Huo, C.; Lundin, D.; Gudmundsson, J.T.; Raadu, M.A.; Bradley, J.W.; Brenning, N. Particle-balance models for pulsed sputtering magnetrons. *J. Phys. D Appl. Phys.* **2017**, *50*, 354003. [[CrossRef](#)]
37. Butler, A.; Brenning, N.; Raadu, M.A.; Gudmundsson, J.T.; Minea, T.; Lundin, D. On three different ways to quantify the degree of ionization in sputtering magnetrons. *Plasma Sources Sci. Technol.* **2018**, *27*, 105005.

38. Huo, C.; Lundin, D.; Raadu, M.A.; Anders, A.; Gudmundsson, J.T.; Brenning, N. On sheath energization and Ohmic heating in sputtering magnetrons. *Plasma Sources Sci. Technol.* **2013**, *22*, 045005. [[CrossRef](#)]
39. Brenning, N.; Gudmundsson, J.T.; Lundin, D.; Minea, T.; Raadu, M.A.; Helmersson, U. The Role of Ohmic Heating in dc Magnetron Sputtering. *Plasma Sources Sci. Technol.* **2016**, *25*, 065024.
40. Thornton, J.A. Magnetron sputtering: Basic physics and application to cylindrical magnetrons. *J. Vac. Sci. Technol.* **1978**, *15*, 171–177. [[CrossRef](#)]
41. Brenning, N.; Gudmundsson, J.T.; Raadu, M.A.; Petty, T.J.; Minea, T.; Lundin, D. A unified treatment of self-sputtering, process gas recycling, and runaway for high power impulse sputtering magnetrons. *Plasma Sources Sci. Technol.* **2017**, *26*, 125003. [[CrossRef](#)]
42. Huo, C.; Lundin, D.; Raadu, M.A.; Anders, A.; Gudmundsson, J.T.; Brenning, N. On the road to self-sputtering in high power impulse magnetron sputtering: Particle balance and discharge characteristics. *Plasma Sources Sci. Technol.* **2014**, *23*, 025017. [[CrossRef](#)]
43. Bohlmark, J.; Lattemann, M.; Gudmundsson, J.T.; Ehasarian, A.P.; Gonzalvo, Y.A.; Brenning, N.; Helmersson, U. The ion energy distributions and ion flux composition from a high power impulse magnetron sputtering discharge. *Thin Solid Film.* **2006**, *515*, 1522–1526. [[CrossRef](#)]
44. Andersson, J.; Ehasarian, A.P.; Anders, A. Observation of  $Ti^{4+}$  ions in a high power impulse magnetron sputtering plasma. *Appl. Phys. Lett.* **2008**, *93*, 071504.



© 2019 by the authors. Licensee MDPI, Basel, Switzerland. This article is an open access article distributed under the terms and conditions of the Creative Commons Attribution (CC BY) license (<http://creativecommons.org/licenses/by/4.0/>).



## Paper IV

### **Oblique angle deposition of nickel thin films by high power impulse magnetron sputtering.**

H. Hajihoseini, M. Kateb, S. Ingvarsson and J. T. Gudmundsson. 2019.

*Beilstein Journal of Nanotechnology* **10**: 1914 – 1921.







# Oblique angle deposition of nickel thin films by high-power impulse magnetron sputtering

Hamidreza Hajihoseini<sup>\*1</sup>, Movaffaq Kateb<sup>1</sup>, Snorri Porgeir Ingvarsson<sup>1</sup>  
and Jon Tomas Gudmundsson<sup>1,2</sup>

## Full Research Paper

[Open Access](#)

### Address:

<sup>1</sup>Science Institute, University of Iceland, Dunhaga 3, IS-107 Reykjavik, Iceland and <sup>2</sup>Department of Space and Plasma Physics, School of Electrical Engineering and Computer Science, KTH Royal Institute of Technology, SE-100 44, Stockholm, Sweden

### Email:

Hamidreza Hajihoseini<sup>\*</sup> - hah107@hi.is

<sup>\*</sup> Corresponding author

### Keywords:

glancing angle deposition (GLAD); high-power impulse magnetron sputtering (HiPIMS); oblique angle deposition; magnetron sputtering; magnetic anisotropy; nickel

*Beilstein J. Nanotechnol.* **2019**, *10*, 1914–1921.

doi:10.3762/bjnano.10.186

Received: 15 June 2019

Accepted: 02 September 2019

Published: 20 September 2019

Associate Editor: E. Meyer

© 2019 Hajihoseini et al.; licensee Beilstein-Institut.  
License and terms: see end of document.

## Abstract

**Background:** Oblique angle deposition is known for yielding the growth of columnar grains that are tilted in the direction of the deposition flux. Using this technique combined with high-power impulse magnetron sputtering (HiPIMS) can induce unique properties in ferromagnetic thin films. Earlier we have explored the properties of polycrystalline and epitaxially deposited permalloy thin films deposited under 35° tilt using HiPIMS and compared it with films deposited by dc magnetron sputtering (dcMS). The films prepared by HiPIMS present lower anisotropy and coercivity fields than films deposited with dcMS. For the epitaxial films dcMS deposition gives biaxial anisotropy while HiPIMS deposition gives a well-defined uniaxial anisotropy.

**Results:** We report on the deposition of 50 nm polycrystalline nickel thin films by dcMS and HiPIMS while the tilt angle with respect to the substrate normal is varied from 0° to 70°. The HiPIMS-deposited films are always denser, with a smoother surface and are magnetically softer than the dcMS-deposited films under the same deposition conditions. The obliquely deposited HiPIMS films are significantly more uniform in terms of thickness. Cross-sectional SEM images reveal that the dcMS-deposited film under 70° tilt angle consists of well-defined inclined nanocolumnar grains while grains of HiPIMS-deposited films are smaller and less tilted. Both deposition methods result in in-plane isotropic magnetic behavior at small tilt angles while larger tilt angles result in uniaxial magnetic anisotropy. The transition tilt angle varies with deposition method and is measured around 35° for dcMS and 60° for HiPIMS.

**Conclusion:** Due to the high discharge current and high ionized flux fraction, the HiPIMS process can suppress the inclined columnar growth induced by oblique angle deposition. Thus, the ferromagnetic thin films obliquely deposited by HiPIMS deposi-

tion exhibit different magnetic properties than dcMS-deposited films. The results demonstrate the potential of the HiPIMS process to tailor the material properties for some important technological applications in addition to the ability to fill high aspect ratio trenches and coating on cutting tools with complex geometries.

## Introduction

The realization of electronics based on utilizing the electron spin degree of freedom, commonly referred to as spintronics, requires the integration of ferromagnetic films with semiconductors [1]. Nickel is a ferromagnetic heavy 3d transition metal that crystallizes in the fcc structure. Because of the negative magnetostriction property of pure nickel, it is used as a magnetic material for certain applications, including ones that utilize magnetostriction. Thin nickel films have also found a wide range of other applications such as decorative coatings [2,3], corrosion-resistant coatings [3,4], optically transparent conductive electrodes [5], contact devices [6], Li-storage materials [7], and as selective absorbers in solar thermal energy conversion [8]. Moreover, a number of nickel-containing alloys exploit the ferromagnetic properties of nickel such as NiTi-based shape memory alloy thin films utilized in micro-actuator applications [9]. It is well known that microstructure, texture and structure of thin films can have significant influence on the magnetic and other functional properties of the films. The magnetic properties of evaporated [10,11], electrodeposited [12–15], chemical-vapor-deposited [16], and dc [17–19] and rf [20–22] magnetron sputtered thin nickel films have been studied for almost ten decades. This has included studies of the magnetic properties while varying film thickness [10,20], grain size, substrate material [11,21] and substrate temperature [19], as well as while stacking into superlattices [23,24].

High-power impulse magnetron sputtering (HiPIMS), sometimes referred to as high-power pulsed magnetron sputtering (HPPMS), is a physical vapor deposition (PVD) technique based on pulsed power technology where the peak power exceeds the time-averaged power by roughly two orders of magnitude [25,26]. By pulsing the cathode target to high peak power density a high ionization fraction of the sputtered material is achieved, which results in a higher quality of the deposited films [27]. It is well known that ferromagnetic materials are difficult to sputter with conventional dc magnetron sputtering since a portion of the magnetic flux is shunted by the magnetic target, thus decreasing the electron confinement, which results in low plasma density and low deposition rate. On the other hand, it has been demonstrated that a small decrease in the magnetic field strength in the HiPIMS process can lead to a significant increase in the deposition rate in that case [28,29]. We have recently reported an increase by a factor of 2 and 2.6 of the HiPIMS deposition rate by 83% and 53% weakening of the magnetic field strength (at racetrack) using vanadium [30] and

titanium [31] targets, respectively. Thus, utilizing HiPIMS for the deposition of ferromagnetic material can be very beneficial.

Oblique deposition, sometimes referred to as glancing angle deposition (GLAD), is known as a PVD technique that leads to a film texture with low density and columnar grain growth that is elongated in the direction of the incoming flux [32]. As a result of this structure, some unique optical [33–35], electrical [36,37], mechanical [37,38] and magnetic [39] properties of thin films have been reported. By employing an ionized distribution flux (i.e., using HiPIMS in GLAD), the angular distribution of the deposited material can be influenced [40–42]. Earlier we have explored the microstructure and magnetic properties of polycrystalline [43] and epitaxially [44] deposited permalloy (Ni<sub>80</sub>Fe<sub>20</sub> atom %) thin films deposited under 35° tilt using dcMS and HiPIMS. The films prepared by HiPIMS present a lower anisotropy field ( $H_k$ ) and coercivity ( $H_c$ ) than films deposited with dcMS. For the polycrystalline films both deposition methods give uniaxial magnetic anisotropy due to the oblique deposition. However, for the epitaxial films dcMS deposition gives biaxial anisotropy while HiPIMS deposition gives a well-defined uniaxial anisotropy. The uniaxial anisotropy induced by the tilt angle was demonstrated in the early 1960s by Smith et al. [39] while depositing permalloy with thermal evaporation. They suggested that a shadow effect causes an in-plane texture perpendicular to the direction of the incoming flux, which corresponds to the easy axis of the film. However, more recently there are reports on a 90° rotation of the easy axis in a Co film deposited at 75° tilt angle [45].

In the present study we investigate the effect of angle of incidence on the structural and magnetic properties of Ni thin films deposited using dcMS and HiPIMS. We chose to work with pure Ni rather than NiFe alloys because it rejects many proposed explanations for uniaxial anisotropy based on alloying, i.e., directional ordering of Fe/Ni atom pairs [46], shape anisotropy of an elongated ordered phase [47], composition variation between grains [48] and, more recently suggested, localized composition non-uniformity [49]. Besides, we do not rotate the substrate during the deposition to simplify the conditions at the cost of losing film thickness uniformity.

## Experimental

The nickel thin films were deposited in a custom-built magnetron sputter chamber [50] with a base pressure of  $4 \times 10^{-6}$  Pa.

For the deposition process, 32 sccm of argon of 99.999% purity was injected into the chamber as the working gas. The working gas pressure was kept at 0.6 Pa using a butterfly valve located between the chamber and a turbomolecular pump. The nickel target was 75 mm in diameter, of 99.95% purity, and 1.59 mm thick but almost 40% eroded at the racetrack center. The magnetic field measured at the target surface over the racetrack shows the value of 39 and 0 mT parallel and perpendicular to the target surface, respectively.

For HiPIMS operation the power was supplied by a SPIK1000A pulse unit (Melec GmbH) operating in the unipolar negative mode at constant voltage, which in turn was fed by a dc power supply (ADL GS30). The discharge current and voltage were monitored using a combined current transformer and a voltage divider unit (Melec GmbH) and the data were recorded with a custom-made LabVIEW program. The pulse length was set at 200  $\mu$ s and the pulse repetition frequency was kept at 100 Hz throughout this study. For dcMS operation, a dc power supply (MDX 1 K, Advanced Energy) was connected to the magnetron. For all films, depositions were made at 150 W average power. This corresponds to a peak current density of  $J_{D,peak} = 0.77$  A/cm<sup>2</sup> for the HiPIMS deposition process when averaged over the entire target area. HiPIMS and dcMS oblique angle depositions were made at substrate tilt angles of 0° (substrate faces the target), 35° and 70° using both deposition methods. In addition, more depositions under 10° and 20° by dcMS and 50° and 60° using HiPIMS were made for better understanding of the magnetic properties of the films. The distance between target and substrate position was 25 cm. We used thermally oxidized Si(001) with an oxide thickness of 100 nm as substrates. However, for the scanning electron microscopy studies, Si(001) substrates with native oxide were used in order to eliminate the charging effect. All films were deposited at room temperature (25 °C) with a grounded substrate holder.

X-ray diffractometry (XRD) was carried out using a Philips X'pert diffractometer (Cu K $\alpha$ , wavelength 0.15406 nm) mounted with a hybrid monochromator/mirror on the incident side and a 0.27° collimator on the diffraction side. A line focus was used with a beam width of approximately 1 mm. The grazing incidence (GI)XRD scans were carried out with the incident beam at  $\theta = 1^\circ$ . Average thickness ( $d_{ave}$ ), average surface roughness and mass density of the films were determined by low-angle X-ray reflectivity (XRR) measurements with an angular resolution of 0.005°, and the data was fitted using the Parrat formalism [51]. A low-density surface layer (around 1 nm) on top of the film had to be included in the model in order to achieve a good fit. This is due to the formation of an oxide or oxynitride surface layer after the films were removed from the vacuum chamber, as has been previously observed and

discussed [52]. However, the reported mass density values are corresponding to the “bulk” part of the film.

The film thickness gradient ( $\Delta d$ ) was characterized by non-contact mode atomic force microscopy (AFM) analysis in an XE-100 multi-mode AFM system (PSIA Inc.) in air (ex situ). For this aim, the edges of the substrate were marked before deposition. After deposition, the samples were sonicated in an ethanol/isopropanol mixture to remove the marker and the nickel on top of it (lift-off process).

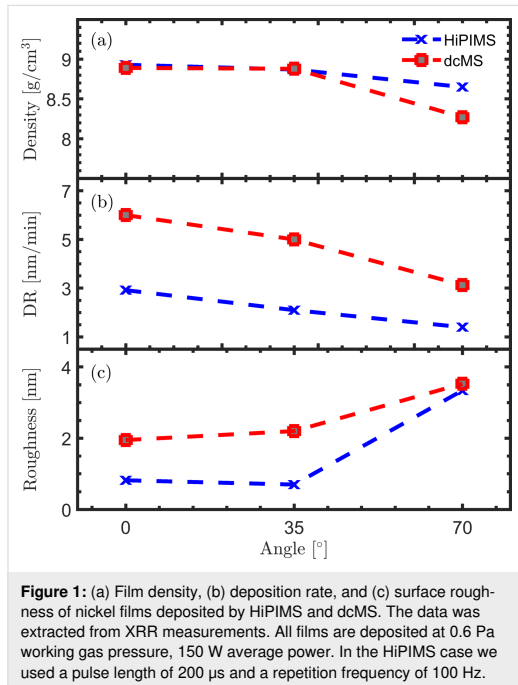
Cross sections of the Ni films were studied using a Leo Supra 25 scanning electron microscope. The acceleration voltage of the electron beam was set to 20 kV and the working distance was kept at 3.5 mm for all images presented here.

Magnetic hysteresis was characterized using a custom-made high-sensitivity magneto-optical Kerr effect (MOKE) looper using a laser source with 632.8 nm wavelength. Coercivity was read directly from the easy-axis loops. In our uniaxial samples the anisotropy field is obtained by extrapolating the linear low-field trace along the hard-axis direction to the saturation magnetization level, a method commonly used when dealing with effective easy-axis anisotropy. Vibrating sample magnetometry (VSM) was performed on  $10 \times 10$  mm<sup>2</sup> sized samples at 300 K. Variable magnetic fields up to  $\pm 1$  T were used for magnetic measurements.

## Results and Discussion

### Thin film structure

Figure 1 shows the film density, deposition rate and surface roughness of Ni films deposited by HiPIMS and dcMS at tilt angles of 0°, 35° and 70°. Both methods result in similar film densities at 0° and 35° (8.90 and 8.87 g/cm<sup>3</sup> respectively). The bulk density of nickel at room temperature is 8.902 g/cm<sup>3</sup>[3]. Increasing the tilt angle to 70° leads to a drop in density for both deposition methods. Data extracted from XRR shows density values of 8.6 g/cm<sup>3</sup> for the HiPIMS-deposited and 8.27 g/cm<sup>3</sup> for the dcMS-deposited film. We calculated the average deposition rate by dividing the average thickness by the deposition time, and it is shown in Figure 1b for each tilt angle. Deposition rates of 2.92, 2.10 and 1.41 nm/min were calculated for HiPIMS deposition at 0°, 35° and 70°, respectively. The dcMS deposition rate is roughly two times that of the HiPIMS rate for the same tilt angles. This is a somewhat lower deposition rate than has been reported for rf magnetron sputtering of Ni in the past [20,21], which might be due to rather long distance between target and substrate (25 cm) in this experiment. In terms of surface roughness, the HiPIMS-deposited film shows 0.8 nm roughness while the dcMS-deposited film shows 1.9 nm for normal deposition. The surface roughness remains



unchanged for deposition at 35°, for both methods. Increasing the tilt angle to 70° leads to a significant change in the surface roughness of the HiPIMS-deposited film (3.3 nm), which is slightly smoother than the dcMS-deposited film (3.5 nm). Note that due to the thickness gradient, fitting the XRR data for films deposited at higher tilt angles includes greater uncertainty. The measured and simulated XRR data are presented in Figure 2 for depositions under tilt angles of 0° and 70°.

To investigate the microstructure of our Ni films, GiXRD analysis was carried out. Figure 3 exhibits a GiXRD pattern of a dcMS-deposited Ni film in the conventional position facing the target. The peak at  $2\theta = 44.5^\circ$  is dominant in the GiXRD pattern. This peak has been assigned to fcc Ni(111). The peak at  $2\theta = 51.8^\circ$  is assigned to fcc Ni(200) and the peak at  $2\theta = 76.3^\circ$  to fcc Ni(220) [ICDD 00-004-0850]. Surprisingly, the method of deposition (HiPIMS and dcMS) and degree of tilt angle do not change the GiXRD pattern (relative peak intensities) of the deposited Ni films. The conventional XRD signal was weak due to the low film thickness (not shown).

Our thickness uniformity measurements show that obliquely deposited HiPIMS films are remarkably more uniform than dcMS-deposited films under the same tilt angle. Table 1 exhibits that depositing by HiPIMS results in 69% (at 35°) and 42% (at 70°) more uniform films than dcMS in terms of thickness.

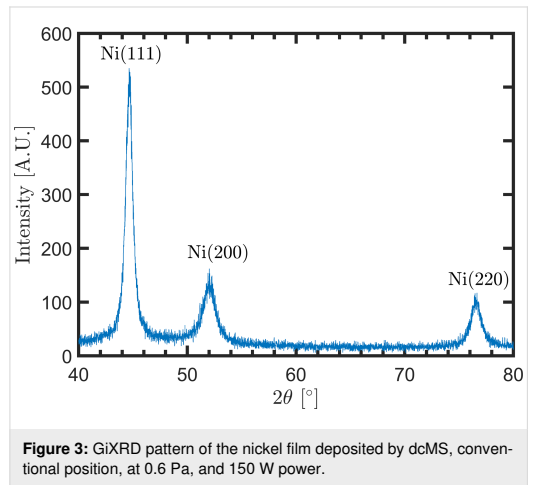
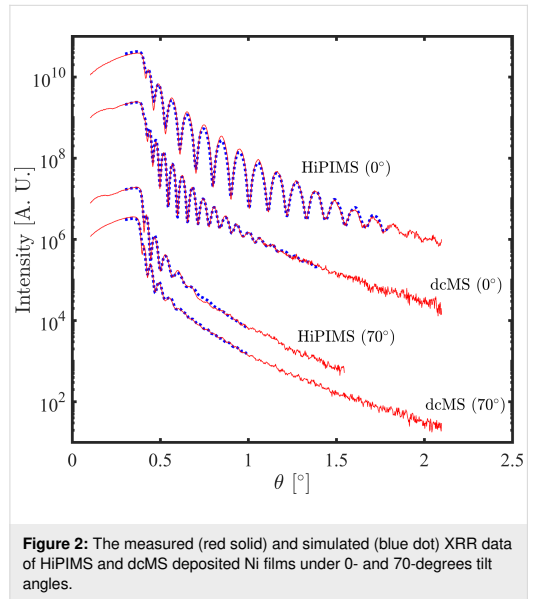


**Table 1:** Thickness uniformity of the nickel films deposited under various tilt angles and deposition methods.  $d_{ave}$  is the average film thickness measured by XRR.  $\Delta d$  is the thickness difference across the deposited film along the direction of the tilt angle.

method	tilt angle [°]	$d_{ave}$ [nm]	$\Delta d$ [nm]	$\Delta d/d_{ave}$ [%]
HiPIMS	35	52	2.6	5
dcMS	35	50	8	16
HiPIMS	70	43	6	14
dcMS	70	50	12	24

Our results agree with the recent findings of Keraudy et al. [53] that HiPIMS-deposited Ni films are denser, better crystallized and exhibit better uniformity than dcMS-deposited films, while the dcMS deposition rate is roughly twice the HiPIMS rate.

Figure 4 depicts cross-sectional SEM images of HiPIMS- and dcMS-deposited films under 70° substrate tilt angle. The dcMS-deposited film exhibits inclined columnar growth with the column length extending through the entire film thickness. In contrast, the HiPIMS-deposited film shows grains that are smaller than the film thickness. The columnar grains of the dcMS-deposited film are grown with 32° incline on the substrate while the HiPIMS film grains do not show a well-defined inclined growth, although some grains are elongated toward the incoming flux.

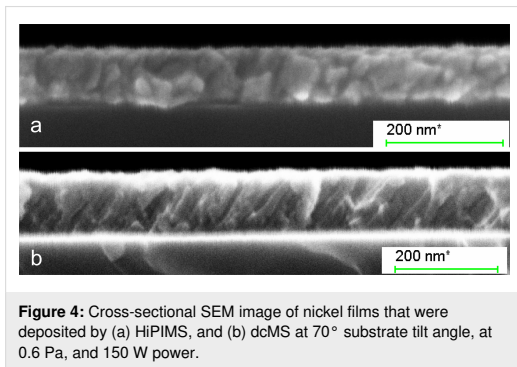


**Figure 4:** Cross-sectional SEM image of nickel films that were deposited by (a) HiPIMS, and (b) dcMS at 70° substrate tilt angle, at 0.6 Pa, and 150 W power.

The angle between columnar grains and substrate normal ( $\beta$ ) is different and generally smaller than the angle between the substrate normal and the target ( $\alpha$ ). Both experimental results [38] and simulations [54] agree on the relation

$$2 \tan \beta = \tan \alpha. \quad (1)$$

According to the Equation 1,  $\beta$  is expected to be around 54° for deposition under 70° tilt angle, while it was measured to be roughly 32° for dcMS-deposited film. This is probably because the abovementioned studies consider a small PVD target and low pressure (collision-free) conditions analogous with electron beam and thermal evaporation methods. However, at our working gas pressure the mean free path is around 11 mm which is remarkably shorter than target to substrate distance (250 mm). Besides, Elofsson et al. [55] show that the melting point of the deposited materials impacts the inclined growth of columns by affecting their surface diffusion. Thus, a variation in  $\beta$  is expected for depositing materials with different melting point.

The less tilted grains and the higher thickness uniformity of HiPIMS-deposited films can be explained by a different distribution angle of incoming flux to the substrate in those discharges. There have been a few investigations on this matter that all agree that the magnetic field plays a significant role in the profile of deposition. We have recently shown that, depending on the stationary magnetic field configuration, HiPIMS deposition may result in a more uniform film thickness than dcMS deposition [31]. Furthermore, Qiu et al. [56] showed that the target voltage, magnetic field strength and geometry can affect the shape of the racetrack and the target utilization. Indeed, in a HiPIMS discharge a wider current distribution on the target is expected due to the remarkably higher discharge current and cathode voltage [57]. In other words, the racetrack area could be wider during HiPIMS operation, which, in turn, can lead to a broader profile of sputtered material in terms of directionality. Furthermore, a potential difference of 1–5 V is expected between the plasma and the grounded substrate [58]. In the presence of highly ionized sputtered materials produced by HiPIMS discharge, this potential difference accelerates the ionized flux toward the substrate normal across the sheath and results in a better thickness uniformity as well as less inclined grain growth [58]. In addition, in the HiPIMS process, energetic ions are likely to have enough kinetic energy to induce some mobility of the film forming species on the film surface, which eliminates the columnar growth caused by the shadow effect. Greczynki et al. [42] and Elofsson et al. [55] have studied the HiPIMS growth of metal films on a tilted substrate as a function of peak discharge current density  $J_{D,peak}$ . They showed that for a higher  $J_{D,peak}$ , and thereby a larger degree of ionization of the sputtered material, a smaller tilt angle of the columnar microstructure is observed, i.e., the columns grow closer to the substrate normal. Thus, for a highly ionized flux fraction of the sputtered species the effects of the line-of-sight deposition are effectively eliminated and the film growth proceeds more or less unaffected by the substrate tilt. They have also experimentally rejected the role of deposition rate on the tilted growth of grains. Furthermore, Alami et al. [59] demonstrated that deposition using a peak current density  $J_{D,peak} = 1 \text{ A/cm}^2$  (close to our  $J_{D,peak} = 0.77 \text{ A/cm}^2$ ) results in film densification and suppression of the columnar structure, and columns start to grow on existing columns or repeated nucleation occurs. As the peak discharge current density was increased further to  $J_{D,peak} = 4 \text{ A/cm}^2$  they observed that a film with a featureless morphology developed.

Smaller grain sizes in HiPIMS-deposited films than in dcMS-deposited films have been previously reported [60,61]. They originate from the bombardment of the film surface by energetic ions during deposition, which constantly creates new sites

for growing new crystallites. This, in consequence, leads to smaller grain sizes [62,63].

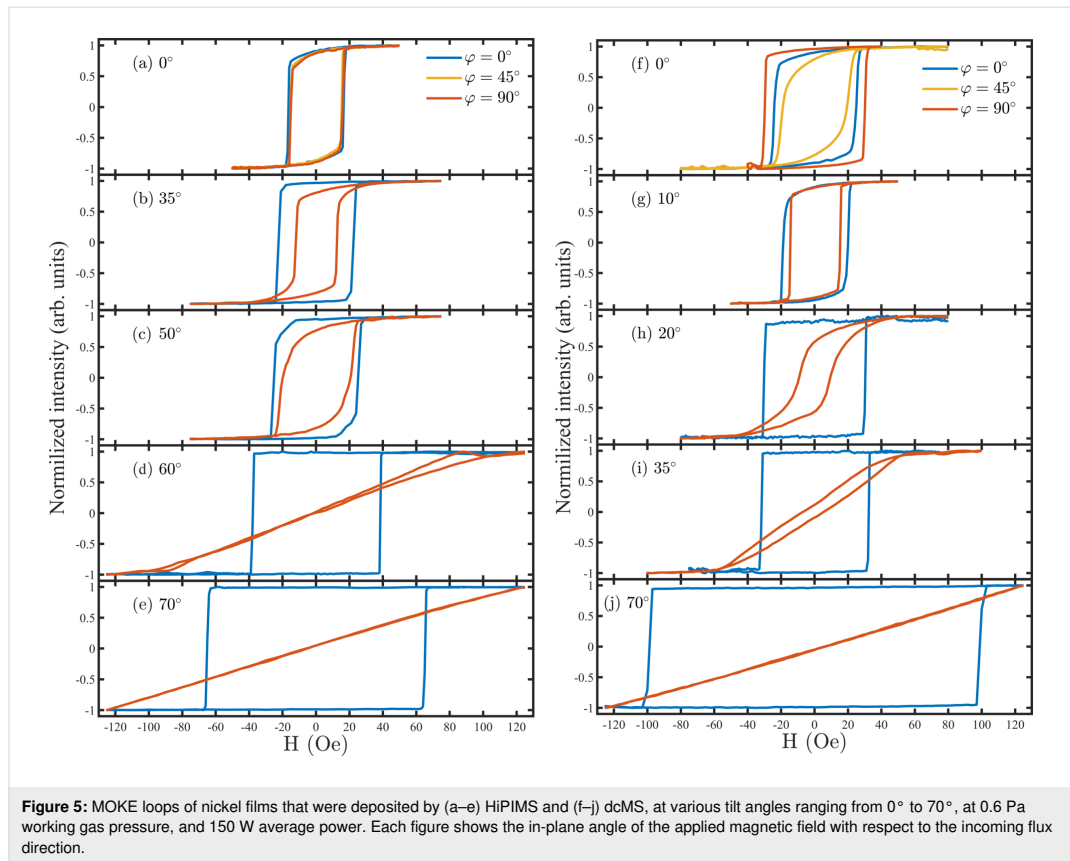
## Magnetic properties

We used MOKE to explore the magnetic properties of the nickel films. The results are shown in Figure 5 for HiPIMS and dcMS-deposited films. The films deposited by HiPIMS at 0, 35° and 50° tilt angles are more or less magnetically isotropic in-plane. However, the films deposited under 60° and 70° present uniaxial behavior, i.e., a linear hard axis along the angle of incoming sputtered flux and a square easy axis perpendicular to that in the plane. The films deposited by dcMS at tilt angles of 0°, 10° and 20° also show more or less isotropic behavior. Further increasing the tilt angle leads to a uniaxial anisotropy in dcMS-deposited films at tilt angles of 35° (Figure 5i) and 70° (Figure 5e).

Thus, for both deposition methods there is an intermediate tilt angle (ca. 50° for HiPIMS and ca. 20° for dcMS) at which the films present hysteresis loops with different values of  $H_c$  when

magnetic field is applied parallel and perpendicular to the incoming flux direction. To determine the window in which a transition occurs from isotropic to uniaxial anisotropy is important for practical purposes. For instance, in the films deposited at these intermediate tilt angles the  $H_c$  value of the loops is different and the loop exhibiting lower  $H_c$  values is more rounded. The latter loop is perpendicular to the angle of incidence and it becomes a hard axis at larger tilt angles.

The coercivity and anisotropy fields of our Ni films are plotted as a function of the tilt angle in Figure 6. It is worth mentioning that regardless of the type of anisotropy, along the easy direction of magnetization,  $H_c$  of the HiPIMS-deposited films increases with increasing tilt angle. This is also true for  $H_k$  for the samples with uniaxial anisotropy. In contrast to the HiPIMS results, dcMS-deposited films present similar  $H_c$  values with increasing tilt angle up to 35° and show an increase with further increase in tilt angle. For deposition at 70° tilt angle, the anisotropy field of both dcMS- and HiPIMS-deposited samples were higher than the measurement range in our MOKE setup.



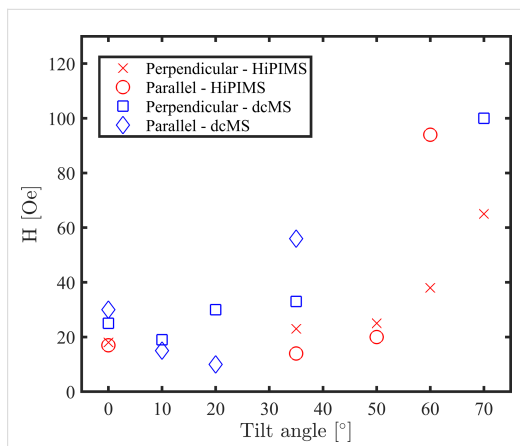


**Figure 6:** The  $H_c$  and  $H_k$  (for samples with uniaxial anisotropy) of our nickel films measured using MOKE with the magnetic field applied parallel and perpendicular to the sputtered flux direction, respectively. Uniaxial anisotropy is presented in HiPIMS samples of 60° and 70°, and in dcMS of 35° and 70°. The  $H_k$  of films deposited at 70° was out of the measurement range.

Interestingly, HiPIMS-deposited Ni films are magnetically softer than dcMS-deposited films at the same tilt angle. We believe that the smaller grain size of HiPIMS-deposited films (shown in Figure 4) is the main reason for soft magnetism of the films. Poolcharuansin et al. [64] have shown that Ni thin film deposition using an inverted gapped-target sputter magnetron results in smaller grain size and consequently magnetically softer films than dcMS-deposited films.

To summarize, transition from isotropic to uniaxial anisotropy occurs above 50° tilt angle for HiPIMS deposition while it is around 35° in dcMS. It is probably due to less inclined columnar growth in HiPIMS-deposited films as is shown in Figure 4. We have studied the in-plane magnetic properties of deposited films using VSM and the results are in agreement with the MOKE study (not shown here).

## Acknowledgements

The authors would like to thank Dr. Fridrik Magnus for his helpful advice on interpretation of MOKE results. This work was partially supported by the University of Iceland Research Fund for Doctoral students, the Icelandic Research Fund Grant Nos. 130029 and 196141.

## ORCID® iDs

Hamidreza Hajihoseini - <https://orcid.org/0000-0002-2494-6584>

Movaffaq Kateb - <https://orcid.org/0000-0002-2518-3988>

Snorri Þorgeir Ingvarsson - <https://orcid.org/0000-0001-8397-8917>

Jon Tomas Gudmundsson - <https://orcid.org/0000-0002-8153-3209>

## References

- Wolf, S. A.; Awschalom, D. D.; Buhrman, R. A.; Daughton, J. M.; von Molnár, S.; Roukes, M. L.; Chtchelkanova, A. Y.; Treger, D. M. *Science* **2001**, *294*, 1488–1495. doi:10.1126/science.1065389
- Dennis, J. K.; Such, T. E. *Nickel and Chromium Plating*, 3rd ed.; Woodhead Publishing: Cambridge, United Kingdom, 1993.
- Davis, J. R. *ASM Specialty Handbook : Nickel, Cobalt, and their Alloys*; ASM International: Materials Park, Ohio, U.S.A., 2000.
- Ahmad, Z. *Principles of Corrosion Engineering and Corrosion Control*; Butterworth-Heinemann: Boston, MA, U.S.A., 2006. doi:10.1016/b978-0-7506-5924-6.x5000-4
- Martínez, L.; Ghosh, D. S.; Giurgola, S.; Vergani, P.; Pruneri, V. *Opt. Mater.* **2009**, *31*, 1115–1117. doi:10.1016/j.optmat.2008.11.019
- Tam, P. L.; Nyborg, L. *Surf. Coat. Technol.* **2009**, *203*, 2886–2890. doi:10.1016/j.surfcoat.2009.03.001
- Zhang, H.; Zhou, Y.-N.; Sun, Q.; Fu, Z.-W. *Solid State Sci.* **2008**, *10*, 1166–1172. doi:10.1016/j.solidstatesciences.2007.12.019
- Lizama-Tzec, F. I.; Macías, J. D.; Estrella-Gutiérrez, M. A.; Cahue-López, A. C.; Arés, O.; de Coss, R.; Alvarado-Gil, J. J.; Oskam, G. J. *Mater. Sci.: Mater. Electron.* **2015**, *26*, 5553–5561. doi:10.1007/s10854-014-2195-5
- Ho, K. K.; Carman, G. P. *Thin Solid Films* **2000**, *370*, 18–29. doi:10.1016/s0040-6090(00)00947-0
- Edwards, R. L. *Phys. Rev.* **1927**, *29*, 321–331. doi:10.1103/physrev.29.321
- Kumar, P.; Ghanashyam Krishna, M.; Bhattacharya, A. K. *Bull. Mater. Sci.* **2009**, *32*, 263–270. doi:10.1007/s12034-009-0040-x
- Ruske, W. *Ann. Phys. (Berlin, Ger.)* **1958**, *457*, 274–286. doi:10.1002/andp.19584570506
- Fisher, J. E. *Thin Solid Films* **1970**, *5*, R39–R40. doi:10.1016/0040-6090(70)90097-0
- Gubbiotti, G.; Carlotti, G.; Tacchi, S.; Liu, Y.-K.; Scheck, C.; Schad, R.; Zangari, G. J. *Appl. Phys.* **2005**, *97*, 10J102. doi:10.1063/1.1846031
- Tang, Y.; Zhao, D.; Shen, D.; Zhang, J.; Li, B.; Lu, Y.; Fan, X. *Thin Solid Films* **2008**, *516*, 2094–2098. doi:10.1016/j.tsf.2007.11.095
- Maruyama, T.; Tago, T. *J. Mater. Sci.* **1993**, *28*, 5345–5348. doi:10.1007/bf00570088
- Yi, J. B.; Zhou, Y. Z.; Ding, J.; Chow, G. M.; Dong, Z. L.; White, T.; Gao, X.; Wee, A. T. S.; Yu, X. J. *J. Magn. Magn. Mater.* **2004**, *284*, 303–311. doi:10.1016/j.jmmm.2004.06.052
- Song, X.-H.; Zhang, D.-L. *Chin. Phys. B* **2008**, *17*, 3495–3498. doi:10.1088/1674-1056/17/9/059
- Sharma, A.; Mohan, S.; Suwas, S. *Thin Solid Films* **2016**, *619*, 91–101. doi:10.1016/j.tsf.2016.10.024
- Miller, M. S.; Stageberg, F. E.; Chow, Y. M.; Rook, K.; Heuer, L. A. *J. Appl. Phys.* **1994**, *75*, 5779–5781. doi:10.1063/1.355560
- Poulopoulos, P.; Vlachos, A.; Grammatikopoulos, S.; Karoutsos, V.; Ioannou, P. S.; Bebelos, N.; Trachylis, D.; Velgakis, M. J.; Meletis, E. I.; Politis, C. J. *Nano Res.* **2015**, *30*, 68–77. doi:10.4028/www.scientific.net/jnanor.30.68
- Muslim, N.; Soon, Y. W.; Lim, C. M.; Voo, N. Y. *Thin Solid Films* **2016**, *612*, 82–86. doi:10.1016/j.tsf.2016.05.049
- Chang, C.-A. *J. Appl. Phys.* **1990**, *68*, 4873–4875. doi:10.1063/1.346127
- Liu, X.; Berger, A.; Wuttig, M. *Phys. Rev. B* **2001**, *63*, 144407. doi:10.1103/physrevb.63.144407
- Gudmundsson, J. T.; Brenning, N.; Lundin, D.; Helmersson, U. *J. Vac. Sci. Technol., A* **2012**, *30*, 030801. doi:10.1116/1.3691832
- Lundin, D.; Sarakinos, K. J. *Mater. Res.* **2012**, *27*, 780–792. doi:10.1557/jmr.2012.8

27. Samuelsson, M.; Lundin, D.; Jensen, J.; Raadu, M. A.; Gudmundsson, J. T.; Helmersson, U. *Surf. Coat. Technol.* **2010**, *205*, 591–596. doi:10.1016/j.surfcoat.2010.07.041
28. Mishra, A.; Kelly, P. J.; Bradley, J. W. *Plasma Sources Sci. Technol.* **2010**, *19*, 045014. doi:10.1088/0963-0252/19/4/045014
29. Čapek, J.; Hála, M.; Zabeida, O.; Klemberg-Sapieha, J. E.; Martinu, L. *J. Phys. D: Appl. Phys.* **2013**, *46*, 205205. doi:10.1088/0022-3727/46/20/205205
30. Hajihoseini, H.; Gudmundsson, J. T. *J. Phys. D: Appl. Phys.* **2017**, *50*, 505302. doi:10.1088/1361-6463/aa96f2
31. Hajihoseini, H.; Čada, M.; Hubička, Z.; Ůnaldi, S.; Raadu, M. A.; Brenning, N.; Gudmundsson, J. T.; Lundin, D. *Plasma* **2019**, *2*, 201–221. doi:10.3390/plasma2020015
32. Hawkeye, M. M.; Brett, M. J. *J. Vac. Sci. Technol., A* **2007**, *25*, 1317–1335. doi:10.1116/1.2764082
33. Robbie, K.; Brett, M. J.; Lakhtakia, A. *Nature* **1996**, *384*, 616. doi:10.1038/384616a0
34. Summers, M. A.; Tabunshchik, K.; Kovalenko, A.; Brett, M. J. *Photonics Nanostruct. - Fundam. Appl.* **2009**, *7*, 76–84. doi:10.1016/j.photonics.2008.12.001
35. Hwangbo, C. K.; Park, Y. J.; Sobahan, K. M. A.; Kim, J. J. *J. Korean Phys. Soc.* **2009**, *55*, 2634–2637. doi:10.3938/jkps.55.2634
36. Kuwahara, K.; Hirota, H. *Jpn. J. Appl. Phys.* **1974**, *13*, 1093–1095. doi:10.1143/jjap.13.1093
37. Martin, N.; Robbie, K.; Carpentier, L. Architecture of Thin Solid Films by the GLAD Technique. In *Nanomaterials and Surface Engineering*; Takadom, J., Ed.; John Wiley & Sons: Hoboken, NJ, U.S.A., 2013; pp 1–30. doi:10.1002/9781118618523.ch1
38. Nieuwenhuizen, J. M.; Haanstra, H. B. *Philips Tech. Rev.* **1966**, *27*, 87–91.
39. Smith, D. O.; Cohen, M. S.; Weiss, G. P. *J. Appl. Phys.* **1960**, *31*, 1755–1762. doi:10.1063/1.1735441
40. Rossmagel, S. M. *J. Vac. Sci. Technol., B: Microelectron. Nanometer Struct.–Process., Meas., Phenom.* **1998**, *16*, 2585. doi:10.1116/1.590242
41. Klawuhn, E.; D' Couto, G. C.; Ashtiani, K. A.; Rymer, P.; Biberger, M. A.; Levy, K. B. *J. Vac. Sci. Technol., A* **2000**, *18*, 1546–1549. doi:10.1116/1.582382
42. Greczynski, G.; Jensen, J.; Hultman, L. *Thin Solid Films* **2011**, *519*, 6354–6361. doi:10.1016/j.tsf.2011.04.031
43. Kateb, M.; Hajihoseini, H.; Gudmundsson, J. T.; Ingvarsson, S. *J. Phys. D: Appl. Phys.* **2018**, *51*, 285005. doi:10.1088/1361-6463/aaaca11
44. Kateb, M.; Gudmundsson, J. T.; Ingvarsson, S. *AIP Adv.* **2019**, *9*, 035308. doi:10.1063/1.5088602
45. Umlor, M. T. *Appl. Phys. Lett.* **2005**, *87*, 082505. doi:10.1063/1.2032592
46. Chikazumi, S. *J. Phys. Soc. Jpn.* **1950**, *5*, 327–333. doi:10.1143/jpsj.5.327
47. Kaya, S. *Rev. Mod. Phys.* **1953**, *25*, 49–53. doi:10.1103/revmodphys.25.49
48. Kench, J. R.; Schuldt, S. B. *J. Appl. Phys.* **1970**, *41*, 3338–3346. doi:10.1063/1.1659422
49. Rodrigues, D. C. M.; Klautau, A. B.; Edström, A.; Rusz, J.; Nordström, L.; Pereiro, M.; Hjörvarsson, B.; Eriksson, O. *Phys. Rev. B* **2018**, *97*, 224402. doi:10.1103/physrevb.97.224402
50. Arnalds, U. B.; Agustsson, J. S.; Ingason, A. S.; Eriksson, A. K.; Gylfason, K. B.; Gudmundsson, J. T.; Olafsson, S. *Rev. Sci. Instrum.* **2007**, *78*, 103901. doi:10.1063/1.2793508
51. Parratt, L. G. *Phys. Rev.* **1954**, *95*, 359–369. doi:10.1103/physrev.95.359
52. Ingason, A. S.; Magnus, F.; Agustsson, J. S.; Olafsson, S.; Gudmundsson, J. T. *Thin Solid Films* **2009**, *517*, 6731–6736. doi:10.1016/j.tsf.2009.05.028
53. Keraudy, J.; Nguyen, D. T.; Ferrec, A.; Jouan, P.-Y. Comparison Between DC and HiPIMS Discharges. Application to Nickel Thin Films. In *International Conference on Engineering Research and Applications (ICERA 2018): Advances in Engineering Research and Application*, Fujita, H.; Nguyen, D. C.; Vu, N. P.; Banh, T. L.; Puta, H. H., Eds.; Springer-Verlag: Cham, Switzerland, 2019; pp 196–203.
54. Dirks, A. G.; Leamy, H. J. *Thin Solid Films* **1977**, *47*, 219–233. doi:10.1016/0040-6090(77)90037-2
55. Elofsson, V.; Magnfält, D.; Samuelsson, M.; Sarakinos, K. *J. Appl. Phys.* **2013**, *113*, 174906. doi:10.1063/1.4804066
56. Qiu, Q.; Li, Q.; Su, J.; Jiao, Y.; Finley, J. *IEEE Trans. Plasma Sci.* **2008**, *36*, 1899–1906. doi:10.1109/tps.2008.927379
57. Wendt, A. E.; Lieberman, M. A. *J. Vac. Sci. Technol., A* **1990**, *8*, 902–907. doi:10.1116/1.576894
58. Alami, J.; Petersson, P. O. A.; Music, D.; Gudmundsson, J. T.; Bohlmark, J.; Helmersson, U. *J. Vac. Sci. Technol., A* **2005**, *23*, 278–280. doi:10.1116/1.1861049
59. Alami, J.; Bolz, S.; Sarakinos, K. *J. Alloys Compd.* **2009**, *483*, 530–534. doi:10.1016/j.jallcom.2008.08.104
60. Velicu, I.-L.; Tiron, V.; Porosnicu, C.; Burducea, I.; Lupu, N.; Stoian, G.; Popa, G.; Munteanu, D. *Appl. Surf. Sci.* **2017**, *424*, 397–406. doi:10.1016/j.apsusc.2017.01.067
61. Lewin, E.; Loch, D.; Montagne, A.; Ehasarian, A. P.; Patscheider, J. *Surf. Coat. Technol.* **2013**, *232*, 680–689. doi:10.1016/j.surfcoat.2013.06.076
62. Ehasarian, A. P.; Hovsepian, P. E.; Hultman, L.; Helmersson, U. *Thin Solid Films* **2004**, *457*, 270–277. doi:10.1016/j.tsf.2003.11.113
63. Alami, J.; Sarakinos, K.; Uslu, F.; Wuttig, M. *J. Phys. D: Appl. Phys.* **2009**, *42*, 015304. doi:10.1088/0022-3727/42/1/015304
64. Poolcharuansin, P.; Laokul, P.; Pasaja, N.; Chingsungnoen, A.; Horprathum, M.; Chindaudom, P.; Bradley, J. W. *Vacuum* **2017**, *141*, 41–48. doi:10.1016/j.vacuum.2017.03.008

## License and Terms

This is an Open Access article under the terms of the Creative Commons Attribution License (<http://creativecommons.org/licenses/by/4.0>). Please note that the reuse, redistribution and reproduction in particular requires that the authors and source are credited.

The license is subject to the *Beilstein Journal of Nanotechnology* terms and conditions: (<https://www.beilstein-journals.org/bjnano>)

The definitive version of this article is the electronic one which can be found at:  
doi:10.3762/bjnano.10.186



## Paper V

### **Sideways deposition rate and ionized flux fraction in dc and high power impulse magnetron sputtering.**

H. Hajihoseini, M. Čada, Z. Hubička, S.Ünaldi, N. Brenning, M. A. Raadu, J. T. Gudmundsson and D. Lundin. 2019.

*Journal of Vacuum Science and Technology A* **38**: 033009.

Copyright © by the Journal of Vacuum Science and Technology A. All rights reserved.  
Permission for reproduction in this thesis granted by the copyright owner.



# Sideways deposition rate and ionized flux fraction in dc and high power impulse magnetron sputtering

Cite as: J. Vac. Sci. Technol. A 38, 033009 (2020); doi: 10.1116/1.5145292

Submitted: 16 January 2020 · Accepted: 24 March 2020 ·

Published Online: 17 April 2020



Hamidreza Hajihoseini,<sup>1,2,a</sup> Martin Čada,<sup>3</sup> Zdenek Hubička,<sup>3</sup> Selen Ünalı,<sup>2</sup> Michael A. Raadu,<sup>4</sup> Niils Brenning,<sup>4,5</sup> Jon Tomas Gudmundsson,<sup>1,4</sup> and Daniel Lundin<sup>2,5</sup>

## AFFILIATIONS

<sup>1</sup>Science Institute, University of Iceland, Dunhaga 3, IS-107 Reykjavik, Iceland

<sup>2</sup>Laboratoire de Physique des Gaz et Plasmas—LPGP, UMR 8578 CNRS, Université Paris-Sud, Université Paris Saclay, 91405 Orsay CEDEX, France

<sup>3</sup>Institute of Physics v. v. i., Academy of Sciences of the Czech Republic, Na Slovance 2, 182 21 Prague 8, Czech Republic

<sup>4</sup>Department of Space and Plasma Physics, School of Electrical Engineering and Computer Science, KTH Royal Institute of Technology, SE-100 44 Stockholm, Sweden

<sup>5</sup>Plasma and Coatings Physics Division, IFM-Materials Physics, Linköping University, SE-581 83 Linköping, Sweden

**Note:** This paper is part of the 2020 Special Topic Collection Festschrift Honoring Dr. Steve Rossnagel.

<sup>a</sup>Electronic mail: hah107@hi.is

## ABSTRACT

The sideways (radial) deposition rate and ionized flux fraction in a high power impulse magnetron sputtering (HiPIMS) discharge are studied and compared to a dc magnetron sputtering (dcMS) discharge, while the magnetic field strength  $|B|$  and degree of balancing are varied. A significant deposition of the film forming material perpendicular to the target surface is observed for both sputter techniques. This sideways deposition decreases with increasing axial distance from the target surface. The sideways deposition rate is always the highest in dc operation, while it is lower for HiPIMS operation. The magnetic field strength has a strong influence on the sideways deposition rate in HiPIMS but not in dcMS. Furthermore, in HiPIMS operation, the radial ion deposition rate is always at least as large as the axial ion deposition rate and often around two times higher. Thus, there are a significantly higher number of ions traveling radially in the HiPIMS discharge. A comparison of the total radial as well as axial fluxes across the entire investigated plasma volume between the target and the substrate position allows for revised estimates of radial over axial flux fractions for different magnetic field configurations. It is here found that the relative radial flux of the film forming material is greater in dcMS compared to HiPIMS for almost all cases investigated. It is therefore concluded that the commonly reported reduction of the (axial) deposition rate in HiPIMS compared to dcMS does not seem to be linked with an increase in sideways material transport in HiPIMS.

Published under license by AVS. <https://doi.org/10.1116/1.5145292>

## I. INTRODUCTION

Ion irradiation is a key tool for controlling the microstructure, phase content, and physical properties of thin films deposited at low substrate temperatures by magnetron sputtering. By ionizing the sputtered atoms of the film forming material, the ion energy at the substrate can be controlled by applying a substrate bias, and collimation of these ions with the plasma sheath adjacent to the substrate surface is made possible. Initially, the ionization of the sputtered material was based on placing a secondary discharge between the source (the cathode target) and the substrate in an

otherwise dc magnetron sputtering (dcMS) tool. The secondary discharge creates a dense plasma that has the role of ionizing a large fraction of the sputtered atoms to create a highly ionized flux of the film forming material.<sup>1–3</sup> More recently, this has been achieved by applying a high power unipolar pulse of low frequency and a low duty cycle to the cathode target. High power impulse magnetron sputtering (HiPIMS) provides a highly ionized flux of the sputtered material, while being compatible with existing magnetron sputtering deposition systems.<sup>4</sup> For HiPIMS operation, pulsed power with power density in the range of several kW/cm<sup>2</sup> is applied

to the cathode target.<sup>5</sup> This leads to a high plasma density of up to  $10^{19} \text{ m}^{-3}$  in the cathode target vicinity, which is up to 3 orders of magnitude higher than in a typical dcMS discharge.<sup>5</sup> The high plasma density results in a significant ionization of the sputtered neutrals, where ionized flux fractions  $F_{\text{flux}}$  well above 50% have been reported.<sup>6–8</sup> The benefits of a highly ionized flux fraction of the sputtered material include denser films,<sup>9</sup> lower surface roughness,<sup>10–12</sup> and improved crystallinity.<sup>13</sup> However, a highly ionized flux of the sputtered material commonly comes at a cost of a lower deposition rate, which has thus far prohibited extensive use of HiPIMS in manufacturing.<sup>4,14,15</sup> In fact, in a parallel study, we demonstrated how a highly ionized flux fraction of the sputtered target material can be traded for a high deposition rate.<sup>16</sup>

The deposition rate in (mainly nonreactive) HiPIMS is commonly found to be lower than that obtained with dcMS, generally in the range of 30%–85% of the dcMS rates, depending on the target material, when operating at the same average power.<sup>9</sup> Back-attraction of metal ions to the target is probably the main cause for the low deposition rate, as suggested by Christie.<sup>17</sup> The back-attraction probability of the ions of the sputtered material is quantified by a parameter referred to as the back-attraction probability  $\beta_t$ . The atoms sputtered off the target and ionized in the cathode vicinity are likely to be back-attracted to the cathode target due to strong electric fields in the presheath and extended presheath.<sup>18,19</sup> Some other mechanisms have also been suggested to contribute to the low deposition rate such as a nonlinear sputter yield effect,<sup>20</sup> guiding effect of the magnetic ( $\mathbf{B}$ ) field,<sup>21</sup> the increased density of the deposited film,<sup>15</sup> sputtering of the substrate (the ion energy can be high), in particular, when negatively biased,<sup>15</sup> and the effect of different ion species on the sputter yield.<sup>15</sup> Furthermore, it has been demonstrated that the presence of spokes has a strong influence on the transport of species toward the substrate.<sup>22,23</sup> However, de los Arcos *et al.*<sup>24</sup> reported a lower ratio of (deposition rate)/power when operating in the spoke-dominated regime than in the dc-like and homogeneous HiPIMS discharge regimes.

It has also been claimed that a significant fraction of the ions of the sputtered material are being transported radially outward in the vicinity of the cathode, across the magnetic field lines, leading to increased deposition rates at the side of the cathode (parallel to the target surface).<sup>21,23</sup> As a consequence, the fraction of the sputtered material reaching a substrate placed in front of the target (facing the target) would be substantially lower in the HiPIMS discharge compared to a dcMS discharge. This was demonstrated by Bohlmark *et al.*,<sup>21</sup> who significantly decreased the sideways deposition rate and increased the axial deposition rate by superimposing an external magnetic field in front of the target while depositing Al in a HiPIMS discharge. Lundin *et al.*<sup>23</sup> found the average radial deposition rates in HiPIMS to be 10% and 25% higher for Ti and Cr, respectively, compared to dcMS. They demonstrated, with time-averaged mass spectrometry measurements of the ion energy distribution of the radially (cross-field) transported ions, a direction-dependent high-energy tail, in agreement with predictions of the anomalous transport mechanism.<sup>23</sup> Similarly, in a previous work, Čada *et al.*<sup>25</sup> revealed inhomogeneous ion fluxes in different directions during HiPIMS operation, in particular, for a reactive atmosphere.

Further evidence for tangential ion ejection in the  $+\mathbf{E} \times \mathbf{B}$  drift direction came from Poolcharuansin *et al.*,<sup>26</sup> using a retarding field analyzer, and Panjan *et al.*,<sup>27</sup> using collector probes, particle energy analyzer, and mass spectrometer. Both of these studies reveal a strong asymmetry in the distribution of electrons and ions and their properties in the plane of the cathode target. Poolcharuansin *et al.*<sup>26</sup> demonstrated that the mean velocity and mean energy of the ions are distributed asymmetrically so that a higher flux of energetic ions escapes the ionization region in the electron  $+\mathbf{E} \times \mathbf{B}$  drift direction. Similar findings were reported by Franz *et al.*<sup>28</sup> who observe asymmetry in the ion flux distribution, higher ion flux in the  $+\mathbf{E} \times \mathbf{B}$  direction compared to the  $-\mathbf{E} \times \mathbf{B}$  direction, as well as pronounced asymmetry in the ion fraction when recorded as a function of the emission angle. Lundin *et al.*<sup>23</sup> claim that the tangential acceleration is the result of a net force that develops between the fast electrons and the slower ions in a cross- $\mathbf{B}$ -field, a process named modified two-stream instability. Poolcharuansin *et al.*<sup>26</sup> extended this analysis and added a centripetal force and a drag force in the equation for ion motion. They present a numerical solution of the equation of ion motion and show that a small fraction of the circulating ion flux, those ions that do not experience collisions, can overcome the radial electric field and leave the discharge volume in the tangential direction.

The magnitude and shape of the magnetic field in the target vicinity are known to have a major influence on the deposition rate in the HiPIMS discharge. There have been a few reports on modifying the magnetic field in order to increase the deposition rate,<sup>29–32</sup> and a significant increase in the deposition rate has been obtained by lowering the confining magnetic field strength.<sup>11,29–31</sup> In an earlier study, we explored the effect of magnetic field strength  $|\mathbf{B}|$  and geometry (degree of balancing) on the deposition rate and ionized flux fraction  $F_{\text{flux}}$  in dcMS and HiPIMS when depositing titanium on a substrate that faces the target.<sup>33</sup> We observed that the dcMS deposition rate was only weakly sensitive ( $\pm 10\%$ ) to variations in the magnetic field strength, while the deposition rate during HiPIMS, operated in a fixed voltage mode, increased roughly 110%, changing from 30% to 90% of the dcMS deposition rate, as  $|\mathbf{B}|$  was decreased. In the same HiPIMS mode,  $F_{\text{flux}}$  decreased with decreasing  $|\mathbf{B}|$  and was about 75% lower for the lowest  $|\mathbf{B}|$ . However, when operating in the fixed peak current mode, the deposition rate instead increased by about 40% with decreasing  $|\mathbf{B}|$ . Here, also,  $F_{\text{flux}}$  increased (about 50%) with decreasing  $|\mathbf{B}|$ . We derived equations that related the measured quantities, the deposition rate and ionized flux fraction, to the ionization probability  $\alpha_t$  and the back-attraction probability of the sputtered species  $\beta_t$ . We showed that the fraction of the ions of the sputtered material that escape back-attraction  $\propto (1 - \beta_t)$  increased by 30% when  $|\mathbf{B}|$  was reduced during operation in a fixed peak current mode, while the ionization probability of the sputtered material  $\alpha_t$  remained roughly constant. Furthermore, we demonstrated that the ionization probability of the sputtered species  $\alpha_t$  increased with increasing  $|\mathbf{B}|$ , due to increased discharge current, when operating in a fixed voltage mode.

In the present work, we extend our previous study to also encompass radial fluxes by exploring the relationships among  $|\mathbf{B}|$ , the magnetic field geometry (level of balancing), the deposition rate, and the ionized flux fraction radially outward in a HiPIMS discharge. The goal is to answer the question of the role of sideways deposition in lowering the deposition rate in HiPIMS and to

establish trends for optimized discharge conditions with focus on high deposition rates and high ionized flux fractions.

## II. EXPERIMENTAL APPARATUS AND METHOD

The experiments were carried out in a custom-built cylindrical vacuum chamber (height 50 cm and diameter 45 cm) made of stainless steel and used in our earlier work.<sup>33</sup> Using a turbo molecular pump backed by a roughing pump, a chamber base pressure of  $4 \times 10^{-6}$  Pa was achieved. The working gas pressure was maintained at 1 Pa by injecting 50 sccm Ar into the chamber and adjusting a butterfly valve located between the chamber and the turbo pump. The deposition system was equipped with a circular 4 in. diameter VTec Magnetron assembly (Gencoa, Liverpool, UK). The magnetron assembly, as well as a probe holder used during measurements, was mounted on movable bellows controlled with millimeter precision, as shown in Fig. 1. This allowed us to perform radial as well as axial scans with high precision. The absolute magnetic field strength  $|\mathbf{B}|$  as well as the geometry of the magnetic field (degree of balancing) above the magnetron target was varied by displacing the center magnet (C) and the outer ring magnet at the target edge (E) using two micrometer screws located on the outer side of the magnetron assembly. We refer to each configuration using the displaced distance (in millimeters) of each magnet from the target backing plate. The notation C0E0 thus refers to a magnet configuration where the center and outer magnets touch the backing plate (zero displacement, i.e., the strongest magnetic field above the target).

We determined the sideways deposition rate and ionized flux fraction for seven different magnet configurations: C0E0, C5E5, C10E10, C0E5, C0E10, C5E0, and C10E0. The magnetic field

distribution above the target for each configuration was reported earlier.<sup>33</sup> For all the configurations, it was found that a magnetic null point was present, and all the configurations were categorized as unbalanced type II.<sup>34</sup> The magnetic null is a measure of the degree of balancing and was located at 43–74 mm from the target surface above the target center. The location of the magnetic null point and  $|\mathbf{B}|$  above the center of the race track are listed in Table I for each of the magnet configurations, where C10E0 is strongly unbalanced and C0E10 is only weakly unbalanced. Throughout this paper, we have used the radial component of the magnetic field above the target race track  $B_{rt}$  recorded at  $z = 11$  mm as a measure of  $|\mathbf{B}|$ , in line with our previous work.<sup>33</sup>

A dc power supply (SR1.5-N-1500, Technix, Créteil, France) and a HiPIMS power supply (HiPSTER 1, Ionautics, Linköping, Sweden) were used to ignite the discharge in dc and HiPIMS operation, respectively. For both cases, an average discharge power was maintained at 300 W. The HiPIMS pulse was always kept at a constant length of 100  $\mu$ s, and the discharge was regulated in two different ways. The first mode of operation is referred to as a fixed voltage mode and was realized by keeping the cathode voltage fixed at 625 V and varying the pulse frequency to achieve the desired average power. The second operating mode is referred to as a fixed peak current mode and was realized by changing the cathode voltage to maintain the peak discharge current at  $I_{D,peak} = 40$  A, corresponding to current density  $J_{D,peak} = 0.5$  A/cm<sup>2</sup>. However, for C10E10, we were not able to reach  $I_{D,peak} = 40$  A due to weak electron confinement and limitation in cathode voltage (1000 V). To achieve the desired average power, the repetition frequency was varied. The discharge parameters are summarized in Table I for dcMS operation, and both operating modes of HiPIMS for all the seven magnet configurations investigated.

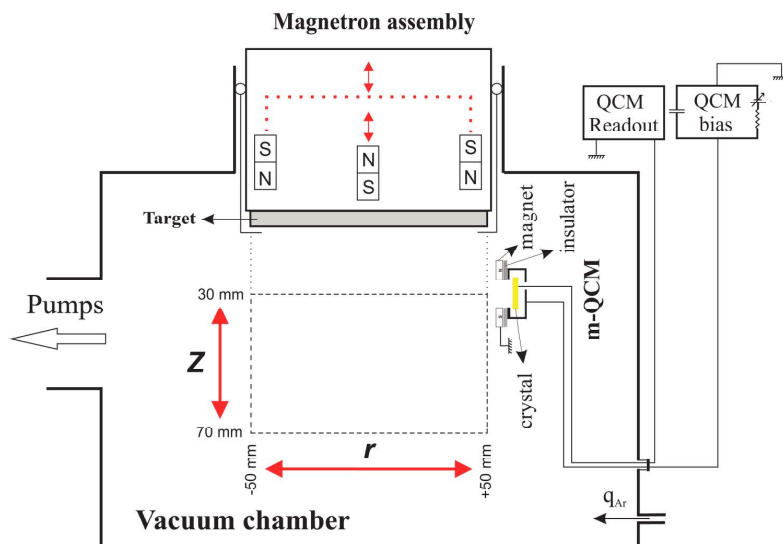


**FIG. 1.** Schematic of the magnetron sputtering chamber. The magnetron assembly and the probe holder with the m-QCM are mounted on movable bellows that can be controlled with millimeter precision. The red arrows indicate linear motion, and the dashed rectangle displays the limits of the investigated (cylindrical) volume.

**TABLE I.** Discharge operating parameters for the investigated dcMS and HiPIMS discharges in a fixed voltage and in fixed peak current modes. The average discharge power was kept at 300 W for all the discharges. For the HiPIMS discharges, the pulse length was 100  $\mu$ s, while the pulse frequency was varied to maintain a constant average power. The absolute magnetic field strength and the degree of balancing were varied by displacing the center magnet (C) and the outer ring magnet at the target edge (E). Each configuration is referred to using the displaced distance (in millimeters) of each magnet from the target backing plate. In this notation, C0E0 refers to a magnet configuration where both the center and outer magnets touch the backing plate.

	Magnet		dcMS		HiPIMS			HiPIMS		
	$B_{rt}$ (Gauss)	$z_{null}$ (mm)	$V_D$ (V)	$I_D$ (A)	Fixed voltage			Fixed peak current		
					$V_D$ (V)	$I_{D,peak}$ (A)	$f_{pulse}$ (Hz)	$V_D$ (V)	$I_{D,peak}$ (A)	$f_{pulse}$ (Hz)
C0E0	238	66	343	0.871	625	80	56	498	40	160
C0E5	217	70	346	0.865	625	67	64	490	40	155
C0E10	213	74	342	0.875	625	46	92	576	40	118
C5E0	181	53	338	0.888	625	62	70	510	40	146
C5E5	161	59	347	0.864	625	37	121	590	40	119
C10E0	137	43	337	0.890	625	40	103	605	40	112
C10E10	111	52	374	0.795	625	15	300			

Figure 2(a) shows the peak discharge current at a fixed voltage, plotted from left to right in the sequence of magnetic configurations that will be used below when presenting the deposition measurements: from the strongest field C0E0 on the left to the weakest field C10E10 on the right. There is an overall decreasing trend of  $I_{D,peak}$  toward the right, decreasing magnetic field strength  $|B|$ , combined with a “saw-tooth” pattern, which is highlighted by dashed lines. We will note below when similar features appear in the deposition data.

We also note that a saw-tooth pattern (but here reversed) is found in  $z_{null}$ , as shown in Fig. 2(b). The magnetic field strength

has a significant influence on the discharge current amplitude and the discharge current waveform which we explored earlier.<sup>33</sup> Both the peak discharge current and the current rise time are influenced by the magnetic field when operating in the fixed voltage mode, and the current rise time varies with  $|B|$  when operating in a fixed peak current mode.

A quartz crystal microbalance (QCM) with a native frequency of 5 MHz and a gold coated surface was used to determine the deposition rate. It was mounted on the probe holder as shown in Fig. 1. By moving the probe holder and/or the magnetron assembly, it was possible to investigate a region defined by  $0 \leq r \leq 50$  and  $30 \leq z \leq 70$  mm (see the dashed rectangle in Fig. 1), where  $r$  is the radial coordinate parallel to the target surface and  $z$  is the axial coordinate perpendicular to the target surface, and  $(r, z) = (0, 0)$  marks the center of the target surface. The center of the target race track was located at approximately  $(r, z) = (30, 0)$  mm. In this work, the material fluxes radially outward, parallel to the target surface, were investigated at three locations  $(r, z) = (50, 35)$  mm,  $(r, z) = (50, 50)$  mm, and  $(r, z) = (50, 70)$  mm. Due to interference with the plasma discharge, it was not possible to move the QCM closer than  $z \geq 30$  mm.

The QCM sensor was the main component in the ion meter (or gridless QCM/m-QCM) used for measuring the ionized flux fraction  $F_{flux}$ . The device is described in detail by Kubart *et al.*<sup>7</sup> and in our previous study.<sup>33</sup> The m-QCM gives either the deposition rate from ions and neutrals or from neutrals only by varying a voltage applied to the biased top QCM electrode, allowing for fast (roughly 1 min) determination of the ionized fraction of the material flux to the sensor head. The ionized fraction of the metal flux was determined using

$$F_{flux} = \frac{R_t - R_n}{R_t} = \frac{R_i}{R_t}, \quad (1)$$

where  $R_t$  is the total mass deposition rate,  $R_i$  is the mass deposition rate due to metal ions, and  $R_n$  is the mass deposition rate of neutral metal atoms, as discussed by Wu *et al.*<sup>35</sup> The deposition rates were

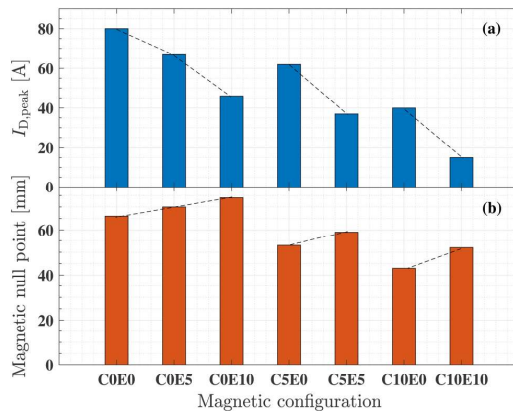


**FIG. 2.** Two discharge operating parameters from Table I, plotted in a sequence of decreasing B-field strength. (a)  $I_{D,peak}$  for fixed voltage operation and (b) the degree of magnetic unbalance quantified by  $z_{null}$ . The dashed lines are drawn to highlight a saw-tooth pattern, which is discussed in the text.

recorded by manually recording the film thickness at a chosen time on a readout unit connected to the QCM. In addition, we tried to minimize errors due to the QCM crystal heating up during the process by making short measurements (typically less than 120 s). However, the error of  $F_{\text{flux}}$  was estimated to be up to 15% for a single result based on the accuracy of the mass deposition rate determination. For sideways measurement, the closer to the target, the higher the error is observed to be, which is due to the small acceptance angle of m-QCM and rather a wide propagation profile of ions. This issue is quantitatively discussed in Sec. IV C.

### III. RESULTS

The deposition rates as well as ionized flux fractions for each of the seven magnet configurations investigated are presented here. For the radial fluxes, we have chosen to focus on the data recorded at  $r = 50$  mm (above the edge of the cathode) at an axial distance of  $z = 35$  mm from the cathode surface. However, deposition rates and ionized flux fractions were also recorded at larger axial distances,  $z = 50$  and  $70$  mm, at the same radial position ( $r = 50$  mm), and comparisons between these different positions will be made where appropriate.

#### A. Deposition rate

The radial deposition rates measured using the m-QCM at  $(r, z) = (50, 35)$  mm are plotted as a bar chart in Fig. 3 for dcMS and HiPIMS discharges operated in a fixed voltage mode and a fixed peak current mode for the investigated magnet configurations. These configurations are on the  $x$ -axis ordered from high  $|\mathbf{B}|$  at the

left to low  $|\mathbf{B}|$  on the right, where the recorded  $B_{r1}$  value above the race track center was used as a measure of  $|\mathbf{B}|$ . For any given magnet configuration, the deposition rate values for dcMS are always the highest, whereas HiPIMS operated at fixed peak current is the second highest (no data available for C10E10) and the HiPIMS fixed voltage mode always yields the lowest values. Overall, the dcMS discharges exhibit sideways deposition rates in a rather narrow range (163–197 Å/min) without any obvious trends with B-field strength or degree of unbalance. For HiPIMS operated in the fixed peak current mode, smaller changes are observed and the deposition rate varies between 72 Å/min and 100 Å/min with no clear trend, although one could infer that the higher B-field cases (C0E0, C0E5, C0E10) have a tendency to yield slightly higher deposition rates. On the other hand, much larger differences are seen when operating in a HiPIMS mode at a fixed voltage, where we see the saw-tooth pattern of Fig. 2, combined with an increase in the sideways deposition rate that varies from 49 Å/min to 124 Å/min with decreasing  $|\mathbf{B}|$ , i.e., a rate increase of up to 150%. The saw-tooth pattern indicates that the deposition rate, in a fixed voltage mode, is inversely correlated with the peak discharge current.

By increasing the axial distance between the cathode surface and the m-QCM, we generally see a significant drop in the recorded radial deposition rate. In Fig. 4, this decrease is illustrated for the HiPIMS fixed voltage mode operation. Again, we see that for this operating mode, the sideways deposition rate increases with decreasing  $|\mathbf{B}|$ , independent of the axial point of measurement and also shows the saw-tooth pattern. In this case, the relative rate change observed varies depending on the magnet configuration. The sideways deposition rate drops in a range of 32% (using

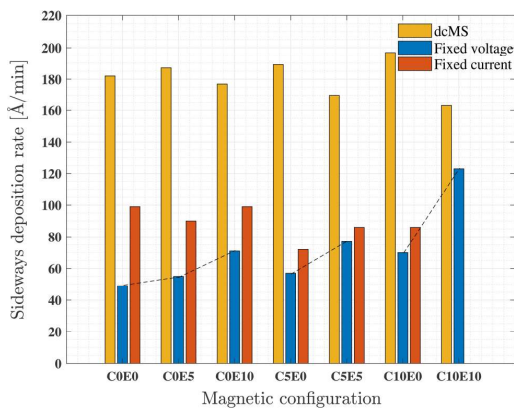


**FIG. 3.** Ti sideways deposition rate recorded for both dcMS and HiPIMS discharges using various magnet configurations. The measurements were made using the m-QCM at a 35 mm axial distance over the edge of the cathode, i.e.,  $(r, z) = (50, 35)$  mm. The magnet configurations on the  $x$ -axis are ordered from high  $|\mathbf{B}|$  on the left to low  $|\mathbf{B}|$  on the right. The recorded  $B_{r1}$  value above the race track was used as a measure of  $|\mathbf{B}|$ . The dashed lines are drawn to highlight the saw-tooth pattern in the fixed voltage mode.

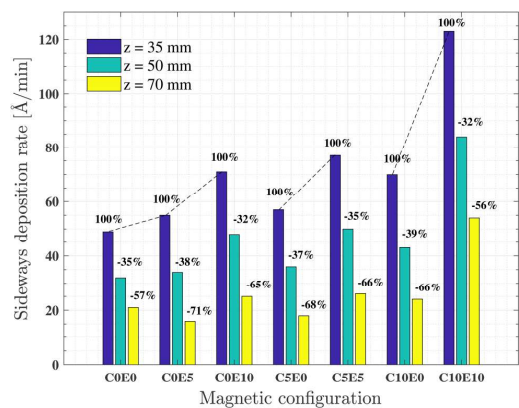


**FIG. 4.** Sideways deposition rate in HiPIMS measured by the m-QCM at  $z = 35, 50,$  and  $70$  mm at the edge of the cathode ( $r = 50$  mm). The discharge was operated in a fixed voltage mode using various magnet configurations. The magnet configurations on the  $x$ -axis are ordered from high  $|\mathbf{B}|$  on the left to low  $|\mathbf{B}|$  on the right. The recorded  $B_{r1}$  value above the race track was used as a measure of  $|\mathbf{B}|$ . The dashed lines are drawn to highlight the saw-tooth pattern in the fixed voltage mode.



C10E10) to 39% (using C10E0) at  $z = 50$  mm as compared to the deposition rate at  $z = 35$  mm. By moving to  $z = 70$  mm, the rate decreases up to 71% using C0E5, while sputtering by C10E10 and C0E0 shows a 56%–57% decrease compared to the value at  $z = 35$  mm. There is clearly a variation in the spatial distribution of the radial flux between the investigated magnetic field configurations in HiPIMS operation. This is different for the dcMS case (not shown), where the relative deposition rate change with  $z$  is almost independent of the magnet configuration, resulting in a 29%–34% decrease at  $z = 50$  mm and a 53%–61% decrease at  $z = 70$  mm compared to our reference position at  $z = 35$  mm. Overall, we see a sharper decrease in the sideways deposition rate in HiPIMS than in dcMS by axially moving away from the cathode. The decrease in the deposition rate is thus more sensitive to the magnet configuration in HiPIMS than in dcMS.

### B. Ionized flux fraction $F_{flux}$

By using the m-QCM, we also recorded the ionized flux fractions  $F_{flux}$  of the sputtered material transported radially. In Fig. 5,  $F_{flux}$  is plotted as a bar chart for the investigated HiPIMS discharges operated in a fixed voltage mode and a fixed peak current mode for the different magnet configurations. Again, these values were recorded at our reference point,  $(r, z) = (50, 35)$  mm. No dcMS values are presented here, since  $F_{flux}$  was always very close to 0%, i.e., within the margin of error, and thus in line with the results reported by Kubart *et al.*<sup>7</sup> using the same technique. In Fig. 5, we find strong variations in  $F_{flux}$  depending on the magnet configuration with no obvious trend with decreasing  $|B|$  for the fixed current

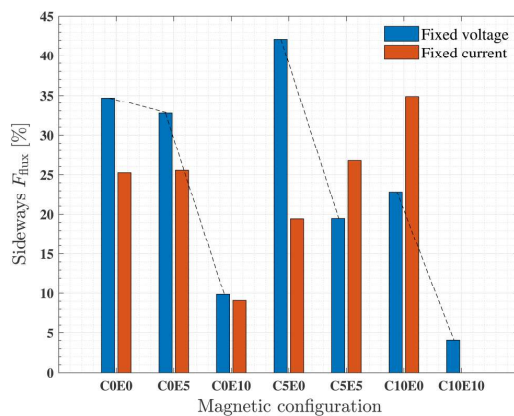


**FIG. 5.** Ionized flux fraction  $F_{flux}$  of HiPIMS discharges running in a fixed voltage and fixed current modes using various magnet configurations. The measurements are carried out at  $(r, z) = (50, 35)$ . The magnet configurations on the x-axis are ordered from high  $|B|$  on the left to low  $|B|$  on the right. The recorded  $B_r$  value above the race track was used as a measure of  $|B|$ . The dashed lines are drawn to highlight the saw-tooth pattern in the fixed voltage mode.

case. However, as highlighted by dashed lines, there is an “inversed” saw-tooth pattern for the fixed voltage case. The absence of a simple trend with decreasing  $|B|$  is particularly striking when comparing magnet configurations C0E10 and C5E0, which are close in terms of  $|B|$ . For these two cases,  $F_{flux}$  increases by 320% in a fixed voltage mode and by 53% in a fixed peak current mode when going from C0E10 to C5E0. We note that this feature can be seen as an abruptly changing trend in the deposition rate and that it is associated with changing trends both in the peak discharge current and in  $z_{null}$ ; see Fig. 2. By comparing  $F_{flux}$  between the fixed voltage and fixed peak current modes for each magnet configuration separately (i.e., no comparison between the different magnet configurations), it is, however, noted that the ionized flux fraction is often higher for the operating mode that generates the highest peak discharge current, such as a fixed voltage mode for C0E0 and a fixed peak current mode for C10E0. This is in line with an explanation for the saw-tooth effect which we will return to in Sec. IV C.

The strong variation in the radial flux fraction versus magnet configuration at the chosen reference point is also seen when investigating the radial ion transport at larger axial distances. This is illustrated in Fig. 6 for a fixed voltage mode, which shows the radial ion flux fraction recorded at  $z = 35$  (reference), 50, and 70 mm. This figure provides a rather complex picture of the ion transport, where the largest fraction of the ions transported radially outward is sometimes found at low  $z$ , such as in the case of C0E0, sometimes at much higher  $z$ , such as in the case of C0E10, and sometimes at a  $z$  location in between, such as in the case of C5E0. This complicated situation is hard to resolve by merely comparing these point-to-point

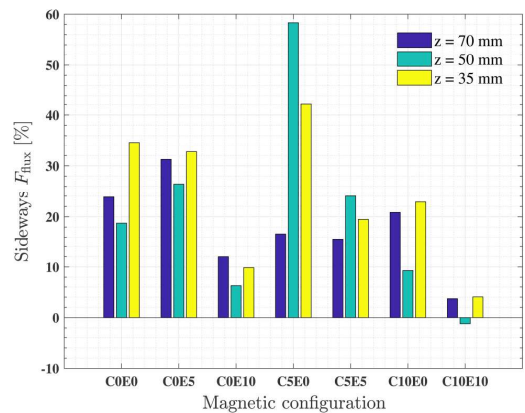


**FIG. 6.** Radial ionized flux fraction of the sputtered material  $F_{flux}$  of HiPIMS discharges running in a fixed voltage mode. The measurements are carried at the edge of the cathode ( $r = 50$  mm) and  $z = 35, 50,$  and  $70$  mm. The magnet configurations on the x-axis are ordered from high  $|B|$  on the left to low  $|B|$  on the right. The recorded  $B_r$  value above the race track was used as a measure of  $|B|$ .



measurements. We can, for example, note that the saw-tooth pattern seen at 35 mm (Fig. 5) has disappeared at 70 mm.

#### IV. DISCUSSION

##### A. Saw-tooth pattern

Figure 2 shows that, for fixed voltage operation, the peak discharge current has an overall decreasing trend toward the right (decreasing  $|\mathbf{B}|$ ), combined with a saw-tooth pattern. Similar features appear in the deposition rate data but only for fixed voltage operation. This is seen in Figs. 3 and 4, where the deposition rates show an overall increase with decreasing  $|\mathbf{B}|$  with the saw-tooth pattern superimposed. The ionized flux fraction in Fig. 5 also shows a saw-tooth pattern, while no clear overall trend with  $|\mathbf{B}|$  is observed. The overall picture is that lower discharge currents are correlated to higher deposition rates and to lower ionized flux fractions. These two trends are understood as follows. Lower discharge currents are associated with a lower plasma density in front of the target. A smaller fraction of the sputtered target material then gets ionized when they pass through the ionization region. This leads to both a higher deposition rate (more neutrals escape ionization and back-attraction) and to a lower ionized flux fraction (fewer neutrals of the film forming material become ionized). Mathematical expressions for these two trends are given in our previous work by Hajihoseini *et al.*<sup>33</sup> The saw-tooth features seen in fixed voltage operation are, therefore, a result of the change in the B-field through a chain of events as follows: (i) changes in the B-field strength and the degree of unbalance, quantified by  $z_{\text{null}}$ , change the effective discharge impedance. When the data are plotted as a function of B-field strength, the variations in  $z_{\text{null}}$ , see Fig. 2(b), create a saw-tooth pattern for the effective discharge impedance. (ii) For a fixed discharge voltage, this leads to a saw-tooth pattern for the discharge current, which consequently leads to a saw-tooth pattern to the probability of ionization  $\alpha_i$ . (iii) Finally, this variation in  $\alpha_i$  gives a saw-tooth pattern to the deposition rate and consequently an inverted saw-tooth pattern in the ionized flux fraction.

##### B. Comparison of radial and axial fluxes

In the interest of comparing the here reported radial deposition rates with typical axial deposition rates during sputtering, let us first recall the axial deposition rates recorded at the substrate position in the same system and for the same discharge configuration, as presented in our previous work.<sup>33</sup> Figure 7 shows the ratio of the radial deposition rate at our reference point,  $(r, z) = (50, 35)$  mm, and the axial deposition rate at the substrate position,  $(r, z) = (0, 70)$  mm,  $R_{t,\text{radial}}(50, 35)/R_{t,\text{axial}}(0, 70)$ , given for the different magnet configurations. Recall that the axial flux refers to the flux onto a substrate, of which the normal is in the direction perpendicular to the target surface, while the radial flux refers to the flux onto a substrate where the normal is directed along the radial direction in a cylindrical coordinate system (i.e., parallel to the target surface and away from the central axis of symmetry). The distance from the center of the target to the probe head at these two positions is 61 mm and 70 mm, respectively. We find that a significant fraction, always more than 65%, compared to the total material flux reaching the substrate is indeed transported radially outward, at least when comparing these

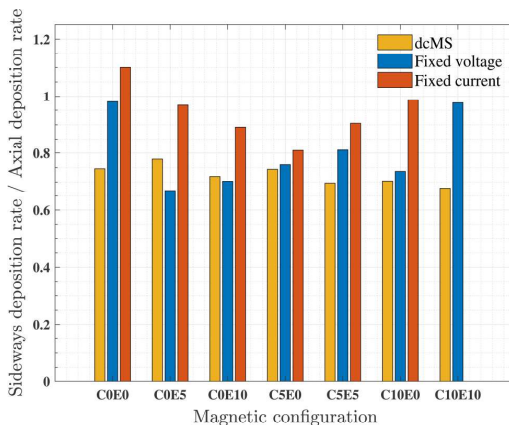


**FIG. 7.** Ratio of the sideways deposition rate and the axial deposition rate for dcMS and HiPIMS in fixed voltage mode and in fixed peak current mode for different magnet configurations. The sideways deposition rate was measured at  $(r, z) = (50, 35)$  with the m-QCM perpendicular to the target surface, and the axial deposition rate was measured at  $(r, z) = (0, 70)$  with the m-QCM facing the target. The magnet configurations on the x-axis are ordered from high  $|\mathbf{B}|$  on the left to low  $|\mathbf{B}|$  on the right. The recorded  $B_{\text{r}}$  value above the race track was used as a measure of  $|\mathbf{B}|$ .

two positions. The dcMS values are generally slightly lower (average fraction of about 72%) than the HiPIMS values (average fraction of about 80% in fixed voltage mode and 95% in fixed peak current mode). These values are close to the values earlier reported by Lundin *et al.*<sup>36</sup> (around 80% in HiPIMS and 70% in dcMS), when investigating radial transport in Ar/Ti discharges. Also, Bohlmark *et al.*<sup>41</sup> demonstrated a significant deposition rate radially during deposition from an Al target on a silicon substrate in a HiPIMS discharge. The radial deposition rate was highest next to the target surface and fell with increased axial distance from the target surface. However, for the first time, we also see strong differences due to the variation of the magnetic field in HiPIMS but much less so in dcMS. The latter result is expected since we have found close to no variation of the axial deposition rate<sup>33</sup> as well as of the radial deposition rate (this work) in dcMS. Looking in more detail at the effect of changing the magnetic field, it is found that the  $R_{t,\text{side}}/R_{t,\text{axial}}$  ratio is sometimes slightly higher in dcMS than in HiPIMS. This is seen when comparing dcMS and HiPIMS in a fixed voltage mode for the two magnet configurations that are the least unbalanced (COE5 and COE10) in Fig. 7. Still, the overall picture is that in the vicinity of the target, HiPIMS operation results in a larger fraction of the film forming material flux being transported radially outward than in dcMS.

Let us now make the same comparison between radial and axial measurements but only focusing on the ion deposition rate. In Fig. 8, the fraction of the ion deposition rate  $R_{i,\text{radial}}$  going sideways at our reference point,  $(r, z) = (50, 35)$  mm, and the axial ion deposition rate  $R_{i,\text{axial}}$  at the substrate position,  $(r, z) = (0, 70)$  mm,

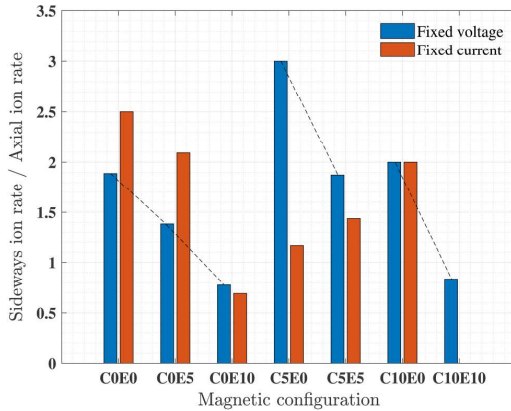


**FIG. 8.** Ratio of sideways ion deposition rate  $R_{i, \text{side}}$  measured at  $(r, z) = (50, 35)$  mm and the axial  $R_{i, \text{axial}}$  measured at  $(r, z) = (0, 70)$  mm for HiPIMS discharges running in fixed voltage and fixed current modes for the seven magnet configurations investigated. The magnet configurations on the x-axis are ordered from high  $|\mathbf{B}|$  on the left to low  $|\mathbf{B}|$  on the right. The recorded  $B_z$  value above the race track was used as a measure of  $|\mathbf{B}|$ . The dashed lines are drawn to highlight the saw-tooth pattern in the fixed voltage mode.

$R_{i, \text{radial}}(50, 35)/R_{i, \text{axial}}(0, 70)$  is given for the different magnet configurations. The latter data set was extracted from our previously reported measurements by Hajihoseini *et al.*<sup>23</sup> From these results, it is seen that the radial ion deposition rate is at least as large as the axial ion deposition rate and often around two times higher, i.e., significantly higher fractions compared to the corresponding fractions of the total deposition rates. The lowest fractions are found for C0E10 and C10E10 and are related to the dramatic drop in the radial deposition rate earlier seen in Fig. 5, a part of the saw-tooth pattern. The overall origin of these differences is dealt with in Sec. IV C.

### C. Analyzing volume-averaged fluxes across boundaries

Based on the radial deposition rate profiles and, more importantly, the ionized flux fraction profiles at different axial distances, Figs. 4 and 6, respectively, there is clearly a strong variation in the spatial flux distribution, where the different magnet configurations investigated give rise to very different results without any obvious trends, at least not with the B-field strength alone. To move beyond these point-to-point measurements, let us make an attempt at analyzing spatially averaged fluxes by introducing a cylindrical volume given by  $0 \leq r \leq 50$  mm and  $30 \leq z \leq 70$  mm (region limited by dashed lines in Fig. 1) and see if any trends and predictions can be established in this case. We calculate the incoming flux into the cylinder through the bottom circular surface ( $z = 30$  mm) and compare it to the flux that leaves the cylinder through the top surface ( $z = 70$  mm) as well as through the side of the cylinder ( $r = 50, 30 \leq z \leq 70$ ). In this way, we can study the integrated

surface flux (neutrals/ions/total) in the radial as well as axial directions. To this purpose, we have interpolated the deposition rates between the measured data points followed by fitting curves on the interpolated data. Then, the total flux passing through each area is calculated by integrating the fitted curves over the corresponding surfaces (top, bottom, and side of the cylinder).

In Fig. 9(a), we compare the total flux (ions and neutrals) across the three different surfaces of the investigated cylindrical volume (bottom of the cylinder at  $z = 30$  mm facing the target, top surface at  $z = 70$  mm facing the typical substrate position, and the cylinder side surface at  $r = 50$  mm) for HiPIMS in a fixed voltage mode. The total flux of the material into the volume is always the greatest, as expected, and increases by up to 139% with decreasing  $|\mathbf{B}|$ . Similar trends for the outflux across the top and side surfaces are seen, where the average radial flux increases by up to 158% with decreasing  $|\mathbf{B}|$ , which is in line with Fig. 3, where we saw up to 146% increase in the sideways deposition rate.

By comparing the absolute values of the influx across the bottom of the cylinder (blue bars) with the outflux across the top

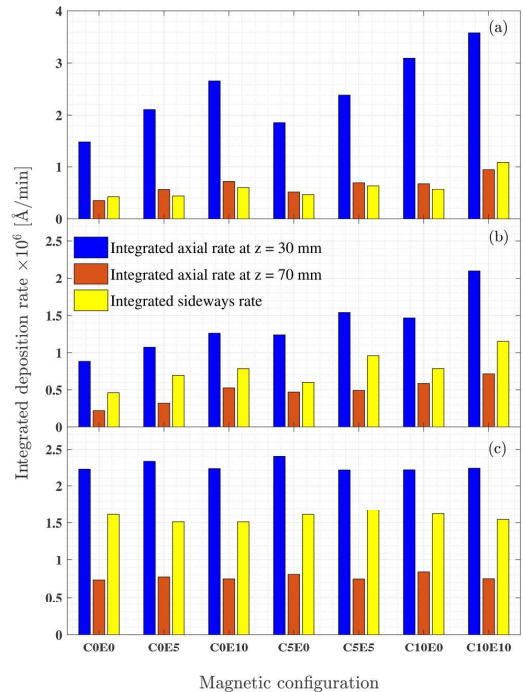


**FIG. 9.** Integrated deposition rate across the three different surfaces (bottom, top, side) of the investigated cylindrical volume. The data were acquired using (a) ion meter (m-QCM), (b) QCM in HiPIMS running in a fixed voltage mode, and (c) QCM in dcMS.

and side surfaces (red and yellow bars, respectively) in Fig. 9(a), it is found that the influx is significantly greater than the outflux (i.e., the flux is not divergence free), which is highlighted in Fig. 10(a), where the total influx (blue bars) is compared to the total outflux (yellow bars). Physically, this is hard to reconcile since we do not expect to lose particles inside the investigated volume. Instead, we believe that it is due to a limited (small) acceptance angle of the m-QCM used in the measurements, which leads to a reduction in the amount of detected particles (ions and neutrals) at high incoming angles with respect to the normal of the sensor head.

To verify this possibility, we carried out additional measurements using a standard QCM (i.e., without the magnetic shielding of the m-QCM) to compare the total flux (ions and neutrals) across the three different surfaces of the cylindrical volume of interest. The results for HiPIMS in a fixed voltage mode are shown in Fig. 9(b), where the main difference is that the relative contribution of the radial flux component is significantly greater. When using the m-QCM, the radial flux component constitutes on average 25%

of the total influx [Fig. 9(a)] compared to 60% when only using the QCM [Fig. 9(b)]. Furthermore, the axial outflux component at  $z = 70$  mm remains essentially unaltered compared to the axial influx at  $z = 30$  mm. Using the QCM results shown in Fig. 9(b), the absolute values of the influx across the bottom of the cylinder were again compared with the outflux across the top and side surfaces and shown in Fig. 10(b). Clearly, there is a much better agreement. It is, therefore, concluded that the axial flux component is rather well accounted for using the m-QCM, whereas the m-QCM fails to account for the total radial flux, in agreement with our hypothesis.

Additional total flux measurements in dcMS using the QCM were also carried out for completeness. The average fluxes across the three surfaces of interest are shown in Fig. 9(c), where again, no significant differences are observed between the different magnetic field configurations in agreement with Fig. 3. The absolute values of the influx across the bottom of the cylinder were compared with the outflux across the top and side surfaces and shown in Fig. 10(c). There is a very good agreement in almost all cases.

Using the more reliable total flux data presented in Fig. 9(b) for HiPIMS in a fixed voltage mode and Fig. 9(c) for dcMS, it is now possible to make new estimates of the radial to axial total flux fraction for the different magnet configurations. A direct comparison with Fig. 7 can be made by calculating the total radial flux across the side surface of the cylinder divided by the total axial flux of the film forming material across the top circular surface at  $z = 70$  mm. The results are shown in Fig. 11. For the HiPIMS case at a fixed voltage, we see about two times higher mass going to the side surface of the cylinder than going axially using the C0E0, C0E5, and C5E5 magnet configurations. However, using C5E0 and

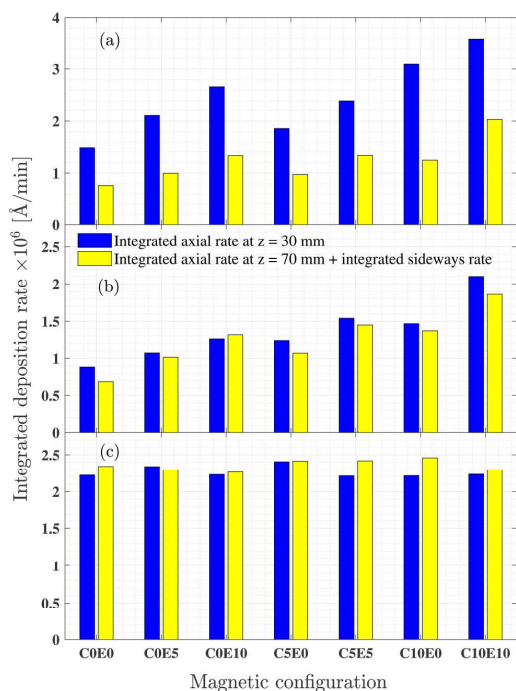


**FIG. 10.** Integrated deposition rate across the bottom surface at  $z = 30$  mm (i.e., into the investigated volume) in comparison with the total integrated rate across the side ( $r = 50$  mm) and top ( $z = 70$  mm) surfaces (i.e., out of the investigated volume) measured using (a) ion meter (m-QCM), (b) QCM in HiPIMS running in a fixed voltage mode, and (c) QCM in dcMS.

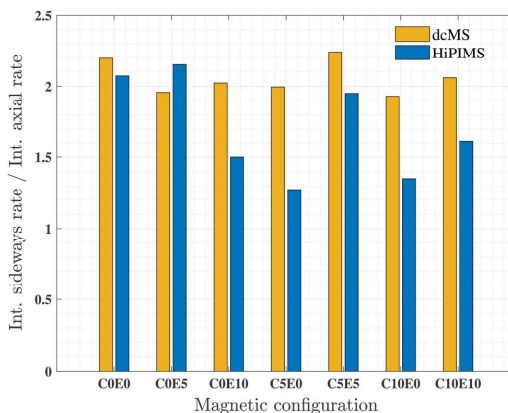


**FIG. 11.** Integrated sideways deposition rate across the cylindrical surface extending from  $z = 30$  to  $70$  mm divided by the integrated axial deposition rate across the bottom surface at  $z = 70$  mm for dcMS and HiPIMS discharges. All data were recorded using a standard QCM.

C10E0, the ratio is around 1.3, which is significantly lower than the dcMS one. For dcMS, this fraction is rather constant at about 200%, i.e., a significantly higher value compared to the 70% reported in Fig. 7. The fact that this fraction is so much larger when integrating the fluxes across the cylinder surfaces compared to point-to-point comparisons is not surprising when considering that the entire surface area of the cylinder side is 320% greater compared to the top circle area. However, what is striking is that the total radial flux of the film forming material is often greater in dcMS compared to HiPIMS. We, therefore, conclude that the commonly reported reduction of the (axial) deposition rate in HiPIMS compared to dcMS does not seem to be linked with an increased sideways transport in HiPIMS.

We were not able to carry out the measurement closer to the cathode (less than 30 mm) due to disturbance of the discharge. However, we could estimate the deposition rate by extrapolating the measured data points. We, therefore, extrapolated our recorded data sets linearly up to the cathode surface followed by curve fitting and integration over the side surface of the cylinder in order to calculate the sideways flux close to the target. The result shows that the radial deposition rate increases with decreasing axial distance to the target, and the majority of the ionized sputtered material is going sideways in the vicinity of the cathode target. This also agrees with the findings of Bohlmark *et al.*,<sup>21</sup> which report the highest sideways deposition rate next to the cathode target.

## V. CONCLUSIONS

The effect of the magnetic confinement on the deposition rate and the ionized flux fraction was explored for both dcMS and HiPIMS deposition from a Ti target. A significant proportion of the film forming material is deposited radially or parallel to the target surface in both discharges. For the same operating conditions, the radial deposition rate is always the highest in dc operation, while it is lower for HiPIMS operation, which is in line with previously reported axial deposition rates at the substrate position. However, in the vicinity of the target, the relative radial flux is higher in HiPIMS than in dcMS. The radial deposition rate decreases with increasing axial distance from the target surface. Furthermore, in HiPIMS, the radial ion deposition rate is always at least as large as the axial ion deposition rate and often around two times higher. Thus, there are a significantly higher number of ions traveling radially than axially in the HiPIMS discharge. A comparison of the total radial as well as axial fluxes across the entire investigated plasma volume between the target and the substrate position allows for revised estimates of radial over axial flux fractions for different magnetic field configurations. It is here found that the relative integrated radial flux of the film forming material is greater in dcMS compared to HiPIMS for almost all cases investigated. We, therefore, conclude that the commonly reported reduction of the (axial) deposition rate in HiPIMS compared to dcMS does not seem to be linked with an increase in sideways material transport in HiPIMS. These findings further support that the back-attraction of the sputtered atoms after ionization is the main reason for the lower deposition rate in the HiPIMS discharge.

## ACKNOWLEDGMENTS

This work was partially supported by the University of Iceland Research Fund for Doctoral students, the Icelandic Research Fund (Grant Nos. 130029 and 196141), the Czech Science Foundation through Project No. 19-00579S and by Operational Program Research, Development and Education financed by the European Structural and Investment Funds, and the Czech Ministry of Education, Youth and Sports (Project No. SOLID21 CZ.02.1.01/0.0/0.0/16\_019/0000760).

## REFERENCES

- <sup>1</sup>S. M. Rossnagel and J. Hopwood, *J. Vac. Sci. Technol. B* **12**, 449 (1994).
- <sup>2</sup>S. M. Rossnagel, *J. Vac. Sci. Technol. B* **13**, 125 (1995).
- <sup>3</sup>S. Rossnagel, in *Ionized Physical Vapor Deposition*, Thin Films, edited by J. A. Hopwood (Academic, San Diego, CA, 2000), Vol. 27, pp. 37–66.
- <sup>4</sup>U. Helmersson, M. Lättemann, J. Bohlmark, A. P. Ehasarian, and J. T. Gudmundsson, *Thin Solid Films* **513**, 1 (2006).
- <sup>5</sup>J. T. Gudmundsson, N. Brenning, D. Lundin, and U. Helmersson, *J. Vac. Sci. Technol. A* **30**, 030801 (2012).
- <sup>6</sup>V. Kouznetsov, K. Macák, J. M. Schneider, U. Helmersson, and I. Petrov, *Surf. Coat. Technol.* **122**, 290 (1999).
- <sup>7</sup>T. Kubart, M. Čada, D. Lundin, and Z. Hubička, *Surf. Coat. Technol.* **238**, 152 (2014).
- <sup>8</sup>D. Lundin, M. Čada, and Z. Hubička, *Plasma Sources Sci. Technol.* **24**, 035018 (2015).
- <sup>9</sup>M. Samuelsson, D. Lundin, J. Jensen, M. A. Raadu, J. T. Gudmundsson, and U. Helmersson, *Surf. Coat. Technol.* **202**, 591 (2010).
- <sup>10</sup>F. Magnus, A. S. Ingason, O. B. Sveinsson, S. Olafsson, and J. T. Gudmundsson, *Thin Solid Films* **520**, 1621 (2011).
- <sup>11</sup>H. Hajihoseini and J. T. Gudmundsson, *J. Phys. D: Appl. Phys.* **50**, 505302 (2017).
- <sup>12</sup>M. Kateb, H. Hajihoseini, J. T. Gudmundsson, and S. Ingvarsson, *J. Vac. Sci. Technol. A* **37**, 031306 (2019).
- <sup>13</sup>J. Alami, P. O. A. Petersson, D. Music, J. T. Gudmundsson, J. Bohlmark, and U. Helmersson, *J. Vac. Sci. Technol. A* **23**, 278 (2005).
- <sup>14</sup>D. Lundin and K. Sarakinos, *J. Mater. Res.* **27**, 780 (2012).
- <sup>15</sup>A. Anders, *J. Vac. Sci. Technol. A* **28**, 783 (2010).
- <sup>16</sup>N. Brenning, A. Butler, H. Hajihoseini, M. Rudolph, M. A. Raadu, J. T. Gudmundsson, T. Minea, and D. Lundin, *J. Vac. Sci. Technol. A* **38**, 033008 (2020).
- <sup>17</sup>D. J. Christie, *J. Vac. Sci. Technol. A* **23**, 330 (2005).
- <sup>18</sup>J. W. Bradley, S. Thompson, and Y. Aranda Gonzalvo, *Plasma Sources Sci. Technol.* **10**, 490 (2001).
- <sup>19</sup>A. Rauch, R. J. Mendelsberg, J. M. Sanders, and A. Anders, *J. Appl. Phys.* **111**, 083302 (2012).
- <sup>20</sup>J. Emmerlich, S. Mráz, R. Snyders, K. Jiang, and J. M. Schneider, *Vacuum* **82**, 867 (2008).
- <sup>21</sup>J. Bohlmark, M. Östbye, M. Lättemann, H. Ljungcrantz, T. Rosell, and U. Helmersson, *Thin Solid Films* **515**, 1928 (2006).
- <sup>22</sup>N. Brenning, D. Lundin, T. Minea, C. Costin, and C. Vitelaru, *J. Phys. D: Appl. Phys.* **46**, 084005 (2013).
- <sup>23</sup>D. Lundin, P. Larsson, E. Wallin, M. Lättemann, N. Brenning, and U. Helmersson, *Plasma Sources Sci. Technol.* **17**, 035021 (2008).
- <sup>24</sup>T. de los Arcos, R. Schröder, Y. Aranda Gonzalvo, V. Schulz-von der Gathen, and J. Winter, *Plasma Sources Sci. Technol.* **23**, 054008 (2014).
- <sup>25</sup>M. Čada, P. Adánek, V. Straňák, Štěpán Kment, J. Olejníček, Z. Hubička, and R. Hippler, *Thin Solid Films* **549**, 177 (2013).
- <sup>26</sup>P. Poolcharuansin, B. Liebige, and J. W. Bradley, *Plasma Sources Sci. Technol.* **21**, 015001 (2012).

- <sup>27</sup>M. Panjan, R. Franz, and A. Anders, *Plasma Sources Sci. Technol.* **23**, 025007 (2014).
- <sup>28</sup>R. Franz, C. Clavero, J. Kolbeck, and A. Anders, *Plasma Sources Sci. Technol.* **25**, 015022 (2016).
- <sup>29</sup>A. Mishra, P. J. Kelly, and J. W. Bradley, *Plasma Sources Sci. Technol.* **19**, 045014 (2010).
- <sup>30</sup>J. Capek, M. Hala, O. Zabeida, J. E. Klemberg-Sapieha, and L. Martinu, *J. Phys. D: Appl. Phys.* **46**, 205205 (2013).
- <sup>31</sup>J. W. Bradley, A. Mishra, and P. J. Kelly, *J. Phys. D: Appl. Phys.* **48**, 215202 (2015).
- <sup>32</sup>J. Alami, Z. Maric, H. Busch, F. Klein, U. Grabow, and M. Kopnarsk, *Surf. Coat. Technol.* **255**, 43 (2014).
- <sup>33</sup>H. Hajihoseini, M. Čada, Z. Hubička, S. Ůnaldi, M. A. Raadu, N. Brenning, J. T. Gudmundsson, and D. Lundin, *Plasma* **2**, 201 (2019).
- <sup>34</sup>B. Window and N. Savvides, *J. Vac. Sci. Technol. A* **4**, 196 (1986).
- <sup>35</sup>L. Wu, E. Ko, A. Dulkan, K. J. Park, S. Fields, K. Leaser, L. Meng, and D. N. Ruzic, *Rev. Sci. Instrum.* **81**, 123502 (2010).
- <sup>36</sup>D. Lundin, U. Helmersson, S. Kirkpatrick, S. Rohde, and N. Brenning, *Plasma Sources Sci. Technol.* **17**, 025007 (2008).



## Paper VI

**Optimization of HiPIMS discharges: The selection of pulse power, pulse length, gas pressure, and magnetic field strength.**

N. Brenning, A. Butler, H. Hajihoseini, M. Rudolph, M. A. Raadu, J. T. Gudmundsson, T. Minea and D. Lundin. 2020.

*Journal of Vacuum Science and Technology A* **38**: 033008.

Copyright © by the Journal of Vacuum Science and Technology A. All rights reserved. Permission for reproduction in this thesis granted by the copyright owner.





# Optimization of HiPIMS discharges: The selection of pulse power, pulse length, gas pressure, and magnetic field strength

Cite as: J. Vac. Sci. Technol. A 38, 033008 (2020); doi: 10.1116/6.0000079

Submitted: 5 February 2020 · Accepted: 18 March 2020 ·

Published Online: 17 April 2020



View Online



Export Citation



CrossMark

Nils Brenning,<sup>1,2,3</sup> Alexandre Butler,<sup>1</sup> Hamidreza Hajihoseini,<sup>4</sup>  Martin Rudolph,<sup>5</sup>  Michael A. Raadu,<sup>2</sup> Jon Tomas Gudmundsson,<sup>2,4</sup>  Tiberiu Minea,<sup>1</sup> and Daniel Lundin<sup>1,3,a)</sup> 

## AFFILIATIONS

<sup>1</sup>Laboratoire de Physique des Gaz et Plasmas—LPGP, UMR 8578 CNRS, Université Paris-Sud, Université Paris-Saclay, F-91405 Orsay Cedex, France

<sup>2</sup>Department of Space and Plasma Physics, School of Electrical Engineering and Computer Science, KTH Royal Institute of Technology, SE-100 44 Stockholm, Sweden

<sup>3</sup>Plasma and Coatings Physics Division, IFM-Materials Physics, Linköping University, SE-581 83 Linköping, Sweden

<sup>4</sup>Science Institute, University of Iceland, Dunhaga 3, IS-107 Reykjavik, Iceland

<sup>5</sup>Leibniz Institute of Surface Engineering (IOM), Permoserstraße 15, 04318 Leipzig, Germany

**Note:** This paper is part of the 2020 Special Topic Collection Festschrift Honoring Dr. Steve Rosnagel.

<sup>a)</sup>**Electronic mail:** [daniel.lundin@liu.se](mailto:daniel.lundin@liu.se)

## ABSTRACT

In high power impulse magnetron sputtering (HiPIMS) operation, there are basically two goals: a high ionized flux fraction of the sputtered target material and a high deposition rate. In this work, it is demonstrated that the former always comes at the cost of the latter. This makes a choice necessary, referred to as the HiPIMS compromise. It is here proposed that this compromise is most easily made by varying the discharge current amplitude, which opens up for optimization of additionally four external process parameters: the pulse length, the working gas pressure, the magnetic field strength, and the degree of magnetic unbalance to achieve the optimum combination of the ionized flux fraction and the deposition rate. As a figure of merit, useful for comparing different discharges,  $(1 - \beta_i)$  is identified, which is the fraction of ionized sputtered material that escapes back-attraction toward the cathode target. It is shown that a discharge with a higher value of  $(1 - \beta_i)$  always can be arranged to give better combinations of ionization and deposition rate than a discharge with a lower  $(1 - \beta_i)$ . Maximization of  $(1 - \beta_i)$  is carried out empirically, based on data from two discharges with Ti targets in Ar working gas. These discharges were first modeled in order to convert measured plasma parameters to values of  $(1 - \beta_i)$ . The combined effects of varying the different process parameters were then analyzed using a process flow chart model. The effect of varying the degree of unbalance in the studied range was small. For the remaining three parameters, it is found that optimum is achieved by minimizing the magnetic field strength, minimizing the working gas pressure, and minimizing the pulse length as far as compatible with the requirement to ignite and maintain a stable discharge.

Published under license by AVS. <https://doi.org/10.1116/6.0000079>

## I. INTRODUCTION

The dc magnetron sputtering (dcMS) discharge is a widely used technique applied to deposit thin films for applications such as integrated circuits, optical coatings, magnetic media, hard and protective coatings, and decorative coatings. However, in dcMS, the sputtered flux consists almost entirely of neutral atoms of the film forming material, and the ions available at the substrate position

are ions of the noble working gas.<sup>1</sup> The development of ionized physical vapor deposition was driven by the need to deposit material into high aspect ratio holes on a semiconductor substrate for back-end-of-line applications such as filling of interlevel vias.<sup>2,3</sup> This was initially achieved by ionizing the sputtered species in the region between the cathode target and the substrate. The ionization was performed by applying a secondary high-density discharge in

this region, either an electron cyclotron resonance discharge<sup>4,5</sup> or an inductively coupled discharge.<sup>6–8</sup> A significant fraction of sputtered species was thereby ionized, and the ionized flux fraction for Cu have been reported to be higher than 80%.<sup>7,8</sup> The ions of the sputtered material can subsequently be accelerated to the substrate by a dc bias to a desired bombarding energy. Furthermore, the directionality can be well controlled as the ions are accelerated perpendicularly to the substrate due to the electric field across the plasma sheath around the substrate.

More recently, it has been demonstrated that a high ionized flux fraction can be achieved by high power impulse magnetron sputtering (HiPIMS).<sup>9</sup> In HiPIMS, short pulses of high power are applied to a standard magnetron sputtering device, which leads to high fractions of ionization of the sputtered species. This has been shown to improve film surface smoothness and mass density<sup>10–13</sup> and to enable control over phase composition and microstructure.<sup>14–16</sup> Also, improved mechanical<sup>17</sup> and optical<sup>11,14</sup> properties, as well as enhanced film adhesion,<sup>18</sup> have been reported. There exist a few reviews on HiPIMS discharge and its properties.<sup>19–21</sup>

However, there is also a drawback as the deposition rate of the HiPIMS discharge is commonly found to be lower than that obtained with dcMS.<sup>19</sup> The HiPIMS deposition rate is typically in the range of 30%–85% of the dcMS rates, depending on the target material, when depositing at same average power.<sup>10</sup> This hampers extensive use of HiPIMS in industry. The main reason for the low deposition rate of the HiPIMS discharge is suggested to be due to the back-attraction of the ions of the sputtered species to the cathode target.<sup>22</sup> This process is described by a parameter  $\beta_t$  that indicates the probability that an ion of the sputtered material returns to the target. Much effort has been devoted to increase the deposition rate of HiPIMS discharges. This has included modifying the magnetic field geometry,<sup>23–25</sup> decreasing the magnetic field strength,<sup>26–28</sup> shortening the pulse length,<sup>29–31</sup> and chopping the pulse into a train of shorter pulses.<sup>32,33</sup> The general conclusion is that increasing the deposition rate in HiPIMS is indeed possible. However, it often comes at the cost of a lower ionized flux fraction of the sputtered material.<sup>29,34</sup>

We will here deal with the problem of optimizing a HiPIMS discharge with the goal to obtain the maximum possible deposition rate without adversely affecting the ionized flux fraction. What can be varied in this optimization process (assuming a given magnetron target material, size, and geometry) are basically five external experimental parameters, herein called process parameters: the pulse length  $t_{\text{pulse}}$ , the discharge current  $I_D$ , the working gas pressure  $p_{\text{gas}}$ , the magnetic field strength  $|\mathbf{B}|$ , herein quantified by the magnetic field strength above the racetrack center  $B_r$ , and the degree of magnetic unbalance. The degree of magnetic unbalance is herein quantified by distance  $z_{\text{null}}$  of the magnetic null point above the target, where a strongly unbalanced configuration exhibits a smaller  $z_{\text{null}}$  compared to a weakly unbalanced configuration. Note that the pulse frequency  $f_{\text{pulse}}$  is not included in this list of process variables for the reason that variations in  $f_{\text{pulse}}$  change neither the ionized flux fraction nor the deposition rate per unit power.  $f_{\text{pulse}}$  is instead, in usual practice, varied to set the desired average power level of the discharge. The cathode voltage is not included because it is not an independent process parameter; with the other process parameters chosen, the variations in discharge current are obtained by varying

the voltage. One effect of such variations in voltage is that the sputter yield varies. This is discussed in the [Appendix](#). Planar magnetron sputtering discharges are commonly operated using argon as working gas in the pressure range of 0.1–4 Pa and an absolute magnetic field strength in the range of 20–50 mT at the target surface above the racetrack, typically provided by permanent magnets. It, thus, follows that each of the process parameters should be optimized as far as compatible with the need to ignite and maintain a stable discharge. We here combine experimental data with modeling in order to unravel how these five process parameters relate to the ionized flux fraction of the sputtered target material and with the deposition rate.

We first note that it is not straightforward how to objectively define if one discharge is better than another even if both the deposition rate and the ionized flux fraction are known. We will argue that the lowest ion back-attraction probability  $\beta_t$  can be used to give an answer to this issue, and that the fraction of ionized sputtered material that escapes back-attraction  $(1 - \beta_t)$  can be used as a figure of merit to compare discharges. The reason is that a discharge with a higher value of  $(1 - \beta_t)$  always can be arranged to give better combinations of ionization and deposition rate than a discharge with a lower  $(1 - \beta_t)$ . Using  $(1 - \beta_t)$  also has the advantage that a single measure of the discharge quality combines and replaces two, the deposition rate and the ionized flux fraction.

The paper is organized as follows. In [Sec. II](#), we show that, in the HiPIMS discharge, a compromise between a high ionization fraction in the flux to the substrate and a high deposition rate is always necessary. We propose that this compromise is most easily made by varying the discharge current density  $J_D$ . In [Sec. III](#), we investigate the room for discharge optimization when  $J_D$  is reserved for this purpose. We base the data analysis on two HiPIMS discharges with Ti targets in Ar working gas, which we herein call the Ti/Ar system. The involved physics is also analyzed here based on a process flow chart model, and we describe a two-step optimization procedure. [Section IV](#), finally, contains a summary. Details of the experiments and the modeling are given in the [Appendix](#).

## II. THEORY AND OBSERVATIONS

It is for fundamental reasons impossible to simultaneously maximize both the deposition rate and the ionized flux fractions in HiPIMS. Let us start by illustrating why this is so. The variables that we will use for the argument are defined in [Table I](#). There are two measures of how good a HiPIMS discharge is: the fraction  $F_{\text{DR,sput}}$  of all the sputtered material that goes to the diffusion region (DR) and the fraction  $F_{\text{ti,flux}}$  of ionized species in that flux. There are also two internal discharge parameters that characterize the physics within the discharge, both taken from the materials pathway model:<sup>22,36</sup> the ionization probability,  $\alpha_t$ , and the ion back-attraction probability,  $\beta_t$ , of the sputtered species.

Three aspects in [Table I](#) are worth commenting: first, as the index in  $F_{\text{DR,sput}}$  indicates, the flux to the DR is normalized to the total sputtered flux in the discharge. An alternative is to make the normalization to dcMS sputtering at the same average power, which we denote as  $F_{\text{DR,dc}}$ ; we will return to the difference between  $F_{\text{DR,sput}}$  and  $F_{\text{DR,dc}}$  in [Sec. IV](#). Second, instead of the actual flux to the substrate, we here use the full flux that is in principle available

**TABLE I.** Definitions of the variables.

Variable	Definition	Comment
IR	Ionization region	A volume between the target and the DR. All ionization is approximated to occur within the IR.
DR	Diffusion region	A volume outside the IR in which the substrate is located.
$\xi$	Transport parameter	The fraction of a flux ( $\xi_{ii}$ for target ions and $\xi_{in}$ for target neutrals), from the IR to the DR, which goes to the substrate.
$F_{ti,flux}$	Ionized flux fraction	The ionized fraction in the flux of sputtered target material from the IR to the DR. Calculated over both the pulse and the afterglow.
$F_{DR,sput}$	Flux fraction to the diffusion region	The fraction of the total sputtered flux from the target, which goes to the DR, either as atoms or ions. Calculated over both the pulse and the afterglow. Proportional to the deposition rate when $\xi_i \approx \xi_{ii} \approx \xi_{in}$ holds.
$\alpha_i$	Ionization probability	The fraction of the sputtered atoms that are ionized in the IR.
$\beta_{i,pulse}$	Back-attracted ion fraction during the pulse	The fraction of ionized sputtered atoms that are attracted back to the target from the IR during the pulse. Usually assumed to be constant within the IRM (Ref. 35)
$\beta_i$	Back-attracted ion fraction, total	The total fraction of ionized sputtered atoms that are attracted back to the target from the IR during the pulse as well as the afterglow.
$\beta_i(t)$	Time-dependent back-attracted ion fraction	The time-dependent fraction of ionized sputtered atoms that are attracted back to the target from the IR.

for deposition, i.e., the flux to the entire DR (where commonly the substrate is located), because this makes our formulas independent of the substrate size and geometry. Third, in addition to the steady-state (constant) values of  $\alpha_i$  and  $\beta_i$  assumed in the original materials pathway model,<sup>22,36</sup> we here define a time-dependent variable,  $\beta_i(t)$ , in order to handle short, nonequilibrium, HiPIMS pulses. In our calculations,  $\alpha_i$  and  $\beta_i$  are defined as time averages over both the pulse and the afterglow, and a new variable,  $\beta_{i,pulse}$  is introduced for the back-attraction probability during the pulse. The latter is used to lock the modeled discharge current to a measured discharge current waveform when running the ionization region model (IRM)<sup>35</sup> (see Appendix for details).

As shown earlier,<sup>34,36,37</sup> two deposition parameters  $F_{ti,flux}$  and  $F_{DR,sput}$  can be expressed as functions of two internal discharge parameters  $\alpha_i$  and  $\beta_i$  as

$$F_{ti,flux} = \frac{\alpha_i(1 - \beta_i)}{(1 - \alpha_i\beta_i)} \quad (1)$$

and

$$F_{DR,sput} = (1 - \alpha_i\beta_i). \quad (2)$$

The desired goals are both a higher  $F_{ti,flux}$  and a higher  $F_{DR,sput}$ . From Eqs. (1) and (2) follows that there is an inescapable conflict between these two goals. Figure 1 shows  $F_{ti,flux}$  and  $F_{DR,sput}$  as functions of  $\alpha_i$  for the example of an assumed fixed value of  $\beta_i = 0.87$ , a typical value for the Ti/Ar system,<sup>34</sup> which we focus on here (a small decrease of  $\beta_i$  with increasing  $J_D$ <sup>34</sup> is disregarded here, since it does not change the concept of a HiPIMS compromise which is the issue of the present section). The experimentally available range in  $\alpha_i$  is illustrated at the top of the figure. Four examples of peak discharge current densities are drawn at the appropriate  $\alpha_i$  values, which have been calculated, for one dcMS

discharge and three HiPIMS Ti/Ar discharge pulses, as described by Hajihoseini *et al.*<sup>37</sup>

Let us briefly go through the information in Fig. 1 in terms of discharge current densities, from low pulse amplitudes to high. At

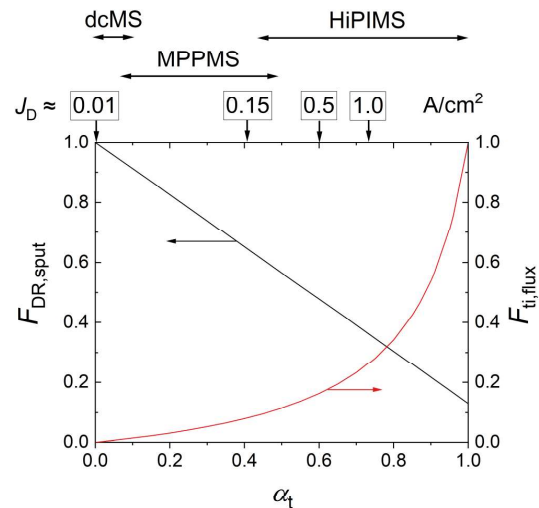


**FIG. 1.** Illustration of the “HiPIMS compromise” for the investigated Ti/Ar system: the necessary choice between a high degree of ionization and a high deposition rate. The black curve (left axis) shows the flux available for deposition from Eq. (2). The red curve (right axis) shows the ionization fraction in that flux from Eq. (1). A value of  $\beta_i = 0.87$  is assumed here, as motivated in Sec. II. At the top of the panel, some typical discharge current densities at the target are drawn at the appropriate  $\alpha_i$  values, which have been calculated, for one dcMS

low discharge current densities,  $J_D \approx 0.01 \text{ A/cm}^2$ , we are in the dcMS regime. Here, the full sputtered flux enters the diffusion region,  $F_{\text{DR,sput}} \approx 1$ . The ionized flux fraction is, however, close to zero. For a middle range, we choose the ionization probability  $\alpha_t \approx 0.5$ , which is obtained for current densities around  $0.15\text{--}0.5 \text{ A/cm}^2$ . As indicated above in the figure,  $0.15 \text{ A/cm}^2$  is in the lower end of the HiPIMS range, as defined in the review by Gudmundsson *et al.*,<sup>21</sup> and in the upper end of a proposed modulated pulse power magnetron sputtering range. When  $\alpha_t \approx 0.5$ , almost half the sputtered flux is lost,  $F_{\text{DR,sput}} \approx 0.5$ , but the ionized flux fraction is rather low,  $F_{\text{ti,flux}} = 13\%$ , although as much as 50% of the sputtered atoms become ionized. In another study of the Ti/Ar system,<sup>34</sup> higher current densities were used up to  $2.5 \text{ A/cm}^2$ . For this current density, the ionization probability  $\alpha_t$  was 0.96, and  $F_{\text{ti,flux}}$  as high as 65%—but this came at the cost of a dramatically reduced deposition rate, through losing more than 80% of the sputtered flux ( $F_{\text{DR,sput}} < 0.2$ ). There is an obvious dilemma here: a high ionized flux fraction  $F_{\text{ti,flux}}$  can only be achieved at the cost of a very large loss in the deposition rate. It also means that we must take both factors, not only the deposition rate, into account when optimizing any given HiPIMS process. This is typically not done.

In summary,

- (1) Varying the pulse amplitude, as quantified by current density  $J_D$ , makes it possible to vary the ionized flux fraction almost in the full theoretically available range  $0 \leq F_{\text{ti,flux}} \leq 1$ .
- (2) A gain in ionization is, however, inescapably coupled to a loss in the deposition rate.  $F_{\text{DR,sput}}$  decreases monotonically with increasing pulse amplitude, from zero loss of a sputtered material at low discharge currents, where  $\alpha_t \approx 0$ , to  $F_{\text{DR,sput}} \rightarrow (1 - \beta_t)$  for high discharge currents, where  $\alpha_t \rightarrow 1$  [Eq. (2)]. For a typical value,  $\beta_t = 0.87$  of the Ti/Ar system, this means (for most applications) an unacceptable loss of 87% of the sputtered material.
- (3) These conclusions are generic, i.e., valid for any HiPIMS discharge with such a high  $\beta_t$  value. A reduction in  $\beta_t$  is the only way to obtain better combinations of the deposition rate and the ionized flux fraction.

We also note that, even if a reduction in  $\beta_t$  can be achieved, the operator will always be faced with the need to choose a compromise discharge current amplitude, favoring either the deposition rate or the ionization fraction. We call this the HiPIMS compromise. The optimization of a HiPIMS discharge, thus, contains two separable sub-projects: minimization of  $\beta_t$  and making the HiPIMS compromise.

One illustrating example of the HiPIMS compromise is reported by Samuelsson *et al.*<sup>38</sup> when depositing Cr films using Ar as working gas. They superimposed HiPIMS and dcMS on a single cathode to vary the time-averaged ion content of the total deposition flux, while keeping the average deposition rate constant. This was realized by keeping the HiPIMS pulse characteristics constant while altering the pulse repetition frequency to adjust the supplied HiPIMS power (and by that also vary the time-averaged discharge current). A dcMS component was added for each choice of HiPIMS pulse frequency to ensure the same average deposition rates in all experiments. By systematically investigating the relationship between the fraction of sputtered flux generated by HiPIMS (and thereby the ionization fraction

of the film forming species) and the influence on microstructure, electrical, and electrochemical properties of the films, the authors found that considerable influence of the studied properties occurred already when only some 40% of the total power was supplied by the HiPIMS technique. Further increase in the HiPIMS power fraction resulted in comparatively minor influence of the studied properties yet significant deposition rate efficiency reduction.

### III. RESULTS AND DISCUSSION

#### A. Optimizing a discharge and the back-attraction probability $\beta_t$

In this work, we use data from two studies of the Ti/Ar system. Experimental details, data, and analysis are given in the Appendix, by Lundin *et al.*,<sup>39</sup> Butler *et al.*<sup>34,40</sup> (same discharge investigated), and by Hajihoseini *et al.*<sup>37</sup> Here, we only describe the results needed for the present discussion. The experiments were made in two different standard, unbalanced (type II), circular magnetrons with Ti targets. In the study by Hajihoseini *et al.*,<sup>37</sup> the magnetic field strength was varied ( $11.1 \text{ mTorr} \leq B_{\text{rt}} \leq 23.8 \text{ mTorr}$ , as measured 11 mm above the racetrack) as well as the degree of magnetic unbalance ( $43 \text{ mm} \leq z_{\text{null}} \leq 74 \text{ mm}$ ). The peak discharge current density was varied in the range of  $0.01\text{--}1 \text{ A/cm}^2$ , where the lower value refers to a dcMS discharge. In the other discharge,<sup>34,39,40</sup> three parameters were varied within typical HiPIMS ranges: the working gas pressure  $p_{\text{gas}}$  ( $0.5\text{--}2 \text{ Pa}$ ), the pulse length  $t_{\text{pulse}}$  ( $100\text{--}400 \mu\text{s}$ ), and the peak discharge current density  $J_{D,\text{peak}}$  ( $0.7\text{--}2.5 \text{ A/cm}^2$ ). While variations in the pulse discharge current amplitude made it possible to vary  $\alpha_t$  almost over the full theoretical range from 0 to 1, see Fig. 1, analysis of these Ti/Ar discharges<sup>34,37</sup> showed that  $\beta_t$  never fell outside the range of  $0.8\text{--}0.95$  in spite of the large variations in discharge current density, working gas pressure, magnetic field strength, the degree of unbalance, and the pulse length. One important question is how important optimization within this rather limited available range in  $\beta_t$  is. Simply put: is optimization worth the effort?

Let us, to answer this question by an example, consider an operator who has made the HiPIMS compromise and decided that for a particular application an ionized flux fraction of 30% is suitable. How does the deposition rate vary in the known range  $0.8 \leq \beta_t \leq 0.95$  if the ionized flux fraction is locked at  $F_{\text{ti,flux}} = 0.30$ ? Figure 2 gives the answer in the graphical form, using four curves obtained from Eqs. (1) and (2). For the dashed curves,  $\beta_t = 0.95$  is assumed.

Following the green dotted line from the value  $F_{\text{ti,flux}} = 0.30$  to the red dashed curve gives the ionization probability  $\alpha_t = 0.9$  (marked by a red square). The black dashed line then shows that at this value of  $\alpha_t$  only 15% of the total sputtered flux enters the diffusion region ( $F_{\text{DR,sput}} = 0.15$ ). Solid lines in Fig. 2 show the effect of reducing the back-attraction to  $\beta_t = 0.8$ . Here, a lower value of  $\alpha_t = 0.69$  is sufficient to maintain  $F_{\text{ti,flux}} = 0.30$  (red circle), and for this  $\alpha_t$  value,  $F_{\text{DR,sput}} = 0.45$  of the total sputtered flux enters the diffusion region. This, compared to the earlier value  $F_{\text{DR,sput}} = 0.15$ , corresponds to an increase in the deposition rate by a factor of three for the same ionized flux fraction of 30%. Optimization is definitely worth the effort.

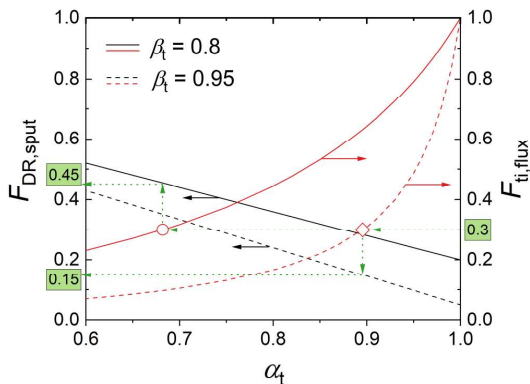


**FIG. 2.** Illustration of that a factor of three improvement in the deposition rate (left-hand axis) can be achieved, by reducing  $\beta_t$  within a realistic range from 0.95 (dashed lines) to 0.8 (solid lines) for the Ti/Ar system.  $F_{ti,flux}$  (right-hand axis) is here maintained at 0.30.

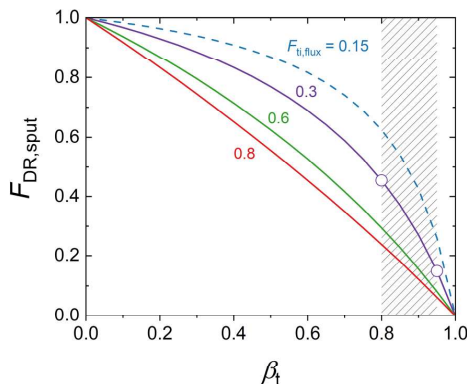


**FIG. 3.** Effect of reducing  $\beta_t$ . A set of curves determined by Eq. (3), giving  $F_{DR,sput}$  (which is proportional to the deposition rate) as a function of  $\beta_t$  for examples of fixed values of the ionized flux fraction  $F_{ti,flux}$ . The available range of  $\beta_t$  found here for the Ti/Ar system is shaded gray. The two cases in Fig. 2, where  $F_{ti,flux} = 0.30$  is assumed, are marked by circles.

In order to generalize this conclusion, we eliminate  $\alpha_t$  from Eqs. (1) and (2) and obtain an equation,

$$F_{DR,sput} = \frac{1 - \beta_t}{1 - \beta_t(1 - F_{ti,flux})}, \quad (3)$$

which can be used to answer the following question: given a predetermined value of the ionized flux fraction, quantified by  $F_{ti,flux}$ , what can be gained in the deposition rate, quantified by  $F_{DR,sput}$ , by reducing  $\beta_t$ ? Figure 3 gives the answer in the graphical form. The attainable range in our studied Ti/Ar system,  $0.8 \leq \beta_t \leq 0.95$ , is shaded gray. We can see that in this range, the deposition rate (proportional to  $F_{DR,sput}$ ) is extremely sensitive to changes in  $\beta_t$ . The gain in the deposition rate achieved by lowering  $\beta_t$  from 0.95 to 0.8 is from a factor three to a factor four, depending on the desired ionized flux fraction. One might say that a low  $\beta_t$  is a kind of hard currency that may be converted to other valuables: either to “buy” higher ionization (at a chosen deposition rate) or to “buy” higher deposition rate (at a chosen ionization fraction). We conclude so far, regarding the internal parameters  $\alpha_t$  and  $\beta_t$ :

- (1)  $\alpha_t$  is easily varied within almost the full theoretical range  $0 \leq \alpha_t \leq 1$  by the discharge current amplitude  $J_D$ , but there is no obvious optimum value.  $J_D$  can be used to make the HiPIMS compromise between the ionization degree and the deposition rate.
- (2)  $\beta_t$  is a variable within a much smaller achievable range,  $0.8 \leq \beta_t \leq 0.95$ , in the studied Ti/Ar system. However, a reduction within this range has a significant effect, increasing the deposition rate (for a fixed value of the ionization degree) by up to a factor of four.
- (3)  $\beta_t$  was in the Ti/Ar system varied by varying the five external process parameters  $J_D$ ,  $t_{pulse}$ ,  $B_{rt}$ ,  $z_{null}$ , and  $p_{gas}$ , which, therefore,

are the available tools for optimization. If  $J_D$  is reserved for setting the  $\alpha_t$  value, only four parameters remain: the pulse length, the magnetic field strength, the degree of magnetic unbalance, and the gas pressure.

As discussed above, the deposition rate alone is not a suitable figure of merit for HiPIMS discharges. It needs to be combined with the ionized flux fraction to be meaningful. Instead, we propose  $(1 - \beta_t)$  to be used as a figure of merit. As can be concluded from Fig. 3,  $(1 - \beta_t)$  gives an approximate measure of the improvement in the deposition rate, at a fixed degree of ionization in the flux to the substrate.

## B. Minimizing $\beta_t$ in the Ti/Ar system: Experiments and modeling

Maximizing  $(1 - \beta_t)$  is, obviously, identical to minimizing  $\beta_t$ . The question to be studied in the present section is how  $\beta_t$  is influenced when the four process parameters ( $t_{pulse}$ ,  $B_{rt}$ ,  $z_{null}$ , and  $p_{gas}$ ) are varied. The involved mechanisms are not yet well understood theoretically, which makes it necessary to tackle the problem empirically. This leads to two requirements: first, experimental data must be taken in such a fashion that the individual effect of each process parameter can be separated from the effects of changing the others; and second, the data must be analyzed in such a way that  $\beta_t$  can be evaluated.

For the first requirement, parameter separability, we need data that are taken when each process parameter  $B_{rt}$ ,  $z_{null}$ ,  $p_{gas}$ , and  $t_{pulse}$  is varied while the other, and also the current density  $J_D$ , are kept constant. Here, we have access to primary data from two discharges in the Ti/Ar system,<sup>34,39</sup> which are briefly described in Sec. III A. A subset of this data satisfies the condition of changing one process parameter at a time and will be used here. For the second



requirement, obtaining  $\beta_i$ , we will build on previous theoretical analysis of that data by Butler *et al.*,<sup>34</sup> Butler,<sup>40</sup> and Hajihoseini *et al.*<sup>37</sup> The experimental details and the analysis are given in the Appendix. We here in the main text only present the results, i.e., how  $\beta_i$  changes when each process parameter is varied. The focus is on the trends not on the absolute values.

The magnetic field was varied in the first discharge, as discussed by Hajihoseini *et al.*,<sup>37</sup> in which a 4" Ti target was used. No systematic effects were found on the deposition rate or on the ionized flux fraction axially from the target, when the degree of unbalance was varied in the studied range, so the parameter  $z_{\text{null}}$  is left out of the discussion here. Note that in a later study, it was observed that the degree of unbalance has an influence on the radial material flux perpendicular to the target.<sup>41</sup> We will not investigate these findings in the present work, since we here focus on the axial flux to a typical substrate facing the target. Figure 4 shows  $\beta_i$  as a function of the magnetic field strength (measured 11 mm above the racetrack center). These  $\beta_i$  values are directly obtained from the measured values of the ionized flux fraction,  $F_{\text{ti,flux}}$ , and of the deposition rate, as described in the Appendix [from Hajihoseini *et al.*,<sup>37</sup> see Eq. (A1)]. There is a clear trend such that  $\beta_i$  is lowered when the magnetic field strength is reduced, highlighted by a least square fitted straight line. Using the line fit, we find that  $\beta_i = 0.96$  for the highest magnetic field strength and  $\beta_i = 0.93$  for the lowest magnetic field strength are within the investigated range. According to Fig. 3, this corresponds to a variation of the deposition rate with about a factor of two depending on ionized flux fraction. We can note that our proposed figure of merit  $(1 - \beta_i)$  changes by a factor of the same order:  $(1 - 0.93)/(1 - 0.96) = 1.8$ .

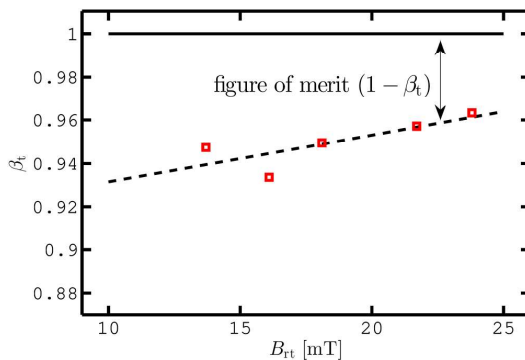


**FIG. 4.**  $\beta_i$  plotted as a function of the magnetic field strength  $B_{ti}$  over the racetrack center. The value of  $\beta_i$  was obtained from Eq. (A1) in the Appendix and based on extracted data on the deposition rate and the ionized flux fraction from Hajihoseini *et al.* (Ref. 37). The data were acquired above the target center at a typical substrate position. The peak discharge current was fixed at 40 A ( $J_{0,\text{peak}} = 0.5 \text{ A/cm}^2$ ), the working gas pressure at 1 Pa, and the pulse length at 100  $\mu\text{s}$ .

For the effect of changing the working gas pressure, we take data from Lundin *et al.*,<sup>39</sup> in which a 2" magnetron target was used. The experiments were made for all 12 combinations of two working gas pressures ( $p_{\text{gas}} = 0.5$  and 2 Pa), two pulse lengths, and three different peak discharge current densities. The trend in  $\beta_i$  with working gas pressure can be assessed from Fig. 5, which is the result of combining experimental data from IRM runs as described in the Appendix. We are here interested only in how  $\beta_i$  varies with the working gas pressure. The cases with 0.5 Pa are marked with crosses and have an average  $\beta_i = 0.84$ , while the cases with 2 Pa that are marked with circles have an average  $\beta_i = 0.93$ . This is a significant difference, which according to Fig. 3 corresponds to a variation of the deposition rate of about a factor of two depending on the ionized flux fraction. Again, we find that our proposed figure of merit  $(1 - \beta_i)$  changes by a factor of the same order:  $(1 - 0.84)/(1 - 0.93) = 2.3$ .

The effect of changing the pulse length on  $\alpha_i$  and  $\beta_i$  has been analyzed by Rudolph *et al.*<sup>42</sup> and that work is here extended. The details are summarized in the Appendix. Rudolph *et al.*<sup>42</sup> used the IRM to model two HiPIMS discharges from Hajihoseini *et al.*<sup>37</sup> and extract their internal discharge parameters. Originally, these were 100  $\mu\text{s}$ -long pulses that were artificially stepwise shortened for the analysis, down to 40  $\mu\text{s}$ . This means that the ion fluxes, up to the artificial pulse end, were determined by real discharge data. After the pulse, the fluxes toward the DR were based on the remaining densities of target species (atoms and ions) in the ionization region (IR) at pulse end. In the model, the authors assume  $\beta_i(\text{afterglow}) = 0$ , which is justified by the switched-off cathode potential during the

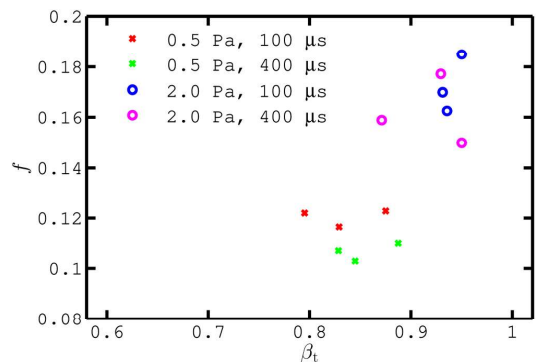


**FIG. 5.** Survey of 12 discharge combinations of pressure, pulse length, and discharge current using data extracted from an experimental study by Lundin *et al.* (Ref. 39), which was analyzed by Butler *et al.* (Ref. 34). Each discharge is represented by the pair  $(f, \beta_i)$ , which gives the best model fit, as exemplified in Fig. 9 in the Appendix, to both the current waveform and the measured ionized flux fraction. The fitting parameter  $f$  denotes the fraction of the discharge voltage that falls over the ionization region (leading to a potential drop  $V_{IR}$ ). Please note that the figure shows only a small part, corresponding to the lower right-hand corner of Fig. 9 in the Appendix, which shows the full range  $0 \leq f \leq 1$  and  $0 \leq \beta_i \leq 1$ .

afterglow and thereby an absent back-attracting electric field in the presheath. This results in a decreasing total  $\beta_t$  (pulse + afterglow) because the relative contribution of the afterglow ions to the flux toward the DR increases steadily for shorter pulses. For those two discharges,  $\beta_t$  is plotted as a function of the pulse length and shown in Fig. 6(a). The trend of decreasing  $\beta_t$  for shorter pulses is clear. For the discharge with a peak discharge current of 41 A ( $J_{D,peak} \approx 0.5 \text{ A/cm}^2$ ),  $(1 - \beta_t)$  increases from 0.14 to 0.32, while for the discharge with a peak discharge current of 76 A ( $J_{D,peak} \approx 1 \text{ A/cm}^2$ ),  $(1 - \beta_t)$  increases from 0.16 to 0.28. This is without compromising the ionized flux fraction that remains constant for the range of pulse lengths investigated.<sup>42</sup> However, the authors note that a decrease in the ionized flux fraction for even shorter pulses is to be expected as some minimum pulse length is required for high electron density to develop and to sputter and ionize target atoms. Figure 6(b) shows that the ionization probability  $\alpha_t$  also decreases with a shorter pulse length. The physical explanation has two components. First, for shorter pulses, a larger fraction of the sputtered atoms is created in the beginning of the pulse and has a smaller probability of ionization due to initially low plasma density. Second, a larger fraction of all sputtered atoms is created close to the pulse end. These atoms have a larger probability to escape ionization, since the electron temperature rapidly drops after the end of the pulse.

### C. Physical mechanisms and their interplay

We have seen in Secs. III A and III B that the external process parameters have a significant influence on the back-attraction probability. Figure 7 shows a flow chart model for the network of mechanisms involved in the HiPIMS deposition process. The left column

contains the process parameters that can be varied,  $J_D$ ,  $B_{t0}$ ,  $p_{gas}$ , and  $t_{pulse}$ , and the right column contains two parameters,  $F_{i,flux}$  and  $F_{DR,sput}$ , that characterize the resulting flux to the substrate. The middle column contains the two internal discharge parameters  $\alpha_t$  and  $\beta_t$ . The arrows denote the mechanism through which a parameter influences another parameter, and their colors indicate the type of influence. A green (filled) arrow marks a cocorrelation, i.e., an increase of the parameter at the start of a green arrow gives an increase in the parameter at the tip, and a decrease gives a decrease. A red (unfilled) arrow marks the opposite, a counter-correlation. We will first go through the arrows one by one and then discuss their interplay. Note that several influence routes of smaller importance are left out of this diagram, although identified for the Ti/Ar system.<sup>34,37</sup>

The mechanisms to the right in Fig. 7, represented by arrows from the discharge parameters (middle column) to the flux parameters (right column), are all determined by Eqs. (1) and (2). They follow from the definitions given in Table I of the four involved parameters  $\alpha_t$ ,  $\beta_t$ ,  $F_{i,flux}$ , and  $F_{DR,sput}$  and are, therefore, generic, i.e., true for any HiPIMS discharge. These relations have been thoroughly analyzed before.<sup>22,27,36</sup> We, therefore, here only briefly review them from the top to the bottom in Fig. 7 with the limited goals to determine the colors of the arrows and to outline the physics involved.

*Influence  $\alpha_t \rightarrow F_{i,flux}$ .* From Eq. (1) follows that  $F_{i,flux}$  increases from 0 to 1 when  $\alpha_t$  is increased from 0 to 1. Such a positive correlation between  $\alpha_t$  and  $F_{i,flux}$  is also physically understandable: if the ion back-attraction  $\beta_t$  is constant, a higher probability of ionization both increases the ionized flux and decreases the neutral flux. Both effects increase the ionized flux fraction, and consequently, we get a green (filled) arrow.

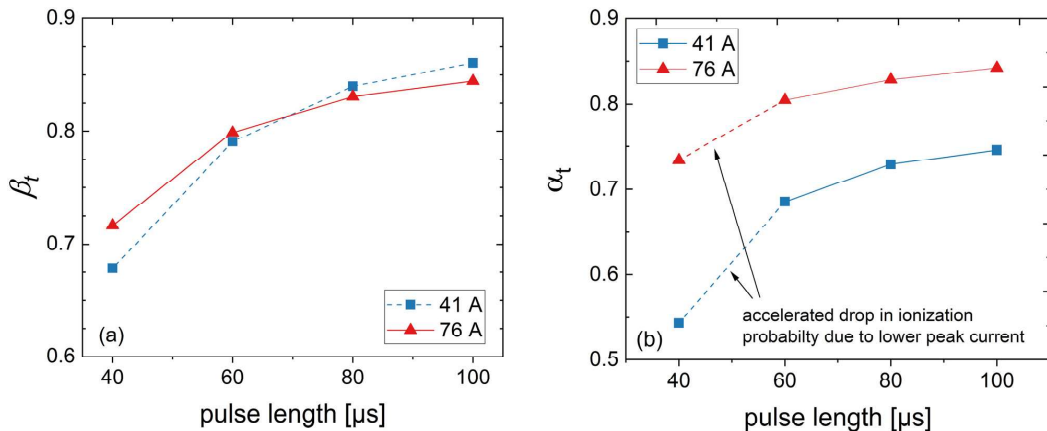


**FIG. 6.** (a) The back-attracted ion fraction  $\beta_t$  and (b) the ionization probability  $\alpha_t$ , as functions of pulse length. Two different peak currents 41 A ( $J_{D,peak} \approx 0.5 \text{ A/cm}^2$ ) and 76 A ( $J_{D,peak} \approx 1 \text{ A/cm}^2$ ) were investigated. The figures were produced using and extending a study by Rudolph *et al.* (Ref. 42). The calculations are described in the Appendix.

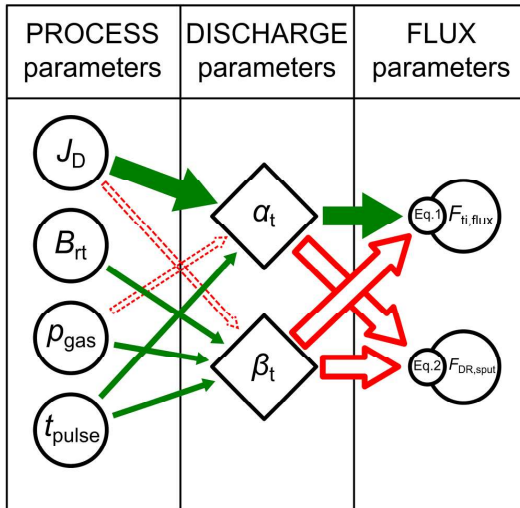


**FIG. 7.** Flow chart that shows the main influences from the external process parameters (to the left), through internal processes represented by parameters  $\alpha_t$  and  $\beta_t$  (in the middle column), and finally to the two flux parameters  $F_{ti,flux}$  and  $F_{DR,sput}$  that are to be optimized (to the right). Routes of smaller importance are left out of this diagram, although identified for the Ti/Ar system (Refs. 34 and 37). Green (filled) arrows indicate a cocorrelation, and red (unfilled) arrows mark a counter-correlation as described in the text. The widths of the arrows indicate the strength of their influence. Figure courtesy of Dr. T. J. Petty.

**Influence  $\alpha_t \rightarrow F_{DR,sput}$ .** Here, Eq. (2) gives a negative influence, since increasing  $\alpha_t$  decreases  $(1 - \alpha_t\beta_t)$ . Also, this can be understood from first principles. A higher ionization probability  $\alpha_t$  transfers particles from the neutral population to the ion population in the total flux toward the substrate. Ions, but not neutrals, are back-attracted. Consequently, more particles become back-attracted and the deposition rate (the sum of the ion and the neutral fluxes) decreases. We here get a red (unfilled) arrow.

**Influence  $\beta_t \rightarrow F_{ti,flux}$ .** From Eq. (1) follows that  $F_{ti,flux}$  decreases monotonically from  $\alpha_t$  to 0 when  $\beta_t$  is increased from 0 to 1. The physical reason is that when a larger fraction of ions is back-attracted, the ionization degree in the flux to the substrate decreases. The arrow  $\beta_t \rightarrow F_{ti,flux}$  becomes red (unfilled).

**Influence  $\beta_t \rightarrow F_{DR,sput}$ .** Also, here, Eq. (2) gives a negative influence: increasing  $\beta_t$  decreases  $(1 - \alpha_t\beta_t)$ . Material is lost from the total deposition flux (ions and neutrals) when more ions are back-attracted. The arrow  $\beta_t \rightarrow F_{DR,sput}$  is, therefore, drawn red (unfilled).

For the mechanisms to the left in Fig. 7, i.e., the arrows from the process parameters (left column) to the discharge parameters  $\alpha_t$  and  $\beta_t$  (middle column), the situation is different. Here, the not fully understood HIPIMS discharge physics comes into play. The colors of these arrows, therefore, strictly apply only to the Ti/Ar

system studied here, being based on the experimental data and the analysis given in Sec. III B. Two arrows on the left side are drawn red (open) but with dashed lines. They represent two anticorrelations,  $J_D \rightarrow \beta_t$  and  $p_{gas} \rightarrow \alpha_t$ , that were identified in the analysis of the data.<sup>34,40</sup> These mechanisms have a smaller relevance for the method of optimization discussed here and are left out of this discussion. For the remaining mechanisms, we again go from the top down.

**Influence  $J_D \rightarrow \alpha_t$ .** Both the IRM runs carried out by Butler *et al.*<sup>34</sup> and the experiments by Hajihoseini *et al.*<sup>37</sup> show that  $\alpha_t$  generally increases with increasing  $J_D$ . For an example, see the  $J_D$  values from Hajihoseini *et al.* which are inserted at the top of Fig. 1 at appropriate  $\alpha_t$  values. The physical reason for this correlation between  $\alpha_t$  and  $J_D$  is that the sputtered species leave the target with a typical sputter speed of a few kilometers per second<sup>43</sup> and then pass through the hot and dense plasma of the ionization region during a finite time. The question is what fraction of the sputtered species becomes ionized during the passage. Electron impact ionization dominates over other mechanisms, and therefore, this fraction increases with increased electron (plasma) density. Higher currents correspond to higher plasma densities and therefore increase the probability that sputtered atoms become ionized. For example, IRM runs based on the discharges from Hajihoseini *et al.*<sup>37</sup> give  $n_e [m^{-3}] \approx 4 \times 10^{18} \times J_D [A cm^{-2}]$  as an approximate formula for a magnetron sputtering discharge of this type and size, which agrees well with the findings of Cada *et al.*<sup>44</sup> The arrow  $J_D \rightarrow \alpha_t$  becomes green (filled).

**Influence  $B_{rt} \rightarrow \beta_t$ .** Here, we get a green (filled) arrow  $B_{rt} \rightarrow \beta_t$  in Fig. 7 from the empirical results shown in Fig. 4. Please note that although  $\beta_t$  itself varies with only a few percent, the relevant figure of merit  $(1 - \beta_t)$  varies with several tens of percent, as shown in Sec. III B. The physical reason for the trend in  $\beta_t$  has been proposed to be that a weaker magnetic field gives a reduction in the (time-average macroscopic) back-attracting electric field in the IR.<sup>27,28</sup> Other possibilities can, however, not be excluded. As one example, the potential structures associated with spokes<sup>45</sup> might depend on the magnetic field strength. This could influence the spoke-related kick-out of ions from the IR and thus change  $\beta_t$ .

**Influence  $p_{gas} \rightarrow \beta_t$ .** Here, we have the empirical conclusions from Sec. III B that a higher pressure is correlated with higher back-attraction, see Fig. 5. This is represented by a green (filled) cocorrelation arrow in Fig. 7. The physical reason for this trend in  $\beta_t$  is not understood, and it is in fact somewhat counter-intuitive. One could have expected that a lower working gas density should force the discharge to rely more on back-attraction of ions of the sputtered species and, therefore, a higher  $\beta_t$ . One possibility for the observed opposite trend is that a smaller fraction  $f$  of the applied power goes to Ohmic heating<sup>46</sup> when the pressure is lower, which can also be deduced from Fig. 5. Since Ohmic heating is associated with an electric potential difference  $V_{IR}$  across the ionization region, a lower  $V_{IR}$  for lower pressures might be the reason for a lower  $\beta_t$ .

**Influence  $t_{pulse} \rightarrow \beta_t$ .** The two pulse lengths used in Butler *et al.*<sup>34</sup> and Butler,<sup>40</sup> 100 and 400  $\mu s$ , did not show any clear effect on  $\beta_t$ , probably because both pulses were too long. We, therefore, here rely on the IRM results described in Sec. III B, which showed a significant decrease in  $\beta_t$  for shorter pulses, see Fig. 6(a). The physical mechanism is demonstrated to involve the release of the ions that are in the ionization region at the end of the HIPIMS pulse, see Appendix for details. For shorter pulses, those released



ions experiencing  $\beta_i \approx 0$  become a larger part of all ions in the total flux to the substrate. We get a green (filled) arrow in Fig. 7.

**Influence  $t_{\text{pulse}} \rightarrow \alpha_i$ .** Also here, we rely on IRM modeling with artificially shortened pulses. Figure 6(b) shows that  $\alpha_i$  decreases when  $t_{\text{pulse}}$  is shortened, i.e., a cocorrelation. The physical reasons are discussed at the end of Sec. III B and result in a larger fraction of the sputtered atoms escape ionization when the pulse is shortened. We get a green (solid) arrow from  $t_{\text{pulse}}$  to  $\alpha_i$ . The physical explanation has two components. First, for shorter pulses, a larger fraction of the sputtered atoms is created in the beginning of the pulse, and these atoms have a smaller probability of ionization due to the initial low plasma density. Second, a larger fraction of all sputtered atoms is created close to the pulse end. These atoms have a larger probability to escape ionization, since the electron temperature rapidly drops after the end of the pulse.

Having determined the type of influence (the colors of the arrows) of the mechanisms in Fig. 7, we now turn to their interplay. We do this by going through the effects on the flux parameters (right-hand column) from varying the process parameters (left-hand column). Before doing this, we recall that the arrows here mark the effect when one parameter was varied (for example,  $B_{\text{rt}}$ ), while the other parameters in the same group (in this case,  $J_{\text{D}}$ ,  $p_{\text{gas}}$ , and  $t_{\text{pulse}}$ ) were kept constant. To a first approximation, combined effects, when several variables are changed, are presumably obtained by adding the effects of the individual variable changes.

The color-coding of the arrows in Fig. 7 makes it easy to assess how the change of a process parameter influences a flux parameter. Two arrows of different colors, along a route, mean that an increase in the initial process parameter leads to a decrease in the final flux parameter. An example of this is the relation between a discharge current density increase and the deposition rate,  $J_{\text{D}} \rightarrow \alpha_i \rightarrow F_{\text{DR,sput}}$ . This route has one green and one red arrow, which gives a counter-correlation. A decrease in the current density (while adjusting the frequency so that the average power is kept constant) leads to a higher deposition rate, a desirable effect. However, the other route starting with current density,  $J_{\text{D}} \rightarrow \alpha_i \rightarrow F_{\text{ti,flux}}$ , has two arrows of the same color, which means a cocorrelation. A decrease in current density, therefore, also has the undesirable effect of a decrease in the ionized flux fraction. This is precisely the dilemma discussed in Sec. II above, which is illustrated in Fig. 1 and which necessitates the HiPIMS compromise.

For two of the three remaining process parameters,  $B_{\text{rt}}$  and  $p_{\text{gas}}$ , there are relatively weak cocorrelations with  $\beta_i$  (narrow, green arrows to the left), followed by strong anticorrelations from  $\beta_i$ , both to  $F_{\text{ti,flux}}$  and  $F_{\text{DR,sput}}$  (broader, red arrows to the right). All four routes from the pair ( $B_{\text{rt}}$ ,  $p_{\text{gas}}$ ) to  $F_{\text{ti,flux}}$  and  $F_{\text{DR}}$  thus contain one red and one green arrow, and therefore, lowering them always lead to desirable effects. No compromises need to be made here: the lowest possible values of the magnetic field and the working gas pressure give an optimized discharge.

For the remaining process parameter,  $t_{\text{pulse}}$ , the situation is more complicated. In the flow chart in Fig. 7, there are, in both routes  $t_{\text{pulse}} \rightarrow F_{\text{DR,sput}}$ , one green and one red arrow. This gives a net anticorrelation, and therefore, the deposition rate (as quantified by  $F_{\text{DR,sput}}$ ) is increased by shortening the pulse length. For the two routes  $t_{\text{pulse}} \rightarrow F_{\text{ti,flux}}$ ; however, the upper route contains two green arrows (a net cocorrelation), while the lower route contains one red

and one green arrow (a net anticorrelation). Thus, we have two counteracting influences from  $t_{\text{pulse}}$  to  $F_{\text{ti,flux}}$ . However, the IRM modeling results given in the Appendix show that, in the studied pulses, these closely balance each other: the variation of the pulse length gave almost no net effect on the time-averaged degree of ionization in the flux. In summary, we can conclude that also the pulse length should be minimized. This maximizes the deposition rate, through both influence routes  $t_{\text{pulse}} \rightarrow F_{\text{DR,sput}}$ , while it has little effect on the ionized flux fraction due to the balance between the two counteracting influence routes  $t_{\text{pulse}} \rightarrow \alpha_i \rightarrow F_{\text{ti,flux}}$  and  $t_{\text{pulse}} \rightarrow \beta_i \rightarrow F_{\text{ti,flux}}$ .

We propose that an optimization procedure based on the findings above can suitably be separated into two separate sub-tasks. One is to make the HiPIMS compromise, i.e., to decide a minimum required level of ionization, in the flux to the substrate, for the application in question. This value can in practice easily be implemented by varying  $J_{\text{D}}$ . The other subtask is to choose the remaining four process parameters to achieve the maximum deposition rate for the chosen level of ionization. Here is a procedure in two steps which uses this approach to maximize the deposition rate in HiPIMS:

- (1) Step 1: Choose the magnetic field strength, the working gas pressure, and the pulse length with the goal to minimize  $\beta_i$ . For the Ti/Ar system (and probably also for other systems where the target and gas properties are similar to Ti and Ar), each of the three process parameters of magnetic field strength, working gas pressure, and pulse length should be minimized as far as compatible with (1) the choice of the other two, and (2) the need to ignite the discharge and reach a desired discharge current amplitude  $J_{\text{D}}$ .
- (2) Step 2: Choose the lowest discharge current in the pulse that gives the desired properties of the deposited film for the application in question. While varying the discharge current, the pulse frequency  $f_{\text{pulse}}$  shall be adjusted to keep the average power fixed.

Please note that the present study assumes single, isolated HiPIMS pulses. More advanced pulse patterns should make further improvements possible but would call for modified optimization procedures. As one example, the HiPIMS pulses can be built up of pulse trains<sup>32,33</sup> with an internal pulse frequency  $f_{\text{train}}$ . If  $f_{\text{train}}$  is sufficiently high, residual plasma in the afterglow can make the ignition of the subsequent subpulses in the train easier. Thereby, shorter individual subpulses can be used, lowering  $\beta_i$  as discussed in Sec. III B. Other versions of more advanced pulse patterns will be discussed in a forthcoming paper.

#### IV. SUMMARY AND CONCLUSIONS

We have explored the possibilities to optimize HiPIMS discharges by varying five external process parameters: discharge current density, the pulse length, working gas pressure, magnetic field strength, and the degree of magnetic unbalance. In the analysis, we have used two dimensionless parameters for the deposition flux, which are not quite standard,  $F_{\text{ti,flux}}$  and  $F_{\text{DR,sput}}$ . They both refer to the total atom and ion fluxes from the IR to the DR that are in principle available for deposition. Using the total fluxes has

the advantage that they are independent of the substrate size and position. As a measure of the deposition rate, we use the total (ion plus neutral) flux to the DR, normalized to the total flux of the sputtered material in the actual discharge, denoted as  $F_{\text{DR,sput}}$ . The advantage of using  $F_{\text{ti,flux}}$  and  $F_{\text{DR,sput}}$  is that these variables give the simple explicit analytical relations in Eqs. (1) and (2), which are central for the present analysis. One major drawback is that it becomes unclear how good the deposition rate is in comparison to dcMS. A measure of more direct relevance than  $F_{\text{DR,sput}}$  for the user is  $F_{\text{DR,dc}}$ : the flux to the DR, in a studied HiPIMS discharge, divided by that in a dcMS discharge operated at the same average power.<sup>10,19,21</sup> The difference between  $F_{\text{DR,dc}}$  and  $F_{\text{DR,sput}}$  is estimated in the Appendix. We find that typically, in the Ti/Ar system studied here, the more established normalization to dcMS ( $F_{\text{DR,dc}}$ ) gives a value that is only 25% different from our normalization to the sputter yield ( $F_{\text{DR,sput}}$ ). We conclude that this difference between  $F_{\text{ti,flux}}$  and  $F_{\text{DR,sput}}$  is not important for our conclusions regarding optimization.

A key observation in this work is that in HiPIMS a high ionized flux fraction always comes at the cost of a low deposition rate. This makes the HiPIMS compromise necessary. We have here described an optimization procedure in which the discharge current density amplitude is reserved for making this compromise. This leaves four “free” process parameters to be optimized: magnetic field strength, degree of magnetic unbalance, working gas pressure, and the pulse length. As a figure of merit, we propose  $(1 - \beta_t)$ , which is the fraction of the ionized sputtered material that escapes back-attraction to the cathode target and where  $\beta_t$  is the back-attracted ion fraction. We have explored the possibilities to maximize  $(1 - \beta_t)$  by varying the four free process parameters empirically, based on data from two discharges with Ti targets in Ar working gas. The discharges were first modeled in order to convert measured discharge data to values of  $\beta_t$ . The combined effects of varying different process parameters were then analyzed using a process flow chart model.

The effect of varying the degree of magnetic unbalance in the studied range was small. For the remaining three parameters, we find that an optimum is achieved by minimizing the magnetic field strength, minimizing the working gas pressure, and minimizing the pulse length. The situation is, however, not quite so simple since there are conflicts between these. The magnetic field must, for example, be strong enough so that the magnetron effect is maintained, and for a given magnetic field, the discharge cannot be ignited if the working gas pressure is too low. Also, there is a conflict between a short pulse length and the need to get a discharge current density high enough for a desired ionization in the material flux. Other conflicts will very likely be identified when optimization is tried in practice. We can here only conclude that each of the three parameters  $B_{\text{rt}}$ ,  $p_{\text{gas}}$ , and  $t_{\text{pulse}}$  shall be made as small as possible, given the choice of the other two, and the need to ignite the discharge and reach a desired pulse current density  $J_D$ . The possible gain in the deposition rate through such an optimization can be quite large, as can be seen from two examples in the studied Ti/Ar system: for a fixed 30% ionized flux fraction, there is an improvement in the deposition rate, by a factor of around two, when the pressure or the magnetic field strength is lowered, from 2 to 0.5 Pa or from 23.8 to 11.1 mT, respectively. Combined effects, when

several variables are changed, are likely obtained by adding the effects of the individual variable changes. Finally, we note that our results strictly apply only to the studied Ti/Ar system. The results probably would be, at least quantitatively, different for other combinations of the target material and the working gas. Of particular interest to explore are targets with much different self-sputtering yields than Ti, and reactive discharges where  $\text{N}_2$  or  $\text{O}_2$  is added to the working gas.

## ACKNOWLEDGMENTS

Discussions with Ulf Helmersson are gratefully acknowledged. N.B. gratefully acknowledges the hospitality of CNRS and University Paris-Sud, Orsay, where much of this study was conducted. N.B. also acknowledges the support from Svensk-Franska Stiftelsen. This work was partially supported by the Icelandic Research Fund (Grant Nos. 130029 and 196141), the Swedish Research Council (Grant No. VR 2018-04139), the Swedish Government Strategic Research Area in Materials Science on Functional Materials at Linköping University (Faculty Grant SFO-Mat-LiU No. 2009-00971), and the Free State of Saxony and the European Regional Development Fund (Grant No. 100336119).

## APPENDIX: DETAILS ON EXPERIMENTS AND MODELING

Here, we give details on the experiments, and on the modeling, which were used in the analysis of the Ti/Ar system.

### 1. CHANGING THE MAGNETIC FIELD: THE EFFECT ON $\beta_t$

In the study by Hajjoseini *et al.*,<sup>37</sup> the confining magnetic field was varied, in which a 4" Ti target was used. The working gas pressure was fixed at 1 Pa, and the pulse length was fixed at 100  $\mu\text{s}$ . The deposition system was equipped with a VTech magnetron assembly (Gencoa, UK), where the central magnet and the outer ring magnet could be displaced individually in the axial direction by micrometer screws. In this way, the magnetic field above the racetrack center ( $z = 11$  mm) was varied in the range of 11.1–23.8 mT. The degree of unbalance was quantified by the distance  $z_{\text{null}}$  from the target surface to the magnetic null point, which is a characteristic feature of type II magnetrons. The range  $43 \leq z_{\text{null}} \leq 74$  mm was covered, with the lower value corresponding to the most strongly unbalanced case. Seven different magnetic field configurations were studied. The individual displacements of the inner and the outer magnets made it possible to disentangle the effect of the magnetic field strength from the effect of the degree of unbalance. For each magnetic field configuration, HiPIMS discharges were studied both in a constant-voltage mode and in a constant-peak-current mode, but only the latter results will be used here. The peak discharge current  $I_{\text{D,peak}}$  was in this mode set to 40 A ( $J_{\text{D,peak}} = 0.5 \text{ A/cm}^2$ ) by adjusting the voltage. The average power was always maintained at 300 W by adjusting the pulsing frequency. Both the ionized flux fraction and the deposition rate were measured, using a gridless quartz crystal microbalance (QCM) sensor, which can measure the deposition rate from both ions and neutrals separately by varying a voltage applied to the biased top QCM electrode, allowing for fast

measurements (~1 min). The design of the device is described in detail by Kubart *et al.*<sup>47</sup> In order to obtain a benchmark for the deposition rates, 300 W dcMS discharges were operated at each magnetic field configuration. A more extended description of the experiments and the data analysis are given by Hajihoseini *et al.*<sup>37</sup>

No systematic effects were found on the deposition rate or on the ionized flux fraction, when the degree of unbalance was varied in the studied range.<sup>37</sup> To illustrate the trends with the magnetic field strength at fixed peak discharge current, a representative subset of the measured deposition rates and ionized flux fractions is shown in Table II. These data were measured at a typical substrate position, over the target center at  $z = 70$  mm. Taking all the data into account (not only the subset in Table II), the following trends were observed when the magnetic field strength was reduced by about a factor two, from 23.8 to 11.1 mT above the racetrack center:

- (1) For dcMS, the deposition rate showed a small increase by ~10%, but there were also variations of about  $\pm 5\%$  from this trend.
- (2) For HiPIMS, there were significant, and desirable, trends in both the deposition rate and the ionized flux fraction. The former increased by 38% and the latter by 53% as the magnetic field strength was reduced, when operating in the fixed peak-current mode.

For the evaluation of  $\beta_t$ , we follow Hajihoseini *et al.*<sup>37</sup> and combine Eqs. (1) and (2) into an equation that gives  $\beta_t$  as a function of  $F_{ti,flux}$  and  $F_{DR,sput}$

$$\beta_t = \frac{1 - F_{DR,sput}}{1 - F_{DR,sput}(1 - F_{ti,flux})}. \quad (A1)$$

Of the two parameters to the right in this equation, only  $F_{ti,flux}$  is directly measured by the QCM detector, while  $F_{DR,sput}$  has to be calculated. This is possible by combining the measured deposition rates in HiPIMS with those in dcMS at the same average power. The calculation is described elsewhere<sup>37</sup> and involves three factors, one that accounts for the difference between HiPIMS and dcMS in the number of ions that hit the target per second (approximately given by the time-averaged discharge current), one that accounts for the ion composition (the fractions of ions of the sputtered species), and one that accounts for differences in the applied potential that changes the sputter yields of the ions. Figure 4 shows the  $\beta_t$  values from Eq. (A1), using the values of  $F_{ti,flux}$  and  $F_{DR,sput}$

**TABLE II.** Selection of results from Hajihoseini *et al.* (Ref. 37) measured at a typical substrate position, above the target center at  $z = 70$  mm using a gridless QCM.

Magnet	dcMS		HiPIMS fixed current	
	Dep. rate (A/min)	$F_{ti,flux}$ (%)	Dep. rate (A/min)	$F_{ti,flux}$ (%)
Weakest $B_{rt}$	116	~0	47	17.2
Strongest $B_{rt}$	92	~0	34	11

obtained this way. There is a clear trend such that  $\beta_t$  is lowered when the magnetic field strength is reduced. This reduction in  $\beta_t$  is the common cause for both the higher ionized flux fraction and the higher deposition rate in Table II. This anticorrelation between  $\beta_t$  and the pair  $(F_{ti,flux}, F_{DR,sput})$  follows directly from Eqs. (1) and (2) and is represented by red (open) arrows in Fig. 7.

## 2. CHANGING THE WORKING GAS PRESSURE: THE EFFECT ON $\beta_t$

In the second HiPIMS discharge, from the experimental study by Lundin *et al.*<sup>39</sup> that was analyzed using the IRM by Butler *et al.*,<sup>34</sup> a 2" magnetron target was used. The experiments were made for all 12 combinations of two working gas pressures ( $p_{gas} = 0.5$  and 2 Pa), three different peak discharge current densities ( $J_{D,peak} = 0.7, 1.0,$  and  $2.5 \text{ A cm}^{-2}$ ), and two pulse lengths (100 and 400  $\mu\text{s}$ ). In each of these combinations, the peak discharge current density was first set by adjusting the discharge voltage. After this, the pulse frequency was adjusted to obtain the same average discharge power for all cases (200 W). Figure 8 gives typical data from these discharges.  $F_{ti,flux}$  is seen to increase with decreasing working gas pressure, typically 10%–30% (depending on discharge current and pulse length) when the pressure was decreased from 2 to 0.5 Pa (the shift between the upper and lower curves in Fig. 8). There is no clear trend with varying the pulse length, and therefore, the 400  $\mu\text{s}$  pulses are not shown.

The deposition rates in this experiment were not measured for the corresponding dcMS cases. Therefore, there was no absolute calibration of the deposition rates;  $F_{DR,sput}$  could not be evaluated, and thus,  $\beta_t$  cannot be obtained from Eq. (A1) as we did above for the other experiment. Instead, we resort to modeling made by Butler *et al.*<sup>34</sup> with the IRM, a plasma chemical, zero dimensional,

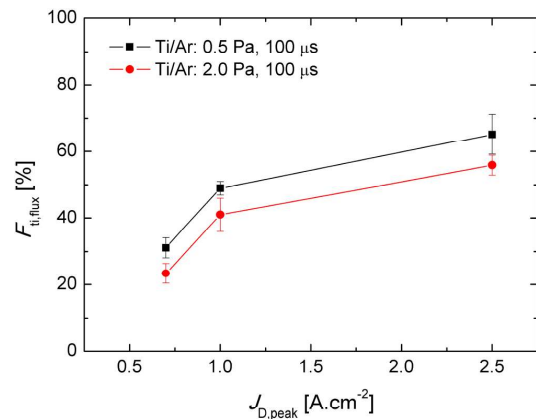


**FIG. 8.** Collected results from measurements of the ionized flux fraction from Lundin *et al.* (Ref. 39) of HiPIMS discharges using a 2" Ti target at two different Ar gas pressures, three different peak discharge current densities, and 100  $\mu\text{s}$ -long pulses.

and time-dependent model for the ionization region above the racetrack. The IRM is written in such a way that experimental data are used to constrain the model so that it reproduces a specific magnetron discharge pulse.<sup>35,48</sup> A short description of this fitting procedure is needed here. First, the IRM model is adapted to the discharge in question as regards to geometry, working gas species, pressure, and target material, and then a HiPIMS pulse is chosen for modeling. The measured discharge voltage  $V_D(t)$  and discharge current  $I_D(t)$  are to this purpose combined to give the electric power  $P_{\text{elec}}(t) = V_D(t)I_D(t)$ , and two fitting parameters are introduced: the ion back-attraction probability during pulse  $\beta_{t,\text{pulse}}$ , and a second parameter, which quantifies the fraction of  $P_{\text{elec}}(t)$  that goes to the electrons in the discharge. In the current version of the code, this second parameter is denoted by  $f$ . For the present discussion, it is sufficient to know that a higher  $f$  corresponds to more efficient electron energization. In different versions of the IRM, different versions of the energy fitting parameter have been used, depending on if one (thermal) or two (thermal plus hot) electron populations are used, and on whether Ohmic heating of the electrons is included or not. The present version is the most advanced of these alternatives. For a survey of various IRM versions, see Huo *et al.*<sup>35</sup>

When the model is run for a pulse, with an assumed combination  $(f, \beta_{t,\text{pulse}})$ , it produces all the (time-dependent) volume-averaged densities and temperatures of the gas and the plasma species inside the IR and also the various particle fluxes out of the IR. The ion and electron fluxes to and from the target are used to obtain a modeled time profile  $I_{\text{IRM}}(t)$  of the discharge current during the pulse. For Fig. 9, the model is first run for  $40 \times 50 = 2000$  different  $(f, \beta_{t,\text{pulse}})$  combinations in the entire possible ranges  $[0,1]$  of  $f$  and  $\beta_{t,\text{pulse}}$ , and then the model is locked to the best case of these. The usual condition for locking the model<sup>35,48</sup> is that this time profile shall agree

with the measured discharge current waveform,  $I_{\text{IRM}}(t) \approx I_D(t)$ . This condition typically constrains  $f$  and  $\beta_{t,\text{pulse}}$  to a crescent-shaped area in the  $(f, \beta_{t,\text{pulse}})$  parameter space, as exemplified by the gray-shaded area in Fig. 9. As can be seen this fitting alone leaves a rather large uncertainty as regards the correct value of  $\beta_{t,\text{pulse}}$ . However, for the here investigated discharges, Butler *et al.*<sup>34</sup> introduced the measured ionized flux fraction  $F_{\text{Ti,flux}}$  as a means to further constrain the model. The condition is that the IRM shall reproduce also  $F_{\text{Ti,flux}}$ . This condition, taken alone, constrains the model to the area marked with blue dots in Fig. 9. Together, the two constraints on  $I_D(t)$  and  $F_{\text{Ti,flux}}$  lock the pair  $(f, \beta_{t,\text{pulse}})$  to the small area marked with red dots. Figure 5 in the main text shows the locations of 12 such best-fit pairs  $(f, \beta_{t,\text{pulse}})$ , one each for the experimentally studied combinations of pressure, discharge current, and pulse length first reported by Lundin *et al.*<sup>39</sup> Each discharge is here represented by a cross or a circle at the best fit  $(f, \beta_{t,\text{pulse}})$  combination from the IRM model. The  $\beta_{t,\text{pulse}}$  values of these fits are the data we will use here. For each of the six combinations of the pulse length and current, there are two data points for different working gas pressures, which means that we have six pairs of data that satisfy the condition that only the pressure is changed. This gives six values of  $\Delta\beta_{t,\text{pulse}} = (\beta_{t,\text{pulse}}(2\text{ Pa}) - \beta_{t,\text{pulse}}(0.5\text{ Pa}))$ . The average of these six values can be rewritten as

$$\langle \Delta\beta_{t,\text{pulse}} \rangle = \frac{\sum \beta_{t,\text{pulse}}(2\text{ Pa}) - \sum \beta_{t,\text{pulse}}(0.5\text{ Pa})}{6} \quad (\text{A2})$$

The average  $\langle \Delta\beta_{t,\text{pulse}} \rangle$  has a simple geometrical interpretation in Fig. 5: the difference, in  $\beta_{t,\text{pulse}}$ , from the average position of the data points at 2 Pa to the average position of the data points at 0.5 Pa.

Butler *et al.*<sup>34</sup> discussed an approximation made in the analysis above. It concerns the  $\text{Ti}^+$  ions that are in the ionization region at the end of the HiPIMS pulse. Since the back-attracting electric field disappears at the pulse end, these ions may experience a reduced  $\beta_t(t)$ . For a 100  $\mu\text{s}$ -long pulse, the authors estimated that the time-integrated number of  $\text{Ti}^+$  ions going from the IR to the DR is approximately ten times the number of  $\text{Ti}^+$  ions that are left in the IR at the pulse end. If these “afterglow ions” retain their directed velocity from the sputtering process, then they are all moving away from the target. For this case, which would give an effective  $\beta_t(t) = 0$  after the pulse, about 10% of the time-integrated (pulse + afterglow) ions flow to the diffusion region was estimated to come during the afterglow. Since there are also neutrals in the afterglow, these 10% (of all ions) should influence the total (time averaged)  $F_{\text{Ti,flux}}$  by less than 10%. The IRM model fitting made by Butler *et al.*<sup>34</sup> was made disregarding this effect. This approximation was supported by the fact that a change from a 100  $\mu\text{s}$  pulse to a 400  $\mu\text{s}$  pulse gave, at most, a marginal influence on the ionized flux fraction.

### 3. CHANGING THE PULSE LENGTH: THE EFFECT ON $\beta_t$

The influence of shorter pulses on the deposition rate and the ionized flux fraction could not be assessed directly from measured data since no pulses shorter than 100  $\mu\text{s}$  were used. Instead, we used and extend a study by Rudolph *et al.*<sup>42</sup> The study was based on two

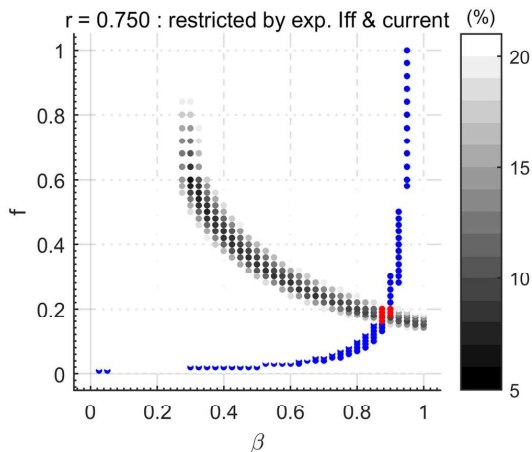


FIG. 9. How  $\beta_t$  is obtained by modeling. An illustration of how the fitting procedure locks the value of  $\beta_{t,\text{pulse}}$  in the IRM code as described in the text.



experimental discharges with 100- $\mu$ s-long pulses with two different peak discharge currents from Hajihoseini *et al.*,<sup>37</sup> which were modeled using the IRM. A computer experiment was made consisting of artificially shortening these two pulses. The shortened pulses in that study had approximately the same peak discharge current as the full length (100- $\mu$ s-long pulse), therefore fulfilling the condition for constructing the flow chart of Fig. 7 that only one process parameter at a time is varied. Only the shortest pulse length investigated (40  $\mu$ s) had a roughly 22% (16%) lower peak current compared to the reference discharge (pulse length of 100  $\mu$ s) with  $J_{D,peak} = 41$  A (76 A). Here, we show the calculation of the internal discharge parameters  $\alpha_i$  and  $\beta_i$  that were not discussed in the previous work.

The IRM uses  $\beta_i(t)$  to calculate the ion fluxes by imposing that, in each time step, the fraction  $\beta_i(t)$  of the ions that leave the ionization region goes to the target, and, consequently, the remaining fraction  $[1 - \beta_i(t)]$  to the DR. In the afterglow, no more ions are back-attracted to the cathode due to the absence of the electric field over the ionization region. In the afterglow, the authors assume no redeposition on the cathode. The time-dependent  $\beta_i(t)$  then becomes

$$\beta_i(t) = \begin{cases} \beta_{i,pulse} & \text{during the pulse,} \\ 0 & \text{between pulses.} \end{cases} \quad (A3)$$

The time-averaged  $\beta_i$  is calculated according to Eq. (A4) for a time period including the pulse and the afterglow,

$$\beta_i = \frac{\sum \text{back-attracted target ions}}{\sum \text{target species ionization events}}. \quad (A4)$$

The decreasing average  $\beta_i$  for shorter pulses [Fig. 6(a)] is a direct consequence of a decreased contribution to the DR flux from the pulse-on time. As the flux from the afterglow typically has a higher ionized flux fraction compared to the flux leaving the IR during the pulse,<sup>42</sup> the time-averaged ionized flux fraction  $F_{i,flux}$  is not adversely affected.

The ionization probability  $\alpha_i$  describes the probability that a sputtered metal species is ionized during a pulse. It is calculated according to the following equation:

$$\alpha_i = \frac{\sum \text{target species ionization events}}{\sum \text{sputtered target species}}. \quad (A5)$$

The slight decrease in ionization probability for shorter pulses [Fig. 6(b)] at least for the pulse lengths down to 60  $\mu$ s stems from the reduced time for ionization as the pulse lengths shortens. A stronger decrease for the shortest pulse length of 40  $\mu$ s is in addition due to the lower peak current for this pulse length [Fig. 6(b)]. The decrease in ionization probability  $\alpha_i$  does not affect the ionized flux fraction because of the simultaneous decrease in the target ion back-attraction  $\beta_i$ , which compensates for the lower ionization probability. That results in a constant ionized flux fraction independent of pulse length—at least for the range of pulse lengths investigated.<sup>42</sup>

#### 4. DIFFERENCE BETWEEN $F_{DR,dc}$ AND $F_{DR,sput}$

Finally, let us estimate the difference between the two different ways to normalize the deposition rate,  $F_{DR,dc}$  and  $F_{DR,sput}$ . For  $F_{DR,dc}$ , the total flux (atoms and ions of the target species), to the DR in the HiPIMS discharge, is divided by the sputtered flux from the target to the IR in a dcMS discharge at the same average power; for  $F_{DR,sput}$ , it is divided by the sputtered flux in the same HiPIMS discharge. Assuming that the sputtered neutral fluxes have the same probability to reach the DR in the HiPIMS as in the dcMS discharge, the difference between  $F_{DR,dc}$  and  $F_{DR,sput}$  is given by the difference between the sputtered fluxes from the target in the two discharges (the studied HiPIMS discharge and a dcMS discharge at the same average power). These fluxes are given by the time-averaged ion current to the target, multiplied by the effective sputter yield  $Y_{eff}$ .  $F_{DR,dc}$  is, at constant power, proportional to  $1/V_D$ , and  $F_{DR,sput}$  is a function of both the discharge voltage  $V_D$  and the ion composition in the ion current to the target. Following Hajihoseini *et al.*,<sup>37</sup> we use  $\zeta$  to denote the fraction of the working gas ions in the ion current to the target [the remaining fraction  $(1 - \zeta)$  being ions of the sputtered species]. The sputter yield of Ar<sup>+</sup> ions on Ti is about 15% larger than that for Ti<sup>+</sup> ions at the same bombarding energy.<sup>37</sup> In our discharges,  $V_D$  is typically in the range of 600–1000 V, and the sputter yield is approximately proportional to the square root of the ion bombarding energy  $q_i V_D$ .<sup>37</sup> At constant power, a higher pulse voltage is compensated by a lower (time-averaged) current, and the sputter yield per unit power, therefore, is  $\propto 1/\sqrt{V_D}$ . For an estimate of a typical difference between  $F_{DR,dc}$  and  $F_{DR,sput}$ , we take a HiPIMS discharge in the middle of the ranges in voltage and ion composition with  $V_D = 800$  V and  $\zeta = 0.5$ . We compare it with a dcMS discharge with  $V_D = 600$  V and  $\zeta = 1$ . The sputtered flux in the dcMS discharge is larger by two factors: one due to the voltage difference and one due to the 7.5% higher yield for pure argon ions than for a 50/50 mix of Ar and Ti ions. This gives  $\frac{F_{DR,sput}}{F_{DR,dc}} \approx \frac{800}{600} \times \sqrt{\frac{600}{800}} \times 1.075 = \sqrt{\frac{800}{600}} \times 1.075 = 1.24$ . We conclude that typically, for the Ti/Ar system studied here, a normalization to the sputter yield ( $F_{DR,sput}$ ) gives a value that is 20%–30% higher than the more established normalization to dcMS at the same power ( $F_{DR,dc}$ ).

#### REFERENCES

- J. T. Gudmundsson and D. Lundin, "Introduction to magnetron sputtering," *High Power Impulse Magnetron Sputtering Fundamentals Technologies Challenges and Application*, edited by D. Lundin, T. Minea, and J. T. Gudmundsson (Elsevier, Amsterdam, 2020), pp. 1–48.
- J. Hopwood, *Phys. Plasmas* **5**, 1624 (1998).
- J. A. Hopwood, "The role of ionized physical vapor deposition in integrated circuit fabrication," *Ionized Physical Vapor Deposition*, edited by J. A. Hopwood (Academic, San Diego, CA, 2000), pp. 1–7.
- W. M. Holber, "Ionization by microwave electron cyclotron resonance plasma," *Ionized Physical Vapor Deposition*, edited by J. A. Hopwood (Academic, San Diego, CA, 2000), pp. 67–94.
- W. M. Holber, J. S. Logan, H. J. Grabarz, J. T. C. Yeh, J. B. O. Caughman, A. Sugerma, and F. E. Turene, *J. Vac. Sci. Technol. A* **11**, 2903 (1993).
- M. S. Barnes, J. C. Forster, and J. H. Keller, U.S. Patent 5,178,739 (January 12, 1993).
- S. M. Rosnagel and J. Hopwood, *Appl. Phys. Lett.* **63**, 3285 (1993).

- <sup>8</sup>S. M. Rossnagel, *J. Vac. Sci. Technol. B* **12**, 449 (1994).
- <sup>9</sup>V. Kouznetsov, K. Macák, J. M. Schneider, U. Helmersson, and I. Petrov, *Surf. Coat. Technol.* **122**, 290 (1999).
- <sup>10</sup>M. Samuelsson, D. Lundin, J. Jensen, M. A. Raadu, J. T. Gudmundsson, and U. Helmersson, *Surf. Coat. Technol.* **205**, 591 (2010).
- <sup>11</sup>V. Sittinger, F. Ruske, W. Werner, C. Jacobs, B. Szyszka, and D. J. Christie, *Thin Solid Films* **516**, 5847 (2008).
- <sup>12</sup>M. Lattemann, U. Helmersson, and J. E. Greene, *Thin Solid Films* **518**, 5978 (2010).
- <sup>13</sup>H. Hajihoseini and J. T. Gudmundsson, *J. Phys. D Appl. Phys.* **50**, 505302 (2017).
- <sup>14</sup>S. Konstantinidis, J. P. Dauchot, and M. Hecq, *Thin Solid Films* **515**, 1182 (2006).
- <sup>15</sup>J. Alami, P. Eklund, J. M. Andersson, M. Lattemann, E. Wallin, J. Bohlmark, P. Persson, and U. Helmersson, *Thin Solid Films* **515**, 3434 (2007).
- <sup>16</sup>F. Cemin, M. Tsukamoto, J. Keraudy, V. G. Antunes, U. Helmersson, F. Alvarez, T. Minea, and D. Lundin, *J. Phys. D Appl. Phys.* **51**, 235301 (2018).
- <sup>17</sup>G. Greczynski *et al.*, *Thin Solid Films* **556**, 87 (2014).
- <sup>18</sup>A. P. Ehasarian, J. G. Wen, and I. Petrov, *J. Appl. Phys.* **101**, 054301 (2007).
- <sup>19</sup>U. Helmersson, M. Lattemann, J. Bohlmark, A. P. Ehasarian, and J. T. Gudmundsson, *Thin Solid Films* **513**, 1 (2006).
- <sup>20</sup>*High Power Impulse Magnetron Sputtering Fundamentals, Technologies, Challenges and Applications*, edited by D. Lundin, T. Minea, and J. T. Gudmundsson (Elsevier, Amsterdam, 2020).
- <sup>21</sup>J. T. Gudmundsson, N. Brenning, D. Lundin, and U. Helmersson, *J. Vac. Sci. Technol. A* **30**, 030801 (2012).
- <sup>22</sup>D. J. Christie, *J. Vac. Sci. Technol. A* **23**, 330 (2005).
- <sup>23</sup>H. Yu, L. Meng, M. M. Szott, J. T. Meister, T. S. Cho, and D. N. Ruzic, *Plasma Sources Sci. Technol.* **22**, 045012 (2013).
- <sup>24</sup>P. Raman, I. A. Shchelkanov, J. McLain, and D. N. Ruzic, *J. Vac. Sci. Technol. A* **33**, 031304 (2015).
- <sup>25</sup>P. Raman, I. Shchelkanov, J. McLain, M. Cheng, D. Ruzic, I. Haehnlein, B. Jurczyk, R. Stubbers, and S. Armstrong, *Surf. Coat. Technol.* **293**, 10 (2016).
- <sup>26</sup>J. Čapek, M. Hála, O. Zabeida, J. E. Klemberg-Sapieha, and L. Martinu, *J. Phys. D Appl. Phys.* **46**, 205205 (2013).
- <sup>27</sup>J. W. Bradley, A. Mishra, and P. J. Kelly, *J. Phys. D Appl. Phys.* **48**, 215202 (2015).
- <sup>28</sup>A. Mishra, P. J. Kelly, and J. W. Bradley, *Plasma Sources Sci. Technol.* **19**, 045014 (2010).
- <sup>29</sup>S. Konstantinidis, J. P. Dauchot, M. Ganciu, A. Ricard, and M. Hecq, *J. Appl. Phys.* **99**, 013307 (2006).
- <sup>30</sup>I. L. Velicu, V. Tiron, and G. Popa, *Surf. Coat. Technol.* **250**, 57 (2014).
- <sup>31</sup>A. Ferrec, J. Kéraudy, and P. Y. Jouan, *Appl. Surf. Sci.* **390**, 497 (2016).
- <sup>32</sup>O. Antonin, V. Tiron, C. Costin, G. Popa, and T. M. Minea, *J. Phys. D Appl. Phys.* **48**, 015202 (2015).
- <sup>33</sup>P. M. Barker, E. Lewin, and J. Patscheider, *J. Vac. Sci. Technol. A* **31**, 060604 (2013).
- <sup>34</sup>A. Butler, N. Brenning, M. A. Raadu, J. T. Gudmundsson, T. Minea, and D. Lundin, *Plasma Sources Sci. Technol.* **27**, 105005 (2018).
- <sup>35</sup>C. Huo, D. Lundin, J. T. Gudmundsson, M. A. Raadu, J. W. Bradley, and N. Brenning, *J. Phys. D Appl. Phys.* **50**, 354003 (2017).
- <sup>36</sup>J. Vlček and K. Burcalová, *Plasma Sources Sci. Technol.* **19**, 065010 (2010).
- <sup>37</sup>H. Hajihoseini, M. Čada, Z. Hubička, S. Únaldi, M. A. Raadu, N. Brenning, J. T. Gudmundsson, and D. Lundin, *Plasma* **2**, 201 (2019).
- <sup>38</sup>M. Samuelsson, D. Lundin, K. Sarakinos, F. Björefors, B. Wälivaara, H. Ljungerantz, and U. Helmersson, *J. Vac. Sci. Technol. A* **30**, 031507 (2012).
- <sup>39</sup>D. Lundin, M. Čada, and Z. Hubička, *Plasma Sources Sci. Technol.* **24**, 035018 (2015).
- <sup>40</sup>A. Butler, "Ionization fractions and fitting parameters in HiPIMS Ti deposition with the ionization region model," Master's thesis (Laboratoire de Physique de Gaz et Des Plasmas, Université Paris-Sud, 2018).
- <sup>41</sup>H. Hajihoseini, M. Čada, Z. Hubička, S. Únaldi, M. A. Raadu, N. Brenning, J. T. Gudmundsson, and D. Lundin, *J. Vac. Sci. Technol. A* **38**, 033009 (2020).
- <sup>42</sup>M. Rudolph, N. Brenning, M. A. Raadu, H. Hajihoseini, J. T. Gudmundsson, A. Anders, and D. Lundin, "Optimizing the deposition rate and ionized flux fraction by tuning the pulse length in high power impulse magnetron sputtering" *Plasma Sources Sci. Technol.* (to be published).
- <sup>43</sup>D. Lundin, C. Vitelaru, L. De Poucques, and N. Brenning, *J. Phys. D Appl. Phys.* **46**, 175201 (2013).
- <sup>44</sup>M. Čada, J. T. Gudmundsson, and D. Lundin, "Electron dynamics in high power impulse magnetron sputtering discharges," *High Power Impulse Magnetron Sputtering Fundamentals Technologies Challenges and Applications*, edited by D. Lundin, J. T. Gudmundsson, and T. Minea (Elsevier, Amsterdam, 2020), pp. 81–110.
- <sup>45</sup>N. Brenning, D. Lundin, T. Minea, C. Costin, and C. Vitelaru, *J. Phys. D Appl. Phys.* **46**, 084005 (2013).
- <sup>46</sup>C. Huo, D. Lundin, M. A. Raadu, A. Anders, J. T. Gudmundsson, and N. Brenning, *Plasma Sources Sci. Technol.* **22**, 045005 (2013).
- <sup>47</sup>T. Kubart, M. Čada, D. Lundin, and Z. Hubička, *Surf. Coat. Technol.* **238**, 152 (2014).
- <sup>48</sup>M. A. Raadu, I. Axnäs, J. T. Gudmundsson, C. Huo, and N. Brenning, *Plasma Sources Sci. Technol.* **20**, 065007 (2011).

## References

- Aijaz, A., Lundin, D., Larsson, P., and Helmersson, U. (2010). Dual-magnetron open field sputtering system for sideways deposition of thin films. *Surface and Coatings Technology*, 204(14):2165 – 2169.
- Alami, J., Eklund, P., Andersson, J. M., Lattemann, M., Wallin, E., Bohlmark, J., Persson, P., and Helmersson, U. (2007). Phase tailoring of Ta thin films by highly ionized pulsed magnetron sputtering. *Thin Solid Films*, 515(7-8):3434–3438.
- Alami, J., Sarakinos, K., Mark, G., and Wuttig, M. (2006). On the deposition rate in a high power pulsed magnetron sputtering discharge. *Applied Physics Letters*, 89(15):154104.
- Alami, J., Stranak, V., Herrendorf, A.-P., Hubicka, Z., and Hippler, R. (2015). Design of magnetic field configuration for controlled discharge properties in highly ionized plasma. *Plasma Sources Science and Technology*, 24(4):045016.
- Anders, A. (2004). Observation of self-sputtering in energetic condensation of metal ions. *Applied Physics Letters*, 85(25):6137–6139.
- Anders, A. (2008). Self-sputtering runaway in high power impulse magnetron sputtering: The role of secondary electrons and multiply charged metal ions. *Applied Physics Letters*, 92(20):201501.
- Anders, A. (2010). Deposition rates of high power impulse magnetron sputtering: Physics and economics. *Journal of Vacuum Science and Technology A*, 28(4):783–790.
- Antonin, O., Tiron, V., Costin, C., Popa, G., and Minea, T. M. (2015). On the HiPIMS benefits of multi-pulse operating mode. *Journal of Physics D: Applied Physics*, 48(1):015202.
- Arnalds, U. B., Agustsson, J. S., Ingason, A. S., Eriksson, A. K., Gylfason, K. B., Gudmundsson, J. T., and Olafsson, S. (2007). A magnetron sputtering system for the preparation of patterned thin films and in situ thin film electrical resistance measurements. *Review of Scientific Instruments*, 78(10):103901.
- Barker, P. M., Lewin, E., and Patscheider, J. (2013). Modified high power impulse magnetron sputtering process for increased deposition rate of titanium. *Journal of Vacuum Science and Technology A*, 31(6):060604.
- Behrisch, R. and Eckstein, W. (1993). Sputtering yield increase with target temperature for Ag. *Nuclear Instruments and Methods in Physics Research Section B: Beam Interactions with Materials and Atoms*, 82(2):255–258.
- Binnig, G., Gerber, C., Stoll, E., Albrecht, T., and Quate, C. (1987). Atomic resolution with atomic force microscope. *EPL (Europhysics Letters)*, 3(12):1281.
- Binnig, G., Quate, C. F., and Gerber, C. (1986). Atomic force microscope. *Physical Review Letters*, 56(9):930.

- 
- Birkholz, M. (2006). *Thin Film Analysis by X-Ray Scattering*. WILEY-VCH Verlag, Weinheim, Germany.
- Birkholz, M. (2019). Thin films and multilayers. In Gilmore, C. J., Kaduk, J. A., and Schenk, H., editors, *International Tables for Crystallography: Powder diffraction, Volume H*, chapter 5.4, pages 581–600. International Union of Crystallography, Chester, United Kingdom.
- Bohlmarm, J., Alami, J., Christou, C., Ehiasarian, A. P., and Helmersson, U. (2005). Ionization of sputtered metals in high power pulsed magnetron sputtering. *Journal of Vacuum Science and Technology A*, 23(1):18–22.
- Bohlmarm, J., Lattemann, M., Gudmundsson, J. T., Ehiasarian, A. P., Gonzalvo, Y. A., Brenning, N., and Helmersson, U. (2006a). The ion energy distributions and ion flux composition from a high power impulse magnetron sputtering discharge. *Thin Solid Films*, 515(5):1522–1526.
- Bohlmarm, J., Östbye, M., Lattemann, M., Ljungcrantz, H., Rosell, T., and Helmersson, U. (2006b). Guiding the deposition flux in an ionized magnetron discharge. *Thin Solid Films*, 515(4):1928–1931.
- Bradley, J. W., Mishra, A., and Kelly, P. J. (2015). The effect of changing the magnetic field strength on HiPIMS deposition rates. *Journal of Physics D: Applied Physics*, 48(21):215202.
- Braüer, G., Szyszka, B., Vergöhl, M., and Bandorf, R. (2010). Magnetron sputtering - Milestones of 30 years. *Vacuum*, 84(12):1354—1359.
- Brenning, N., Butler, A., Hajihoseini, H., Rudolph, M., Raadu, M. A., Gudmundsson, J. T., Minea, T., and Lundin, D. (2020). Optimization of HiPIMS discharges: The selection of pulse power, pulse length, gas pressure, and magnetic field strength. *Journal of Vacuum Science and Technology A*, 38(3):033008.
- Brenning, N., Gudmundsson, J. T., Raadu, M. A., Petty, T. J., Minea, T., and Lundin, D. (2017). A unified treatment of self-sputtering, process gas recycling, and runaway for high power impulse sputtering magnetrons. *Plasma Sources Science and Technology*, 26(12):125003.
- Britun, N., Michiels, M., Godfroid, T., and Snyders, R. (2018). Ion density evolution in a high-power sputtering discharge with bipolar pulsing. *Applied Physics Letters*, 112(23):234103.
- Čada, M., Adámek, P., Straňák, V., Kment, Š., Olejníček, J., Hubička, Z., and Hippler, R. (2013). Angle-resolved investigation of ion dynamics in high power impulse magnetron sputtering deposition system. *Thin Solid Films*, 549:177–183.
- Čapek, J., Hála, M., Zabeida, O., Klemberg-Sapieha, J. E., and Martinu, L. (2013). Deposition rate enhancement in HiPIMS without compromising the ionized fraction of the deposition flux. *Journal of Physics D: Applied Physics*, 46(20):205205.
- Castaing, R. (1952). Application des sondes électroniques à une méthode d'analyse ponctuelle chimique et cristallographique. *These Université de Paris 1951*.
- Chapin, J. S. (January 1974). The planar magnetron. *Research/Development*, 25(1):37 – 40.
- Chapman, B. (1980). *Glow Discharge Processes: Sputtering and Plasma Etching*. John Wiley & Sons, New York.
- Christie, D. J. (2005). Target material pathways model for high power pulsed magnetron sputtering. *Journal of Vacuum Science and Technology A*, 23(2):330–335.



- Christou, C. and Barber, Z. H. (2000). Ionization of sputtered material in a planar magnetron discharge. *Journal of Vacuum Science and Technology A*, 18(6):2897–2907.
- Egerton, R. F. (2016). *Physical Principles of Electron Microscopy: An Introduction to TEM, SEM, and AEM*. Springer International Publishing, Cham, Switzerland, 2 edition.
- Ehiasarian, A. P., Münz, W. D., Hultman, L., Helmersson, U., and Petrov, I. (2003). High power pulsed magnetron sputtered CrN<sub>x</sub> films. *Surface and Coatings Technology*, 163-164:267–272.
- Ehiasarian, A. P., New, R., Münz, W.-D., Hultman, L., Helmersson, U., and Kouznetzov, V. (2002). Influence of high power densities on the composition of pulsed magnetron plasmas. *Vacuum*, 65(2):147–154.
- Ehiasarian, A. P., Wen, J. G., and Petrov, I. (2007). Interface microstructure engineering by high power impulse magnetron sputtering for the enhancement of adhesion. *Journal of Applied Physics*, 101(5):054301.
- Emmerlich, J., Mráz, S., Snyders, R., Jiang, K., and Schneider, J. M. (2008). The physical reason for the apparently low deposition rate during high power pulsed magnetron sputtering. *Vacuum*, 82(8):867–870.
- Ferrari, A. C., Libassi, A., Tanner, B. K., Stolojan, V., Yuan, J., Brown, L., Rodil, S. E., Kleinsorge, B., and Robertson, J. (2000). Density, *sp*<sup>3</sup> fraction, and cross-sectional structure of amorphous carbon films determined by x-ray reflectivity and electron energy-loss spectroscopy. *Physical Review B*, 62(16):11089.
- Ferrec, A., Kéraudy, J., and Jouan, P.-Y. (2016). Mass spectrometry analyzes to highlight differences between short and long HiPIMS discharges. *Applied Surface Science*, 390:497–505.
- Ferreira, F., Serra, R., Oliveira, J. C., and Cavaleiro, A. (2014). Effect of peak target power on the properties of Cr thin films sputtered by HiPIMS in deep oscillation magnetron sputtering (DOMS) mode. *Surface and Coatings Technology*, 258:249–256.
- Fetisov, I. K., Filippov, A. A., Khodachenko, G. V., Mozgrin, D. V., and Pisarev, A. A. (1999). Impulse irradiation plasma technology for film deposition. *Vacuum*, 53(1-2):133–136.
- Fetisov, I. K., Khodachenko, G. V., and Mozgrin, D. V. (1991). Quasy-stationary high current forms of low pressure discharge in magnetic field. In Palleschi, V. and Vaselli, M., editors, *Proceedings of the XX international conference on phenomena in ionized gases : Il Ciocco (Barga, Italy) 8th - 12th July 1991*, pages 474–475.
- Ganesan, R., Akhavan, B., Dong, X., McKenzie, D. R., and Bilek, M. M. M. (2018). External magnetic field increases both plasma generation and deposition rate in HiPIMS. *Surface and Coatings Technology*, 352:671–679.
- Gibson, P. N. (2011). Grazing incidence X-ray methods for near-surface structural studies. In Friedbacher, G. and Bubert, H., editors, *Surface and Thin Film Analysis: A Compendium of Principles, Instrumentation, and Applications*, pages 311–327. Wiley-VCH Verlag & Co, Weinheim, Germany.
- Gill, W. D. and Kay, E. (1965). Efficient low pressure sputtering in a large inverted magnetron suitable for film synthesis. *Review of Scientific Instruments*, 36(3):277–282.

- 
- Goldstein, J. I., Newbury, D. E., Michael, J. R., Ritchie, N. W. M., Scott, J. H. J., and Joy, D. C. (2018). *Scanning Electron Microscopy and X-Ray Microanalysis*. Springer Science + Business Media, New York, 4 edition.
- Green, K. M., Hayden, D. B., Juliano, D. R., and Ruzic, D. N. (1997). Determination of flux ionization fraction using a quartz crystal microbalance and a gridded energy analyzer in an ionized magnetron sputtering system. *Review of Scientific Instruments*, 68(12):4555–4560.
- Grove, W. R. (1852). On the electro-chemical polarity of gases. *Philosophical Magazine, Series 4*, 4(28):498–514.
- Gudmundsson, J. T. (2008). Ionized physical vapor deposition (IPVD): Magnetron sputtering discharges. *Journal of Physics: Conference Series*, 100:082002.
- Gudmundsson, J. T., Brenning, N., Lundin, D., and Helmersson, U. (2012). The high power impulse magnetron sputtering discharge. *Journal of Vacuum Science and Technology A*, 30(3):030801.
- Gudmundsson, J. T. and Lundin, D. (2020). Introduction to magnetron sputtering. In Lundin, D., Minea, T., and Gudmundsson, J. T., editors, *High Power Impulse Magnetron Sputtering: Fundamentals, Technologies, Challenges and Applications*, pages 1–48. Elsevier, Amsterdam, The Netherlands.
- Gudmundsson, J. T., Lundin, D., Stancu, G. D., Brenning, N., and Minea, T. M. (2015). Are the argon metastables important in high power impulse magnetron sputtering discharges? *Physics of Plasmas*, 22(11):113508.
- Hajihoseini, H. and Gudmundsson, J. T. (2017). Vanadium and vanadium nitride thin films grown by high power impulse magnetron sputtering. *Journal of Physics D: Applied Physics*, 50(50):505302.
- Hajihoseini, H., Kateb, M., Ingvarsson, S., and Gudmundsson, J. T. (2018). Effect of substrate bias on properties of HiPIMS grown vanadium nitride films. *Thin Solid Films*, 663:126–130.
- Hajihoseini, H., Kateb, M., Ingvarsson, S., and Gudmundsson, J. T. (2019a). Oblique angle deposition of nickel thin films by high-power impulse magnetron sputtering. *Beilstein Journal of Nanotechnology*, 10:1914–1921.
- Hajihoseini, H., Čada, M., Hubička, Z., Ünaldi, S., Raadu, M. A., Brenning, N., Gudmundsson, J. T., and Lundin, D. (2019b). The effect of magnetic field strength and geometry on the deposition rate and ionized flux fraction in the HiPIMS discharge. *Plasma*, 2:201–221.
- Hajihoseini, H., Čada, M., Hubička, Z., Ünaldi, S., Raadu, M. A., Brenning, N., Gudmundsson, J. T., and Lundin, D. (2020). Sideways deposition rate and ionized flux fraction in dc and high power impulse magnetron sputtering. *Journal of Vacuum Science and Technology A*, 38(3):033009.
- Hala, M., Viau, N., Zabeida, O., Klemberg-Sapieha, J. E., and Martinu, L. (2010). Dynamics of reactive high-power impulse magnetron sputtering discharge studied by time- and space-resolved optical emission spectroscopy and fast imaging. *Journal of Applied Physics*, 107(4):043305.
- Hecimovic, A. and Ehasarian, A. P. (2011). Temporal evolution of the ion fluxes for various elements in HiPIMS plasma discharge. *IEEE Transactions on Plasma Science*, 39(4):1154–1164.
- Helmersson, U., Lattemann, M., Alami, J., Bohlmark, J., Ehasarian, A. P., and Gud-

- mundsson, J. T. (2005). High power impulse magnetron sputtering discharges and thin film growth: A brief review. In *Proceedings of the 48th Society of Vacuum Coaters Annual Technical Conference*, pages 458 – 464, Albuquerque, New Mexico. Society of Vacuum Coaters.
- Helmersson, U., Lattemann, M., Bohlmark, J., Ehiasarian, A. P., and Gudmundsson, J. T. (2006). Ionized physical vapor deposition (IPVD): A review of technology and applications. *Thin Solid Films*, 513(1-2):1–24.
- Hopwood, J. (1998). Ionized physical vapor deposition of integrated circuit interconnects. *Physics of Plasmas*, 5(5):1624–1631.
- Hopwood, J. A. (2000). The role of ionized physical vapor deposition in integrated circuit fabrication. In Hopwood, J. A., editor, *Ionized Physical Vapor Deposition*, volume 27 of *Thin Films*, pages 1–7. Academic Press, San Diego, California.
- Huo, C., Lundin, D., Raadu, M. A., Anders, A., Gudmundsson, J. T., and Brenning, N. (2014). On the road to self-sputtering in high power impulse magnetron sputtering: particle balance and discharge characteristics. *Plasma Sources Science and Technology*, 23(2):025017.
- Huo, C., Raadu, M. A., Lundin, D., Gudmundsson, J. T., Anders, A., and Brenning, N. (2012). Gas rarefaction and the time evolution of long high-power impulse magnetron sputtering pulses. *Plasma Sources Science and Technology*, 21(4):045004.
- Ingason, A. S., Magnus, F., Agustsson, J. S., Olafsson, S., and Gudmundsson, J. T. (2009). In-situ electrical characterization of ultrathin TiN films grown by reactive dc magnetron sputtering on SiO<sub>2</sub>. *Thin Solid Films*, 517(24):6731–6736.
- Iseki, T. (2009). Target utilization of planar magnetron sputtering using a rotating tilted unbalanced yoke magnet. *Vacuum*, 84(2):339–347.
- Jagtap, R. N. and Ambre, A. H. (2006). Atomic force microscopy (AFM): Basics and its important applications for polymer characterization: An overview. *Indian Journal of Engineering and Materials Sciences*, 13(4):368–384.
- Kadlec, S. (2007). Simulation of neutral particle flow during high power magnetron impulse. *Plasma Processes and Polymers*, 4(S1):S419–S423.
- Kadlec, S., Quaeysaegens, C., Knuyt, G., and Stals, L. M. (1997). Energy distribution of ions in an unbalanced magnetron plasma measured with energy-resolved mass spectrometry. *Surface and Coatings Technology*, 89(1–2):177–184.
- Kay, E. (1963). Magnetic field effects on an abnormal truncated glow discharge and their relation to sputtered thin-film growth. *Journal of Applied Physics*, 34(4):760–768.
- Kelly, P. J. and Arnell, R. D. (2000). Magnetron sputtering: a review of recent developments and applications. *Vacuum*, 56(3):159 – 172.
- Keraudy, J., Nguyen, D. T., Ferrec, A., and Jouan, P.-Y. (2019). Comparison between DC and HiPIMS discharges. application to nickel thin films. In Fujita, H., Nguyen, D. C., Vu, N. P., Banh, T. L., and Puta, H. H., editors, *International Conference on Engineering Research and Applications (ICERA 2018): Advances in Engineering Research and Application*, volume 63 of *Lecture Notes in Networks and Systems*, pages 196–203. Springer-Verlag, Springer, Cham.
- Klawuhn, E., D’Couto, G. C., Ashtiani, K. A., Rymer, P., Biberger, M. A., and Levy, K. B. (2000). Ionized physical-vapor deposition using a hollow-cathode magnetron source for advanced metallization. *Journal of Vacuum Science and Technology A*, 18(4):1546–1549.

- 
- Knoll, M. and Theile, R. (1939). Elektronenabtaster zur strukturabbildung von oberflächen und dünnen schichten. *Zeitschrift für Physik*, 113(3-4):260–280.
- Konstantinidis, S., Dauchot, J., and Hecq, M. (2006a). Titanium oxide thin films deposited by high-power impulse magnetron sputtering. *Thin Solid Films*, 515(3):1182–1186.
- Konstantinidis, S., Dauchot, J. P., Ganciu, M., and Hecq, M. (2006b). Influence of pulse duration on the plasma characteristics in high-power pulsed magnetron discharges. *Journal of Applied Physics*, 99(1):013307.
- Konstantinidis, S., Dauchot, J. P., Ganciu, M., and Hecq, M. (2006c). Transport of ionized metal atoms in high-power pulsed magnetron discharges assisted by inductively coupled plasma. *Applied Physics Letters*, 88(2):021501.
- Kouznetsov, V., Macák, K., Schneider, J. M., Helmersson, U., and Petrov, I. (1999). A novel pulsed magnetron sputter technique utilizing very high target power densities. *Surface and Coatings Technology*, 122(2-3):290–293.
- Kubart, T., Čada, M., Lundin, D., and Hubička, Z. (2014). Investigation of ionized metal flux fraction in HiPIMS discharges with Ti and Ni targets. *Surface and Coatings Technology*, 238:152–157.
- Laue, M. V. (1912). Zwei einwände gegen die relativitätstheorie und ihre widerlegung. *Physikalische Zeitschrift*, 13:118–120.
- Leroy, W. P., Konstantinidis, S., Mahieu, S., Snyders, R., and Depla, D. (2011). Angular-resolved energy flux measurements of a dc- and HIPIMS-powered rotating cylindrical magnetron in reactive and non-reactive atmosphere. *Journal of Physics D: Applied Physics*, 44(11):115201.
- Lieberman, M. A. and Gottscho, R. A. (1994). Design of high-density plasma sources for materials processing. In Francombe, M. and Vossen, J., editors, *Physics of Thin Films, vol. 18*, pages 1 – 119. Academic Press, New York.
- Liebig, B., Braithwaite, N. S. J., Kelly, P. J., Chistyakov, R., Abraham, B., and Bradley, J. (2011). Time-resolved plasma characterisation of modulated pulsed power magnetron sputtering of chromium. *Surface and Coatings Technology*, 205:S312–S316.
- Lifshin, E. (2001). Electron microprobe analysis. In Cahn, K. H. J. B. R. W., Flemings, M. C., Ilschner, B., Kramer, E. J., Mahajan, S., and Veyssièrè, P., editors, *Encyclopedia of Materials: Science and Technology*, pages 2563–2569. Pergamon Press, London, United Kingdom, 2 edition.
- Low, K., Nafarizal, N., Sahdan, M. Z., Kadir, M. A., bin Ahmad, M. K., Yeon, M. S. A., Ammar, Z., Ahmad Saad, F. S., and Mohd Zain, A. F. (2014). Influence of dissipation power in copper sputtering plasma measured by optical emission spectroscopy. *Advanced Materials Research*, 832:243–247.
- Lundin, D., Brenning, N., Jadernas, D., Larsson, P., Wallin, E., Lattemann, M., Raadu, M. A., and Helmersson, U. (2009). Transition between the discharge regimes of high power impulse magnetron sputtering and conventional direct current magnetron sputtering. *Plasma Sources Science and Technology*, 18(4):045008.
- Lundin, D., Hecimovic, A., Minea, T., Anders, A., Brenning, N., and Gudmundsson, J. T. (2020a). Physics of high power impulse magnetron sputtering discharges. In Lundin, D., Minea, T., and Gudmundsson, J. T., editors, *High Power Impulse Magnetron Sputtering: Fundamentals, Technologies, Challenges and Applications*, pages 265–332. Elsevier, Amsterdam, The Netherlands.

- Lundin, D., Larsson, P., Wallin, E., Lattemann, M., Brenning, N., and Helmersson, U. (2008). Cross-field ion transport during high power impulse magnetron sputtering. *Plasma Sources Science and Technology*, 17(3):035021.
- Lundin, D., Minea, T., and Gudmundsson, J. T., editors (2020b). *High Power Impulse Magnetron Sputtering: Fundamentals, Technologies, Challenges and Applications*. Elsevier, Amsterdam, The Netherlands.
- Lundin, D., Sahab, S. A., Brenning, N., Huo, C., and Helmersson, U. (2011). Internal current measurements in high power impulse magnetron sputtering. *Plasma Sources Science and Technology*, 20(4):045003.
- Lundin, D. and Sarakinos, K. (2012). An introduction to thin film processing using high power impulse magnetron sputtering. *Journal of Materials Research*, 27(5):780–792.
- Lundin, D., Čada, M., and Hubička, Z. (2015). Ionization of sputtered Ti, Al, and C coupled with plasma characterization in HiPIMS. *Plasma Sources Science and Technology*, 24(3):035018.
- Macák, K., Kouznetsov, V., Schneider, J., Helmersson, U., and Petrov, I. (2000). Ionized sputter deposition using an extremely high plasma density pulsed magnetron discharge. *Journal of Vacuum Science and Technology A*, 18(4):1533 – 1537.
- Magnus, F., Ingason, A. S., Olafsson, S., and Gudmundsson, J. T. (2012). Nucleation and resistivity of ultrathin TiN films grown by high power impulse magnetron sputtering. *IEEE Electron Device Letters*, 33(7):1045 – 1047.
- Mahieu, S., Ghekiere, P., Depla, D., and De Gryse, R. (2006). Biaxial alignment in sputter deposited thin films. *Thin Solid Films*, 515(4):1229–1249.
- Marturi, N. (2013). *Vision and Visual Servoing for Nanomanipulation and Nanocharacterization using Scanning Electron Microscope*. PhD thesis, Université de Franche-Comté, France.
- Mattox, D. M. (1998). *Handbook of physical vapor deposition (PVD) processing: Film Formation, Adhesion, Surface Preparation and Contamination Control*. Noyes Publications, Westwood, New Jersey.
- Miccoli, I., Edler, F., Pfnür, H., and Tegenkamp, C. (2015). The 100th anniversary of the four-point probe technique: the role of probe geometries in isotropic and anisotropic systems. *Journal of Physics: Condensed Matter*, 27(22):223201.
- Mishra, A., Kelly, P. J., and Bradley, J. W. (2010). The evolution of the plasma potential in a HiPIMS discharge and its relationship to deposition rate. *Plasma Sources Science and Technology*, 19(4):045014.
- Mozgrin, D. V. (1994). *High-current low-pressure quasi-stationary discharge in a magnetic field: Experimental research*. PhD thesis, Moscow Engineering Physics Institute (MePhi), Moscow, Russian Federation.
- Mozgrin, D. V., Fetisov, I. K., and Khodachenko, G. V. (1995). High-current low-pressure quasi-stationary discharge in a magnetic field: Experimental research. *Plasma Physics Reports*, 21(5):400–409.
- Murphy, B. E. (2014). *The physico-chemical properties of fullerenes and porphyrin derivatives deposited on conducting surfaces*. PhD thesis, Trinity College Dublin.
- Musil, J. and Kadlec, S. (1990). Reactive sputtering of tin films at large substrate to target distances. *Vacuum*, 40(5):435–444.
- Musil, J., Kadlec, S., and Münz, W.-D. (1991). Unbalanced magnetrons and new sputtering systems with enhanced plasma ionization. *Journal of Vacuum Science and*

- 
- Technology A*, 9(3):1171 – 1177.
- Nagao, K. and Kagami, E. (2011). X-ray thin film measurement techniques. pole figure measurement. *The Rigaku Journal*, 27(2):6–14.
- Nakano, T., Hirukawa, N., Saeki, S., and Baba, S. (2013). Effects of target voltage during pulse-off period in pulsed magnetron sputtering on afterglow plasma and deposited film structure. *Vacuum*, 87:109–113.
- Ohring, M. (2002). *Materials Science of Thin Films*. Academic Press, San Diego, California, 2 edition.
- Parratt, L. G. (1954). Surface studies of solids by total reflection of X-rays. *Physical Review*, 95(2):359–369.
- Paulitsch, J., Schenkel, M., Zufraß, T., Mayrhofer, P., and Münz, W.-D. (2010). Structure and properties of high power impulse magnetron sputtering and DC magnetron sputtering CrN and TiN films deposited in an industrial scale unit. *Thin Solid Films*, 518(19):5558–5564.
- Penning, F. M. (1936). Die glimmentladung bei niedrigem druck zwischen koaxialen zylindern in einem axialen magnetfeld. *Physica*, 3(9):873–894.
- Pessoa, R. S., Fraga, M. A., Santos, L. V., Galvão, N. K. A. M., Maciel, H. S., and Massi, M. (2015). Plasma-assisted techniques for growing hard nanostructured coatings: an overview. In Aliofkhaezrai, M., editor, *Anti-Abrasive Nanocoatings: Current and Future Applications*, pages 455–479. Woodhead Publishing, Cambridge, United Kingdom.
- Poolcharuansin, P., Bowes, M., Petty, T. J., and Bradley, J. W. (2012). Ionized metal flux fraction measurements in HiPIMS discharges. *Journal of Physics D: Applied Physics*, 45(32):322001.
- Poolcharuansin, P. and Bradley, J. W. (2010). Short and long-term plasma phenomena in a HiPIMS discharge. *Plasma Sources Science and Technology*, 19(2):025010.
- Raadu, M. A., Axnäs, I., Gudmundsson, J. T., Huo, C., and Brenning, N. (2011). An ionization region model for high power impulse magnetron sputtering discharges. *Plasma Sources Science and Technology*, 20(6):065007.
- Raman, P., Shchelkanov, I., McLain, J., Cheng, M., Ruzic, D., Haehnlein, I., Jurczyk, B., Stubbers, R., and Armstrong, S. (2016). High deposition rate symmetric magnet pack for high power pulsed magnetron sputtering. *Surface and Coatings Technology*, 293:10–15.
- Raman, P., Shchelkanov, I. A., McLain, J., and Ruzic, D. N. (2015). High power pulsed magnetron sputtering: A method to increase deposition rate. *Journal of Vacuum Science and Technology A*, 33(3):031304.
- Revel, A., Minea, T., and Costin, C. (2018). 2D PIC-MCC simulations of magnetron plasma in HiPIMS regime with external circuit. *Plasma Sources Science and Technology*, 27(10):105009.
- Rohde, S. L. (1994). Unbalanced magnetron sputtering. In Francombe, M. H. and Vossen, J. L., editors, *Plasma Sources for Thin Film Deposition and Etching*, volume 18 of *Physics of Thin Films*, pages 235–288. Academic Press, New York.
- Rossnagel, S. (2000). Ionization by radio frequency inductively coupled plasma. In Hopwood, J. A., editor, *Ionized physical vapor deposition*, volume 27 of *Thin Films*, pages 37–66. Academic Press, San Diego, California.
- Rossnagel, S. M. and Hopwood, J. (1993). Magnetron sputter deposition with high

- levels of metal ionization. *Applied Physics Letters*, 63(24):3285–3287.
- Rossnagel, S. M. and Hopwood, J. (1994). Metal ion deposition from ionized magnetron sputtering discharge. *Journal of Vacuum Science and Technology B*, 12(1):449–453.
- Rossnagel, S. M. and Kaufman, H. R. (1988). Current-voltage relations in magnetrons. *Journal of Vacuum Science and Technology A*, 6(2):223 – 229.
- Samuelsson, M., Lundin, D., Jensen, J., Raadu, M. A., Gudmundsson, J. T., and Helmersson, U. (2010). On the film density using high power impulse magnetron sputtering. *Surface and Coatings Technology*, 202(2):591–596.
- Sarakinos, K., Alami, J., and Konstantinidis, S. (2010). High power pulsed magnetron sputtering: Scientific and engineering state of the art. *Surface and Coatings Technology*, 204(11):1661–1684.
- Sarakinos, K. and Martinu, L. (2020). Synthesis of thin films and coatings by high power impulse magnetron sputtering. In Lundin, D., Minea, T., and Gudmundsson, J. T., editors, *High Power Impulse Magnetron Sputtering: Fundamentals, Technologies, Challenges and Applications*, pages 333–374. Elsevier, Amsterdam, The Netherlands.
- Schiller, S., Goedicke, K., Reschke, J., Kirchoff, V., Schneider, S., and Milde, F. (1993). Pulsed magnetron sputter technology. *Surface and Coatings Technology*, 61(1–3):331 – 337.
- Sigmund, P. (1969). Theory of sputtering. I. Sputtering yield of amorphous and polycrystalline targets. *Physical Review*, 184(2):383–416.
- Sigmund, P. (1987). Mechanisms and theory of physical sputtering by particle impact. *Nuclear Instruments and Methods in Physics Research Section B: Beam Interactions with Materials and Atoms*, 27(1):1–20.
- Stancu, G. D., Brenning, N., Vitelaru, C., Lundin, D., and Minea, T. (2015). Argon metastables in HiPIMS: Validation of the ionization region model by direct comparison to time resolved tunable diode-laser diagnostics. *Plasma Sources Science and Technology*, 24(4):045011.
- Sultan, M., Gudmundsson, J. T., Manolescu, A., Teodorescu, V. S., Ciurea, M. L., and Svavarsson, H. G. (2019). Efficacy of annealing and fabrication parameters on photo-response of SiGe in TiO<sub>2</sub> matrix. *Nanotechnology*, 30(36):365604.
- Sultan, M. T., Gudmundsson, J. T., Manolescu, A., Teodorescu, V. S., Ciurea, M. L., and Svavarsson, H. G. (2020). Obtaining SiGe nanocrystallites between crystalline TiO<sub>2</sub> layers by HiPIMS without annealing. *Applied Surface Science*, 511:145552.
- Svadkovski, I. V., Golosov, D. A., and Zavatskiy, S. M. (2002). Characterisation parameters for unbalanced magnetron sputtering systems. *Vacuum*, 68(4):283–290.
- Swann, S. (1987). Spatial distribution of sputtered atoms from magnetron source. *Journal of Vacuum Science & Technology A: Vacuum, Surfaces, and Films*, 5(4):1750–1754.
- Sze, S. M. and Ng, K. K. (2006). *Physics of semiconductor devices*. John Wiley & sons.
- Tesař, J., Martan, J., and Rezek, J. (2011). On surface temperatures during high power pulsed magnetron sputtering using a hot target. *Surface and Coatings Technology*, 206(6):1155–1159.
- Velicu, I.-L., Tiron, V., and Popa, G. (2014). Dynamics of the fast-HiPIMS discharge during FINEMET-type film deposition. *Surface and Coatings Technology*, 250:57–64.
- Vitelaru, C., Lundin, D., Stancu, G. D., Brenning, N., Bretagne, J., and Minea, T. (2012).

- 
- Argon metastables in hipims: time-resolved tunable diode-laser diagnostics. *Plasma Sources Science and Technology*, 21(2):025010.
- Vlcek, J., Zustin, B., Rezek, J., Brucalova, K., and Tesar, J. (2009). Pulsed magnetron sputtering of metallic films using a hot target. In *Proceedings of the 52nd Annual Technical Conference Society of Vacuum Coaters, May 9 – 14, 2009, Santa Clara, California*, pages 219–223, Albuquerque, New Mexico. Society of Vacuum Coaters.
- Voigtländer, B. (2015). *Scanning Probe Microscopy, Atomic Force Microscopy and Scanning Tunneling Microscopy*. Springer, Heidelberg.
- Von Ardenne, M. (1938). Das elektronen-rastermikroskop. *Zeitschrift für Physik*, 109(9-10):553–572.
- Vossen, J. L. and Cuomo, J. J. (1978). Glow discharge sputter deposition. In Vossen, J. L. and Kern, W., editors, *Thin Film Processes*, volume 4, pages 11–73. Academic Press, New York.
- Waits, R. K. (1978). Planar magnetron sputtering. *Journal of Vacuum Science and Technology*, 15(2):179 – 187.
- Widjonarko, N. E. (2016). Introduction to advanced x-ray diffraction techniques for polymeric thin films. *Coatings*, 6(4):54.
- Window, B. and Savvides, N. (1986). Charged particle fluxes from planar magnetron sputtering sources. *Journal of Vacuum Science and Technology A*, 4(2):196–202.
- Wu, B., Haehnlein, I., Shchelkanov, I., McLain, J., Patel, D., Uhlig, J., Jurczyk, B., Leng, Y., and Ruzic, D. N. (2018). Cu films prepared by bipolar pulsed high power impulse magnetron sputtering. *Vacuum*, 150:216–221.
- Wu, L., Ko, E., Dulkan, A., Park, K. J., Fields, S., Leeser, K., Meng, L., and Ruzic, D. N. (2010). Flux and energy analysis of species in hollow cathode magnetron ionized physical vapor deposition of copper. *Review of Scientific Instruments*, 81(12):123502.
- Yamashita, M. (1989). Fundamental characteristics of built-in high-frequency coil-type sputtering apparatus. *Journal of Vacuum Science and Technology A*, 7(2):151–158.
- Yang, P., Ren, C., Wang, D., Qi, X., Guo, S., and Ma, T. (2009). Influence of additional magnetic field on plasma parameters in magnetron sputtering. *Vacuum*, 83(11):1376 – 1381.
- Yu, H., Meng, L., Szott, M. M., Meister, J. T., Cho, T. S., and Ruzic, D. N. (2013). Investigation and optimization of the magnetic field configuration in high-power impulse magnetron sputtering. *Plasma Sources Science and Technology*, 22(4):045012.
- Yushkov, G. Y. and Anders, A. (2010). Origin of the delayed current onset in high power impulse magnetron sputtering. *IEEE Transactions on Plasma Science*, 38(11):3028–3034.



